Roughness of fault surfaces : analyses and implications for the heterogeneity of seismic rupture

Thibault Candela

UNIVERSITÉ DE GRENOBLE

THÈSE

Pour obtenir le grade de

DOCTEUR DE L'UNIVERSITÉ DE GRENOBLE

Spécialité : **TERRE, UNIVERS, ENVIRONNEMENT**

Arrêté ministériel : 7 août 2006

Présentée par

Thibault Candela

Thèse dirigée par **François Renard** et
codirigée par **Michel Bouchon**

préparée au sein du **Laboratoire ISTerre**
dans **l'École Doctorale TUE**

La Rugosité des Failles : Analyse et Conséquences sur l'Hétérogénéité des Ruptures Sismiques

Thèse soutenue publiquement le **23/03/2011**,
devant le jury composé de :

Mr Raúl Madariaga
Professeur à l'ENS de Paris (Rapporteur)
Mr Yann Klinger
Chargé de Recherche à l'IPG de Paris (Rapporteur)
Mr Jean Schmittbuhl
Directeur de Recherche à l'IPG de Strasbourg (Président)
Mlle Karen Mair
Professeur au PGP Oslo (Examinateur)
Mr François Renard
Professeur à l'ISTerre Grenoble (Directeur de thèse)
Mr Michel Bouchon
Directeur de Recherche à l'ISTerre Grenoble (Directeur de thèse)

Remerciements

C’est ici que je me dois de jeter un coup d’oeil en arrière (une fois n’est pas coutume) afin de remercier le bon nombre de personnes formidables qui m’ont accompagné et encouragé durant ma thèse et même avant…

Tout d’abord, je tiens à remercier chaleureusement mes deux directeurs François et Michel pour leur aide et leur soutien sans faille ! Nos discussions, souvent animées, ont toujours été très productives. Merci François d’avoir eu constamment confiance en moi dès mon arrivé en thèse à Grenoble. Ton optimisme intarissable, même face à mes idées les plus loufoques, fut un véritable moteur pour mon travail de recherche. Dans mes moments de doutes, je n’avais qu’à franchir la porte de ton bureau pour me regonfler le moral. Michel, même si nous n’avons pas le même jargon scientifique, tu as su m’entendre et me conseiller à chaque fois que je t’ai sollicité. Ton extrême gentillesse a su tempérer mon entêtement face aux flots d’hypothèses souvent naïves que je proposais. Merci à vous deux pour votre énorme générosité humaine, et j’espère sincèrement que ce n’est que le début d’une véritable amitié.

En me remémorant l’intégralité des membres de mon jury, à savoir Raul Madariaga, Yann Klinger, Karen Mair et Jean Schmittbuhl je me rends compte de la chance qu’il m’ait été donné d’échanger mes idées avec ces spécialistes d’horizons « geo-scientifiques » variées. Je tiens à les remercier de m’avoir fait l’honneur de bien vouloir évaluer mon travail.

Merci à toutes les personnes de l’ex-LGCA et de l’ex-LGIT qui m’ont aidé au cours de ma thèse. Oui ! J’étais donc ISTerrien avant l’heure ! (Elle est pour toi celle-ci Jéjé). En premier lieu, je tiens à remercier Claudine, Claudie, Christine, et Aurore, qui ont su prendre avec sourire toutes mes bourdes administratives. Merci Pascale pour tes prouesses dans la recherche bibliographique et ta patience face à mes questions redondantes… Un grand merci à Maria pour sa bonne humeur quotidienne. Merci à Rodolphe pour avoir su régler chacun de mes petits « bobos informatiques » !
La chaleur humaine qui déborde du troisième étage de la maison des géosciences fut pour moi un véritable poumon durant ces dernières années. Je tiens à remercier ici tous les « chercheurs confirmés » de l’ex-LGCA qui contribuent à cette ambiance exceptionnelle: Catherine, Pascale, Emilie, Alexandra, Laurence, Etienne, Matthias, German, Stéphane(s), Thierry, Emilie, Pierre, Alex, Julien, Pieter, Jean, Olivier, Manu(s), Eric…

Merci également à tous les membres de l’équipe « Mécanique des failles » qui ont subit mes nombreuses présentations à l’oral, souvent laborieuses… Je te remercie David pour avoir pris sur ton temps pour décortiquer mes analyses farfelues ! Merci à Jean-Pierre et Mai Linh pour les nombreuses discussions passionnées que nous avons eu ensemble sur les failles et plus particulièrement sur le terrain face à celle de « Punchbowl », « La Clery » et « La Vuache ». Je pense ici également à Seb qui par son caractère de guerrier, me montre la voie à suivre pour continuer dans le monde de la recherche. Anne-Marie, milles mercis pour ton extrême gentillesse et pour ton travail… C’est en lisant certaines de tes publications pendant mon Master qu’il m’est apparut évident de concentrer mes efforts sur la compréhension de la mécanique des failles. A ce stade, j’en profite ici pour remercier l’ensemble des professeurs de Montpellier, à qui je dois l’intégralité de ma formation universitaire en géologie et qui ont su me donner l’envie de me lancer dans une thèse. Merci à Jacques Malavieille et Alain Chauvet, qui ont accompagnés mes premiers pas dans l’étude des zones de failles et qui ont su m’encourager afin de persévérer dans cette voie. Promis ce papier sur Taiwan on va l’achever !

Je souhaite ici évoquer et remercier les personnes que j’ai eu la chance de côtoyer lors de collaborations aussi bien en France qu’à l’étranger. En premier lieu un grand merci à Jean

Schmittbuhl et Renaud Toussain qui, face à ma mémoire bien souvent trop courte, m'ont patiemment aiguillé pour l'utilisation du rugosimètre à chacun de mes séjours sur Strasbourg. Jean, ta rigueur scientifique et ta modestie font de toi un modèle. Les discussions à la fois captivantes et interminables que nous avons eues autour du couple « bière-Kebab » restent à mes yeux des moments magiques. Merci également pour ce crochet en Turquie, et je salue par la même occasion Hayrullah Karabulut ! Je remercie sincèrement Emily, Nicholas, Jamie… qui ont pris le temps de déchiffrer mes longues phrases désastreuses en « franglais » lors de mes nombreux passages à Santa Cruz… Un immense merci à Emily Brodsky pour m'avoir emmener en face de miroir de failles hors normes. Je remercie également deux éminences grises de la physique des séismes: Yehuda Ben-Zion et Giulio Di Toro. Chaque rencontre avec ces derniers fut des instants importants, riches en conseils. Enfin, mes séjours au PGP d'Oslo ont été agréablement agrémentés par la présence de nombreuses personnes que je remercie ici : Karen Mair, Dag Kristian Dysthe, Stéphane Santucci, Joachim Mathiesen, Delphine Croizé. Karen, une véritable pépite ce Caol Ila !

C'est parti ! J'amorce à présent les amis qui ont jalonnés les sentiers rugueux empruntés durant mon expérience de thèse. Merci à tous les étudiants, thésards, Masters de l'ex- LGCA, ex-LGIT, et, soyons fou, de l'ISTerre, qui m'ont accompagnés durant ces dernières années. Allez, je me lance ! Ma révérence au trois lascars du bureau 349 : Chichi pour ton pragmatisme qui est presque devenu un reflexe chez toi et m'a souvent régalé, Toto pour ta quiétude face à mes assauts sarcastiques quotidiens et parce que tu es de loin le meilleur ! Ah Delu… merci d'avoir toujours été là pour m'accompagner dans mes virées épicuriennes ! Ne changes pas, ne bouges pas, j'arrive d'ici peu… Je vais placer ici directement ta douce Shaz, qui a subit à peu près toutes mes déviances machistes… merci milles fois d'avoir été là ! Un grand merci à TSL, dit « la force tranquille » qui m'a fait souvent relativisé face à mon stress permanent. Vient naturellement le Marcaillou, et son immense efficacité dans la besogne, dont j'aurais aimé m'inspirer un peu plus. Je remercie ici les anciens, à savoir : Bobby (merci pour le Big up à Patou), Marion (plus jamais de vélo…), Jérémie, Thomas…vos fantômes hantent les locaux de l'ex-LGCA… Merci Carcaille pour toutes les fois que tu m'as sorti la tête de mon écran avec tes histoires courtes. Un grand merci à Manu qui m'a à la fois supporté en carto et lors de nos débats à teneur « politico-bituresque »… Je remercie également le Steph (alias Schwarzy), arrivé sur le tard, mais qui ne cesse de me surprendre par sa facilité à l'ineptie ! J'en arrive à l'irremplaçable Jejé ! Qu'est ce que j'aurais fait sans toi, et tes innombrables « ca va toi ? ». Tu n'as jamais failli… Merci ! Je suis fier d'être ton ami.

Comment ne pas remercier mes amis de longue date : Patou, Flopi, Virginie, Charlotte, Jeannot, Soussouss... qui savent à quels points je leur attache de l'importance... Je serais donc bref : Merci à tous ! Je réalise la chance que j'ai de vous avoir rencontré lors de mes années Montpelliéraines.
Je passe au noyau dur : les Arlésiens ! Je suis parti dans mes cailloux… mais vous avez toujours été là… sûrement moi pas autant que vous… Merci infiniment ! Pour ne citer qu'eux : Vinzqui, Nico, Tétée, Roger, Mathieu, Mimi (Thais !!)… Je vous aime ! Spécial remerciement à Emilie, Guigue, et Stouf pour s'être déplacés pour ma soutenance !

Enfin, je ne saurai jamais assez remercier ma famille qui m'a soutenu, voire supporté (et me supportera encore) depuis mes premiers pas… Merci Papa, Merci Maman, Merci Romain (et Sophie !), Merci Damien (et Cécile, Lucille !) : Je vous dois tout ! Et suis plus que fier et heureux de me rendre compte au fil des années que vous êtes une partie de ce que je suis !

Thibault, Printemps 2011

Résumé

Les aspérités géométriques d'un plan de faille contrôlent en partie toutes les étapes de la rupture sismique, depuis sa nucléation jusqu'à l'arrêt du séisme. L'objectif de ce travail est de caractériser la morphologie des surfaces de faille sur la large gamme d'échelles spatiales impliquées dans les tremblements de terre, puis d'explorer son influence sur l'organisation spatiale du glissement et des contraintes. L'approche utilisée inclue des observations de terrain couplées à une étude numérique et théorique.

La combinaison de méthodes récentes de mesures topographiques (LiDAR, rugosimètre laser, interféromètre à lumière blanche), qui couvrent des gammes d'échelles spatiales complémentaires, permet de proposer un modèle géométrique cohérent de cinq zones de failles étudiées (Alpes françaises, Apennins, Turquie, Californie, Nevada). La rugosité des surfaces de failles montre des propriétés de dépendance d'échelle, et plus précisément suit un régime auto-affine anisotrope (l'exposant de rugosité est $H_{//} = 0.6$ dans la direction du glissement et $H_{\perp} = 0.8$ dans la direction perpendiculaire) depuis la centaine de micromètres jusqu'à plusieurs dizaines de mètres. En complément, l'analyse de la rugosité des ruptures de surface de huit tremblements de terre continentaux majeurs montre qu'un unique régime auto-affine anisotropique et sans longueur caractéristique est maintenu jusqu'à l'épaisseur de la croute sismogénique. Cette description de la géométrie des surfaces de failles et des traces de ruptures, est indépendante du contexte géologique. Plus particulièrement, cette étude met en avant que dès lors qu'un glissement cumulé métrique est atteint sur une faille, la complexité géométrique des portions actives des zones de failles est maintenue quel que soit le déplacement supplémentaire accommodé. Finalement, motivé par des observations de terrain, il est proposé que le processus dominant à l'origine de la rugosité des surfaces de failles puisse être l'interaction mécanique et la coalescence de segments multi-échelles.

Deux conséquences émergent de cet état de rugosité. Les distributions spatiales du champ de glissement d'une part et du champ des contraintes lors d'un tremblement de terre d'autre part peuvent être expliquées par la présence de deux interfaces rugueuses auto-affines pressées élastiquement et cisaillées. Notamment, en utilisant un modèle numérique de propagation d'une rupture sur une interface hétérogène, la corrélation entre la rugosité 3-D des failles et la distribution spatiale 2-D du glissement dans le plan est clarifiée. Il est proposé que les hétérogénéités spatiales du glissement visibles sur les modèles cinématiques de rupture sismique soient préférentiellement dominées par les complexités géométriques locales plutôt que par la dynamique du front de rupture lui-même. Par ailleurs, les propriétés auto-affines des lèvres de la faille impliquent que les fluctuations spatiales de la chute de contrainte lors d'un séisme augmentent vers les courtes longueurs d'ondes ; ce qui est confirmé par des observations sismologiques. En considérant un modèle de rupture en cascade, il est alors probable que les failles sont fortement inhomogènes, avec des grands tremblements de terre composés d'une somme de petites aspérités multi-échelles qui subissent de fortes chutes de contrainte. Cette étude met en lumière l'importance des hétérogénéités locales en contrainte et en glissement dans la mécanique des tremblements de terre, et propose de les relier à des propriétés morphologiques self-affines de la surface de faille.

Abstract

Geometrical asperities on fault planes partially control all stages of earthquake genesis, from the nucleation of a rupture, to its arrest. The present study aims at characterizing the geometrical morphology of fault surfaces on the wide range of spatial length scales involved in earthquakes, and exploring its influence on the spatial organization of slip and stresses during an earthquake. The approach combines field observations, numerical analysis and theory.

Using recent methods of high resolution topographic measurements (LiDAR, laser profilometer, white light interferometer), spanning complementary ranges of spatial length scales, a consistent geometrical model emerges for the five fault zones (French Alps, Apennines, Turkey, California, Nevada) studied here. The morphology of the fault surface, i.e. its roughness, is scale dependent, and more specifically follows a self-affine anisotropic regime (the roughness exponent is $H_{//} = 0.6$ in the slip direction and $H_{\perp} = 0.8$ perpendicular to it) from the scale of hundred of micrometers to several tens of meters. In addition, the roughness analysis of the surface rupture of height major continental earthquakes shows that a single self-affine regime is maintained up to the thickness of the seismogenic crust, without any characteristic length scale. This description of the geometry of the fault scarps and rupture traces is independent of the geological context. More particularly, this study highlights that once a fault has achieved a cumulated a small offset no larger than one meter, the roughness of the active portion of the fault zone is maintained even if further slip is accommodated. Finally, motivated by field observations, it is proposed that the main process causing the roughness of fault surfaces can be the mechanical interaction and coalescence of multi-scale segments.

Based on a numerical and theoretical approach, the spatial distribution of both the slip and stress fields during an earthquake can be understood by the presence of two self-affine rough interfaces elastically squeezed and sheared. Using a numerical model of rupture propagation on a heterogeneous interface, the link between the 3-D fault roughness and the 2-D spatial distribution of the slip is clarified. It is proposed that the spatial heterogeneity of the slip observed on kinematic models of earthquake rupture is preferentially dominated by the local geometrical complexity rather than the dynamic of rupture itself. Moreover, the self-affine properties of the fault interfaces imply that the spatial fluctuations of the stress drop after a rupture event increase towards shorter wavelengths. Considering a rupture cascade model, it is likely that the faults may be considered as highly inhomogeneous with large earthquakes composed by a sum of multi-scales ruptures of small asperities with large stress drop within an average fault surface with small stress drop. This study emphasizes the importance of local stress and slip heterogeneities on the mechanics of earthquakes and proposes to relate these parameters to the self-affine morphology of the fault surfaces.

Table des matières / Table of contents

Chapter 1:

Introduction

1.1. Introduction

Sous les conditions de basse pression et température de la partie supérieure de la lithosphère terrestre, les roches se fracturent en réponse au chargement tectonique. Cette fracturation se traduit par la présence de failles à toutes les échelles, le long desquelles la déformation est localisée. Les failles correspondent à des interfaces rugueuses où les contraintes au sein de la roche ont causé une perte de cohésion du matériau, accompagnée d'un glissement. La surface de faille est alors la trace laissée derrière lui par le front de propagation de la rupture. La propagation d'une faille par fracturation et glissement frictionnel peut être lente et stable, ou bien rapide et catastrophique. Ce dernier cas correspond à l'occurrence d'un tremblement de terre qui est la manifestation de la relaxation brutale d'énergie stockée sous forme élastique. La morphologie géométrique (i.e. rugosité) d'un plan de faille joue un rôle important dans l'initiation de la rupture en concentrant les contraintes aux niveaux d'aspérités, dans sa propagation et son arrêt en freinant le glissement. Les modèles cinématiques mettent en évidence l'hétérogénéité spatiale de la distribution du glissement durant un tremblement de terre, et révèlent indirectement le premier ordre de la complexité de la surface de faille en profondeur. L'unique accès d'une fine description de la morphologie des failles aux échelles impliquées durant le glissement, provient des observations de failles exhumées. Dans un premier temps, j'ai analysé sur le terrain la rugosité des surfaces de failles depuis la taille du grain jusqu'à l'échelle kilométrique. Cette première partie avait pour but de répondre à plusieurs questions scientifiques, à savoir : (i) Comment et par quels outils peut-on caractériser au plus juste la rugosité des failles ? (ii) Est-il possible de décrire ces surfaces avec un nombre restreint de paramètres ou cela nécessite t-il la connaissance exacte de toute la topographie ? (iii) Existe-t-il un modèle géométrique universel qui puissent décrire les surfaces de failles naturelles ou des variabilités se dégagent suivant l'échelle d'observation et le contexte tectonique ? Puis, dans un second temps, j'ai exploré les implications de la géométrie non triviale des failles sur la mécanique des tremblements de terre au travers de modèles théoriques et numériques. Plus particulièrement, j'ai essayé de comprendre comment cette rugosité participe à l'hétérogénéité des champs de glissement et de contrainte le long de la faille, observée par les sismologues ?

1.2. Complexité géométrique des zones de failles

Les processus complexes modelant les zones de failles et contrôlant les tremblements de terre ne peuvent être observés directement dans l'intérieur de la terre qui reste essentiellement opaque. Malgré les progrès croissants dans l'imagerie géophysique des zones de failles en profondeur, les images obtenues sont des versions floutées de leur réelle structuration. L'unique moyen à ce jour de quantifier précisément la géométrie des zones de failles reste les observations de surfaces. Deux types de données de surface s'offrent alors à nous : (i) les zones de failles profondes exhumées à la surface, soit par l'érosion ou directement par le déplacement consécutif aux tremblements de terre ; (ii) les traces de la rupture sismique laissée à la surface lors de la propagation des grands tremblements de terres récents. L'ensemble de la section 1.2 qui suit a pour but d'exposer une vue d'ensemble de la connaissance actuelle sur la structuration des zones de failles et leur évolution géométrique. Une comparaison entre les différents types de données disponibles (modélisations analogiques en laboratoire, forages des roches de failles en profondeur, inversions sismologiques, observations de surfaces) sera également apportée.

1.2.1. Anatomie d'une zone de faille à l'échelle de l'affleurement

A l'échelle de l'affleurement, les observations de terrains mettent en évidence que l'endommagement consécutif aux déplacements successifs dans la zone de faille existe sous des formes diverses (Chester et Logan, 1986; Chester *et al*., 1993; Billi *et al*., 2003; Agosta et Aydin, 2006; Chambon *et al*., 2006). Néanmoins, deux principales textures se dégagent (Figure 1.1) : un noyau étroit (de l'ordre du centimètre au mètre d'épaisseur) où l'essentiel du déplacement est accumulé, bordé par une zone d'endommagement (de l'ordre du décimètre à plusieurs centaines de mètres d'épaisseur). Le noyau de la faille est constitué de roches dites cataclastiques à ultra-cataclastiques généralement dominées par un texture granuleuse. La zone d'endommagement qui accommode une déformation moindre est généralement caractérisée par une fracturation intense, dont l'intensité décroit non linéairement lorsqu'on s'éloigne du noyau (Sagy et Brodsky, 2009 ; Mitchell et Faulkner, 2009). A l'intérieur du noyau, à la surface (Sagy et Brodsky, 2009) comme en profondeur (Boullier *et al*., 2009), il est observé que la plupart du glissement se localise le

long d'une bande d'épaisseur pluri-millimétriques à millimétriques qu'on nomme communément la zone de glissement principal (Figure 1.1). Il est important de préciser que cette bande est souvent composée de plusieurs interfaces parallèles ultrafines (submillimétriques à micrométriques). Ces interfaces sont interprétées comme la juxtaposition des derniers épisodes de déplacements cosismiques, même si le débat reste vigoureux sur les indices formels de l'occurrence du glissement rapide associé aux tremblements de terres (e.g. Cowan, 1999). Quoiqu'il en soit, il est important de noter que cette zone de glissement principal, là où l'essentiel du déplacement rapide ou lent s'est localisé, correspond également au miroir de faille poli et/ou strié qu'il est commun d'observer en surface (Power *et al*., 1987 ; Renard *et al*., 2006 ; Sagy *et al*, 2007 ; Sagy et Brodsky, 2009).

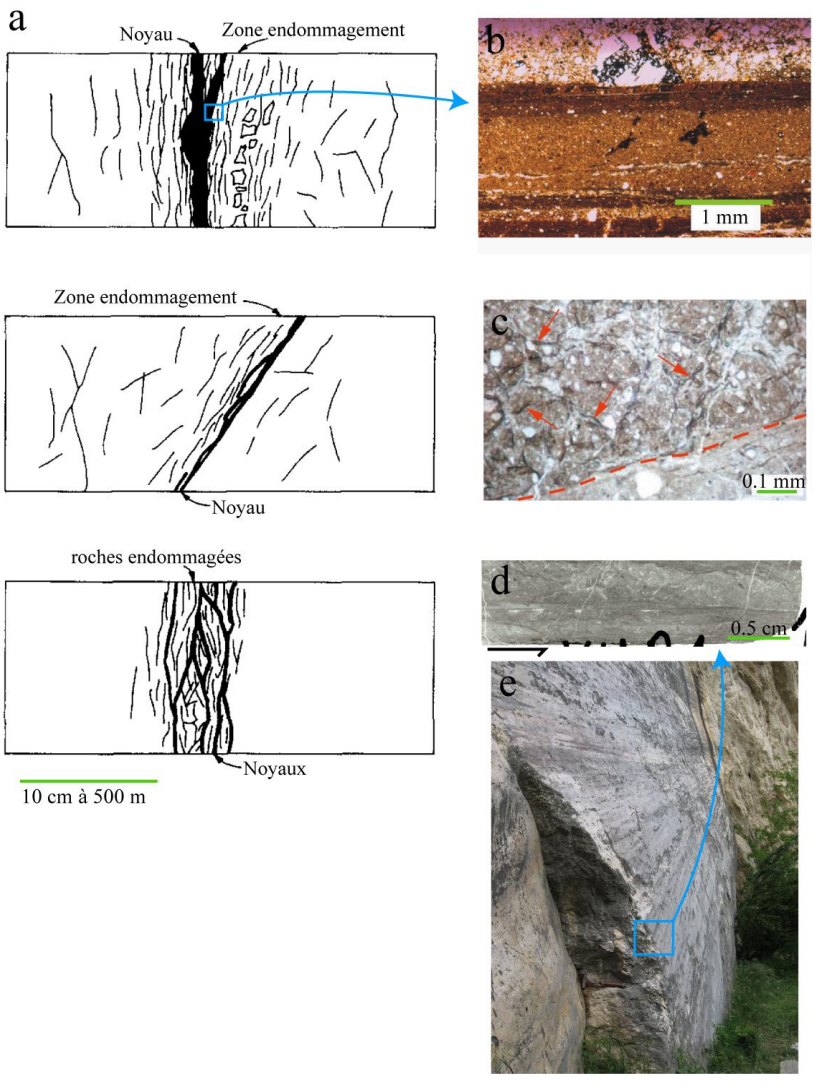

Figure 1.1. *Anatomie des zones de failles. (a) Coupes schématiques montrant les différentes positions du noyau* à *l'intérieur d'une zone de faille (modifié de Walls et Morris, 1986). (b) Microphotographie de la zone de glissement principal de la faille de « Flowers Pit » dans l'Oregon, constituée de plusieurs surfaces de glissement subparallèles. L'interface du haut de la photographie, entre la zone de glissement principal et la roche endommagée correspond au miroir de faille (modifié de Sagy et Brodsky, 2009). (c) Microphotographie de la zone de glissement principal du séisme de Chi-Chi en profondeur. Deux bandes de glissement subparallèles sont identifiées. La ligne rouge en pointillé marque leur frontière (modifié de Boullier et al., 2009). (d) Photographie d'une lame mince de la zone de glissement principal de la faille de la Vuache (Alpes) constituée de plusieurs surfaces de glissement subparallèles. L'extrémité inferieure de la lame mince correspond au miroir de faille (communication personnelle d'A-M Boullier). Miroir de faille de la Vuache en vue transverse (photo prise par F. Renard).*

La zone d'endommagement peut se retrouver de façon symétrique en bordure du noyau mais également uniquement d'un seul coté (Chester *et al*., 1993; Evans et Chester, 1995 ; Wallas et Morris, 1986). Il est également commun que l'architecture de la zone de faille soit plus complexe et fasse apparaitre de multiples noyaux sous forme d'un réseau anastomosé, enrobant des roches de failles endommagées (Wallas et Morris, 1986 ; Bruhn *et al*., 1994 ; Power et Tullis, 1989 ; Faulkner *et al*., 2003 ; Chambon *et al*., 2006; Mitchell et Faulkner, 2009). On retient donc que les observations de terrains des zones de failles exposées révèlent une architecture cohérente dans laquelle une large zone d'endommagement hautement fracturée est recoupée par un ou plusieurs noyaux étroits qui sont généralement eux-mêmes recoupée par des surfaces de glissement (ou miroirs de faille) qui accommodent la majorité du glissement (Figure 1.1).

1.2.2. Comparaison des observations de terrain avec des observations géophysiques

La plupart des études discutées dans la partie précédente sont basées sur des observations directes de l'architecture des zones de failles à la surface. La question donc subsiste quant à la préservation de cette structuration à des profondeurs sismogéniques. La plus haute résolution spatiale (de l'ordre du mètre à quelques dizaines de mètres) possible de l'architecture des zones de failles en profondeur est probablement donnée par la modélisation de la forme des ondes sismiques guidées. Ces ondes piégées dans la zone de faille sont générées par une interférence

constructive des ondes réfléchies à l'intérieur des couches à faibles vitesses de la zone de faille. Les observations collectées sur plusieurs zones de failles (Leary *et al*., 1987; Li *et al*., 1990, 1997 ; Ben-Zion et Malin, 1991; Ben-Zion *et al*., 1992 ; Hough *et al*., 1994 ; Ben-Zion *et al*., 2000 ; Nishigami *et al*., 2000 ; Kuwahara et Ito, 2000), avec ce type de méthode géophysique, mettent en évidence une zone à faibles vitesses globale d'une largeur allant de la dizaine à la centaine de mètres. Actuellement, il est donc impossible par les techniques d'imageries géophysiques de distinguer les détails de la zone de faille comme les noyaux et les surfaces de glissement. Au premier ordre, il est donc probable que la zone à faibles vitesses soit la continuité en profondeur de la zone de faille observée à la surface.

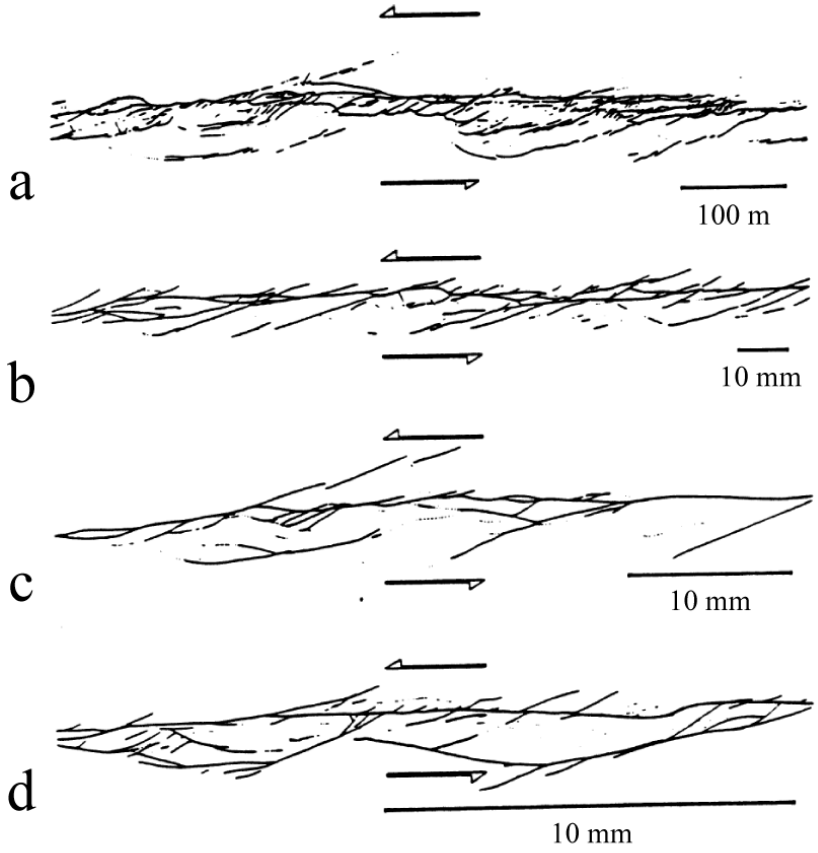

Figure 1.2. *Comparaison de la structuration des zones de failles a différentes échelles. (a) Tremblement de terre de Dasht-e-Bayaz en Iran. (b, c, d) Zones de cisaillements expérimentales. Modifié de Tchalenko (1970).*

1.2.3. Géométrie des zones de failles à l'échelle pluri-kilométrique

Les zones de failles, lorsqu'elles sont cartées suffisamment en détail, se trouvent être composées de segments discontinus. Les travaux de Tchalenko et Ambraseys (1970), Tchalenko (1970), Tchalenko et Berberian (1975) ont mis en évidence, sur la trace de la rupture de surface du tremblement de terre de Dasht-e-Bayaz Iran (M 7.3, 1968), que cette segmentation est préservée à différentes échelles (depuis la centaine de mètres à la dizaine de kilomètres (Figure 1.2).

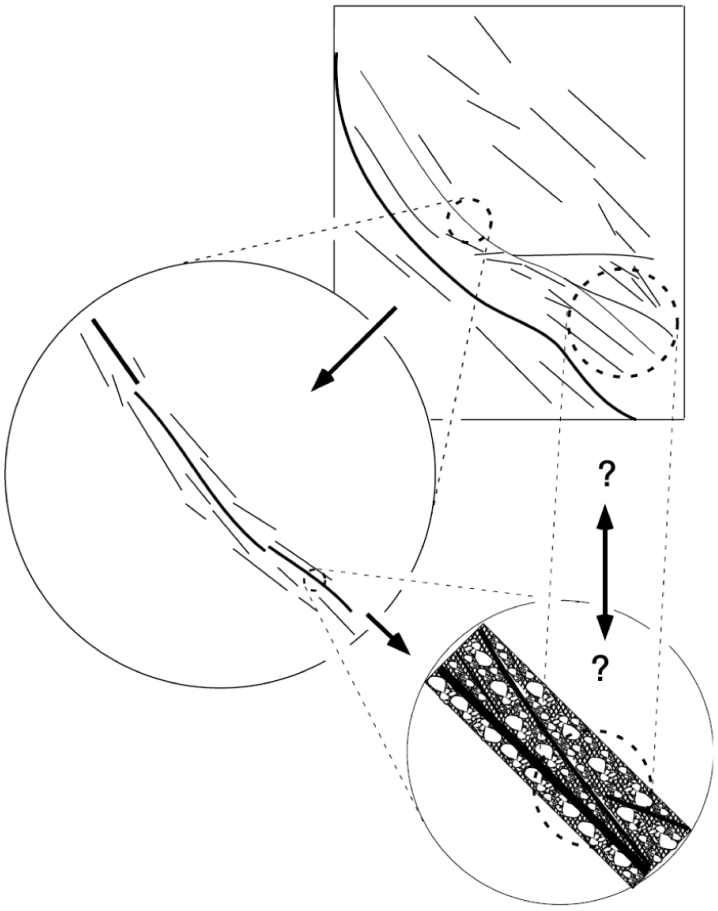

Figure 1.3. *Vue schématique en carte de la structuration des failles à différentes échelles. A l'échelle de la frontière entre deux plaques tectoniques, la déformation cisaillante est distribuée sur un réseau de failles. Chaque faille individuelle majeure dans ce réseau est elle-même constituée par des segments de différentes échelles. Chacun de ces segments s'organise structuralement sous forme de bande de localisation du déplacement au sein de la roche endommagée. Les flèches entre les différentes échelles suggèrent la possibilité que les éléments structuraux clés se répètent aux différentes échelles. D'après Ben-Zion et Sammis (2003).*

Cette géométrie complexe a aussi été identifiée à petites échelles dans les modèles analogiques de zones de cisaillement (Figure 1.2) menés par Tchalenko (1970). A l'échelle globale d'une plaque tectonique, l'ouest de la Californie peut être considéré comme un compartiment de la plaque pacifique séparé de la plaque Nord Américaine par une zone de faille (Figure 1.3). Cette faille contient plusieurs segments plurikilométriques qui forment les segments subparallèles majeurs du système de San Andreas. Chaque segment est lui-même constitué par des sous segments. La structuration de la zone de faille à l'échelle de l'affleurement décrite dans la partie 1.2.1 semble donc se répéter à toutes les échelles, à savoir : des zones de localisations de la déformation bordées par des zones d'intense fracturation et de roches endommagées. Ce type d'observation met en évidence que les failles pourraient être apparentées à des objets fractals (e.g. Mandelbrot, 1983) avec des surfaces rugueuses et une géométrie segmentée et hétérogène à toutes les échelles.

1.2.4. Le concept d'objet fractal (dimension fractale et exposant de Hurst)

Mandelbrot (1983) fut le premier à introduire le concept d'objet fractal auto-similaire en observant que la topographie des surfaces de fracture métalliques présentait des propriétés d'invariance d'échelle. La dimension fractale D d'un objet fractal auto-similaire caractérise la tendance de l'objet à remplir de façon plus ou moins dense une partie du plan, si c'est une courbe, ou d'une partie de l'espace s'il s'agit d'une surface. Les objets géométriques classiques ont une dimension 1, 2 ou 3. Les objets fractals ont une dimension fractale réelle. On emploie en général un certain nombre de méthodes afin d'estimer la dimension fractale d'un objet fractal auto-similaire. On peut citer par exemple la méthode de dénombrement de boîtes, qui consiste dans sa version la plus simple à paver l'espace à l'aide de boîtes de taille donnée et à compter le nombre de boîtes nécessaires au recouvrement de l'objet auto-similaire dans son intégralité. Il existe alors une gamme d'échelles où le nombre de boîtes est une loi de puissance de la taille des boîtes. L'exposant de la loi de puissance est l'opposé de la dimension fractale D de l'objet. La méthode du diviseur consiste à mesurer la longueur de la courbe en l'approximant par une ligne brisée formée de segments dont les sommets appartiennent à la courbe et qui ont tous même extension horizontale. Plus cette dernière est petite, plus la mesure prend en compte le détail des diverses

circonvolutions de la courbe, de sorte que la longueur calculée dépend de l'extension horizontale des segments comme une loi de puissance d'exposant 1 - D (Brown, 1995).

Cependant, la description auto-similaire considère toutes les directions de l'espace comme équivalentes, ce qui convient mal à la description d'une topographie où la dimension normale au plan moyen de la propagation de la fracture est à priori non-équivalente aux dimensions qui définissent le plan de propagation. Mandelbrot (1985) introduisit ensuite la notion d'auto-affinité, une description qui se révéla bien décrire l'invariance d'échelle observée dans de nombreux systèmes désordonnés (Voss, 1985) et plus généralement dans de nombreux problèmes physiques (Mandelbrot, 1986). Cette description est en particulier utile pour décrire la rugosité des failles (Schmittbuhl *et al.*, 1993). Si l'on échantillonne la distribution des hauteurs le long d'un profil extrait d'une surface de faille (cf. chapitre 2), on constate que l'invariance d'échelle au sens statistique telle que la définit la description auto-similaire ne tient pas : si l'on diminue la taille de la fenêtre d'observation sans modifier son rapport d'aspect, on constate que le profil n'a plus la même allure; il semble s'être dilaté verticalement. Par contre, il existe un rapport d'aspect pour l'agrandissement qui laisse le profil statistiquement inchangé par agrandissement. Plus exactement, il existe un paramètre H tel que la transformation

$$\begin{aligned} x &\mapsto s\, x \\ z &\mapsto s^{H}\, z \end{aligned} \tag{1.1}$$

laisse le profil statistiquement inchangé pour tout rapport d'échelle s. Ainsi, la direction z n'est plus équivalente à la direction x. Le paramètre H est généralement dénommé exposant de Hurst ou exposant de rugosité. L'auto-similarité apparaît comme un cas particulier d'auto-affinité ($H = 1$).

Le profil auto-affine présenté à la Figure 1.4 illustre l'invariance d'échelle auto-affine. On présente à la Figure 1.4b une vue rapprochée où la fenêtre d'observation a été divisée par $1/s = 4$ horizontalement. On a ajusté l'échelle verticale d'un facteur s^{H} pour le profil auto-affine. On constate visuellement que ce nouveau rapport d'aspect lui conserve un aspect similaire alors que si l'échelle verticale est ajustée d'un facteur s, ce même profil auto-affine semble s'être dilaté verticalement.

L'exposant de Hurst quantifie la décroissance de la fonction de corrélation, c'est-à-dire la persistance des corrélations d'altitudes le long du profil (ou de manière équivalente, l'importance des détails de petite échelle relativement aux détails de grande échelle). Cela se traduit par un aspect des profils d'autant plus réguliers, en particulier aux petites échelles, que l'exposant de rugosité est élevé (voir Figure 1.4).

Les méthodes développées pour déterminer la dimension fractale des objets auto-similaires peuvent être employées pour déterminer l'exposant de rugosité d'un profil auto-affine, mais avec précaution. Lorsqu'elles sont utilisées correctement, elles mettent en évidence une relation entre l'exposant de rugosité et une dimension fractale pour le profil : $D + H = 2$.

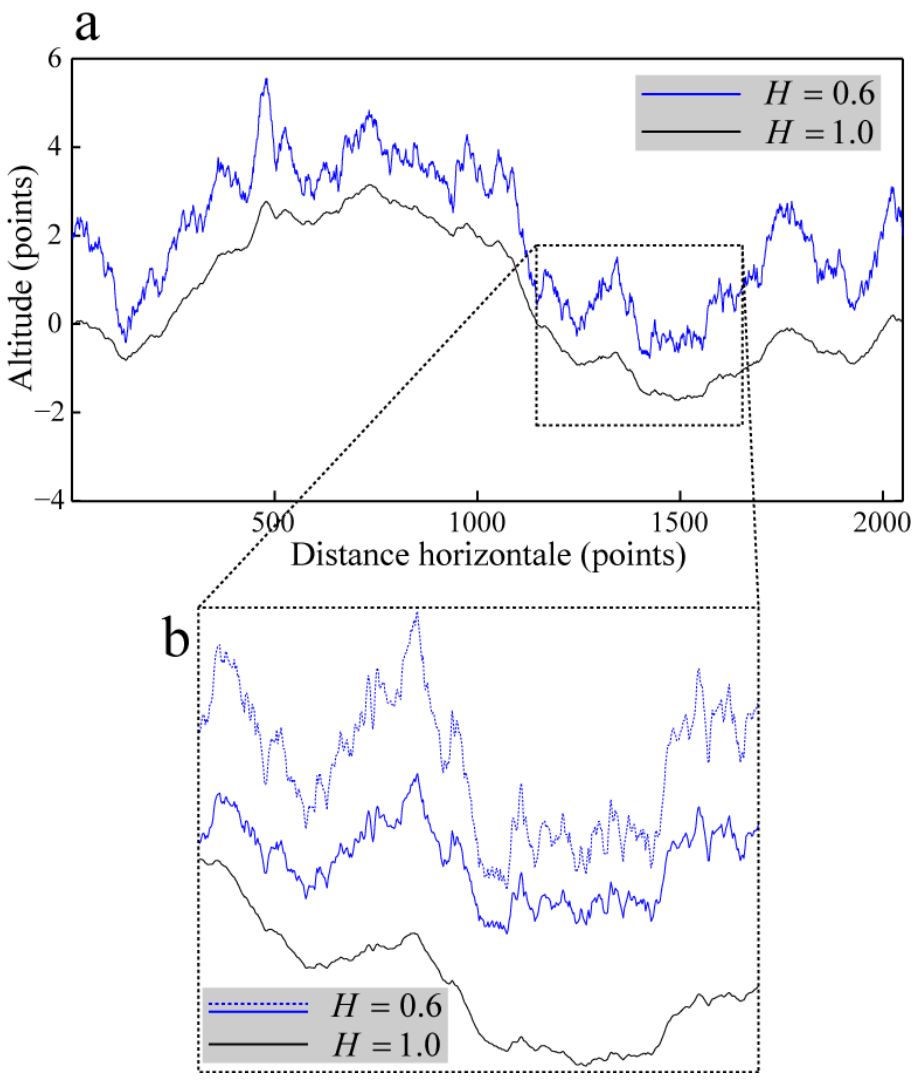

Figure 1.4. *Comparaison de profils auto-similaires ($H = 1$) et auto-affines ($H = 0.6$). (a) Les deux profils ont été générés numériquement à l'aide d'un algorithme qui est exposé au chapitre 2. On a fourni au générateur aléatoire de nombre la même valeur initiale dans les deux cas, ce qui explique qu'ils présentent les mêmes fluctuations de grande longueur d'onde. Ils ont ensuite été normalisés de la même façon, avec un écart-type unité. (b) Vue rapprochée des profiles présentés en (a), limitée au cadre dessiné sur cette figure. L'échelle horizontale a été multipliée par* 4 *pour les deux profiles. L'échelle verticale a été multipliée par* 4 *pour le profile auto-similaire, et pour le profile auto-affine par* 4 *(le profile bleu en pointillé) dans un cas et dans l'autre cas (le profile bleu en trait plein) par* $4^{0.6}$*. Un zoom isotrope sur le profile auto-similaire lui conserve son aspect alors que le profile auto-affine semble dilaté verticalement. Un zoom anisotrope est nécessaire pour que le profile auto-affine garde une extension verticale apparente identique.*

En pratique, on préférera employer des techniques spécifiquement adaptées à la géométrie auto-affine. Un certain nombre de quantités calculées à partir de la distribution des hauteurs du profil, telles que la fonction d'auto-corrélation, le spectre de Fourier ou la transformée en ondelettes, dépendent de l'échelle en suivant une loi de puissance dont l'exposant est relié linéairement à H (cf. chapitre 2).

1.2.5. Invariance d'échelle de la géométrie des zones de failles

1.2.5. A. A l'échelle de la carte

De nombreux travaux ont donc été menés afin de quantifier les propriétés géométriques des zones de failles avec en toile de fond le concept d'invariance d'échelle. Avant de présenter leurs résultats, il est important de préciser que nous avons remplacé la dimension fractale donnée dans la plupart de ces études par le coefficient de Hurst. Aviles *et al*. (1987) en utilisant la méthode du diviseur ont montré que la zone de faille principale de San Andreas est caractérisée par un coefficient de Hurst de l'ordre de 1 +- 0.004. En incluant les failles secondaires à la zone de faille principale de San Andreas, Okubo et Aki (1987) suggèrent que H = 0.8 +- 0.2, en se basant sur une variante de la technique standard du dénombrement de boîtes. Hirata (1989) indique que la zone de faille du système du Japon est auto-similaire sur une gamme d'échelle comprise entre 2 km et 20 km en utilisant la méthode de dénombrement de boîtes. Sammis *et al*. (1992),

toujours en appliquant la même méthode, ont démontré que le réseau de failles au sein du domaine géothermal du nord de la Californie est défini par un coefficient de rugosité de l'ordre de 0.1 pour une gamme d'échelle comprise entre 0.8 km et 10 km. Pour résumer, l'ensemble de ces résultats convergent vers le fait que les zones de failles (à l'échelle de la carte) présentent une géométrie complexe invariante avec l'échelle.

1.2.5. B. A l'échelle de l'affleurement

A l'échelle de l'affleurement, les études pionnières de Power *et al*. (1987) ont montré que les surfaces principales de glissement (i.e. les miroirs de failles) sont également caractérisées par une géométrie fractale depuis le centimètre jusqu'à la dizaine de mètres. Néanmoins, leurs études basées uniquement sur quelques profils 1-D par miroir de faille, ne permettaient d'acquérir qu'une vision détaillée de sa géométrie. Récemment, grâce au développement d'un outil permettant de scanner l'ensemble du miroir de faille, le LIDAR (LIght Detection And Ranging), Renard *et al*. (2006) et Sagy *et al*. (2007) ont mis en évidence que la géométrie du miroir de faille pouvait être décrite par une géométrie auto-affine. Ces travaux soulignent que la complexité géométrique de la zone de faille semble persister jusqu'à l'échelle centimétrique.

1.2.6. Vers une régularisation géométrique de la zone de faille ?

La notion de « régularisation géométrique » renvoi à l'idée intuitive selon laquelle la zone de faille se simplifierait en abandonnant ou lissant la complexité des structures (segments) initiales au cours des glissements successifs. Ben-Zion et Sammis (2003) préconisent alors qu'il est nécessaire de séparer les unités structurales initiales abandonnées de celles qui participent activement à l'accommodation du glissement, afin de mettre en évidence une éventuelle régularisation de la géométrie de la zone de faille avec le glissement. Les études présentées précédemment sur la caractérisation de la géométrie des zones de failles à l'échelle kilométrique prennent en considération la totalité des structures et n'individualisent pas celles accommodant la plupart du glissement actuel. En conséquence, en suivant le raisonnement de Ben-Zion et Sammis (2003), même si la zone de faille prise dans sa totalité révèle une complexité invariante avec l'échelle, il est probable que la déformation active se localise sur une zone géométriquement plus simple.

Les traces de ruptures permettent effectivement d'individualiser la morphologie des segments actifs. Les travaux de Wesnousky (1988) sur l'analyse des tracés de zones de failles majeures en Californie et en Turquie, montrent que la densité des plus grands espacements (i.e. supérieur à 1 km) séparant les segments de premier ordre diminue avec le glissement accumulé (Figure 1.5). Récemment, les travaux de Klinger (2010) révèlent que, quel que soit le déplacement total accumulé, les segments constituant la trace de la rupture à la surface de 10 tremblements de terre décrochant présentent une longueur maximale de ~ 18 km (Figure 1.6). Ce résultat suggère donc que la complexité de la faille tend à se maintenir quelque soit le déplacement accumulé. Klinger (2010) souligne que ses résultats récents sont probablement compatibles avec ceux plus anciens de Wesnousky (1988). En effet, le lissage du tracé de la faille semble concerner uniquement les complexités géométriques de grandes échelles comme l'espacement plurikilométrique entre deux segments, paramètre sur lequel Wesnousky (1988) a focalisé son étude.

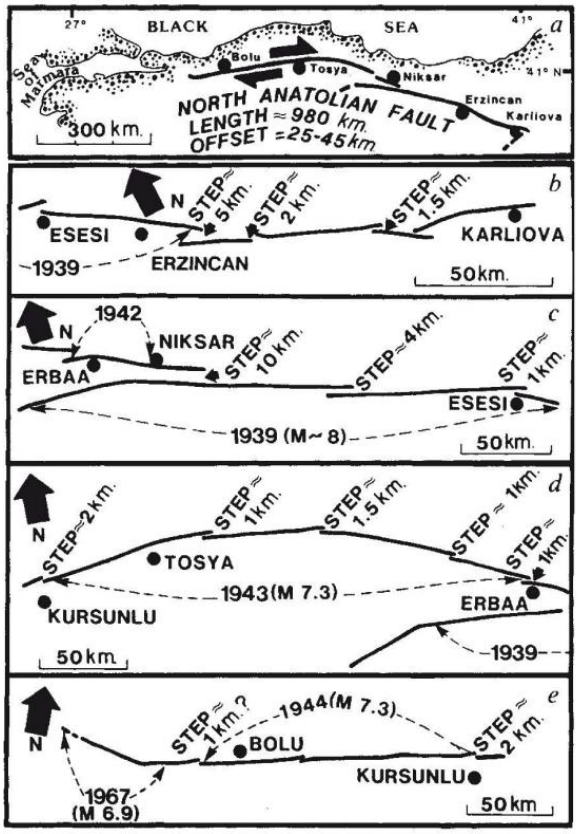

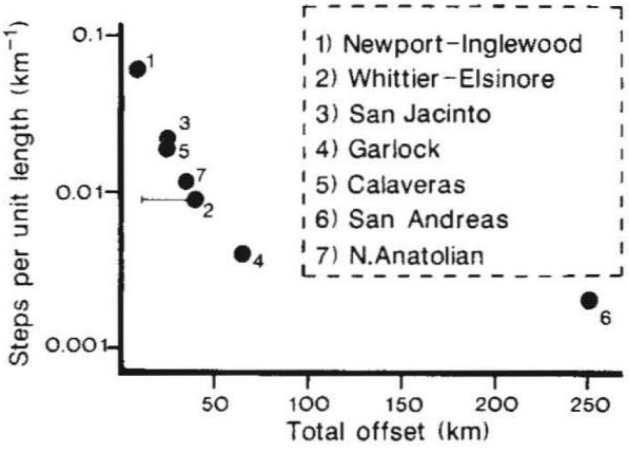

Figure 1.5. *Régularisation géométrique des complexités de premier ordre le long des failles. (gauche) Tracés des principaux segments de la faille nord anatolienne (Turquie) montrant des ruptures historiques. La position des espacements supérieurs à 1 km entre les segments majeurs dénombrés par Wesnousky (1988) est indiquée. (droite) Graphique du nombre d'espacements (supérieurs à 1 km) par unité de longueur des traces des zones de failles majeures en Californie et en Turquie, en fonction du déplacement géologique accumulé. Tiré de Wesnousky (1988).*

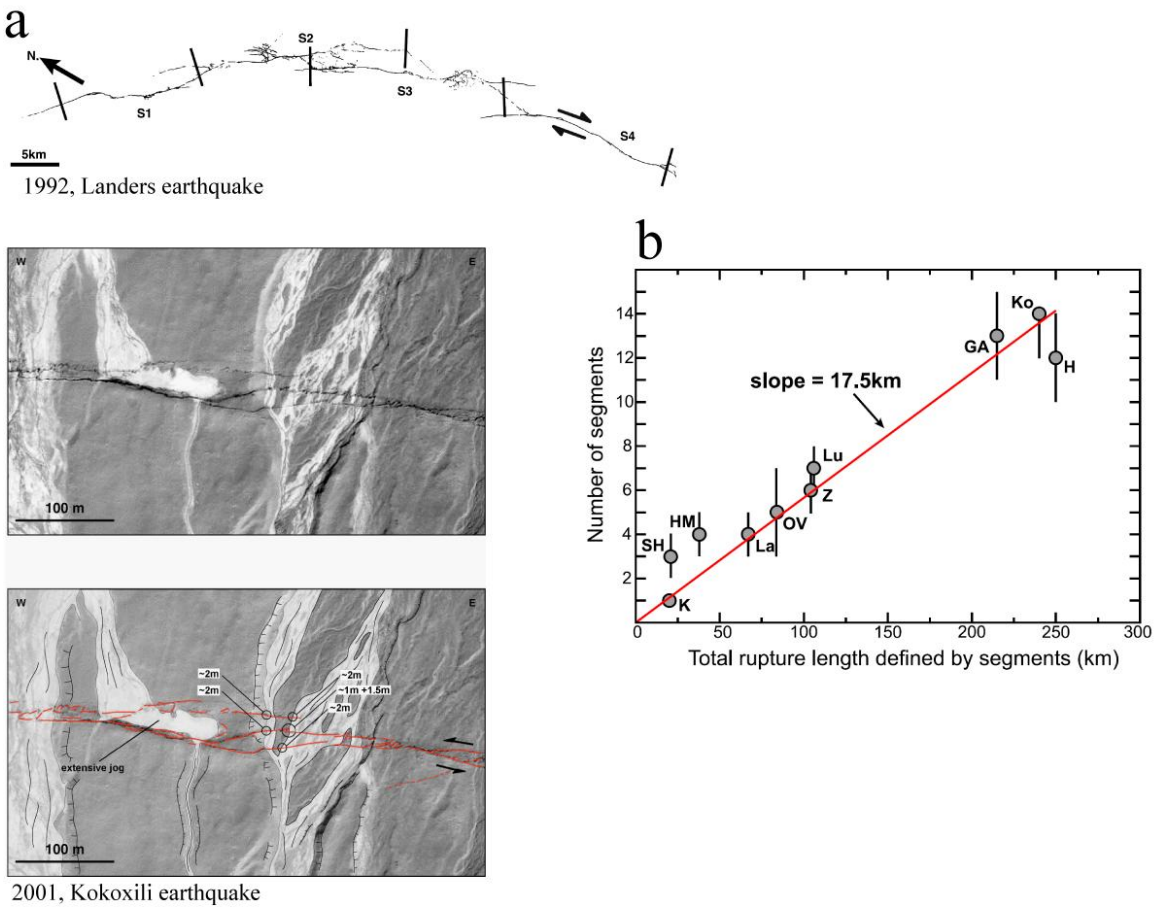

Figure 1.6. *Persistance de la taille maximale des segments constituant le tracé des ruptures. (a) Cartographie fine de terrain de la rupture de surface du tremblement de terre de Landers (haut), et images satellites haute résolution d'une portion du tracé du séisme de Kokoxili (Chine) donnant accès* à *des détails structuraux jusqu'à une précision spatiale de ~ 50 cm (bas). Dans l'exemple du tremblement de terre de Landers, Klinger (2010) suggère que son tracé puisse être au minimum constitué par 4 segments. (b) Graphique du nombre de segments de taille maximale en fonction de la longueur totale des ruptures de surface de 10 séismes décrochant récents. Modifié de Klinger et al., (2005) et Klinger (2010).*

A une échelle plus fine, Power *et al*. (1987) et Renard *et al*. (2006), en étudiant la morphologie des miroirs de failles avec une résolution spatiale centimétrique, caractérisent également la géométrie de la surface de glissement principal qui accommode la majeure partie du glissement actuel. Ces deux études mettent en avant que les miroirs de failles restent complexes et caractérisés par une géométrie fractale. Néanmoins, Sagy *et al*. (2007) en scannant des miroirs de failles de la même manière que Renard *et al*. (2006), observent que ces derniers se lissent avec le déplacement accumulé. Soulignons cependant que dans les travaux de Sagy *et al*. (2007), même si les surfaces de glissement principal sont lissées avec le déplacement accumulé, elles préservent une géométrie fractale.

En définitive, même si un faisceau d'observation semble indiquer que les failles comportent des hétérogénéités géométriques à toutes les échelles, il reste encore à les quantifier de façon précise. Par exemple : (i) le régime auto-affine observé par Renard *et al*. (2006) à l'échelle d'un unique miroir de faille est-il maintenu sur plusieurs failles dans des environnements tectoniques variés, et persiste-t-il à l'échelle de la centaine de mètres voir de plusieurs kilomètres des traces de ruptures ? (ii) Existe-t-il des échelles caractéristiques bornant différentes gammes d'échelles dominées par des processus variés modelant la surface de faille ? (iii) Au contraire, est-ce qu'un unique régime fractal (par exemple auto-affine) se dégage et soutiendrait l'hypothèse d'un processus universel à l'origine de la structuration de la faille ? Les observations de Klinger (2010) tendent à suggérer qu'une longueur caractéristique maximale de segment persiste quel que soit l'environnement tectonique des failles. Cependant, cette analyse apporte une information uniquement à cette échelle spécifique et il reste encore à définir si une organisation spatiale cohérente persiste jusqu'à l'échelle du grain. A ce sujet, aux échelles spatiales inferieures au centimètre, la caractérisation fine des propriétés géométriques des surfaces de glissement principal reste encore à établir. En outre, la comparaison entre les corrélations spatiales des hétérogénéités géométriques des traces de ruptures et celles plus fines à l'échelle de l'affleurement des miroirs de failles permettraient probablement de faire progresser le débat sur une éventuelle régularisation géométrique des failles avec le déplacement.

1.3. De la fracturation au frottement

Dans les conditions de la croûte terrestre, en particulier dans sa partie supérieure, la grande majorité des roches répond de façon élastique puis fragile aux déformations qui leurs sont imposées. La déformation fragile est caractérisée macroscopiquement par la création et la propagation de fissures et de failles au sein des matériaux rocheux. La propagation d'une faille combine à la fois la fracturation du matériau à ses extrémités et la friction des interfaces néoformées. La fracturation et le frottement sont représentés par des critères de seuil, qui relient le mouvement dans le milieu à une chute de contrainte cisaillante sur la surface de faille. Dans la théorie de la mécanique de la fracturation, une énergie de fracture caractéristique par unité d'aire est nécessaire pour que le crack se propage. Dans la mécanique du frottement, la rupture est supposée apparaitre quand la contrainte sur la faille atteint la valeur seuil de la résistance aux frottements. Dans l'ensemble de la section 1.3 qui suit, nous nous penchons de façon distincte sur (i) la mécanique de la fracturation et plus précisément sur le mécanisme de croissance et de coalescence de fissures à l'intérieur de la roche, qui donne lieu à la formation d'une faille macroscopique (partie 1.3.1) ; puis sur la mécanique du frottement et plus précisément sur la résistance frictionnelle d'une interface déjà présente, avant l'épisode de glissement (partie 1.3.2). Nous verrons dans la section 1.4 que ces deux mécanismes peuvent être représentés de manière unifiée.

1.3.1. Mécanique de la fracturation

La mécanique élastique linéaire de la fracturation est une approche qui prend ses racines dans le bilan énergétique de la propagation d'un crack formulé par Griffith (1920). Il s'agit d'une approche de la mécanique des milieux continus dans laquelle un crack est idéalisé mathématiquement par une fente plate et étroite dans un milieu élastique homogène. Dans cette approche, une singularité de contraintes existe à l'extrémité du crack. L'introduction des forces de cohésion a permis de supprimer l'incohérence mécanique liée aux singularités, en modifiant l'évolution du champ de contraintes à proximité de la tête de fracture. La force de cohésion a pour conséquence d'empêcher la chute brutale de la contrainte cisaillante à l'extrémité du crack.

Elle agit dans une zone d'épaisseur non-nulle appelée zone de cohésion, ou "process zone", ou bien encore "breakdown zone". Dans un modèle élastique non-linéaire de crack (e.g. Dugdale, 1960 ; Barenblatt, 1962), la chute de contrainte $\Delta\sigma$ (MPa) est spécifiée sur un crack à l'intérieur d'un solide sous contrainte et le déplacement résultant des murs du crack est calculé. Quand on applique un tel modèle aux failles, il est supposé que la chute de contrainte correspond à la contrainte cisaillante appliquée moins la contrainte de friction résiduelle sur la faille. L'énergie de fracturation G_c ($J.m^{1/2}$) dépensée en tête d'une faille de longueur l (m) pour sa propagation est donnée par :

$$G_c = \left(\Delta\sigma \sqrt{\frac{l}{2\pi}} \right)^2 \qquad (1.2)$$

Dans l'hypothèse d'une chute de contrainte constante et indépendante de la longueur de la faille, G_c et par la même occasion l'intensité de la contrainte à l'extrémité du crack sont alors supposées évoluer linéairement avec la longueur de la faille. L'hypothèse de la chute de contrainte constante implique que le déplacement cisaillant évolue linéairement avec la longueur de la rupture. Les principales observations de terrains qui montrent cette évolution linéaire sont les mesures du déplacement accumulé par une faille sur des échelles de temps géologiques, en fonction de sa longueur totale (Elliott, 1976 ; Watterson, 1986 ; Walsh et Watterson, 1988 ; Marrett et Allmendinger, 1991 ; Cowie et Scholz 1992; Dawers *et al.*, 1993; Schlische *et al.*, 1996). Néanmoins, un modèle de croissance de la faille par avancements et déplacements incrémentaux progressifs (Cowie et Scholz, 1992) est nécessaire afin de justifier que ces mesures puissent valider l'hypothèse d'une chute de contrainte constante pour un événement individuel de rupture. Les observations sismologiques montrent également en général une chute de contrainte constante quelle que soit la taille de l'événement individuel de rupture (e.g. Kanamori, 1994; Abercrombie, 1995). Même si un faisceau de présomptions semble valider l'hypothèse d'une chute de contrainte stable, le débat sur son éventuelle variabilité avec l'échelle reste encore ouvert et l'implication de la rugosité de la faille dans ce paramètre clé sera alors discutée dans la section 1.5 de ce chapitre d'introduction.

Le modèle de fracturation présenté dans cette partie spécifie les conditions sous lesquelles un crack individuel se propage dans un milieu élastique homogène. La faille macroscopique se forme depuis la coalescence de micro-cracks, lesquels eux-mêmes s'initient et se développent en accord avec cette théorie. De ce fait, la totalité du processus de développement de la surface de faille rugueuse, évoluerait de la même façon que la théorie de la mécanique de la rupture le prédit. L'essence du principe suivi est que la propriété de l'ensemble (la faille) est une fonction des propriétés des sous parties (les cracks cisaillant). Cette approche simplifiée, soulève la question fondamentale de l'origine de la rugosité des failles, à savoir : est-elle régie par les interactions mécaniques des cracks cisaillant multi-échelles ? En d'autres termes la coalescence des cracks par interactions mécanique, donnant naissance à une faille macroscopique est-elle à l'origine de la rugosité ? La validation de cette hypothèse reste encore un problème épineux, et demande probablement l'élaboration de modèles mécaniques d'endommagement (e.g. Main, 2000; Schmittbhul *et al*., 2003) du fait de la complexité du processus et de l'hétérogénéité des microstructures de la roche. La clé de ce problème semble résider dans la quantification du comportement collectif régissant la complexité des interactions mécaniques entre les cracks multi-échelles et les hétérogénéités préexistantes du milieu.

1.3.2. Mécanique du frottement et seuil de résistance au glissement

La plupart des phénomènes associés au frottement peuvent se comprendre sur la base des lois phénoménologiques du frottement énoncées dès le 17ème siècle par Amontons (1699) puis Coulomb (mais déjà mises en évidence par Léonard de Vinci 200 ans auparavant). Amontons et Coulomb ont montré que pour déplacer un objet sur une surface plane, une force tangentielle à l'interface minimale F est nécessaire afin de dépasser la force frictionnelle F_f qui s'oppose au mouvement. Cette force minimale est directement proportionnelle au chargement normal N à l'interface (ici le poids de l'objet). Autrement dit, l'objet ne commence à se déplacer que lorsque : $F = F_f = \mu_s N$, μ_s définissant le coefficient de frottement statique. De plus, Amontons et Coulomb ont mis en évidence que μ_s ne dépend pas de l'aire de contact de l'objet frottant. Ce dernier résultat très contre-intuitif a défié l'imagination des scientifiques plusieurs siècles avant que Bowden et Tabor (1950, 1964) dans leur théorie de la friction des métaux n'en

proposent une explication. La clé de ce phénomène est la rugosité de surface. A cause de cette rugosité, les zones de contact réel entre les surfaces sont bien plus petites que l'aire de contact apparente entre les surfaces, telle qu'elle nous apparait de visu. Une conséquence immédiate est que le chargement normal auquel on soumet l'objet ne se répartit que sur les aspérités en contact et non sur l'ensemble de la surface de l'objet. En conséquence la contrainte normale au sein de ces contacts, $\sigma_{n(contact)} = N / A_{reelle}$, est bien plus grande que celle que l'on attendrait a priori si le chargement normal se répartissait sur l'ensemble de la surface, $\sigma_{n(apparente)} = N / A_{apparente}$. Bowden et Tabor (1950, 1964) supposent alors qu'au niveau des contacts, les métaux s'écrasent de façon plastique, jusqu'à ce que l'aire de contact réelle soit juste suffisante pour supporter le chargement normal. L'aire réelle du contact est alors directement proportionnelle à la force appliquée : $A_{reelle} = N / p$, où p est la dureté du matériau (une mesure de la résistance du matériau à l'écrasement). Ce mécanisme permet de retrouver les lois d'Amontons-Coulomb. En effet, l'aire frottante étant l'aire réelle, on s'attend à ce que la force frictionnelle tangentielle soit proportionnelle à cette aire : $F_f = s\, A_{reelle}$. Le coefficient de proportionnalité s correspond à la résistance au cisaillement au niveau des contacts. En utilisant l'expression précédente pour l'aire de contact réelle, $A_{reelle} = N / p$, on aboutit à une force frictionnelle qui prend la forme d'une loi d'Amontons-Coulomb : $F_f = \mu_s\, N$, avec $\mu_s = s / p$. Cette explication de Bowden et Tabor (1950, 1964) permet de comprendre la proportionnalité de la force de frottement vis-à-vis de la force normale, mais également l'indépendance du coefficient de frottement vis-à-vis de la surface apparente de contact. Cette explication repose cependant sur l'hypothèse de déformation plastique des aspérités, qui, si elle est pertinente pour des métaux, pose question pour d'autres matériaux au comportement élasto-plastique tels que les roches de la croute terrestre. De fait, Archard (1957) puis Greenwood et Williamson (1966), ont montré que le point clé du raisonnement précédent, c'est à dire la proportionnalité entre aire de contact réelle et chargement normal, est maintenu même dans le cadre d'aspérités qui se déforment élastiquement, par un effet de moyenne statistique sur l'ensemble des aspérités en contact.

La simplicité des résultats présentés ci-dessus cache cependant la complexité des mécanismes de déformation qui peuvent être à l'œuvre lors de l'acquisition des contacts de

l'interface puis de leur cisaillement. Pour ne citer que cet exemple, des mécanismes activés thermiquement (e.g. processus de dissolution-recristallisation ou de déformation plastique) peuvent considérablement augmenter l'aire réelle de contact (Dieterich et Kilgore, 1994, 1996) ou leur adhérence (Hirth et Rice, 1980). Ces processus physico-chimiques responsables du renforcement en fonction du temps de l'état statique des interfaces peuvent être simplement compris comme une cicatrisation des contacts avec le temps (Rabinowicz, 1951) résultant dans une augmentation de la résistance frictionnelle.

En compilant des expériences de frottement sur une grande variété de roches et une large gamme de chargements, Byerlee (1978) a montré que le coefficient de frottement statique est étonnamment stable hormis pour certains minéraux argileux. Ces résultats confirment que le seuil de résistance au cisaillement des failles est linéairement proportionnel à la charge normale appliquée sur l'interface. Il faut alors préciser que localement, au niveau des aspérités, la contrainte normale sera bien plus grande que la magnitude du chargement appliqué sur l'interface. De ce fait le seuil de résistance au cisaillement au niveau de l'aspérité, relié linéairement à la contrainte normale par le coefficient de frottement statique, sera lui aussi bien plus grand que le seuil de résistance global de l'interface. Dans le cadre d'une surface de faille rugueuse, on peut alors s'attendre à une distribution spatiale hétérogène du seuil de résistance frictionnelle le long de l'interface.

1.4. Variation de la contrainte pendant le glissement

Une fois le seuil de résistance au frottement statique atteint, le mouvement sur la faille peut être quasi-statique, ou bien dynamique, selon l'évolution de la résistance au cours du glissement. On peut raisonner de façon simple par analogie avec un système bloc-ressort (Figure 1.7). Le glissement sur la faille est simulé par le mouvement du bloc sur l'interface. Le chargement s'effectue au travers d'un ressort de rigidité k, qui représente l'élasticité du milieu environnant la faille.

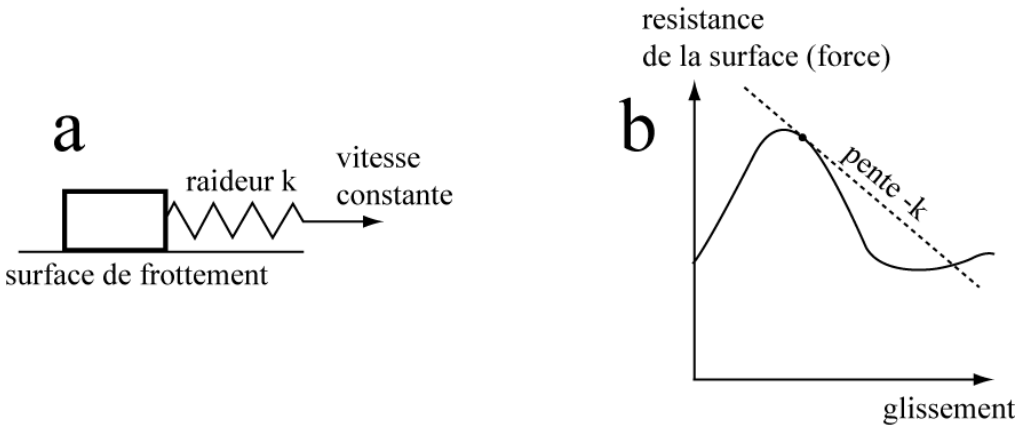

Figure 1.7. *Modèle bloc-ressort illustrant l'origine des instabilités frictionnelles. (a) Schéma synoptique du problème considéré. (b) Diagramme force-déplacement montrant un cas hypothétique instable dans lequel la force de résistance frictionnelle chute avec le déplacement* à *une vitesse plus grande que le système de chargement peut répondre. Dans le cas où la force de résistance frictionnelle chute moins vite que la décharge du ressort, le glissement reste stable.*

Le forçage est imposé à l'extrémité du ressort à vitesse constante, ce qui simule le chargement tectonique lointain. Si la résistance au niveau de la faille augmente avec le déplacement, son mouvement est stable, l'ensemble bloc-ressort se charge. Si la résistance diminue au cours du déplacement, alors deux cas peuvent se présenter. Soit cette diminution est plus faible que la décharge du ressort, c'est-à-dire que la pente de la courbe force-déplacement est plus faible que $-k$, alors le ressort peut suivre le mouvement, et le bloc glisse de façon stable quasi-statique. Si la diminution de résistance est rapide, avec une pente plus forte que $-k$, le ressort se décharge alors plus lentement que la faille. La force appliquée est donc plus importante que ce que peut soutenir l'interface : il y a un déséquilibre de force qui se traduit par une accélération. Le mouvement est donc instable. Le mouvement va ralentir lorsque la droite de pente $-k$ recoupe la courbe de résistance de la faille. Ce type d'instabilité est appelée couramment « stick-slip » dans la terminologie anglo-saxonne. L'observation expérimentale de ce comportement dans les roches a conduit Brace et Byerlee (1966) à le proposer en tant que mécanisme des tremblements de terre. Outre ce comportement d'affaiblissement en glissement (ou « slip-weakening »), la friction dynamique, qui est le seuil de contrainte atteint lorsque la faille est mise en mouvement, dépend de la vitesse de glissement. Plus la vitesse de glissement est rapide, plus le seuil de friction

dynamique est bas. D'autre part, suite à une augmentation de la vitesse de glissement, la friction augmente quasi instantanément, avant de diminuer progressivement pour atteindre la valeur de friction dynamique. Ces caractéristiques ont été mises en évidences par des expériences de frottement d'interfaces (voir par exemple Dieterich, 1979; Marone, 1998) ou des expériences de propagation de rupture dans des matériaux (par exemple Ohnaka et Chen, 1999). Ces résultats ont permis de construire des lois de friction de type « rate-and-state », qui modélisent l'évolution de la friction en fonction de la vitesse de glissement, et d'une variable d'état liée à l'état de la surface. Ces lois sont utilisées dans les modèles de cycle sismique, et de sismicité en générale.

Revenons sur le comportement d'affaiblissement en glissement (i.e. le fait que la résistance au frottement diminue au cours du déplacement), qui est nécessaire à la fois pour le cas d'une propagation quasi-statique ou sous-critique de la rupture et pour le cas instable de la rupture rapide sismique. Comme présenté précédemment, dans le cas général d'une faille sous chargement tectonique lointain, la contrainte cisaillante localement sur le plan de faille augmente depuis un état initial τ_0 jusqu'au seuil de résistance au frottement τ_s. C'est à ce moment que la rupture commence à se propager et la contrainte cisaillante chute jusqu'à l'arrêt du glissement lorsque le seuil frictionnel final τ_f est atteint. La Figure 1.8 illustre la complexité de la variation de la contrainte cisaillante lors du glissement en un point de la faille. Dans les études sismologiques, il est difficile de déterminer cette variation complexe du fait des difficultés techniques rencontrées dans l'enregistrement et le traitement des ondes hautes fréquences. Afin d'étudier la physique des tremblements de terre dans les applications sismologiques, le comportement est généralement simplifié et suit le modèle d'affaiblissement en glissement (Kanamori et Rivera, 2006). Dans ce cas (Figure 1.9a), la contrainte cisaillante chute depuis le seuil de résistance frictionnel τ_s jusqu'à la valeur du frottement dynamique τ_d et reste constante jusqu'à la fin du glissement. Le seuil du frottement dynamique n'est atteint qu'après une certaine quantité de déplacement. On parle de distance de glissement critique d'affaiblissement d_c.

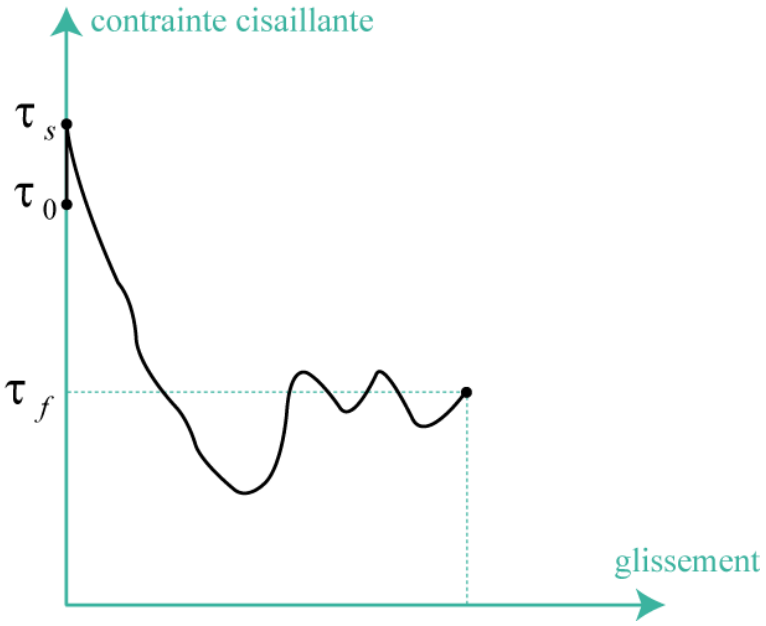

Figure 1.8. *Variation complexe de la contrainte cisaillante en fonction du déplacement en un point sur la faille. Au commencement du processus de rupture, la contrainte cisaillante augmente depuis* τ_0 *jusqu'au seuil de résistance au frottement statique* τ_s *puis la contrainte chute dans un trajet complexe jusqu'à sa valeur finale* τ_f *à l'arrêt du glissement. Modifié de Kanamori et Rivera (2006).*

Afin d'unifier l'avancement de la faille par fracturation avec le glissement frictionnel sur la partie néoformée, on peut raisonner de la façon suivante en un point de la faille. Une fois que la résistance statique est atteinte en ce point (qui peut être l'extrémité de la faille), le passage de τ_s à τ_d, i.e. la chute de contrainte, matérialise la dissipation progressive de la force de cohésion dans la « breakdown zone » au cours du glissement d_c. Durant cet épisode, l'énergie nécessaire à l'initiation de la rupture cisaillante (surface grise sur la Figure 1.9a) correspond à l'énergie de fracturation G_c dissipée lors de la création de la nouvelle interface dans la zone de cohésion, i.e. au niveau du point considéré. Depuis d_c jusqu'à l'arrêt du glissement, l'énergie est alors dissipée essentiellement par chaleur lors du frottement.

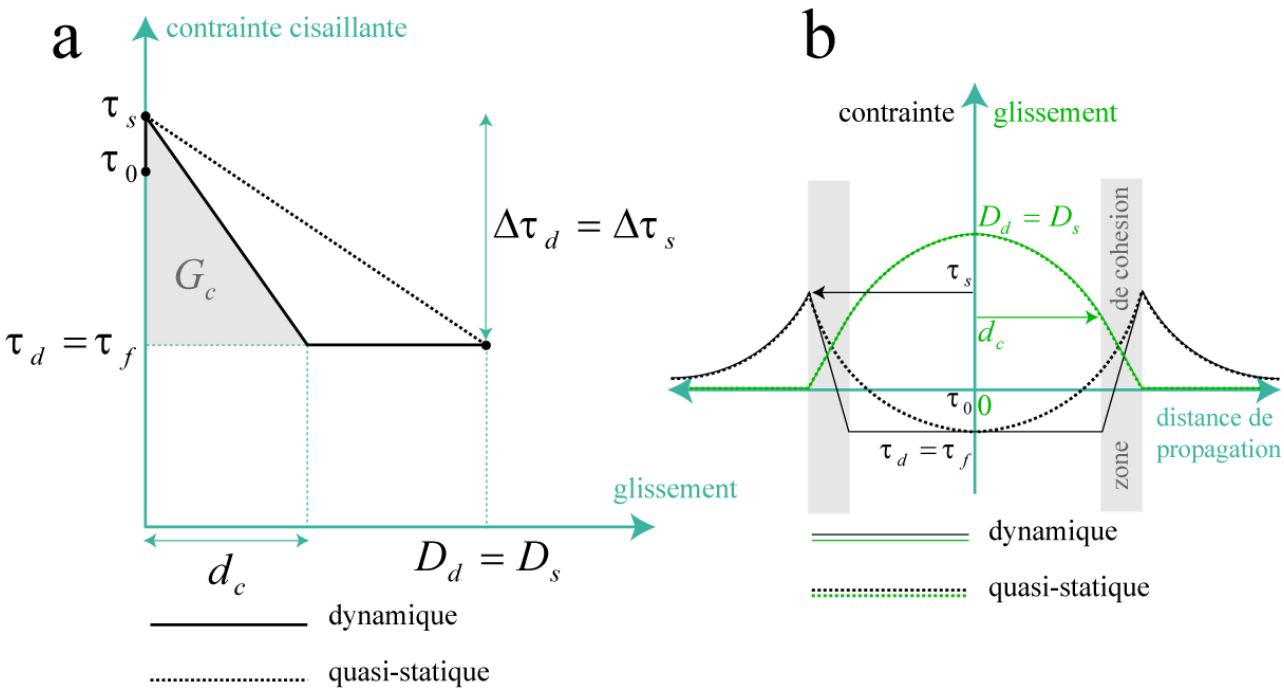

Figure 1.9. *Modèle d'affaiblissement en glissement en un point de la rupture ou pour le cas d'une faille aux propriétés frictionnelles homogènes. (a) Variation simplifiée de la contrainte en fonction du glissement. Dans le cas dynamique, la contrainte cisaillante chute depuis* τ_s *jusqu'au seuil de frottement dynamique* τ_d *sur une distance critique d'affaiblissement* d_c*, puis reste constante jusqu'à l'arrêt du glissement. Au cours du glissement critique d'affaiblissement, l'énergie de fracturation* G_c *nécessaire à l'initiation de la rupture cisaillante matérialise la disparition progressive de la force de cohésion sur l'interface lors de la chute de contrainte dynamique* $\Delta\tau_d = \tau_s - \tau_d$*. Dans le cas quasi-statique, la contrainte cisaillante chute progressivement depuis* τ_s *jusqu'à la contrainte finale, sans émettre de radiation et le système est alors purement dissipatif. (b) Profiles schématiques de glissement et de contraintes le long d'un faille élastique homogène. Inspiré de Andrews (1976, 1980), Kanamori et Rivera (2006), Ben-Zion (2003).*

Si la contrainte cisaillante chute de façon quasi-statique, alors la résistance au cisaillement se dégrade progressivement durant le déplacement et l'évolution du système est alors purement dissipatif, i.e. toute l'énergie est dissipée en fracturation et travail frictionnel, et aucune énergie n'est radiée (on parle de « silent earthquake » ou de « creep»).

La Figure 1.9b illustre les profils de variation de contraintes et de glissement le long d'une faille élastique (Andrews, 1976, 1980), avec des propriétés frictionnelles spatialement homogènes. Dans le modèle dynamique, la contrainte cisaillante chute rapidement au cours du glissement critique d'affaiblissement, puis reste au seuil de frottement dynamique jusqu'à l'arrêt de la rupture. Dans le modèle quasi-statique, la chute de contrainte est progressive au cours du glissement depuis le seuil de résistance statique jusqu'à la contrainte cisaillante finale.

Ces modèles présentés ci-dessus traduisent l'évolution de la contrainte cisaillante avec le déplacement, uniquement en un point sur l'interface ou bien peuvent correspondre au cas d'une faille aux propriétés frictionnelles homogènes. Dans le paragraphe qui suit, les évidences de l'hétérogénéité spatiale en glissement et en contrainte le long de la rupture seront présentées et discutées au regard de l'implication probable de la géométrie des failles dans cette complexité.

1.5. Hétérogénéité spatiale du glissement et de la contrainte

La quantité de modèles cinématiques issus de données géophysiques accumulée ces dernières années (voir http://www.seismo.ethz.ch/srcmod pour une base de donnée en ligne des modèles) renseigne sur les complexités multiples que présentent les tremblements de terre au niveau de la source.

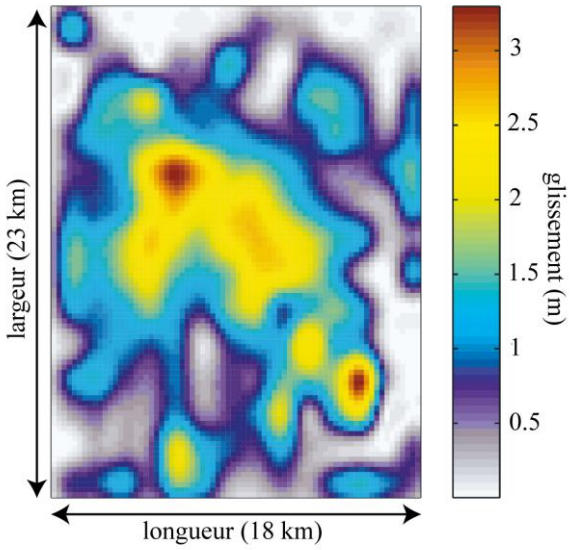

Figure 1.10. *Modèle cinématique illustrant l'hétérogénéité spatiale du glissement sur le plan de la faille du tremblement de terre de Northridge en 1994. Modifié de Tinti et al. (2005).*

D'un point de vue méthodologique, les inversions de mouvements forts ont considérablement évolué depuis leur apparition dans les années 80. Les données utilisées ne se limitent plus aux seuls mouvements forts enregistrés. Par exemple, Wald et Heaton (1994) ont rajouté l'utilisation de mesures géodésiques ; Hernandez *et al*. (1999) ont rajouté l'utilisation de mesures d'interférométrie radar pour contraindre les modèles cinématiques de la rupture. Les modèles directs se sont améliorés, par exemple Tinti *et al*. (2005) proposent une nouvelle fonction source de glissement permettant de se rapprocher au maximum d'une caractérisation dynamique. En permettant de scruter les détails spatio-temporels de la rupture, les modèles cinématiques mettent en évidence une grande hétérogénéité et une grande variabilité du glissement (et donc de la variation de contrainte) lors d'un tremblement de terre (Figure 1.10). Les modèles cinématiques nous amènent alors à considérer la rupture macroscopique de la faille comme un processus d'intégration des hétérogénéités présentes à une échelle inferieure. La rupture macroscopique de la faille peut alors être schématisée comme une chaine de systèmes bloc-ressort unitaire (Figure 1.11).

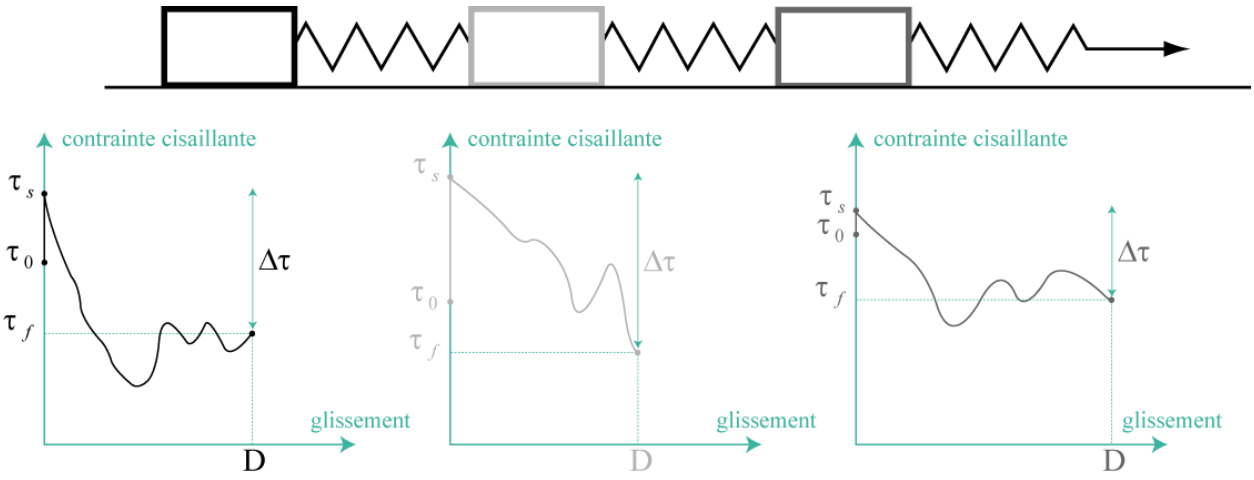

Figure 1.11. *Diagramme schématique de systèmes bloc-ressort unitaires illustrant la complexité de la rupture macroscopique le long de la faille. La variation de la contrainte cisaillante avec le glissement pour chaque bloc matérialise la rupture en des points discrets de la faille.*

Chacun des blocs matérialise la rupture en un point de la faille et chacune de ces ruptures unitaires interagit avec les autres ruptures de manière à faire émerger un comportement collectif. Les variations de la contrainte et du glissement enregistrées en chaque point peuvent être alors diverses et complexes, à la différence d'un modèle de rupture dynamique homogène. Les modèles de rupture dynamique basés sur le concept d'affaiblissement en glissement se doivent donc d'introduire une variabilité spatiale dans les paramètres constitutifs de la rupture, par exemple en faisant varier d_c, le seuil de résistance statique, ou bien le seuil de frottement dynamique. Rappelons alors que la vision cinématique de la rupture réduit les modélisateurs à utiliser des critères stochastiques pour décrire la variabilité spatiale des paramètres constitutifs (i.e. une multitude de calculs de rupture avec une variation spatiale discrète ou régis par une loi de puissance des paramètres constitutifs) (Zoller *et al*., 2005 ; Ripperger *et al*., 2007 ; Hok, 2008). En effet, les inversions cinématiques permettent uniquement de contraindre l'hétérogénéité spatiale du glissement et de la chute de contrainte. Les expériences de friction en laboratoire sont néanmoins susceptibles d'apporter des informations supplémentaires quant à la variabilité des paramètres constitutifs à incorporer dans les modèles numériques. Cependant, les disparités entre les valeurs observées en laboratoire (e.g., Brace and Byerlee, 1966) et celles typiquement estimées par les sismologues (e.g. Kanamori, 1994; Abercrombie, 1995) soulèvent le problème épineux du changement d'échelle. En effet, en laboratoire, la chute de contrainte est généralement dix à cent fois plus élevée que les valeurs estimées par les sismologues pour les grands tremblements de terre. Dans le même sens, les distances critiques d'affaiblissement d_c observées pour les gros séismes sont typiquement de l'ordre du mètre, alors que dans les expériences de friction en laboratoire, elles sont de l'ordre du millimètre. Il faut alors préciser que les sismologues travaillent à partir des images cinématiques, et manquent du coup les petites échelles (<1 km), qui sont pourtant susceptible de porter la plus grande variabilité (Marsan, 2006 ; Madariaga, 1979). En d'autres termes, les expériences de laboratoire traduisent-elles les hétérogénéités en contrainte et en glissement aux petites échelles, lissées et homogénéisées dans les approches sismologiques? Cette question ramène à un autre problème fondamental : quelle est la part entre les hétérogénéités dynamiques, i.e. générées par les processus en jeu lors des évènements de ruptures, et celles liées à la géométrie du plan de faille ? En effet, les modèles

cinématiques ne permettent pas de déterminer si l'origine de cette hétérogénéité en contrainte et en glissement est liée à des complexités géométriques locales. En d'autres termes, d'un coté l'hétérogénéité en contrainte et en glissement peut résulter de la dynamique du front de rupture lui-même qui laisse la faille dans un état hétérogène (Horowitz et Ruina, 1989 ; Carlson et Langer, 1989). D'un autre coté, la géométrie de la faille est susceptible de contrôler (i) l'initiation de la rupture en contrôlant la concentration des contraintes sur l'interface et donc la variabilité spatiale du seuil de résistance statique, comme énoncé précédemment ; (ii) la propagation de la rupture en affectant le glissement frictionnel ; et (iii) l'arrêt des tremblements de terre par la segmentation de premier ordre (Wesnousky, 2006; Manighetti *et al*., 2007) ou par les aspérités de plus petites échelles qui peuvent progressivement stopper la rupture (Hok, 2008).

1.6. Plan du manuscrit

Dans ce travail de thèse, j'ai mené une caractérisation multi-échelle des propriétés géométriques des failles. Pour se faire, l'utilisation combinée de lasers scanners haute résolution (LIDAR, profilomètre laser, interféromètre à lumière blanche) a permis de quantifier la topographie de surfaces de glissements exhumées dans des environnements tectoniques variés (Alpes, Apennins, Turquie, Californie, Nevada) depuis l'échelle pluri-décamétrique jusqu'à la taille du grain. Afin d'étendre mon analyse jusqu'à l'échelle kilométrique, la rugosité des traces de ruptures de surface de 8 tremblements de terre continentaux récents a également été étudiée. Ce large spectre de mesures visait à obtenir une image cohérente, précise et spatialement continue des propriétés géométriques des failles. Le modèle de la topographie multi-échelle des failles qui émerge de mon analyse, a ensuite été utilisé afin d'évaluer les conséquences probables de la rugosité des failles sur la mécanique des tremblements de terre, notamment sur la distribution spatiale du glissement et des contraintes lors d'un événement de rupture. Le chapitre 2 est une étude de la précision et de la fiabilité des outils statistiques permettant d'estimer les corrélations spatiales éventuelles de la topographie des surfaces de failles. Le chapitre 3 présente l'ensemble des résultats révélés par l'analyse des surfaces de failles exhumées et des traces de ruptures. Le chapitre 4 présente une approche numérique visant à démontrer le rapport de

corrélation probable entre la géométrie des failles et l'hétérogénéité spatiale du glissement visible sur les modèles cinématiques de rupture sismique. Le chapitre 5 présente un modèle théorique révélant l'implication probable de la rugosité des failles sur la variabilité spatiale de la chute de contrainte le long du plan de faille. Le chapitre 6 est une étude théorique et numérique de l'effet de la rugosité sur la répartition des contraintes dans une couche visco-elastique (i.e. de matériel endommagé) entourée par deux surfaces de failles. Enfin, le chapitre 7 présente une perspective mettant en avant l'organisation structurale des zones de failles observées sur le terrain, et visant à donner des pistes quant aux processus à l'origine de la rugosité des failles étudiées.

Les principales conclusions apportées par l'ensemble de ces travaux peuvent se résumer de la manière suivante :

(i) Un unique modèle géométrique auto-affine caractérise l'ensemble des zones de failles étudiées depuis l'échelle du grain jusqu'à l'épaisseur de la croute sismogénique.

(ii) Cette description des surfaces de failles exhumées et des traces de ruptures, lesquelles sont toutes deux des marqueurs de la morphologie des structures actives des zones de failles, est indépendante du contexte géologique et plus particulièrement du déplacement accumulé.

(iii) Les hétérogénéités spatiales en glissement et en contrainte observées par les sismologues le long des failles, peuvent être expliquées par le poinçonnement suivit du cisaillement de deux interfaces rugueuses auto-affines (i.e. comme il serait le cas en profondeur). Les fluctuations 2-D (dans le plan) du glissement et de la chute de contrainte sont caractérisées respectivement par : un régime d'auto-affinité similaire à celui de la rugosité 3-D des lèvres de la faille, une magnitude qui augmente vers les petites échelles.

Chapter 2:

Characterization of fault roughness at various scales: implications of three-dimensional high resolution topography measurement

2.1. Chapter 2 overview (Présentation du Chapitre 2)

2.1.1. Introduction

Dans ce chapitre, je présente un article publié dans la revue *Pure and Applied Geophysics* (Candela *et al.*, 2009). Cette étude vise à tester la fiabilité et la précision des méthodes statistiques qui permettent d'estimer les propriétés auto-affines d'une surface rugueuse. A l'aide de surfaces auto-affines synthétiques (Bierme *et al.*, 2007 ; Clausel et Vedel, 2008), deux sortes de biais ont étés identifiés : les artefacts inhérents à l'acquisition des données naturelles et les erreurs intrinsèques des méthodes statistiques elle mêmes. Des résultats préliminaires sur la morphologie des surfaces de failles naturelles sont également présentés.

2.1.2. Presentations at international meetings

2009, European Geosciences Union, General assembly, Vienna (Austria):

Candela T., Renard F., Bouchon M., Brouste A., Marsan D., Schmittbuhl J., and Voisin C., Characterization of Fault Roughness at Various Scales: Implications of Three-Dimensional High Resolution Topography Measurements. *Geophysical Research Abstracts*, Vol. 11, EGU2009-1984.

2008, European Geosciences Union, General assembly, Vienna (Austria):

Candela T., Renard F., Schmittbuhl J., Bouchon M., Roughness of Fault Surfaces: Implications of High Resolution Topography Measurements at Various Scales. *Geophysical Research Abstracts*, Vol. 10, EGU2008.

2.1.3. Contributors to Chapter 2

J'ai personnellement produit tout les résultats de ce chapitre. Les mesures topographiques acquises sur le terrain (LiDAR) ont été effectuées par F. Renard et C. Voisin. Les mesures topographiques en laboratoire des échantillons des surfaces de failles, ont été réalisées par moi-même à l'institut de physique du globe de Strasbourg en collaboration avec J. Schmittbuhl.

2.2. Characterization of Fault Roughness at Various Scales: Implications of Three-Dimensional High Resolution Topography Measurements

Thibault Candela [1], François Renard [1, 2], Michel Bouchon [3], Alexandre Brouste[4], David Marsan[5], Jean Schmittbuhl[6], and Christophe Voisin[3]

[1]*University Joseph Fourier - Grenoble I, Laboratoire de Géodynamique des Chaînes Alpines, CNRS-OSUG, BP 53, 38041 Grenoble, France (Thibault.Candela@ujf-grenoble.fr, françois.renard@ujf-grenoble.fr).*

[2]*Physics of Geological Processes, University of Oslo, Oslo, Norway.*

[3]*University Joseph Fourier - Grenoble I, Laboratoire de Géophysique Interne et Tectonophysique, CNRS-OSUG, Grenoble, France (christophe.voisin@ujf-grenoble.fr, michel.bouchon@ujf-grenoble.fr).*

[4]*University of Le Mans, Laboratoire Manceau de Mathématiques, CNRS, Université du Maine, Le Mans, France (Alexandre.Brouste@univ-lemans.fr).*

[5]*University of Savoie, Laboratoire de Géophysique Interne et Tectonophysique, CNRS, Le Bourget du Lac, France (david.marsan@univ-savoie.fr)*

[6]*UMR 7516, Institut de Physique du Globe de Strasbourg, Strasbourg, France.*

Abstract

Accurate description of the topography of active faults surfaces represents an important geophysical issue because this topography is strongly related to the stress distribution along fault planes, and therefore to processes implicated in earthquake nucleation, propagation, and arrest. To date, due to technical limitations, studies of natural fault roughness either performed using laboratory or field profilometers, were obtained mainly from 1-D profiles. With the recent development of Light Detection And Ranging (LIDAR) apparatus, it is now possible to measure accurately the 3-D topography of rough surfaces with a comparable resolution in all directions, both at field and laboratory scales. In the present study, we have investigated the scaling properties including possible anisotropy properties of several outcrops of two natural fault surfaces (Vuache strike-slip fault, France, and Magnola normal fault, Italy) in limestones. At the field scale, digital elevation models of the fault roughness were obtained over surfaces of 0.25 m^2 to 600 m^2 with a height resolution ranging from 0.5 mm to

20 mm. At the laboratory scale, the 3-D geometry was measured on two slip planes, using a laser profilometer with a spatial resolution of 20 μm and a height resolution less than 1 μm.

Several signal processing tools exist for analyzing the statistical properties of rough surfaces with self-affine properties. Among them we used six signal processing techniques: (i) the root-mean-square correlation (RMS), (ii) the maximum-minimum height difference (MM), (iii) the correlation function (COR), (iv) the RMS correlation function (RMS-COR), (v) the Fourier power spectrum (FPS), and (vi) the wavelet power spectrum (WPS). To investigate quantitatively the reliability and accuracy of the different statistical methods, synthetic self-affine surfaces were generated with azimuthal variation of the scaling exponent, similar to what is observed for natural fault surfaces. The accuracy of the signal processing techniques is assessed in terms of the difference between the "input" self-affine exponent used for the synthetic construction and the "output" exponent recovered by those different methods. Two kinds of biases have been identified: artifacts inherent to data acquisition and intrinsic errors of the methods themselves. In the latter case, the statistical results of our parametric study provide a quantitative estimate of the dependence of the accuracy with system size and directional morphological anisotropy.

Finally, based on this parametric study, we used the most reliable techniques (RMS-COR, FPS, WPS) to analyse field data. These three methods provide complementary results. The FPS and WPS methods determine a robust characterization of the fault surface roughness in the direction of striations and perpendicular to them. The RMS-COR method allows investigating the azimuth dependence of the scaling exponent. For both field and laboratory data, the topography perpendicular to the slip direction displays a similar scaling exponent $H_{\perp} = 0.8$. However, our analysis indicates that for the Magnola fault surface the scaling roughness exponent parallel to the mechanical striation is identical at large and small scales $H_{//} = 0.6 - 0.7$ whereas for the Vuache fault surface it is characterized by two different self-affine regimes at small and large scales. We interpret this cross-over length scale as a witness of different mechanical processes responsible for the creation of fault topography at different spatial scales.

2.2.1. Introduction

Knowledge of the detailed fault geometry is essential to understand some major processes involved in faulting such as grain comminution or asperities abrasion during slip, geometrical heterogeneity of the stress field that controls earthquake nucleation (Campillo *et al.*, 2001;

Voisin *et al.*, 2002a), rupture propagation, and arrest (Voisin *et al.*, 2002b). Establishing correlations between geometrical properties of fault roughness (Power *et al.*, 1987, 1988; Power and Tullis, 1991; Schmittbuhl *et al*., 1993; Lee and Bruhn, 1996; Power and Durham, 1997; Renard *et al.*, 2006; Sagy *et al.*, 2007), seismic behavior of faults (Okubo and Aki, 1987; Parson, 2008), frictional strength and critical slip distance (Scholz, 2002), wear processes during fault zone evolution (Power *et al.*, 1988) represents a fundamental issue to understand seismic faulting.

At the laboratory scale, Amitrano and Schmittbuhl (2002) highlight a complex coupling between fault gouge generation and fault roughness development. At larger scale, asperities control the slip distribution of earthquake (Peyrat *et al.*, 2004). Indeed asperities on active fault planes concentrate the stress (Marsan, 2006; Schmittbuhl *et al.*, 2006) and therefore may control earthquake nucleation (Lay *et al.*, 1982; Scholz, 2002) and the propagation of the rupture to its ultimate arrest (Aki, 1984). High resolution relocations of earthquakes using the multiplet technique have shown streaks of earthquake along several faults in California (Rubin *et al.*, 1999). This pattern has been interpreted as resulting from the presence of an organized large scale roughness (asperities) resisting slip (Schaff *et al.*, 2002).

Despite recent progress in seismology, the imaging of fault planes over a large range of scales at depth is not yet available. A quasi-unique access to high resolution description of the fault plane comes from exhumed fault scarp observations. This requires, of course, that the main morphological patterns of faults mapped at the surface of the earth persist at least across the seismogenic zone. Due to technical limitations, prior comparative studies of natural fault roughness were mainly based on 1D profilometry (Power *et al.*, 1987, 1988; Power and Tullis, 1991; Schmittbuhl *et al*., 1993; Lee and Bruhn, 1996; Power and Durham, 1997). These 1D measurements have shown that fault roughness can be characterized by a scale invariance property described by a self-affine geometry (see section 2.2.2 for the definition of self-affinity) with a roughness scaling exponent close to 0.8 for profiles oriented in a direction perpendicular to the striations observed on the fault plane. Such striations are aligned in the direction of slip. The value of 0.8 is similar to what was measured for tensile cracks (Power *et al*., 1987; Schmittbuhl *et al*., 1995b; Bouchaud, 1997). Moreover, the influence of slip was also quantified: the fault surfaces have smaller roughness amplitude along the slip direction than perpendicular to it (Power *et al.*, 1988; Power and Tullis, 1991; Lee and Bruhn, 1996; Power and Durham, 1997). The compiled fault roughness statistics of several studies (Power and Tullis, 1991; Lee and Bruhn, 1996; Ben-Zion and Sammis, 2003) suggest a change in scaling properties between large and short length scales. However, considering the noise in

their data, these authors underlined that it was not possible to decipher whether this variation was related to small-scale surface weathering of the fault scarp or to the faulting process itself.

With the recent development of high resolution distancemeters, it is now possible to use accurate statistical approaches to quantify fault roughness. Indeed, portable 3D laser scanners (also called LiDAR, Light Detection And Ranging) allow mapping fault surface outcrops over scales of 0.5 mm to several tens of meters. The accuracy of the measurements enables a reliable quantification of the data. Renard *et al.* (2006) and Sagy *et al.* (2007) demonstrated precisely the scaling invariance and anisotropy properties of fault topography using ground based LIDAR and laboratory profilometers. In these previous studies, statistical analysis of fault roughness was carried out with a single signal processing tool. However, Schmittbuhl *et al.* (1995a, 1995b) recommend the simultaneous use of different methods in order to appreciate the confidence in the measured scaling invariance properties.

In the present study, we use new roughness data to extend the type of measurements made by Renard *et al*. (2006) and Sagy *et al.* (2007) and propose a parametric study of the statistical results of fault topography, using multiple signal processing tools. In order to investigate the reliability and accuracy of the different signal processing methods, synthetic self-affine surfaces were generated with azimuthal variation of the scaling exponent. These synthetic rough surfaces are completely characterized by two different self-affine exponents prescribed in perpendicular directions. When comparing these synthetic surfaces to natural faults, one should keep in mind that any self-affine model can only describe a real surface to a finite degree of accuracy, and only within a finite range of scales. After this systematic study, we used the most reliable and accurate techniques to investigate the scaling properties and anisotropy of several outcrops of two natural fault surfaces that have been measured using 3D laser scanners in the field and a laser profilometer in the laboratory.

This paper is organized as follows. In section 2.2.2, following a brief explanatory discussion of the self-affine notion, the generation process of synthetic self-affine surfaces with a directional morphological anisotropy is described. In section 2.2.3, statistical methods to define the self-affine properties are reviewed. Section 2.2.4 is devoted to the systematic study of the accuracy of the methods. Section 2.2.5 is devoted to the acquisition of data on natural fault. In section 2.2.6, analysis of the roughness, covering six orders of magnitude of length scales, is performed on several outcrops of two natural faults. Finally, in section 2.2.7, we conclude by linking our findings on the statistical properties of natural fault topography to

the results of earlier studies, with the ultimate goal of developing a more mutually consistent description of fault asperities geometry.

2.2.2. Generation of self-affine surfaces

2.2.2. A Self-affinity in 1D and 2D

Surface roughness analysis provides a statistical characterization of a surface which is simpler and easier to use than a complete deterministic description. In geophysics, Brown and Scholz (1985) and Power *et al*. (1987) demonstrated the self-similar property of natural fault surfaces at field scale. Coming from statistical physics, a more general scaling transformation has been proposed: self-affinity (Mandelbrot, 1985; Mandelbrot, 1986; Voss, 1985) that was successfully used for the quantitative description of fault roughness (Schmittbuhl *et al.*, 1993, Renard *et al.*, 2006).

A self-affine 1D profile remains unchanged under the scaling transformation $\delta x \rightarrow \lambda\, \delta x$, $\delta z \rightarrow \lambda^{H} \delta z$ for 1D profiles (Figure 2.1) extracted from a surface (Meakin, 1998). Here, δx is the coordinate along the profile and δz is the roughness amplitude. For a self-affine profile, the scaling exponent H, also called Hurst exponent, lies in the range $0 \leq H < 1$. Accordingly, self-affinity implies that a profile appears less rough as the scale increases. In other words, if a profile is self-affine, a magnified portion of it will appear statistically identical to the entire profile if different magnifications are used in the x and z-directions (Figure 2.1).

For 2D surfaces, this self-affinity property can be described for sets of 1D parallel profiles extracted from the surface. Moreover, if the surface is striated along some given orientation, anisotropic scaling behavior can emerge if H varies for different directions in the plane of the surface. An anisotropic self-affine surface $Z(x, y)$ with coordinates (x, y) obeys the property: $Z\left(\lambda^{1/H_{//}} x, \lambda^{1/H_{\perp}} y\right) = \lambda\, Z(x, y)$, where λ is a positive dilation factor, $H_{//}$ and $H_{\perp}$ are the Hurst exponents, comprised between 0 and 1, in two perpendicular directions of the surface. $H_{//}$ is defined along a direction parallel to the main striations, and $H_{\perp}$ is defined along a direction perpendicular to the striation (Figure 2.1b).

2.2.2. B. Synthetic anisotropic self-affine surfaces

To calculate synthetic fault surfaces (Figure 2.1b), we used a Fourier based method to simulate a matrix scaling random Gaussian field on a 2D grid, where an anisotropy matrix

$E = \begin{pmatrix} 1/H_{//} & 0 \\ 0 & 1/H_{\perp} \end{pmatrix}$ was introduced when calculating the 2D Gaussian random field. The eigenvalues of this matrix correspond to the inverse of the two roughness exponents $H_{//}$, and $H_{\perp}$ that characterize the self-affine properties of the generated surface in two perpendicular directions (Bierme *et al.* 2007, Clausel and Vedel, 2008). The code to generate an anisotropic 2D self-affine surface, written in Matlab©, is given in the appendix 2.A and can be run easily on a desktop computer.

In the following sections, we decompose the signal processing analysis of rough surfaces in two stages. Firstly, we present the six signal processing tools used to estimate the self-affine property of an isotropic surface with a single Hurst exponent (Figure 2.1a), as observed for example for fresh mode I brittle fractures in rocks (Power *et al.*, 1987; Schmittbuhl *et al.*, 1995b; Bouchaud, 1997). For this, we have synthesized several isotropic surfaces with an exponent in the range [0.1 - 0.9] and grid sizes in geometrical series: 129 × 129 points, 513 × 513 points, 2049 × 2049 points. Secondly, we analyse synthetic anisotropic surfaces (Figure 2.1b) with $H_{//}$ in the range [0.7 - 0.9] and $H_{\perp}$ in the range [0.4 - 0.9].

2.2.3. Statistical signal processing methods

We have used six different methods that characterize the amplitude of the roughness at various spatial wavelengths. All these methods, presented in the following sub-sections, are based on the analysis of 1D profiles (Figure 2.1c) that are extracted from the 2D Digital Elevation Model (DEM) of 2D surfaces (Figure 2.1a, b). For each surface, a set of 1D parallel profiles in a specific direction are extracted, detrended and then analyzed. Then, the properties are averaged over all the 1D profiles to characterize the 2D surface in the chosen direction. To study the azimuthal dependence of the statistical properties of the surfaces, we have extracted profiles in several directions, following a 360° rotation. Estimating the statistical properties of the surface in various directions (Renard *et al.*, 2006) allows characterizing a morphological anisotropy.

For the application to natural fault surfaces, we also tested how the noise in the data and the presence of missing points could affect the estimation of fault surface. Indeed, the raw scanner data consist of clouds of points, with x, y, and z coordinates, sampled more or less regularly. Sometimes, data are missing (vegetation on the fault plane, low reflectivity of the scanner light beam), and the surface is incomplete. An interpolation is then necessary, which induce a bias in the estimation of scaling exponents that need to be estimated too.

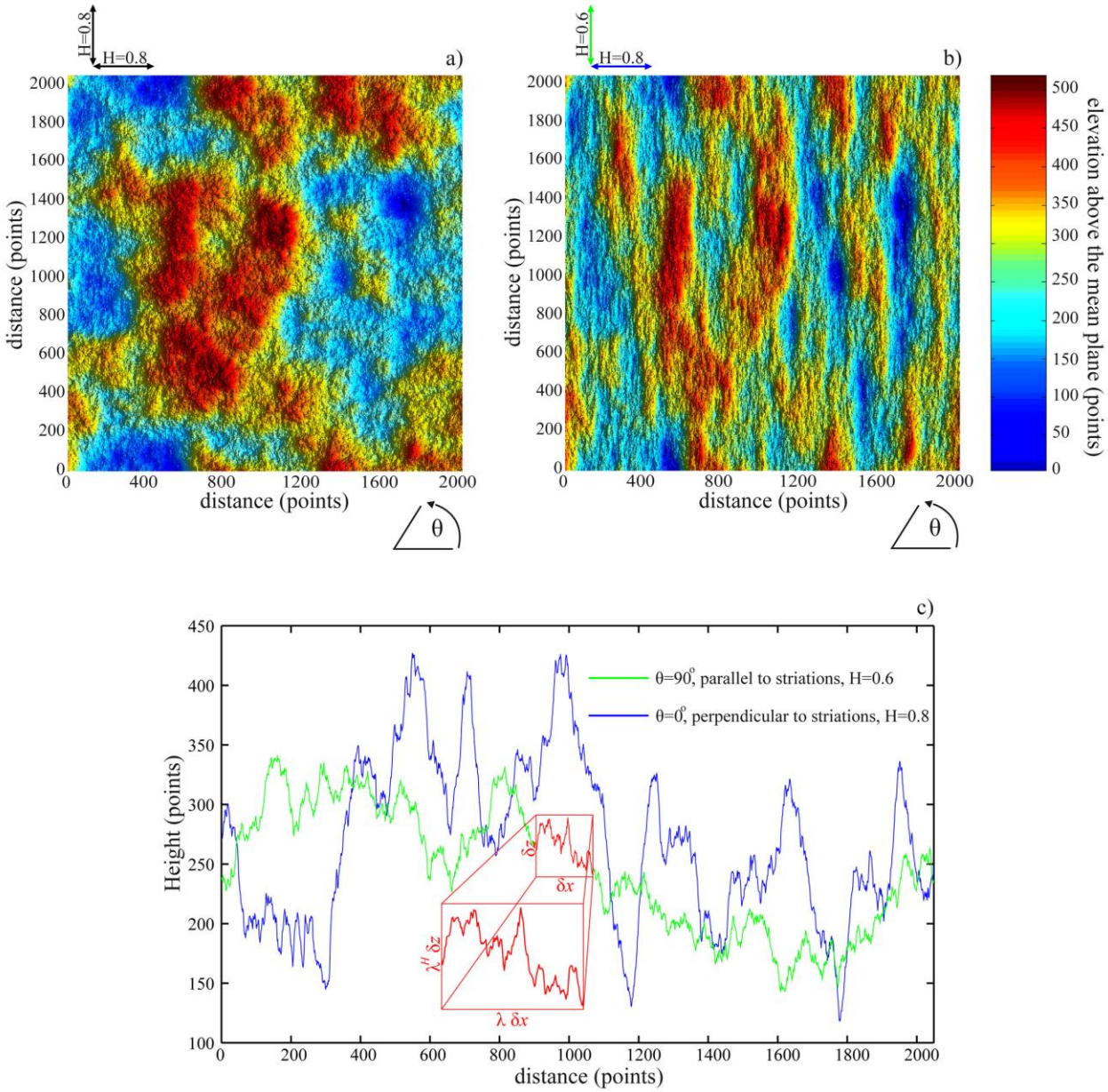

Figure 2.1. *Digital Elevation Models (DEM) of 2D synthetic self-affine surfaces (up) and 1D profiles (down) generated using the algorithm of the appendix. (a) Surface with an isotropic self-affine property characterized by a Hurst exponent of 0.8. (b) Anisotropic self-affine surface with two Hurst exponents ($H_{//} = 0.6$ and $H_{\perp} = 0.8$) in perpendicular directions. (c) Representative 1D profiles extracted in two perpendicular directions of surface (b). Inset: magnified portion of a profile along the $H_{//}$ direction (parallel to the striations), which has a statistically similar appearance to the entire profile when using a rescaling $\delta x \rightarrow \lambda\, \delta x$, $\delta z \rightarrow \lambda^{H} \delta z$.*

2.2.3. A. Root-mean-square correlation (RMS) and maximum-minimum height difference (MM) methods

Consider a 1D profile L(x) that is divided into windows of width δx and indexed by the position of the first point x_0 of the band. The standard deviation $\sigma(\delta x)$ of the height $L(x)$ and the height difference $h(\delta x)$ between the maximum and minimum height are computed for each band, and then averaged over all the possible bands of fixed width δx spanning the profile, by varying the origin x_0. We then obtain $\langle\sigma(\delta x)\rangle$ and $\langle h(\delta x)\rangle$, where both quantities follow a power law for a self-affine profile: $\langle\sigma(\delta x)\rangle \propto \delta x^H$ and $\langle h(\delta x)\rangle \propto \delta x^H$ (Schmittbuhl *et al*. 1995a).

Note that this technique is useful when H is not too close to 0 or 1, where a significant error can be measured (see Figures 2.3a, b – 2.4a, b). Usually, levelling off of $\sigma(\delta x)$ at small δx values is due to the noise in the data (see Figure 2.7c, d), and leveling-off at large δx is due to the finite size of the profile.

2.2.3. B. Height-height correlation function (COR) method

For a signal $L(x)$, we consider the height-height correlation function defined by $C(\Delta x) = \left[\left\langle (L(x) - L(x+\Delta x))^2 \right\rangle\right]^{1/2}$, which estimates the average height-height difference between two points of the profile separated by a distance Δx. For a self-affine profile, the correlation function follows a power-law such that $C(\Delta x) \propto \Delta x^H$ where H is the Hurst exponent.

2.2.3. C. Standard deviation of the correlation function (RMS-COR) method

For a profile $L(x)$ containing N points, the height difference ΔL between each pair of points separated by a distance Δx is calculated. The window size Δx is varied between the sampling distance and the size of the system and, for a given Δx, the standard deviation of the height difference $\sigma(\Delta L_{\Delta x})$ is calculated. For a self-affine surface this measurement follows a power-law such that $\sigma(\Delta x) \propto \Delta x^H$. This method was successfully applied to characterize the self-affine properties of the Vuache fault plane (Renard *et al.* 2006).

2.2.3. D. Fourier power spectrum (FPS) method

The Hurst exponent H can be estimated from the Fourier power spectrum which has a power law form for a 1D self-affine profile (Barabasi and Stanley, 1995; Meakin, 1998). For each parallel profile, the Fourier power spectrum $P(k)$, *i. e*. the square of the modulus of the Fourier transform, is calculated as a function of the wave-number k. Then the spectrum of the whole surface is calculated by stacking all the 1D Fourier transforms to reduce the noise associated with individual profiles. For each profile of length L containing N increments, the spatial frequencies range between $1/L$ and the Nyquist frequency $N/2L$ (*i.e.* the reciprocal of the interval between data points). When plotting the power spectrum as a function of k in log-log space, a self-affine function reveals a linear slope, which is itself a function of the Hurst exponent H through $P(k) \propto k^{-1-2H}$.

2.2.3. E. Average wavelet coefficient power spectrum (WPS) method

The average wavelet coefficient method consists of decomposing the input signal into amplitudes that depend on position and scale. The wavelet transform of each 1D profile $L(x)$ is defined as $W_{a,b} = \frac{1}{\sqrt{a}} \int_{-\infty}^{+\infty} \psi\left(\frac{x-b}{a}\right) L(x)\, dx$ where ψ is the wavelet function. Then the wavelet coefficients are averaged over the translation factor b for each length scale a: $W_a = \langle W_{a,b} \rangle_b$. If the profile is self-affine, the wavelet transform verifies statistically that, for any positive dilatation factor λ, $W_{a,b}[L(\lambda x)] = \lambda^H W_{a,b}$. Accordingly, the averaged wavelet coefficients scale as $W_a \propto a^{H+1/2}$. A wide range of wavelet functions can be used. For a simple and efficient implementation, we chose the Daubechies wavelet of order 12 as suggested in Simonsen *et al*. (1998).

2.2.4. Quantitative estimation of the accuracy of roughness analysis methods

2.2.4. A. Synthetic isotropic and anisotropic rough surfaces

Figures 2.1a and 2.1b display the topography of synthetic rough surfaces where the data set includes 2049 × 2049 points regularly spaced on a grid. Figure 2.1a shows an isotropic rough surface, whereas Figure 2.1b shows an anisotropic surface, with corrugations elongated parallel to the direction of smaller Hurst exponent (analogue to the direction of slip on a natural fault surface) and covering a wide range of scales.

The roughness amplitude of a profile parallel to the striation direction (green curve in Figure 2.1c) is smaller than that of a perpendicular profile. The profile extracted along the direction with the smallest exponent (green curve) appears more jagged at small scales compared to a perpendicular profile, showing the different effects of the anisotropy of the surface on the waviness and amplitude of the profiles.

The outputs of the statistical methods described in section 2.2.3 are represented on Figure 2.2 Each curve is calculated by averaging the outputs of all possible parallel 1D profiles extracted from the anisotropic surface of Figure 2.1b. The results are represented in a log-log plot, allowing visualizing the linear portion of the curve that characterizes a power-law distribution (Figure 2.2). This linear portion is binned in a small number of increments, and a power-law fit is performed to extract the Hurst exponent that characterizes the self-affinity of the profile. The best fits are performed for each curve and a value of the "output" self-affine exponent is then calculated for all the six signal processing methods.

Using the RMS correlation function, we have also extracted sets of parallel profiles in several directions, at an angle θ to the direction of the striations. For each set of profile, we have calculated the correlation function and estimated the value of H. The angular dependence of H could be represented on a polar plot (inset in Figure 2.2d) (Renard *et al*., 2006). The anisotropy of such plot characterizes the anisotropy of the surface: an isotropic surface is represented as a circle of radius H, whereas an anisotropic one has a more complex elliptical shape.

2.2.4. B. Isotropic surfaces: effect of size and input exponent on the output estimation of the Hurst exponent

The comparison between the input Hurst exponent used to calculate an isotropic synthetic surface and the output Hurst exponent estimated using the six different methods is represented on Figure 2.3, for different system sizes. The RMS, MM, COR and RMS-COR methods are all mainly sensitive to the value of the input self-affine exponent (the typical trend of the curve is not parallel to the diagonal). Small self-affine exponents are systematically overestimated whereas large exponents are underestimated. In contrast, the error for the WPS method is mainly function of the system size (the response is more or less parallel to the diagonal). The FPS method appears the most accurate technique, with only slight sensitivity to the input self-affine exponent and size effects. This conclusion should however be interpreted cautiously as the algorithm used to generate the synthetic surface is based on a Fourier transform approach. The conclusion of this comparison tests is that the FPS, WPS,

and RMS-COR methods are the most reliable because they have a small dependence on the value of the input Hurst exponent and a slight dependence on system size.

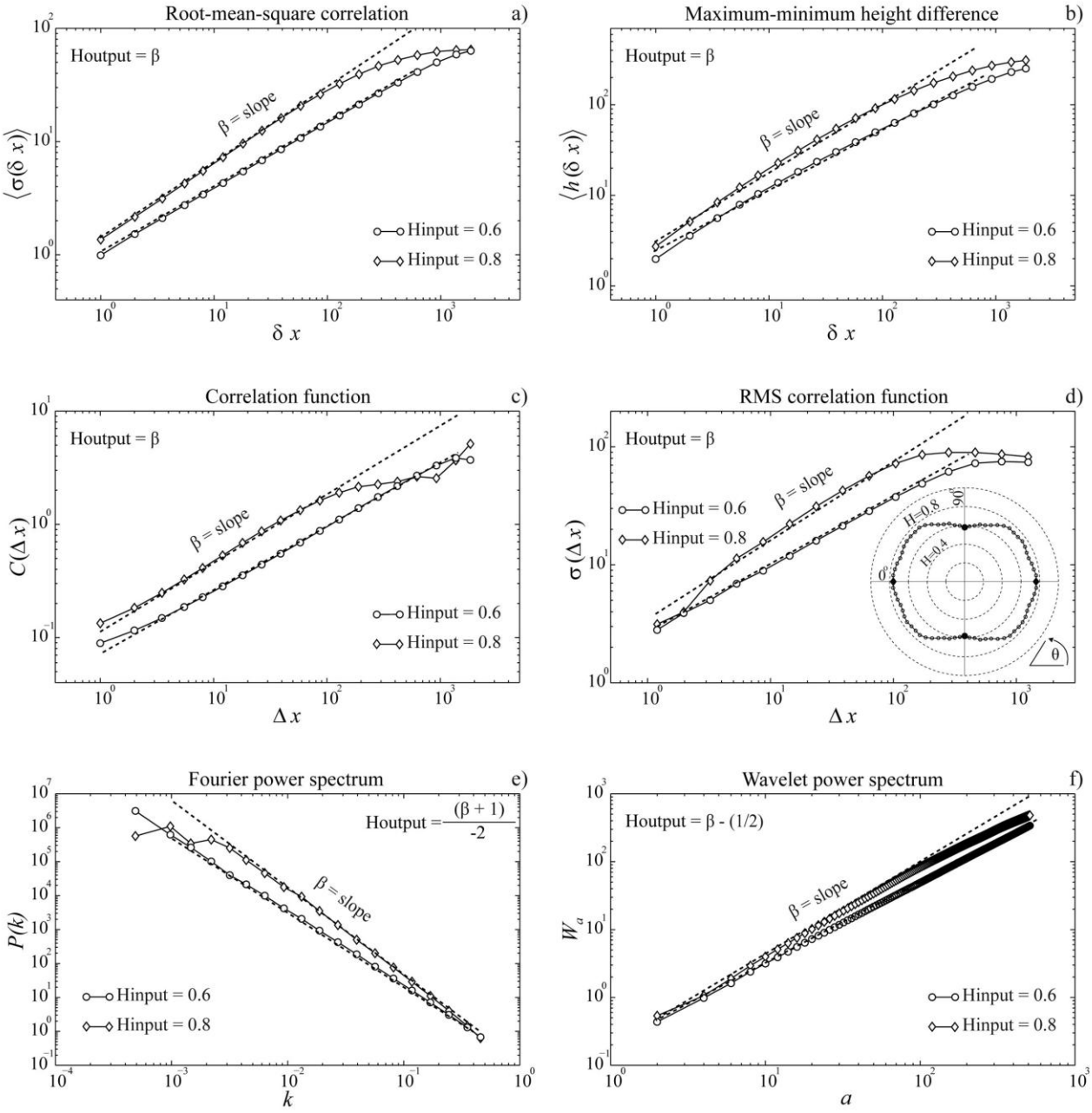

Figure 2.2. *Outputs of the six signal processing techniques applied on the data of the anisotropic self-affine surface shown in Figure 2.1b. (a) Root-mean-square correlation (RMS), (b) maximum-minimum height difference (MM), (c) correlation function (COR), (d) RMS correlation function (RMS-COR), (e) Fourier power spectrum (FPS), (f) Wavelet power spectrum (WPS). The dashed lines represent fits of the curves to obtain the output* β*. The inset in (d) displays a polar plot of* H *obtained by the RMS-COR method and allowing then to determine the azimuth dependence of* H*. The black points correspond to the Hurst exponents for the two profiles shown on this plot.*

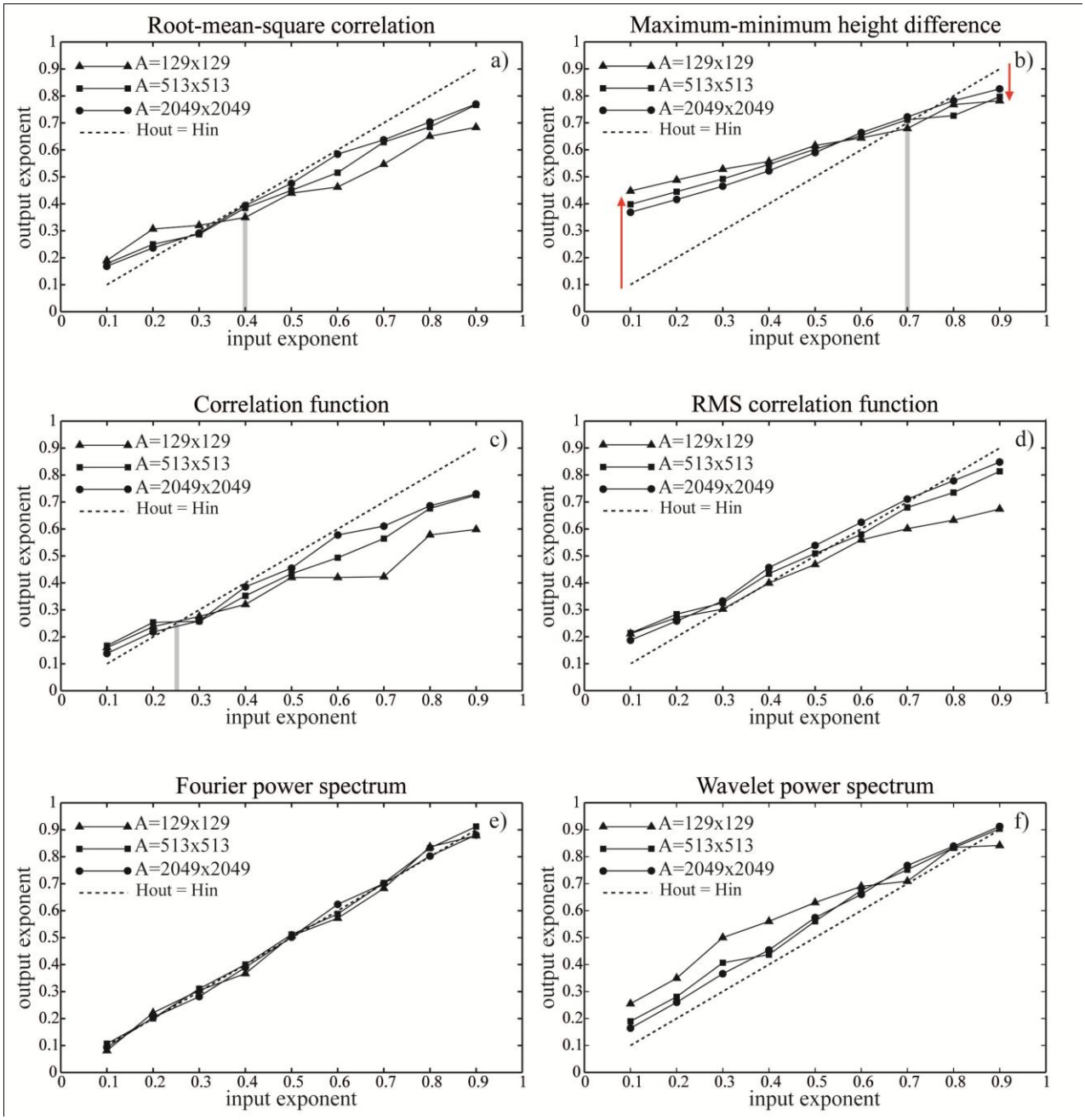

Figure 2.3. *Comparisons between the "input" Hurst exponents introduced in the construction of isotropic fractional Brownian surfaces and the "output" exponent measured on these surfaces using the six independent signal processing techniques. The three outputs illustrate effects of system size. (a) Root-mean-square correlation (RMS), (b) maximum-minimum height difference (MM), (c) correlation function (COR), (d) RMS correlation function (RMS-COR), (e) Fourier power spectrum (FPS), (f) Wavelet power spectrum (WPS). The gray line in (a), (b), and (c) indicate for which input exponent the error in the estimation is closest to zero.*

2.2.4. C. Anisotropic surfaces: Interaction between the two input roughness exponents

For synthetic self-affine anisotropic surfaces, we have calculated the error on the estimation of the two Hurst exponents. For this, we have built surfaces (2049x2049 points, similar to Figure 2.1b) for which the Hurst exponents $H_{input//}$ and $H_{input\perp}$ in two perpendicular directions were varied in the range [0.4 – 0.9]. We have then used the six signal processing techniques to estimate the values of these same exponents. The absolute error in the estimation of each Hurst exponent (Figure 2.4) depends on the input value of these parameters and also on the amplitude of their difference ($H_{input//} - H_{input\perp}$).

This error is particularly large for the RMS (up to 20%), MM (up to 25%), and COR (up to 35%) methods. When the input anisotropy ($H_{input//} - H_{input\perp}$) increases, the absolute error on the two output exponents increases accordingly. The absolute error is smaller in the direction of the smallest exponent (analogue to the direction of striation on a natural fault surface) than perpendicular to it. Moreover, it is also noteworthy to mention that these three techniques show significant errors in the estimation for input exponents close to 0.8-0.9 even if the anisotropy is minimal, demonstrating the limited reliability of these methods to detect an exponent close to one.

The RMS-COR analysis is also sensitive to the input anisotropy (Figure 2.4d), however such an effect is not strongly pronounced (the absolute errors are smaller, up to 15%). For this method, the error does not depend on the values of the two input Hurst exponents. For example, with a synthetic surface defined by $H_{input//}$ = 0.8 and $H_{input\perp}$ = 0.6, the absolute error in the estimation of each Hurst exponent is almost identical. As shown in Figure 2.4d, when anisotropy is small, the errors do not increase significantly for input values close to 1 unlike the three previous methods.

The FPS and WPS analysis are only slightly sensitive to the “input” anisotropy and the estimated Hurst exponents do not depend on the input exponent values. Our analysis clearly shows that the FPS, the WPS and, to a lesser extent, the RMS-COR methods are the most reliable. More precisely, the RMS-COR and the WPS techniques slightly underestimate and overestimate, respectively, the roughness exponent compared to the FPS method.

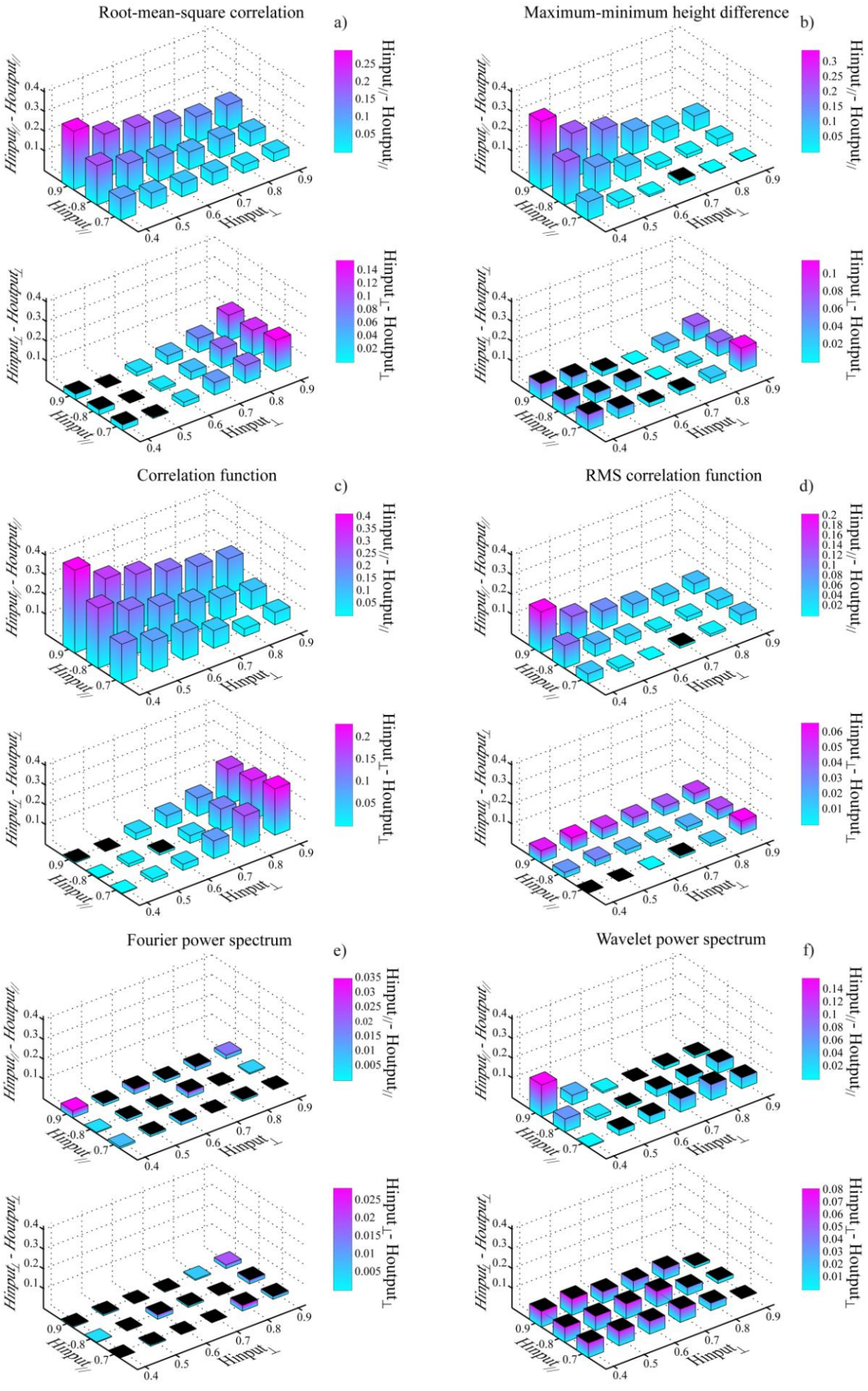
Root-mean-square correlation
a)
Maximum-minimum height difference
b)
Correlation function
c)
RMS correlation function
d)
Fourier power spectrum
e)
Wavelet power spectrum
f)
Hinput// - Houtput//
Hinput⊥ - Houtput⊥
Hinput//
Hinput⊥

Figure 2.4. *Intrinsic errors in the estimation of the Hurst exponents for anisotropic synthetic surfaces characterized by two Hurst exponents* $H_{input//}$ *and* $H_{input\perp}$ *in perpendicular directions (2049x2049 points, similar to Figure 2.1b). For each signal processing method, histogram plots are represented where the horizontal axes contains the Hurst exponents* $H_{input//}$ *and* $H_{input\perp}$ *used as inputs to generate the synthetic surface. The vertical axis represents the difference between the input exponent and the estimated output Hurst exponent, using the six different methods. For each method, two histogram plots are represented: the upper one shows the difference (*$H_{input//} - H_{output//}$*) and the lower one the difference (*$H_{input\perp} - H_{output\perp}$*). The black top surfaces on the histogram bars indicate a negative difference (overestimation of the output exponent) and the color ones a positive difference (underestimation of the output exponent). (a) Root-mean-square correlation (RMS), (b) maximum-minimum height difference (MM), (c) correlation function (COR), (d) RMS correlation function (RMS-COR), (e) Fourier power spectrum (FPS), (f) Wavelet power spectrum (WPS).*

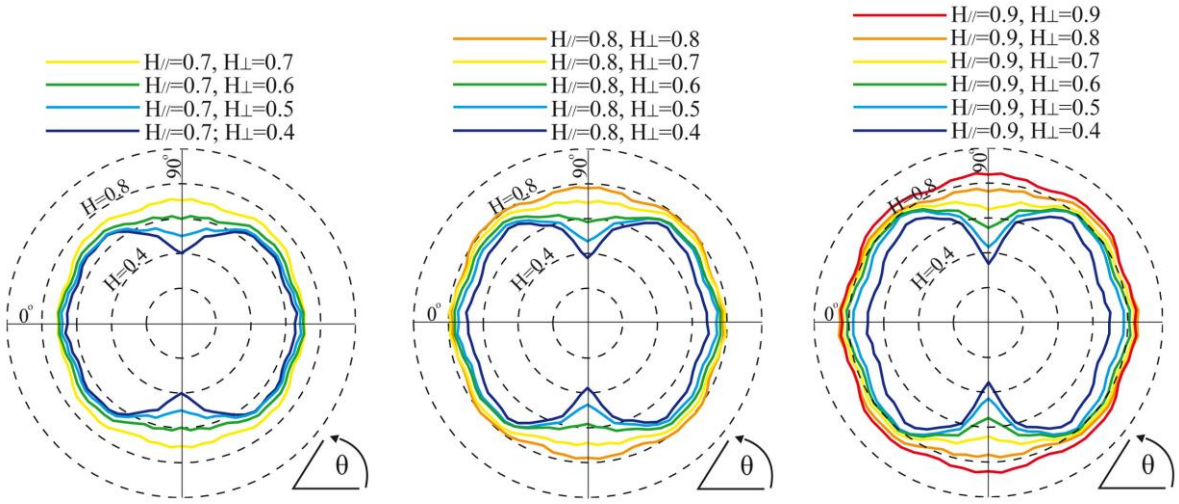

Figure 2.5. *Polar plots of the angular dependence of the two Hurst exponents* $H_{//}$ *and* $H_{\perp}$ *for synthetic anisotropic surfaces with principal directions oriented at angles* $\theta_{//} = 0°$ *and* $\theta_{\perp} = 90°$. *The Hurst exponents* $H_{//,\perp}(\theta)$, *as defined by the slope* $\beta = H$ *in Figure 2.2d, were calculated on series of 1D profiles extracted at an angle* θ *on 2049x2049 points surfaces. Three series of simulations are represented here for three values of* $H_{//}$ *in the range [0.7 – 0.9]. For each polar plot, the different curves corresponds to successive values of* $H_{\perp}$. *The dashed lines correspond to the values of the output Hurst exponent measured with the RMS correlation method (center dashed circle:* $H = 0.2$, *outer dashed circle:* $H = 1$*).*

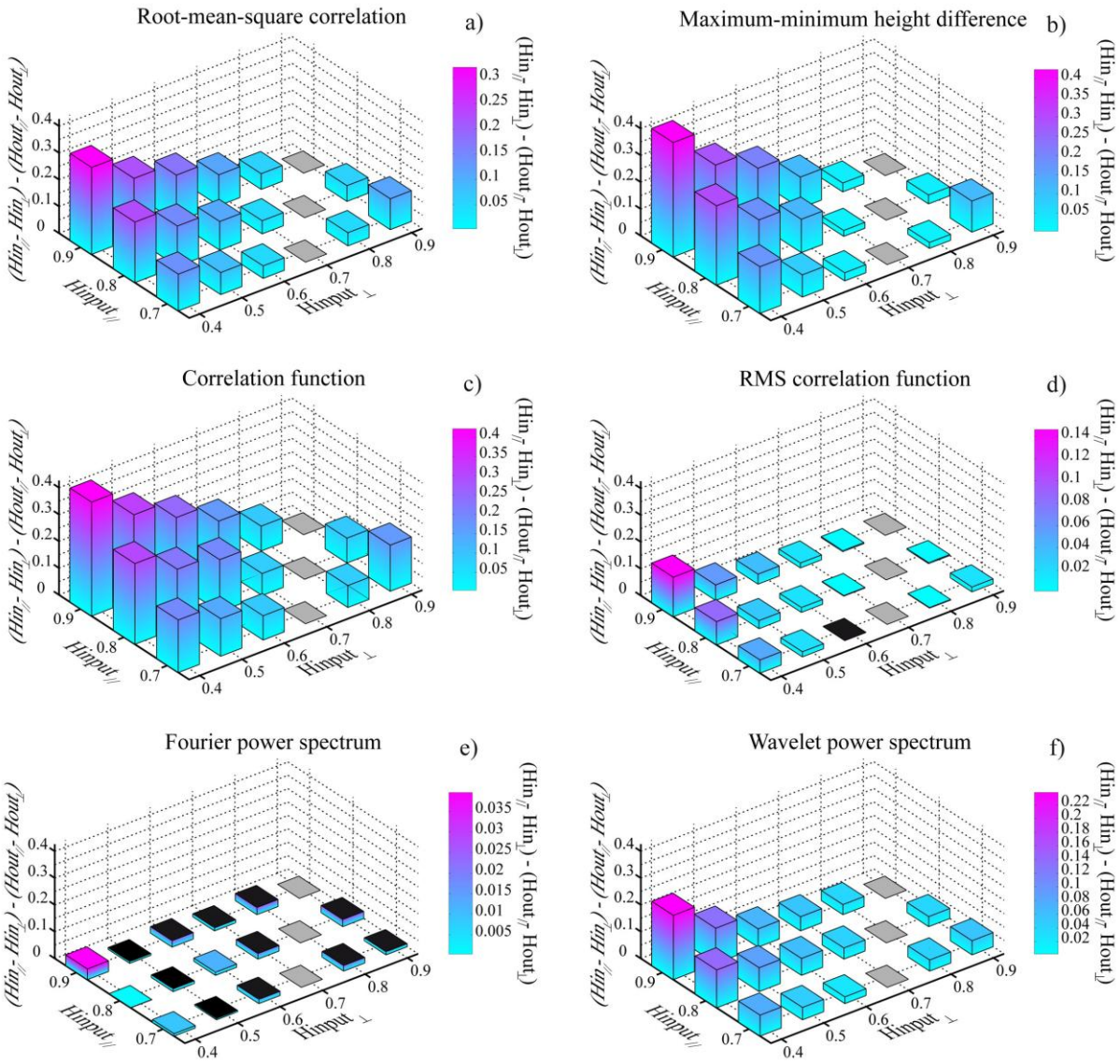

Figure 2.6. *Quantification of the intrinsic errors on the estimation of the anisotropy of the surface ($H_{//} - H_{\perp}$). The difference between the "input" anisotropy (difference between the two "input" Hurst exponents) introduced in synthetic surfaces (2049x2049 points, similar to Figure 2.1b), minus the "output" anisotropy is represented for the six signal processing methods: (a) Root-mean-square correlation (RMS), (b) maximum-minimum height difference (MM), (c) correlation function (COR), (d) RMS correlation function (RMS-COR), (e) Fourier power spectrum (FPS), (f) Wavelet power spectrum (WPS). Bars with black top surface indicate an overestimation ("input" anisotropy - "ouput" anisotropy < 0) and colored top surfaces indicate an underestimation ("input" anisotropy - "ouput" anisotropy > 0). Gray bars indicate isotropic surfaces ($H_{//} = H_{\perp}$), thus without errors.*

We have also analyzed the azimuthal dependence of the Hurst exponent for synthetic anisotropic self-affine surfaces. Comparisons of the "output" anisotropy estimated using the RMS-COR method and the "input" anisotropy is represented on Figure 2.5. We have used this

technique because it does not require interpolation of the profiles, whereas the FPS and WPS methods would need regularly spaced data point. A significant directional morphological anisotropy of surfaces is visible on these polar plots of H even if a low "input" anisotropy is imposed, thus demonstrating the reliability of the RMS-COR method to detect a slight morphological anisotropy. Remarkably, following a 360° rotation, the azimuth variation of H is not progressive. When departing a few degrees from the direction of the smallest "input" exponent, the "output" exponent is already very close to the largest "input" exponent. This property of anisotropic self-affine surface is not well understood yet.

A tentative way to calculate the error on the anisotropy that is made when estimating the anisotropy of the surface $\left|H_{//} - H_{\perp}\right|$ is represented on Figure 2.6. This plot indicates the error on the estimation of the anisotropy of the surface, and therefore provides some bounds on the accuracy of the determination of this property. Almost all methods underestimate the anisotropy, except the Fourier power spectrum which slightly overestimates it. For the RMS, MM, and COR methods, when the "input" anisotropy $\left|H_{//} - H_{\perp}\right|$ increases, the absolute error on the "output" anisotropy increases accordingly. Moreover, this absolute error is similar for all surfaces with the same "input" anisotropy, whatever the values of the two "input" self-affine exponents.

The determination of the "output" anisotropy with the RMS-COR, FPS, and WPS methods is less sensitive to the "input" anisotropy, except for the highest anisotropy, thus demonstrating the robustness of these three methods to determine the azimuth dependence of the statistical properties of an anisotropic self-affine surface. More precisely, estimates reported for the WPS method are somehow systematically lower than the two others techniques.

2.2.4. D. Effect of noise

In all physical measurements, noise is present in the data because of the limited resolution of the measuring device. Such noise is usually described using Gaussian statistics with a zero mean and a constant variance. We have analyzed how the presence of noise in synthetic data could alter the estimation of the Hurst exponent. For this, we have calculated synthetic anisotropic surfaces and added a Gaussian noise with a standard deviation equal to 1/200 of the standard deviation of the rough surface (Figure 2.7a, b). This artificial alteration of the synthetic surface mimics measurements biases obtained on natural data, for example due to electronic noise in the measurement device or due to weathering of the fault surface.

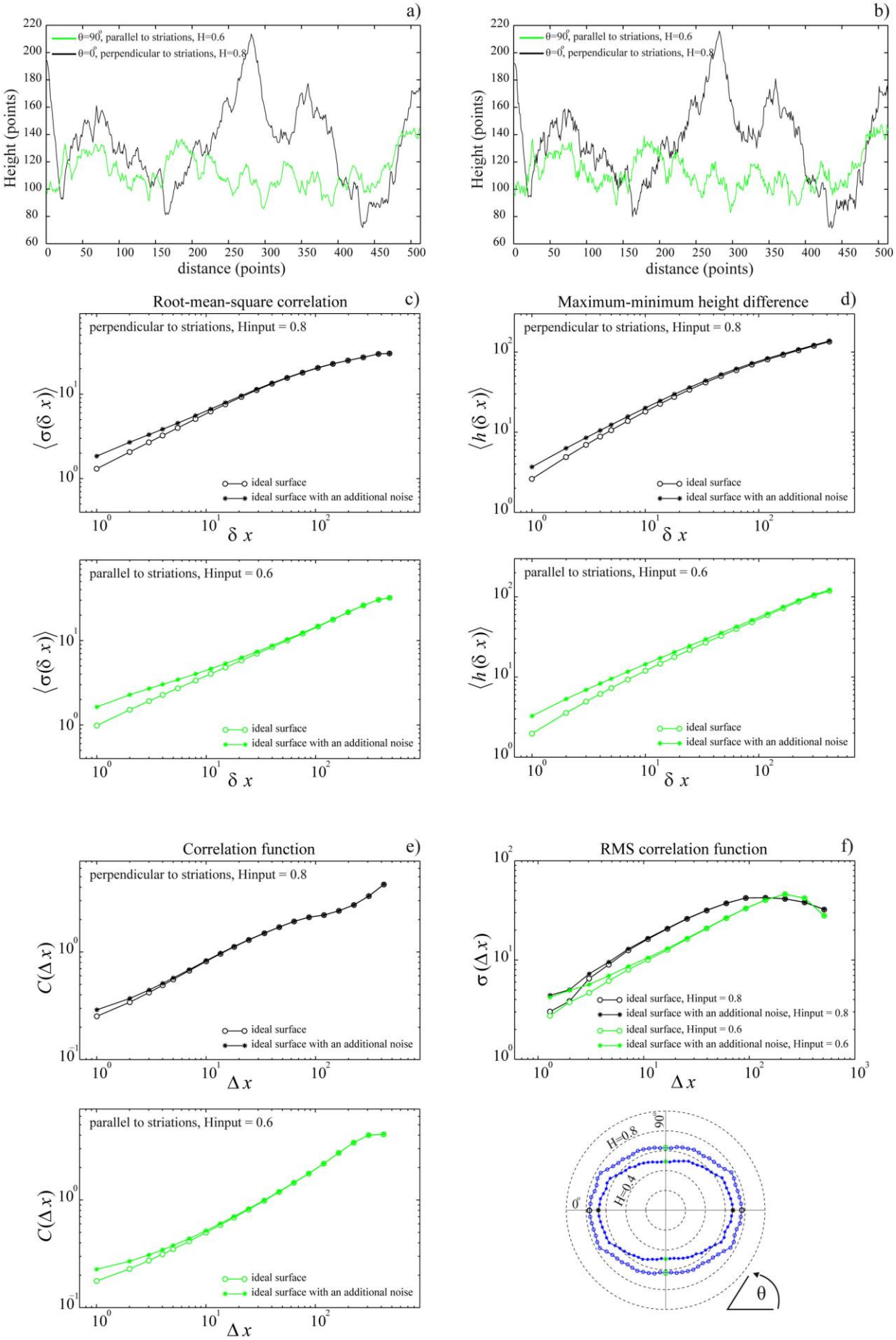
a)
b)
θ=90°, parallel to striations, H=0.6
θ=0°, perpendicular to striations, H=0.8
Height (points)
distance (points)
Root-mean-square correlation
c)
Maximum-minimum height difference
d)
perpendicular to striations, Hinput = 0.8
parallel to striations, Hinput = 0.6
ideal surface
ideal surface with an additional noise
⟨σ(δ x)⟩
⟨h(δ x)⟩
δ x
Correlation function
e)
RMS correlation function
f)
C(Δx)
σ(Δx)
Δx
ideal surface, Hinput = 0.8
ideal surface with an additional noise, Hinput = 0.8
ideal surface, Hinput = 0.6
ideal surface with an additional noise, Hinput = 0.6
H=0.8
H=0.4
θ

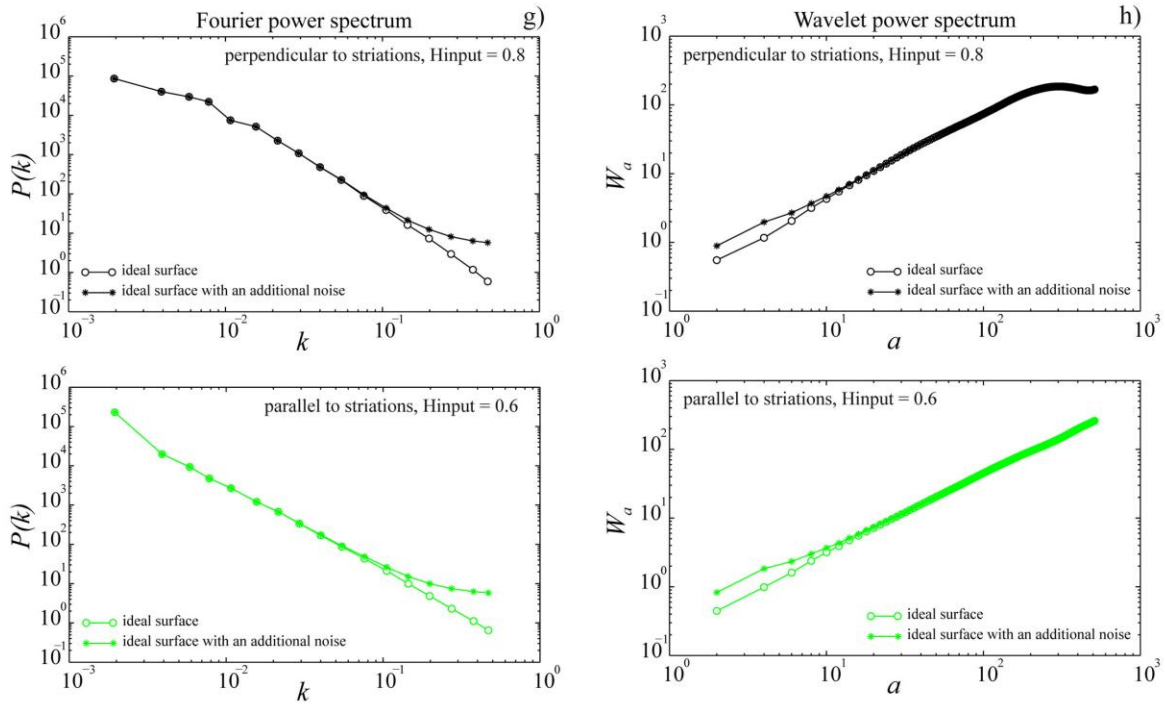

Figure 2.7. *Influence of an additional noise on the self-affinity property of an anisotropic synthetic surface (513x513 points) characterized by two Hurst exponents ($H_{//} = 0.6$ and $H_{\perp} = 0.8$) in perpendicular directions. The Gaussian white noise is characterized by a standard deviation two hundred times smaller than the roughness amplitude of the synthetic surface. (a) Example of 1D profiles extracted in two perpendicular directions of an "ideal" surface. (b) The same profiles but with an additional noise. Note that altered profiles appear more jagged or rougher at small scale compared the noise-free profiles. Analyses of those altered surfaces are performed with the six independent self-affine methods: (c) Root-mean-square correlation (RMS), (d) maximum-minimum height difference (MM), (e) correlation function (COR), (f) RMS correlation function (RMS-COR), (g) Fourier power spectrum (FPS), (h) Wavelet power spectrum (WPS). For each method, except the RMS-COR function, two plots are represented: the upper plot shows the difference between the noise-free surface and the altered surfaces in the direction of the largest exponent and the lower one in direction of the smallest exponent. For the RMS-COR technique, the upper plot represents the difference between the noise-free and the altered surface in both directions: perpendicular and parallel to striations. The lower subplot displays two polar plot of H obtained with the noise-free and the biased surfaces. Note that the flattening of the scaling behavior at large scales is related to a finite size effect.*

We have then estimated the Hurst exponents using the six signal processing methods and compared the results with the noise-free analysis. The results confirm that adding noise to the synthetic data induces a leveling-off of the curves at small length scales (Renard *et al*., 2006;

Sagy *et al*., 2007) and therefore a possible underestimation of the Hurst exponent, for all the six signal processing methods (Figure 2.7c-h).

Despite the fact that the Gaussian white noise added is isotropic, each plot (Figure 2.7c-h) indicates that the effect of noise is slightly dependent on the azimuth of the profile: the underestimation of the Hurst exponent is more pronounced along striations than perpendicularly to them. Indeed, the addition of noise in the rough signal preferentially alters the roughness at small scales, and therefore has a stronger effect on the profiles parallel to the striations because they are characterized by a smaller amplitude at large length scales compared to the profiles perpendicular to the striations.

For the RMS, MM and RMS-COR methods, the noise does affect not only the small length scales but also the large length scales. Indeed, such an effect is strongly pronounced for these three methods and, slopes of the curves in Figure 2.7c-f lead to a significant underestimation of the actual value of the self-affine exponents. Notably, the polar plot of H from a surface with added noise obtained with the RMS-COR technique (see Figure 2.7f) shows errors of 10 % and 20 % on the Hurst exponent measured in directions perpendicular and parallel to striations, respectively.

Conversely, the COR, FPS, and WPS techniques are less sensitive to the addition of noise. At large scale, the noise appears as a negligible correction, and even if the curves are affected at small scales, the estimation of the self-affine exponent is less affected.

2.2.4. E. Effect of missing data

When considering natural fault measurements, local weathering and/or the presence of vegetation may form patches of missing data. To study their influence on estimation of fault surface properties, we generated incomplete data sets removing an increasing percentage of clusters of points from a synthetic surface that initially contained 513x513 points (Figure 2.8). For the FPS and WPS methods, the incomplete cloud of points was interpolated across the gaps (Figure 2.8b), using a linear fit. However, for the RMS-COR method, the biased data can be used without interpolation of the holes (Figure 2.8c).

Typically, in our natural data sets 5 % of interpolated holes is the maximum percentage of spurious points removed from the raw scanner data. The results (Figure 2.8d-f) indicate that the RMS-COR, FPS and WPS analysis show an error of only 4 % on the Hurst exponent estimated on a surface with 40 % holes compared to a complete surface. Therefore, 5% of missing points does not affect significantly the measurement of surface properties, whatever the technique employed.

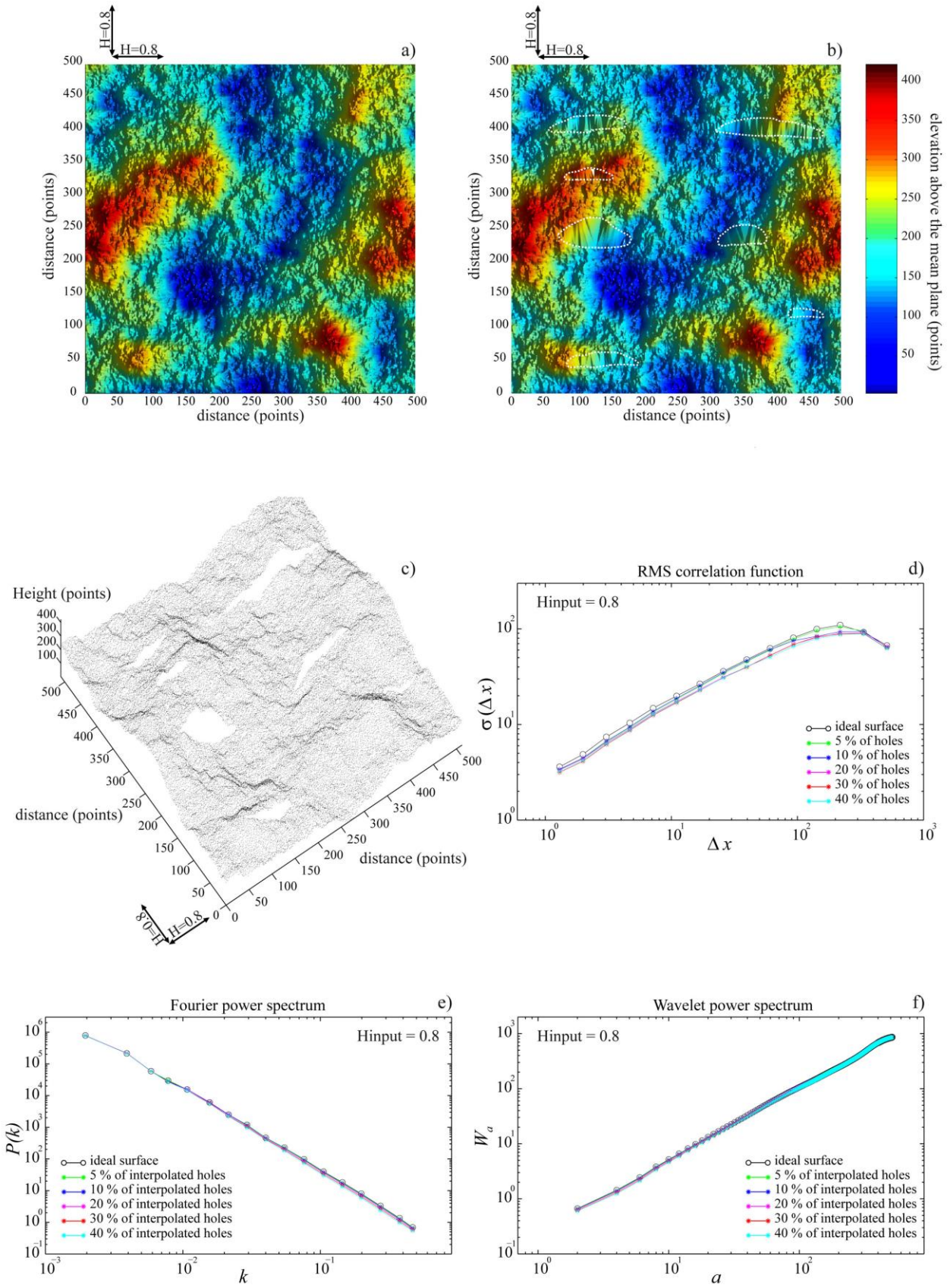
a)
b)
c)
d)
e)
f)
H=0.8
distance (points)
elevation above the mean plane (points)
Height (points)
RMS correlation function
Hinput = 0.8
σ(Δx)
Δx
ideal surface
5 % of holes
10 % of holes
20 % of holes
30 % of holes
40 % of holes
Fourier power spectrum
P(k)
k
5 % of interpolated holes
10 % of interpolated holes
20 % of interpolated holes
30 % of interpolated holes
40 % of interpolated holes
Wavelet power spectrum
W_a
a

Figure 2.8. *Influence of the interpolation of missing data on the estimation of the Hurst exponent. (a) Synthetic surface (513x513points) with H = 0.8. (b) Same surface with 5% of holes (white dashed lines) that have been interpolated. c) 3D view of the surface in a) with the holes. (d) RMS correlation function (RMS-COR), (e) Fourier power spectrum (FPS), (f) Wavelet power spectrum (WPS). The different curves on each plot present the result of the analysis for five different percentages of missing points (5%, 10%, 20%, 40%).*

2.2.5. Quantitative Acquisition of roughness data on natural faults at various scales

2.2.5. A. Acquisition of the data on the field and in the laboratory

The roughness data of several fault samples were acquired at various scales using five different scanning devices (Table 2.1). At the laboratory scale, we used a home-made laser profilometer (Meheust, 2002), where a sample, set on a 2-axis moving table, is scanned by measuring the distance between the sample and a laser head. The horizontal scanning steps are either 20 or 24 micrometers and the vertical resolution is better than 1 micrometer.

On field outcrops, we measured several surfaces with four different LIDARs, where two main technologies were used. The S10 system (Table 2.1) contains a laser source and two cameras; the distance between the laser head and a surface point is measured by triangulation. The maximum shooting distance is around 15 m and the resolution in the distance measurement is close to 0.5 mm. Surfaces of several square meters can be measured with this system. The main drawback of this system is that it must be operated during night time otherwise the day light may blind the cameras.

The other three LIDAR systems (Table 2.1) are based on the same technology and were built by three different companies: a light pulse is sent from a laser head and the time of flight to the target point is measured, allowing calculating the distance, knowing light velocity. The whole target surface is scanned by rotating the laser head at constant angular velocity. The main advantages of this technology is that fast scanning rates can be achieved (up to 5000 points/s), the shooting distance can be as large as 1500 m and the system can be operated even under day light. However, compared to the S10 system, the measurement accuracy is lower, between 1 and 2 cm. Note also that if the laser wavelength is in the infra-red range, absorption by water present on the target surface might also alter the quality of the data.

We have used these scanning measurement devices on two faults in limestones, where outcrop fault planes were scanned at various scales. Hand samples of slip surfaces were also collected and measured with the laboratory profilometer.

Table 2.1. *Characteristics of the field and laboratory scanner devices.*

3D scanner device	S10	GS100	LMS Z420i	Ilris-3D	Lab. Profilometer
Company	Trimble	Trimble	Riegl	Optech	Univ. Strasbourg
Resolution (dx)	0.5 mm	10 or 20 mm	20 mm	20 mm	20 or 24 μm
Noise on the data	0.9 mm	4.5 mm	10.2 mm	20 mm	< 1 μm
Acquisition speed	70 pts/s	5000 pts/s	5000 pts/s	2500 pts/s	60 pts/s

2.2.5. B. The Magnola normal fault

The Magnola fault outcrop, in the Fuccino area, is part of the extensive fault system in Central Apenines (Italy). This 15-km long normal fault shows microseismic activity and offsets limestone beds with a vertical displacement larger than 500 meters and a slight shear component witnessed by mechanical striations dipping at a 85° angle on the fault plane. This site is characterized by recent exhumation of the fault (Palumbo *et al*. 2004, Carcaillet *et al*. 2008) with less alteration by weathering than older exhumed portions of the fault. Recent earthquakes have exposed a ~10-m thick band of fresh limestone (Figure 2.9a) where mechanical striations and grooves at all scales are still visible. We have scanned several sub-surfaces of the fault wall (Table 2.2, Figure 2.9b) and collected one hand sample from the roof of the fault for laboratory measurements (Table 2.2, Figure 2.9c). This sample, that shows mechanical striations, was excavated from below the ground surface, to get a slip surface preserved from climatic weathering. The larger outcrop surfaces show evidence of erosion and some karstic water outlets provided holes for vegetation. Small bushes and grass outcrops had to be removed either directly from the fault plane, or from the LIDAR data. The result was incomplete data sets of the fault surface, with missing points in the records. Nevertheless, elongated bumps and depressions at large scales (Figure 2.9b), and grooves and ridges at small scales (Figure 2.9c) aligned parallel to slip can be observed. Note that 1D

profiles (Figure 2.9d, e) extracted from the Digital Elevation Model (DEM) of both the field surface (Figure 2.9d) and hand sample (Figure 2.9e) appear to be rough at all scales.

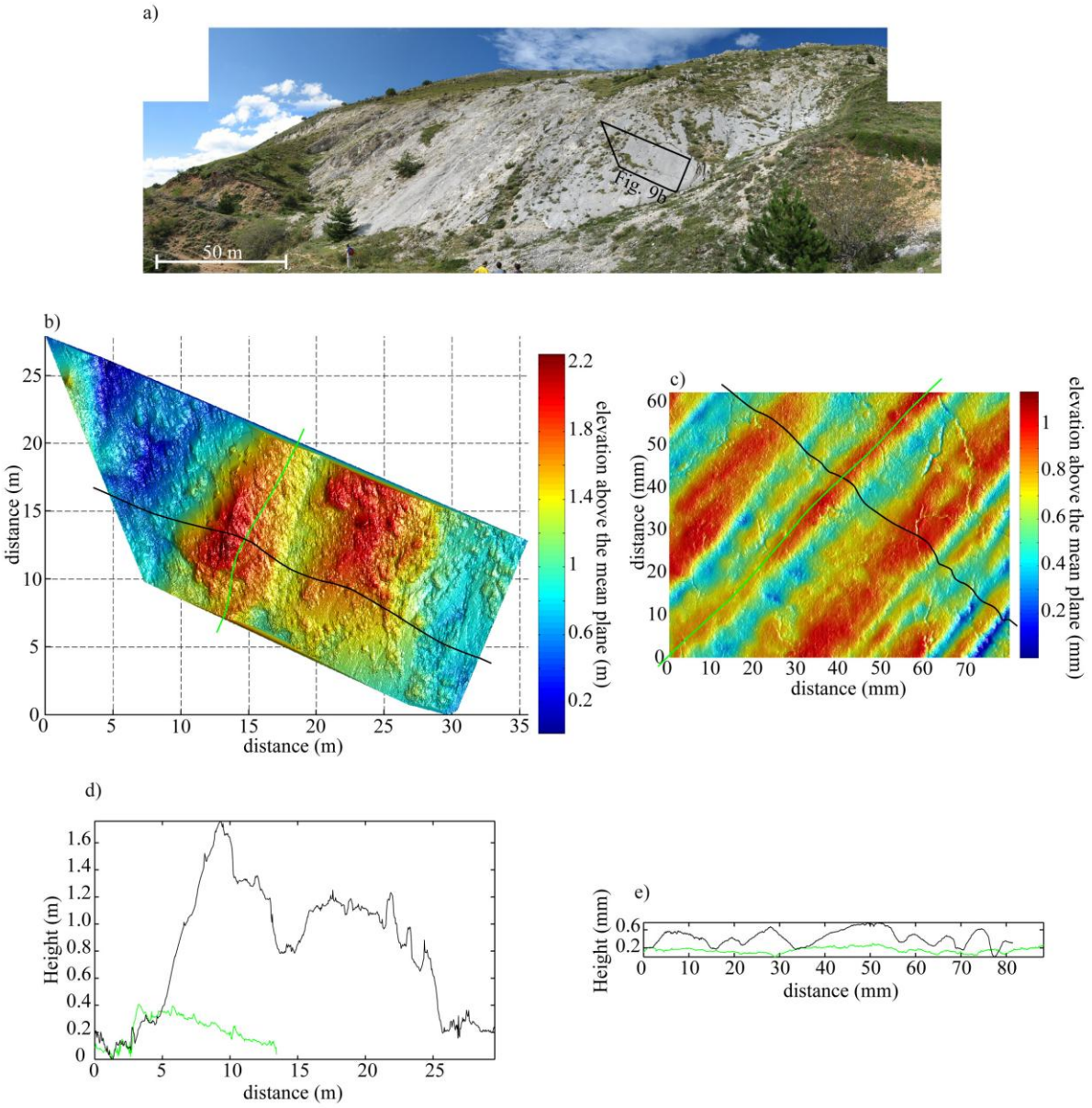

Figure 2.9. *3D scanner data of the Magnola fault slip surface at different scales. (a) Photograph of the fault surface, showing significant weathering and covering by vegetation. The black polygon corresponds to the surface shown below. (b) Digital Elevation Model (DEM) of the surface A32 (Table 2.2). The LIDAR data contain 799,830 points, sampled on a roughly regular grid of ~40 x ~40 mm. The measurements were performed on a ~20 x ~20 mm grid and then averaged on a coarser grid. The resolution of the elevation is 20 mm. The fault surface shows elongated bumps (red) and depressions (blue), which have a pitch of approximately 85°, and indicating a main normal slip motion. The corrugation, with maximum amplitude of around 2.2 m, can be observed at all scales down to the measurement resolution. (c) DEM of hand sample M2 (Table 2.2) that contains 3999 x 3120 points on a regular mesh of 20 x 20 μm^2. The surface contains grooves (blue) and ridges (red) aligned parallel*

to slip and with maximum amplitude of around 1.2 mm. (d) and (e) Example of 1D profiles extracted from the DEM of surface A32 (d) and hand sample M2 (e), in directions perpendicular (black profile) and parallel (green profile) to striations. The position of extracted profiles is shown by a black line (perpendicular to striations) and a green line (parallel to striations) on each scan surface. Note the vertical exaggeration (x10) in order to highlight the roughness of parallel and normal profiles at all scales for field and laboratory data. The reduction of the amplitude of parallel profiles compared to normal profiles is an expected consequence of striations.

2.2.5. C. The Vuache strike-slip fault

The Vuache fault is an active strike-slip fault system in the western part of the French Alps (Thouvenot *et al.* 1998). The fault outcrop we analyzed lies on a short segment that connects to the main Vuache fault and is no longer active. This fault was analyzed in Renard *et al*. (2006) and we present here new data of large and small scale slip surfaces (Figure 2.10).

Table 2.2. *Fault surfaces analyzed in this study.*

Fault	**Surface area, dx**	**Scanner**
Vuache, SURF1	17 x 10 m, 20 mm	GS100
Vuache, SURF7	24 x 11 m, 30 mm	GS100
Vuache, SURF6	45 x 9 m, 20 mm	LMS Z420i
Vuache, SMALL	10 x 9 cm, 24 μm	Lab. Profilometer
Vuache, SURF-JPG	0.5 x 0.5 m, 1 mm	S10
Magnola, A32	35 x 15 m, 20 mm	Optech
Magnola, M2	7.2 x 4.5 cm, 20 μm	Lab. Profilometer

This fault has a mainly strike-slip component, witnessed by large elongated bumps and depressions associated with linear striations of smaller size observed at all scales up to the resolution of the scanners LIDAR (Figure 2.10c-e). Conversely, the laboratory data show that the surface below the centimeter scale appears more polished and only smooth decimeter ridges persist (Figure 2.10f). Moreover, Figure 2.10h shows that 1D profiles extracted from the hand sample fault plane also appear clearly smooth at small scale. This observation is confirmed when we perform an isotropic dilation of profiles (Figure 2.10h). In a different

way, we observe a roughness at all scales on profiles extracted from field surfaces (Figure 2.10g).

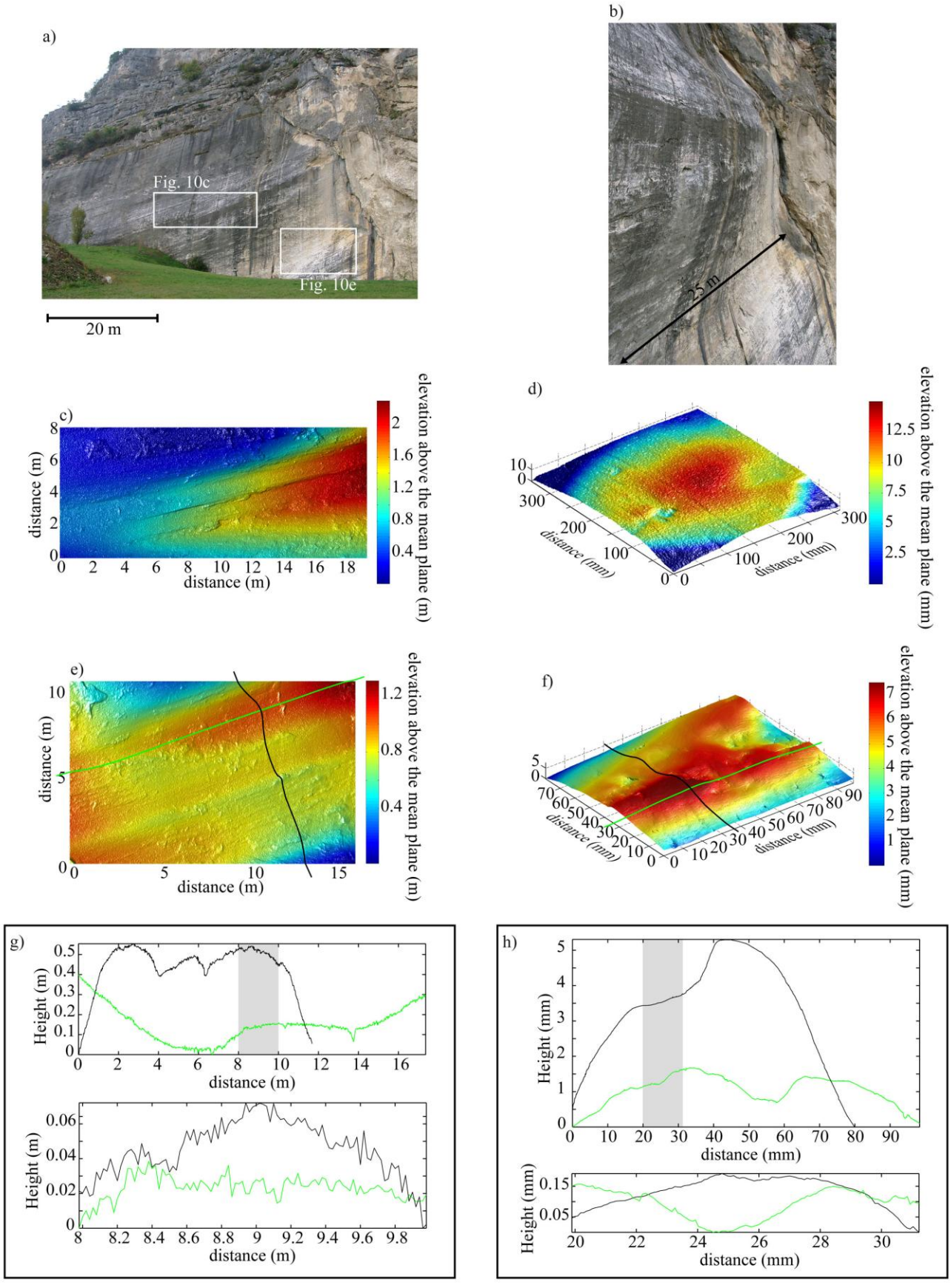

Figure 2.10. *3D data of the Vuache fault slip surface at all scales. (a) Photograph of the outcrop, where the white boxes correspond to the surfaces shown in (c) and (e). (b) Lateral photograph of the slip plane that highlights its remarkable waviness. (c-e) Fault surface topography of SURF1 and SURF6 (Table 2.2). Each surface contains approximately 450,000 points sampled on a constant grid of 20 x 20 mm. The resolution of the elevation is 10.2 mm for (c) and 4.5 mm for (e), respectively. The surfaces show large elongated bumps (red) and depressions (blue) with maximum amplitude of around 2 m associated with linear striations of smaller size (grooves and ridges). Both geometrical patterns with a pitch of 15-25° indicate a strike-slip motion with a small normal component. (d) DEM of the bumpy zone SURF-JPG (Table 2.2) that contains 107,606 points sampled on a regular grid of 1 x 1 mm. Note the vertical exaggeration. The resolution of the elevation is 0.9 mm. (f) DEM of the hand sample SMALL (Table 2.2) that contains 4099 x 3333 points on constant grid of 24 x 24 μm^2. The resolution of the elevation is less than one micrometer. The scans clearly show a smoothing of the roughness from large to small scales. Large fault surface measured on the field have asperities over the entire range of observed scales down to the measurement resolution. Conversely, the laboratory data show that the surface below the centimeter scale appears more polished and only smooth decimeter ridges persist. (g) and (h) Example of 1D profiles extracted from the DEM of surface SURF6 (e) and hand sample SMALL (f), in directions perpendicular (black profile) and parallel (green profile) to striations. The position of extracted profiles is shown by a black line (perpendicular to striations) and a green line (parallel to striations) on each scan surface. For each surfaces, lower subfigures represent zooms on portion of profiles (located by grey zones on the upper profiles) which have been detrended and dilated with identical ratios over the horizontal and the vertical directions.*

The fault offsets meter-scale beds of limestones and the fault plane was exhumed ten years ago by the activity of a quarry. As a consequence, the LIDAR measurements could be performed on fresh surfaces, where weathering was minimum and no vegetation had developed on the fault plane. For these surfaces, the data recovery was excellent, greater than 99.5%. We therefore obtained the topography of the surfaces without holes in the data, making the signal processing results reliable.

2.2.6. Roughness results and interpretation

2.2.6. A. Magnola Fault

The roughness analysis results of the Magnola fault outcrop and hand sample are shown on Figure 2.11. To focus our analysis on the scaling properties of amplitude of the roughness versus wavelength, i.e. the Hurst exponent, we chose to normalize the Fourier power spectrum and the averaged wavelet coefficients spectrum by their respective prefactors

(Figure 2.11a-d). Indeed, for a self-affine profile, the power spectrum and averaged wavelet coefficient behave respectively as: $P(k) \propto A_k\, k^{-1-2H}$ and $W_a \propto A_a\, a^{H+1/2}$ where prefactors A_k and A_a define the overall amplitude of the roughness. We will see later in the paper how to characterize and compare these prefactors.

On each plot (Figure 2.11a-d) both Lidar data (upper curve), acquired with the Optech scanner (Table 2.2), and laboratory profilometer data (lower curve) are represented, showing a scaling behavior over 5.5 orders of magnitude of length scales (50 μm to approximately 20 m). Each curve represents an average over a large set of parallel 1D profiles extracted from the DEM of the fault surface shown on Figure 2.9. The level of noise for the field LIDAR scanner (Table 2.1) is estimated as the height of the flat part of the spectrum at small length scales and is indicated by the black arrows (Figure 2.11). The flattening of the scaling behavior at large scales is related to a finite size effect.

The FPS and WPS techniques performed along and perpendicular to the slip direction (Figure 2.11a-d) indicate that the power laws can easily be connected for the field and laboratory data, demonstrating the robustness of the scaling behavior. Moreover, our results highlight a significant directional morphological anisotropy over a wide range of scales: the profiles parallel to the slip direction are rougher than perpendicular ones (Power *et al.*, 1988; Power and Tullis, 1991; Lee and Bruhn, 1996; Power and Durham, 1997; Renard *et al*., 2006; Sagy *et al*., 2007). These two methods estimate a similar Hurst exponent perpendicular to the slip orientation ($H_\perp = 0.8$) across the whole range of scales investigated in this study, a property similar to fresh mode I fracture surfaces (Power *et al*., 1987; Schmittbuhl *et al*., 1995b, Bouchaud, 1997). However, the FPS technique indicates a greater anisotropy, $\left|H_{//} - H_\perp\right| = 0.2$, where $H_{//}$ represents the Hurst exponent in the direction of slip, than quantified by the WPS method ($\left|H_{//} - H_\perp\right| = 0.1$). Moreover, the WPS method overestimates the self-affine exponent along the slip direction ($H_{//} = 0.7$) compared to the FPS method ($H_{//} = 0.6$). An attempted explanation of these last two differences is given by our parametric study of synthetic rough surfaces: the WPS method slightly overestimates the roughness exponents when measuring couples of Hurst exponents in perpendicular directions with range of values similar to those of natural fault surface (0.6 to 0.9). Notably, the exponents accuracy with anisotropic surface of 2049 x 2049 points and for two Hurst exponents in perpendicular direction of 0.8 and 0.6 is numerically estimated as -0.01 and -0.06 for the wavelet method, respectively (Figure 2.4f). For example, an amount of -0.06 should be added to the measured

minimal exponent with the WPS analysis to obtain the actual one. Accordingly, on natural fault surface with two perpendicular exponents of 0.8 and 0.6 calculated by the FPS, the estimated Hurst exponent in direction parallel to slip is systematically lower than with the WPS method (Figures 2.11, 2.13). Moreover, since the error on the output Hurst exponent is greater in direction of slip than perpendicularly to it, consequently the output anisotropy decreases, as observed on natural fault surface (Figure 2.11, 2.13).

Our estimations obtained on the hand sample with the RMS-COR function (see Figure 2.11e) show that the minimum Hurst exponent ($H = 0.6$) is at 85°, in the direction of slip, and the maximum Hurst exponent ($H = 0.8$) is almost in the perpendicular direction. These two extremes values of the self-affine exponent correspond also to those determined at all scales by the FPS and WPS methods. At the field scale (see Figure 2.11e), the minimum ($H = 0.4$) and maximum ($H = 0.7$) Hurst exponents are observed in directions similar to that for the hand sample. However, the results obtained with the RMS-COR method suggest that the roughness exponent of the Magnola fault surface is smaller at the field scale compared to the laboratory scale, regardless of the azimuth. We ascribe this variation to natural weathering (pitting) of the exposed fault surface at short wavelengths, as Power and Tullis (1991).

Indeed, the section of the Magnola fault surface (Figure 2.9b) shows an increase of the roughness amplitude at short wavelengths created by weathering. Other sections of the Magnola fault surface, that are not presented in this study, display evidence of strong alteration at short length scales leading to a significant reduction of the Hurst exponent, regardless of azimuth. Conversely, the clean hand sample (Figure 2.9c), that shows mechanical striations, should represent the actual topography of the fault surface at short length scales, related to the faulting process before the action of climatic weathering. This hypothesis is supported by the fact that the fresh slip plane, scanned in laboratory, displays the same self-affine RMS-COR regimes in the directions parallel and perpendicular to slip than those estimated using the FPS and WPS methods. The increase of roughness at short wavelengths on the field surface due to the erosion appears to be similar to the effect of an additional noise tested on “ideal” synthetic surfaces (Figure 2.7). In both cases, the Hurst exponent decreases in all directions. Our statistical study led on synthetic surfaces shows that the noise effect is more pronounced when using the RMS-COR technique. To summarize, the roughness scaling estimated using the RMS-COR calculated on the weathered field surface exhibits a decrease of the Hurst exponent in all directions, which is not observed with the FPS and WPS techniques.

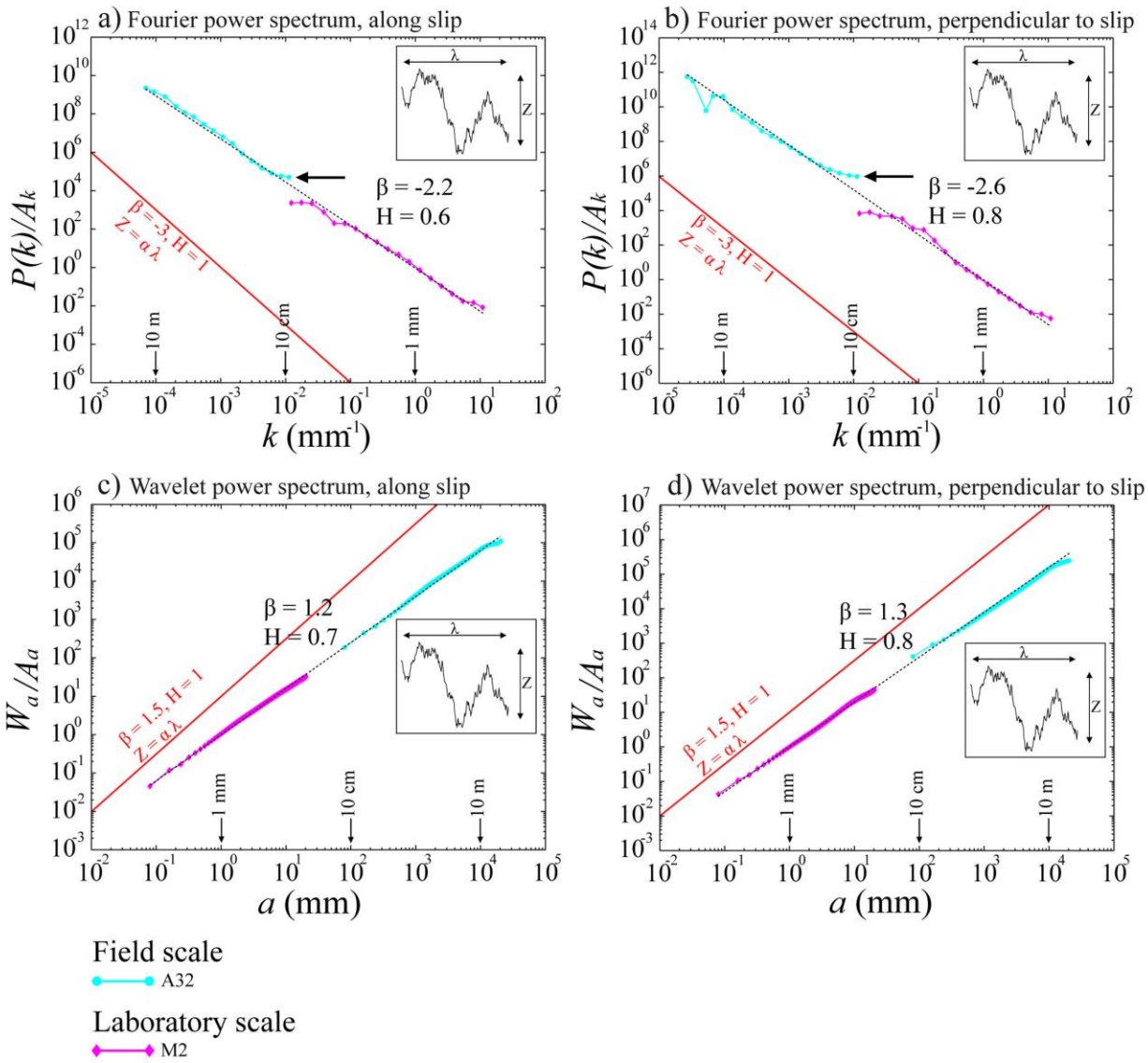
a) Fourier power spectrum, along slip
P(k)/Ak
k (mm-1)
β = -2.2
H = 0.6
β = -3, H = 1
Z = αλ
10 m
10 cm
1 mm
b) Fourier power spectrum, perpendicular to slip
β = -2.6
H = 0.8
c) Wavelet power spectrum, along slip
Wa/Aa
a (mm)
β = 1.2
H = 0.7
β = 1.5, H = 1
d) Wavelet power spectrum, perpendicular to slip
β = 1.3
H = 0.8
Field scale
A32
Laboratory scale
M2

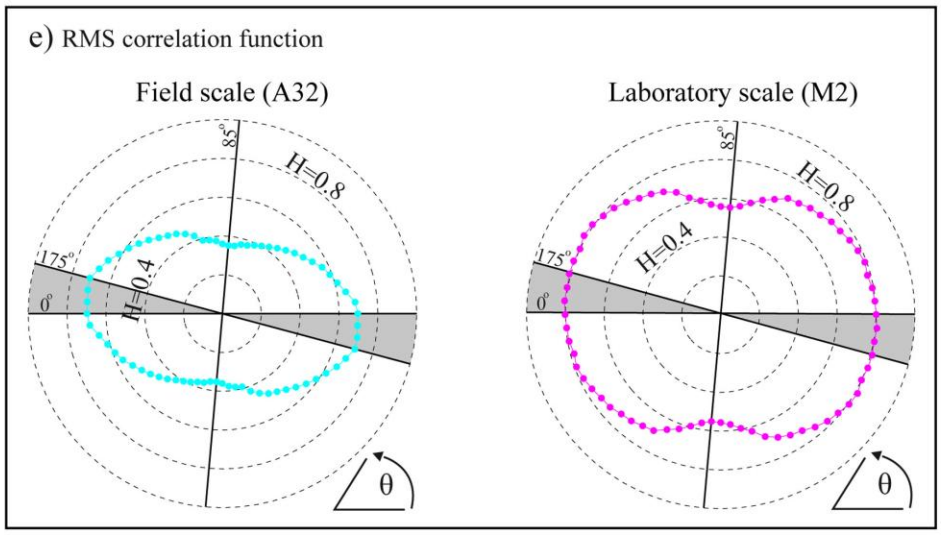
e) RMS correlation function
Field scale (A32)
Laboratory scale (M2)
H=0.8
H=0.4
85°
175°
0°
θ

Figure 2.11. *Roughness scaling analysis from the best preserved outcrops of the Magnola fault plane, scanned using ground based LIDAR (surface A32, Figure 2.9b), or using the laboratory profilometer (hand sample M2, Figure 2.9c). (a-b) Fourier Power Spectrum (FPS) normalized, and (c-d) Wavelet power spectrum (WPS) normalized along two directions, parallel and perpendicular to the direction of slip, are represented in log-log plots. Power-law fits (black dotted line) are performed for each curve and the corresponding slopes (β) and roughness exponents (H) are indicated above the spectra. The inset displays an example of the amplitude (Z) and the wavelength (λ) of a rough profile. Contours (red lines) of constant amplitude (Z) to wavelength (λ) ratio, reflecting a self-similar behavior, are provided to allow easier interpretation of the spectra. Black arrows indicate the level of noise of the LIDAR. (e) Surface anisotropy revealed by the angular variation of the Hurst exponent determined by the RMS correlation function method. The polar plot of H on the left and the right sides correspond to data of the field surface and hand sample shown on Figure 2.9, respectively.*

On the polar plot of H obtained at the laboratory scale (see Figure 2.11e), when departing a few degrees from the direction of slip, the Hurst exponent is close to the value of the maximum Hurst exponent measured in the direction perpendicular to mechanical striations. Such behavior is also visible on 'ideal" synthetic surfaces (Figure 2.5). In other words, the azimuth of the maximum Hurst exponent is not well-defined (gray shadows on Figure 2.11e), while the minimum exponent corresponds to a specific orientation. Note that this property is less visible on the polar plot of the altered field fault section (see Figure 11e) where the angular variation of H is more progressive.

To obtain a full description of the fault asperity geometry, the prefactor of the scaling function has also to be characterized. For instance, using the standard deviation $\sigma(\delta x)$ of the height $L(x)$, the prefactor can be designed as: $\sigma(\delta x) = l_r^{1-H} (\delta x)^H$ where the prefactor l_r denotes a length scale, also known as the topothesy of the fault roughness (Simonsen *et al*., 2000; Schmittbhul *et al*., 2006; Schmittbhul *et al*., 2008). The topothesy corresponds physically to the length scale for which the slope of the rough profile is equal to 1: $\sigma(l_r) = l_r$. In other words, l_r is the theoretical length scale over which the rough profile has a mean slope of 45°. The smaller l_r, the flatter the profile appears on a macroscopic scale.

Figures 2.12a& b show respectively the scaling of the RMS along the slip and perpendicular to it, of the field surface topography and of the hand sample surface topography. From the best fit of these curves, we estimate the roughness exponent and the topothesy (Figure 2.12c) of these two surfaces, along two perpendicular directions. For both scales, the local slope of the surface is always significantly smaller than that for the range of

scales that we explored, i.e. from 40 mm to 30 m for the field surface and from 0.04 to 90 mm for the hand sample surface, as shown on Figure 2.12a, b. In other words, the estimated prefactors are very small showing that these surfaces are rather smooth.

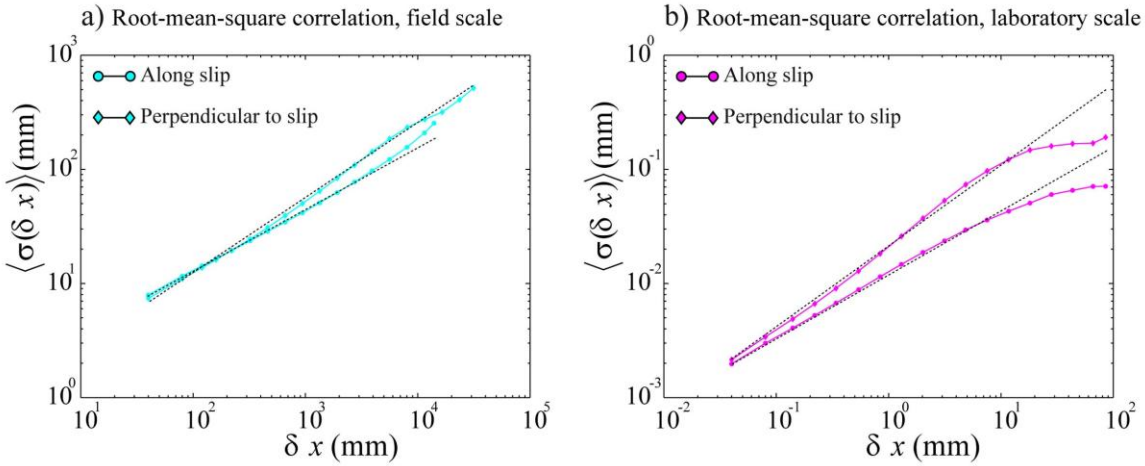

c) Topothesy of the Magnola fault surface

		Field scale	Laboratory scale
Magnola fault surface	Perpendicular to slip	0.12 mm	3.1×10^{-7} mm
	Parallel to slip	0.82 mm	4.6×10^{-5} mm

Figure 2.12. *Scaling of the root-mean-square correlation function (RMS) for the Magnola fault surface topography at field scale (a) and laboratory scale (b) along slip direction and perpendicular to it. The best fits (black dotted lines) of the form* $\sigma(\delta x) = l_r^{1-H} (\delta x)^H$ *define the roughness exponent H and the topothesy* l_r *(c).*

2.2.6. B. Vuache Fault

As already explained for the Magnola fault results, the Fourier power spectrum and the averaged wavelet coefficients are normalized by their respective prefactors A_k and A_a in order to directly compare the different slopes of the scaling laws.

The FPS and WPS techniques highlight a significant directional morphological anisotropy over six orders of spatial scales (Figure 2.13a-d). Profiles parallel to slip have a smaller Hurst exponent than perpendicular ones (Power *et al.*, 1988; Power and Tullis, 1991; Lee and Bruhn, 1996; Power and Durham, 1997; Renard *et al.*, 2006; Sagy *et al.*, 2007). These two methods, applied to series of profiles perpendicular to the direction of slip, indicate that the power laws of individual surfaces can easily be connected across the wide range of scales investigated (Figure 2.13b, d), and the value of $H_\perp = 0.8$ is similar to what was measured on the Magnola normal fault surface. However, in the slip parallel direction there is

a slight change in the magnitude of $H_{//}$ located in the length scale range between 5 mm and 2 cm (gray shadows on Figure 2.13a, c). $H_{//} = 0.75$ is larger below this length scale range than at larger length scales, where $H_{//} = 0.65$ and $H_{//} = 0.7$ for the FPS and WPS methods, respectively. The smoother aspect of the Vuache fault surface in the direction of slip compared to the perpendicular direction is an obvious and expected consequence of striations, but the smallest directional morphological anisotropy at the laboratory scale compared to the field scale is novel in this study. At the field scale, the morphology of the elongated bumps and depressions along the slip direction is different from the grooves and striations observed at the laboratory scale (Figure 2.10). As the fault Vuache outcrop is quite fresh, and was preserved from the climatic erosion, we propose that this cross-over in the slope at length scale of several millimeters is significant. We interpret this cross-over length scale as a witness of different mechanical processes responsible for the creation of fault topography at different spatial scales.

Our results obtained at the field and intermediate scales with the RMS-COR function (see left and center plots on Figure 2.13e) show that the minimum Hurst exponent ($H_{//} \in [0.55 - 0.6]$) is oriented at 20° with respect to the horizontal, indicating the fault had a normal component and not only a strike-slip one. The maximum value $H = 0.75$ is located for an almost perpendicular direction. These two extremes values of the self-affine exponent are slightly lower when estimated using the RMS-COR function than when using the FPS or the WPS methods. This slight underestimation with the RMS-COR technique is consistent with our results on synthetic surfaces for the accuracy in this range of parameters (Figure 2.4). Indeed, our parametric study with synthetic anisotropic surfaces shows that the estimation of *H* calculated with the RMS-COR technique slightly underestimates its actual value (Figure 2.4d). At the laboratory scale (see right plot on Figure 2.13e), $H_{//} = 0.8$ and $H_{\perp} = 0.9$ are located in orientations similar to that for the three larger surfaces measured on the field. However, the polar plot of H calculated using the RMS-COR function suggests an increase of the scaling exponents in all directions, while the estimation using the FPS or WPS techniques underlined that the exponent increased only along the slip direction. In addition, the two exponents $H_{//}$ and $H_{\perp}$ for the hand sample are overestimated when calculated with the RMS-COR method compared to the FPS and WPS techniques. The latter observation cannot be explained by the results of our parametric study on synthetic surfaces. As a consequence of the extremely smooth aspect of the hand sample at small scales (Figure 2.10f,

h), the RMS-COR method could lose its robustness. However, a new reliable result is that the directional morphological anisotropy calculated by the RMS-COR function significantly decreases at the laboratory scale, as observed with the FPS and WPS techniques.

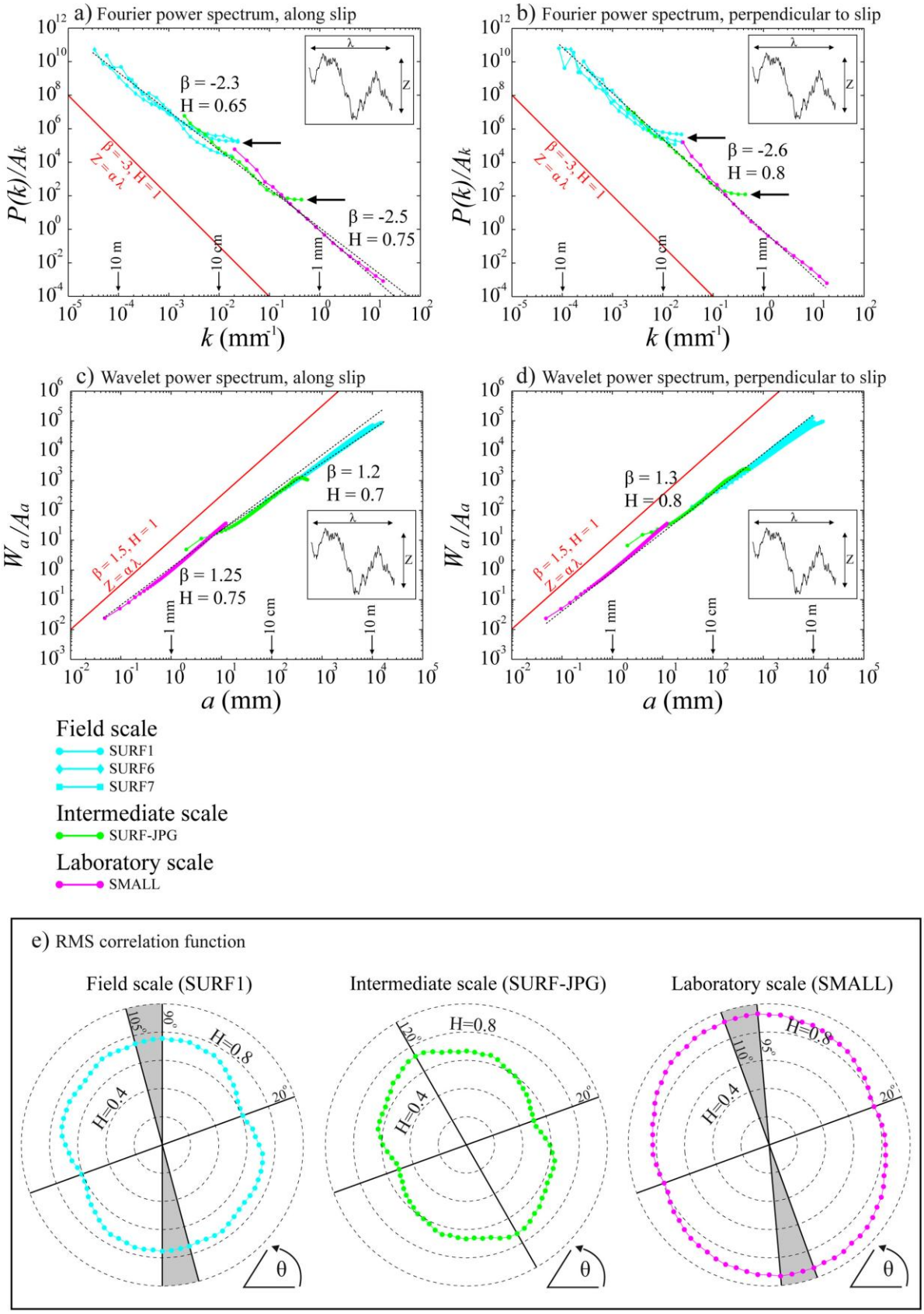

Figure 2.13. *Roughness scaling analysis from five surfaces (Figure 2.10, Table 2.2) of the Vuache fault, covering 6 orders of magnitude of frequencies or wavelengths (40 μm to approximately 40 m). The data collected contain four surfaces (blue and green curves) that have been scanned using LIDAR and one hand sample (magenta curve) measured by laboratory profilometer. (a-b) Fourier power spectrum (FPS) normalized and (c-d) Wavelet power spectrum (WPS) normalized along two directions, parallel and perpendicular to the direction of slip, are represented in log-log plots. Power law fits (black dotted line) are shown for each curve and the corresponding slopes (β) and roughness exponents (H) are indicated next to the spectra. Each curve is an average over a series of parallel profiles extracted from the DEM shown on Figure 2.10. The level of noise for the Lidar scanners is estimated as the height of the flat part of the spectrum at small length scales and is indicated by the black arrows. The flattening of the scaling behavior at large scales is related to a finite size effect. Contours (red lines) of constant amplitude (Z) to wavelength (λ) ratio, reflecting a self similar surface, are also indicated a guide for the eye. The inset displays an example of the amplitude (Z) and the wavelength (λ) of a rough profile. (e) Roughness anisotropy revealed by the angular variation of the Hurst exponent determined by the RMS-COR method. The polar plots of H on the left, in the center and on the right correspond to data of the field surface, the intermediate scale section and hand sample, respectively (see Figure 2.10).*

As already observed on the polar plot of H calculated on the Magnola fault surface (Figure 2.11e), the azimuth of the maximum Hurst exponent is less constrained (gray shadows on Figure 2.13e) than the single specific orientation of the striations. Remarkably, despite the weak anisotropy of the hand sample topography, the slip direction is always significant, demonstrating the accuracy and reliability of the RMS-COR method.

We also estimated the topothesy of the Vuache fault surface (Figure 2.14) when computing the standard deviation $\sigma(\delta x)$ of the height $L(x)$. As for the Magnola fault data, the prefactor l_r lies always outside the range of scales that we explored, i.e. from 20 mm to 15 m for the field surface and from 0.024 mm to 80 mm for the laboratory surface, as shown on Figure 2.14a-b. In other words, the topothesy of the measured fault planes represents a theoretical value, that is very small (see Figure 2.14c) and that confirms that fault surfaces are rather smooth. Moreover, it is of interest to note that at the field scale, the topothesy value of the Vuache fault surface (Figure 2.14c) is similar to that of the Magnola fault (Figure 2.12c). However, at laboratory scale this quantity is significantly lower for the Vuache hand sample compared to that of the Magnola. This characteristics highlights the smoothing of the Vuache

fault plane at small scale as already observed on the DEM (Figure 2.10f), the 1D profiles of the Vuache hand sample (Figure 2.10h), and the roughness scaling analysis (Figure 2.13).

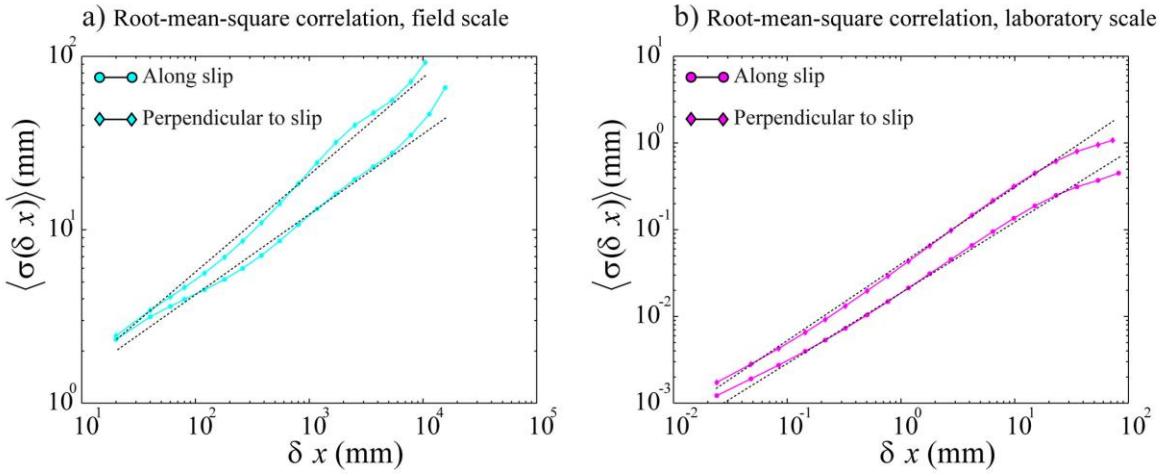

c) Topothesy of the Vuache fault surface

		Field scale	Intermediate scale	Laboratory scale
Vuache fault surface	Perpendicular to slip	0.27 mm	$1x10^{-3}$ mm	$7.5x10^{-13}$ mm
	Parallel to slip	0.63 mm	$1.4x10^{-3}$mm	$1.1x10^{-9}$ mm

Figure 2.14. *Scaling of the root-mean-square correlation function (RMS) for the Vuache fault surface topography at field scale (a) and laboratory scale (b) along slip direction and perpendicular to it. The best fit of the form* $\sigma(\delta x) = l_r^{1-H} (\delta x)^H$ *defines the roughness exponent H and the topothesy* l_r *(c).*

2.2.7. Discussion & Conclusion

The six statistical tools used in this study have different responses to the effect of two kinds of biases, the intrinsic errors of the methods (Figures 2.3, 2.4, 2.5, 2.6) and the artifacts inherent in data acquisition (Figures 2.7, 2.8). Using a parametric approach, where we varied the size of the surface and its anisotropy, we selected the three most reliable and accurate methods (RMS-COR, FPS, WPS) for roughness analysis of natural fault topography (Figures 2.11, 2.13). The FPS and WPS techniques allow obtaining a robust description of the fault asperity geometry in the direction of slip and perpendicular to it (Figures 2.11a-d, 2.13a-d). In an additional way, the RMS-COR technique is robust to characterize the angular variation of *H* (Figures 2.11e, 2.13e). The Hurst exponent estimation at various scales for the natural slip surfaces displays the same trends and provides a consistent and robust characterization of

their scaling regimes. We emphasize that the slight variations in the results given by each one of these methods fall within the range of error estimated by our parametric study (see section 4).

One of the most robust results of our scaling analysis is that the FPS and the WPS methods estimate a same Hurst exponent equal to 0.8 in the direction perpendicular to slip, over approximately 6 orders of magnitude of length scales for two different fault surfaces (Figures 2.11b, d and 2.13b, d). However, in the slip direction two different scaling behaviors are highlighted: the Magnola fault surface shows an identical scaling regime at large and small scales (Figure 2.11a, c). Conversely, the scaling property of the Vuache fault roughness exhibits a cross-over in the slope at length scale of several millimeters (Figure 2.13a, c). In other words, the scaling property of this fault surfaces is similar at large scales but changes at small scales. The statistical analyses (Figure 2.13) and the scan of the Vuache fault surface (Figure 2.10) clearly show a smoothing of the roughness below a length scale of several millimeters.

The scaling regime of 0.8 measured in the direction perpendicular to slip is a classical result already observed for tensile cracks (Power *et al*., 1987; Schmittbuhl *et al*., 1995b, Bouchaud, 1997), indicating that the topography of the fault surface in the direction perpendicular to slip has not registered the effect of shear. Along slip, the general interpretation is that mechanical wear processes, such as frictional ploughing, cause striations that reduce the amplitude of the large scale roughness (Power *et al.*, 1987, 1988; Power and Tullis, 1991; Power and Durham, 1997; Sagy *et al.*, 2007) and accordingly the Hurst exponent. Nevertheless, our scaling analysis seems to indicate different mechanical processes responsible for the creation of fault topography at different spatial scales.

Prior comparative studies of natural fault roughness based on 1D profilometry (Power and Tullis, 1991; Lee and Bruhn, 1996) suggest a change in scaling properties between large and short length scales. However, due to technical limitations, their measures were not sufficiently accurate to decipher if this variation was related either to small-scale surface weathering of the fault scarp or to the faulting process itself.

From laboratory experiments Chen and Spetzler (1993) suggest that the break in slope at length scales of several millimeters is caused by a change in the dominant mode of deformation from small-scale intergranular cracking to intragranular cracking at a larger scale. We think this interpretation does not apply to the Magnola and Vuache faults because the grain scale of these limestones is very small (< 0.1mm), well below the observed cross-over length scale.

Recently, Sagy *et al.* (2007) observed that faults with large cumulated slip display surfaces with elongate, quasi elliptical bumps at field scale and are polished at small scales. Conversely, fault with a small cumulative slip are rough on all scales. Sagy and Brodsky (2009) proposed that the waviness of the large slip fault surface reflects variations of thickness of the cohesive layer under the slip surface formed as boudinage structures (Johnson and Fletcher, 1994; Smith, 1977; Twiss and Moores, 1992, Goscombe *et al*., 2004). Therefore, they evoke two different deformation mechanisms between large and small scales: abrasion caused by frictional sliding at the origin of the smoothing at small scales, and "boudinage" creating elongated bumps and depression at large scales.

From our study of natural fault roughness, we observe large elongated bumps and depressions in slip direction on two different fault planes (Figures 2.9b, 2.10a-e). There is no evidence that the small segment, polished at small scale (Figure 2.10f, h), that connects to the main Vuache fault has accumulated more slip than the Magnola fault surface that is rough at all scales (Figure 2.9b, c). Therefore, we propose that large elongated bumps and depressions of several meters in length with maximum amplitude of around 2 m may reflect the processes of lateral growth and branching that links together several fault surfaces, during all the stages of the evolution of the fault zone, as suggested by Lee and Bruhn (1996) and Libicki and Ben-Zion (2005).

At small scales, two different kinds of scaling regime are observed on the two fault surfaces, (Figures 2.11, 2.13), both being linked to mechanical wear process. Frictional sliding is expressed through ploughing of small asperities and is responsible for the small scale abrasional striations on the Magnola fault surface (Figure 2.9c). This mechanism is also responsible for the polishing of the Vuache fault surface below the centimeter scale (Figure 2.10f, h). One should keep in mind that only one hand sample was measured for each surface and therefore it is possible that differences of the scaling behavior between the two fault planes reflect spatial heterogeneity of core fault at small scales. Notably, on the Vuache fault, although the surface appears polished at the laboratory scale on the whole surface, zones with striations due to ploughing elements could be present. A more extensive study of fault roughness in several different faults should therefore bring more information on the mechanisms at work during faulting.

Acknowledgments: We would like to thank Jim Dieterich and an anonymous reviewer for helpful comments. We acknowledge Benoit Dubacq for technical help on *Matlab* and

Sebastien Boutareaud for encouragements and constructive comments that helped to improve this work. Anne-Marie Boullier, Jean-Pierre Gratier, Mai-Linh Doan, Emily Brodsky are really thanked for fruitful discussions on the Vuache fault surface. We also acknowledge a research grant from the program TUNES at the University Joseph Fourier – Grenoble I.

2.2.8. Appendix 2.A

```
function RoughSurf = Synthetic2DFault(N,H1,H2)

% This Matlab(c) function creates a self-affine 2D surface,
% with a directional anisotropy (courtesy of Hermine Bierme,
% Univ. Paris V, France), when H1 is different from H2.
% Input parameters:
% N = size of the surface: (2^(N+1)+1) x (2^(N+1=+1)
% Typically N must be between 8 and 11 when running on a
desktop computer.
% H1, H2: Hurst exponents in two perpendicular directions
% must be positive, smaller than 1.
% Output result:
% RoughSurf: rough surface of size (2^(N+1)+1) x (2^(N+1=+1),
% with two perpendicular directions of self-affinity
% characterized by Hurst exponents H1 and H2, l1 = 1/H1 and
% l2 = 1/H2 represent the eigen values of the anisotropy
% diagonal matrix
l1 = 1/H1;
l2 = 1/H2;
X = (-2*2^N:2:2*2^N)/(2^(N+1));
X(2^N+1) = 1/2^N;
Y = (-2*2^N:2:2*2^N)/(2^(N+1));
Y(2^N+1) = 1/2^N;
XX = X(ones(1,2*2^N+1),:);
YY = Y(ones(1,2*2^N+1),:)';
clear X Y

% rho is the pseudo-norm associated to the eigen values l1 and
l2
% rho(x,y)=(abs(x)^(2/l1) + abs(y)^(2/l2) )^(1/2)
rho = sqrt(abs(XX).^(2/l1)+abs(YY).^(2/l2));
clear XX YY

%phi is the spectral density of the field built from rho
phi = rho.^(1 + (l1+l2)/2);
clear rho

% W = Fourier transform of the anisotropic Gaussian field
Z = randn(2*2^N+1,2*2^N+1);
```

```
W = fftshift(fft2(Z))./phi;
clear Z
T = real(ifft2(ifftshift(W)));
RoughSurf = T-T(2^N+1,2^N+1);

% Plot the 2D rough surface
imagesc(RoughSurf);
axis equal
axis tight
```

Chapter 3:

Roughness of fault surfaces over nine decades of length scales: self-affinity, variability, and absence of characteristic length scale

3.1. Chapter 3 overview (Présentation du Chapitre 3)

3.1.1. Introduction

Dans ce chapitre, je présente un article prêt à être soumis à la revue *Journal of Geophysical Research*. Cette étude regroupe l'ensemble des mesures topographiques acquises et analysées durant ma thèse. En utilisant la méthode statistique qui s'est révélée la plus robuste au regard du travail présenté dans le chapitre 2, il est démontré que la rugosité des surfaces peut être décrite par un modèle géométrique auto-affine légèrement anisotropique. Cette description est valable depuis l'échelle de quelques centaines de micromètres jusqu'à l'épaisseur de la croute sismogenique, et ne dépend pas du contexte géologique (lithologie, composante principale du déplacement, et le déplacement accumulé) des zones de failles analysées.

3.1.2. Presentations at international meetings

2010, American Geophysical Union, Fall meeting, San Francisco (USA):

Renard, F., Candela, T., Klinger, Y., Bouchon, M., Schmittbuhl, J., Mair, K., and Brodsky, E., Roughness of fault surface: evidence of self-affine morphology from the submillimetric scale to large earthquake surface rupture. Abstract T33B-2243.

2010, "Physico-chemical processes in seismic faults", Workshop, Padova (Italy):

Candela, T., and Renard F., Self-affinity and variability of the morphology of fault surfaces – High resolution topography measurements over nine decade of spatial scales.

3.1.3. Contributors to Chapter 3

J'ai personnellement produit tout les résultats de ce chapitre. Les mesures topographiques des failles de Corona Height (San Francisco) et de Dixie Valley (Nevada) ont été acquises sur le terrain par E.E. Brodsky, F. Renard et moi-même. Les scans de la faille de la Vuache-Sillingy et ceux de la faille de Magnola, ont été effectués par F. Renard et C. Voisin. La faille de Bolu (Turquie) a été scannée par J. Schmittbuhl et moi-même. Les mesures topographiques en laboratoire des échantillons des surfaces de failles, ont été réalisées par moi-même à l'institut de

physique du globe de Strasbourg en collaboration avec J. Schmittbuhl. Les données acquises avec l'interféromètre à lumière blanche ont été effectuées par moi-même au laboratoire de « Physics of Geological Processes » en collaboration avec K. Mair. Les données de traces de ruptures ont été acquises par Y. Klinger.

3.2. Roughness of fault surfaces over nine decades of length scales: self-affinity, variability, and absence of characteristic length scale

Thibault Candela[1], François Renard[1,2], Yann Klinger [3], Karen Mair[2], Jean Schmittbuhl [4], and Emily E. Brodsky[5]

[1]ISTerre, University Joseph Fourier - Grenoble I, CNRS, OSUG, BP 53, 38041 Grenoble, France.

E-mail: Thibault.Candela@ujf-grenoble.fr; francois.renard@ujf-grenoble.fr

[2]Physics of Geological Processes, University of Oslo, Oslo, Norway. E-mail : karen.mair@fys.uio.no

[3]Institut de Physique du Globe de Paris, CNRS, 4 pl. Jussieu, Boite 89, F-75005 Paris Cedex 05, France. E-mail : klinger@ipgp.jussieu.fr

[4]UMR 7516, Institut de Physique du Globe de Strasbourg, Strasbourg, France. E-mail: Jean.Schmittbuhl@eost.u-strasbg.fr

[5]Department of Earth and Planetary Sciences, University of California–Santa Cruz, Santa Cruz, California 95064, USA. E-mail: ebrodsky@es.usc.edu

Abstract

We propose that fault surface topography can be characterized by an anisotropic self-affine morphology with no characteristic length scale from the micrometer scale to the thickness of the seismogenic zone. Using several high resolution laser distancemeters and laboratory profilometers, we have measured the topography of five exhumed slip surfaces (French Alps, Turkey, California, Nevada, Appenines). A consistent model emerges as the morphology of the slip surfaces can be described by a straight line covering five decades of length-scales in a log-log plot where the axes are the fault roughness and the spatial length scale. Therefore fault roughness is scale dependent, with a common self-affine behavior described by two parameters:

a power-law exponent H, found constant among all the faults studied and slightly anisotropic ($H_{//} = 0.58 \pm 0.07$ in the direction of slip and $H_{\perp} = 0.81 \pm 0.04$ perpendicular to it), and a pre-factor which shows a quite large variability. We have also analyzed the roughness of the surface rupture of eight major continental earthquakes that occurred in the past 20 years. For a range of scales between 200 m and 50 km, these ruptures show the same self-affine behavior ($H_R = 0.8 \pm 0.1$), extending the range of scales to nine decades, without characteristic length and indicating that a unique physical process may be at work. This description of the scanned fault scarps and the rupture traces, which both are markers of the morphology of the active structures of fault zone, is independent of the geological context and particularly the cumulated displacement.

3.2.1. Introduction

The morphology of fault planes controls the dynamics of faulting and slip. Recent studies attempted to reconstitute the spatio-temporal history of slip and stress on a fault during a large earthquake (Bouchon, 1997; Mai and Beroza, 2002) and showed that both coseismic slip and stress appear to be very heterogeneous along the fault plane. A possible explanation is that the fault plane is rough and asperities concentrate stress and slip heterogeneities at various spatial scales (Schmittbuhl *et al.*, 2006). Indeed, earthquake and fault activity create and destroy this roughness that participates to the heterogeneity of the stress field in the fault zones. Other studies have also shown the importance of non-planar structures in the rupture propagation (e.g. Aochi and Madariaga, 2003); and the close relationship between the rupture geometry and its propagation velocity (Vallée *et al.*, 2008; Bouchon *et al.*, 2010). Numerical models of earthquake rupture and strong motion need accurate $3D$ morphological models of fault surfaces, necessary to improve simulations of rupture scenarios.

As direct observations are very difficult at the depths of the earthquake nucleation, data of exhumed faults scarps (Power *et al.*, 1987; Renard *et al.*, 2006; Sagy *et al.*, 2007; Candela *et al.*, 2009; Brodsky *et al*., 2011 and references therein) or earthquakes surfaces ruptures (Wesnousky, 2006, 2008; Klinger, 2010) provide a means to characterize the fault plane morphology over a wide range of spatial scales.

Pioneering fault roughness measurements (Brown and Scholz, 1985; Power *et al.*, 1987; Power and Tullis, 1991; Schmittbuhl *et al.*, 1993; Power and Durham, 1997) performed on exhumed scarps found that their roughness can not be described by a single number such as the standard deviation of the roughness amplitude. Rather, fault surface topography was observed as non-stationary and more particularly fractal, the amplitude of the topography increasing with the wavelength under consideration. More precisely, Schmittbuhl *et al.* (1993) proposed that a self-affine fractal concept might provide useful model to describe natural fault surfaces.

A 1D rough profile (Figure 3.1) is self-affine if it remains statistically invariant under the scaling transformation $\delta x \to \lambda \delta x, \delta z \to \lambda^H \delta z$ (Feder, 1988; Meakin, 1998), where δx is the coordinate along the $1D$ profile and δz is the roughness amplitude. For a self-affine profile, the scaling exponent H, which is also called Hurst exponent (or roughness exponent), lies in the range $0 \le H \le 1$. Accordingly, if a profile is self-affine, different magnification factors will be needed in the directions parallel and perpendicular to the profile for a small portion of the profile to appear statistically similar to the entire profile (Figure 3.1). As a consequence the slope at large scales along a self-affine profile scales as $s = \delta z / \delta x \ \alpha \ \delta x^{H-1}$, and tends to flatten for long wavelengths, suggesting a significant role of the small spatial scales (Schmittbuhl *et al.* 1995).

All these pioneering studies measured $1D$ profiles using mechanical profilometers and the noise was quite significant in the data. Only discrete information of the whole fault surface geometry was obtained. Recently, with the development of a new generation of $3D$ laser scanners, fast and accurate acquisitions of topographic data are now available (Renard *et al.*, 2006; Sagy *et al.*, 2007; Candela *et al.*, 2009; Brodsky *et al.*, 2011). These first results showed that fault surfaces are rough at all scales and morphologically anisotropic with a Hurst exponent smaller in the slip direction than perpendicular to it.

In the present study, we investigate roughness properties of five fault surfaces in different geological context (various lithology, accumulated displacement, tectonic regime) using three independent scanner devices (LiDAR, laser profilometer, white light interferometer), spanning a range of scales from the micrometer to tens of meters. In addition, we analyzed the geometry of eight high resolution rupture traces of large continental earthquakes. Our data set gives access to the scaling properties of fault surface roughness from the micrometer scale to several tens of

kilometers. We characterize the scaling of both data sets (fault surface scanned and ruptures traces) using the same statistical tool, i.e. the Fourier power spectrum analysis. This technique is both well-suited and robust to characterize self-affine roughness of fault zones (Candela *et al.*, 2009).

A self-affine model implies that the Fourier spectrum as a function of either the spatial frequency or wavelength plots as a linear trend in log-log coordinates. Two parameters describe such a self-affine model in the spectral domain: the slope of the power spectrum and its pre-factor on a log-log plot of the Fourier spectrum. The slope (directly proportional to H) describes how the roughness changes with scale, while the pre-factor determines the magnitude of the surface elevation at a given scale (Power and Tullis, 1991). We computed these two parameters for the fault surfaces and rupture traces in order to decipher if a global tendency is observed. In addition, we study the fluctuations of these two parameters.

In section 3.2.2, both the characteristics of the fault surface scanned and rupture traces are detailed. section 3.2.3 is devoted to the presentation and the application of the roughness analysis method. In section 3.2.4, our results indicate that a global anisotropic self-affine model with two different Hurst exponents in perpendicular directions could fit the entire data set of fault scarps, despite different geological context. The variability of the pre-factor at the scale of a single fault zone is observed and explained by means of a synthetic self-affine surface model. Secondly, we highlight that a global self-affine regime could fit the eight earthquake ruptures traces. In section 3.2.5, we show that our data collectively suggest that a unique self-affine behavior is maintained from the micrometric scale to the large earthquake surface rupture without characteristic length. The variability of the pre-factors for each data set (fault surfaces and ruptures traces) is discussed with respect to the different geological context sampled and more particularly the accumulated slip.

3.2.2. Fault roughness data

3.2.2. A. Exhumed fault scarps

We have analyzed five natural fault surfaces which were selected because of their particularly well preserved slip surfaces, large exposures and few pits or weathering patterns (see Table 3.1). Existing data sets on the Vuache (Renard *et al.*, 2006; Candela *et al.*, 2009,

Angheluta *et al.*, 2011) and Magnola (Candela *et al.*, 2009) faults have been updated and extended with three new faults (Corona Height, Dixie Valley, and Bolu). A complete list of our fault data is given in Table 3.1.

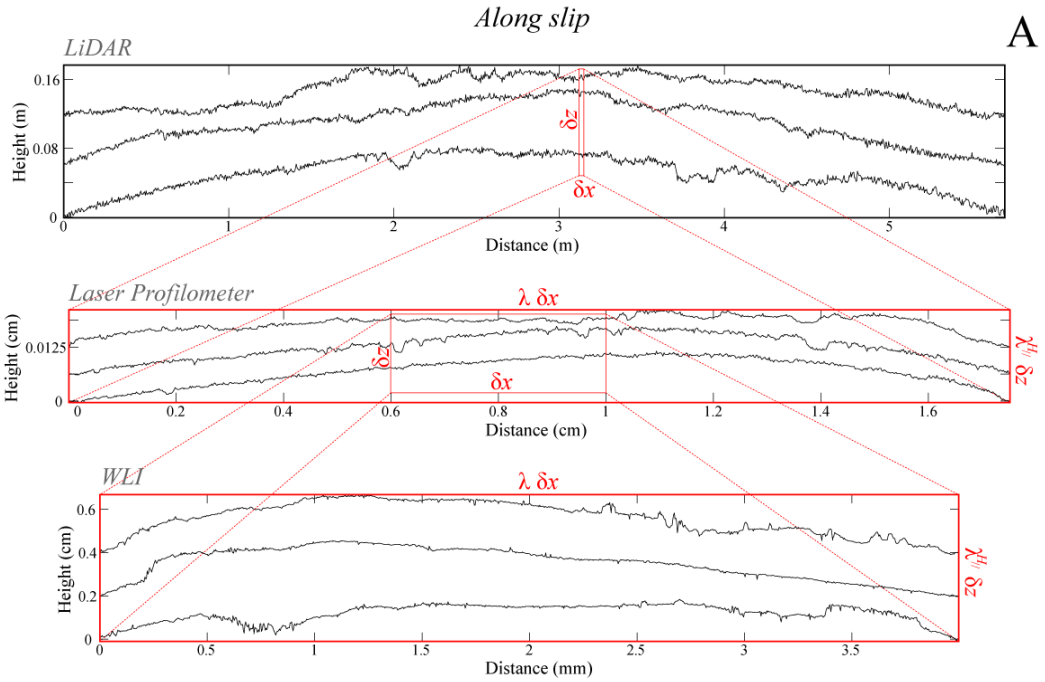

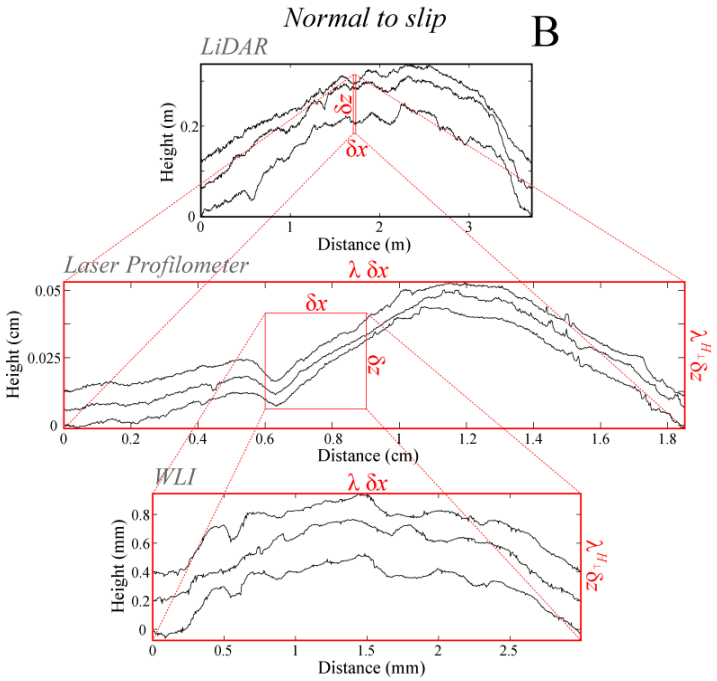

Figure 3.1. *1D profiles from the Corona Heights fault surface parallel and perpendicular to slip. A: Profiles along slip direction and B: perpendicular to it. For both directions, a magnified portion of the profiles has a statistically similar appearance to the entire profiles when using the scaling transformation* $\delta x \to \lambda \delta x, \delta z \to \lambda^{H_{//,\perp}} \delta z$ *. For each scale, profiles have been shifted vertically for clarity.*

Corona Heights and Dixie Valley faults cut through silicate rocks. The Dixie Valley (Basin and Range province in Nevada) fault surface has a mainly normal slip component and cross-cuts through rhyolite. Chemical changes during faulting have altered the mineralogy and chemical composition of the rock near the fault surface (Power *et al.*, 1987; Power and Tullis, 1989, 1992). Indeed, the material that forms the fault surface consists almost entirely of secondary quartz, a mineral which is extremely resistant to weathering. Based on gravity studies, combined with reflection seismology studies (Okaya and Thompson, 1985), Power and Tullis (1989), estimated that the total normal slip is probably between 3 and 6 km. Geologic and mineralogic constraints indicate that the slickenside surface formed at depths of less than 2 km and temperatures less than $270\ ^{o}C$ (Power and Tullis, 1989). Major historic earthquakes and microearthquakes activity occurred on the region of the studied fault scarp (Wallace and Whitney, 1984; Dozer, 1986). Additionally, Power and Tullis (1989) have argued that seismic faulting played a role in the development of the slickenside surfaces, based on textural features they described in the fault surface materials.

The Corona Heights strike-slip fault (Figure 3.2) located in the Castro district of San Francisco, cross-cuts brown Franciscan cherts, and was exposed by post-1906 earthquake quarrying. This fault constitutes a segment of the San Andreas Fault system. The relatively recent exposure of the fault and the high resistance of cherts to weathering allows for excellent preservation of the slip surface (Figure 3.2). In most places on the outcrop an anastomosing set of slip surface is present (Figure 3.2). Individual patches of the fault surfaces may have been activated at different times and different depths. Although the total slip for the fault zone as a whole could be large (kilometric), individual surfaces could have recorded smaller (metric) displacements which are difficult to precisely estimate due to the absence of well-defined structural markers.

Table 3.1. Laser Scanner Characteristics and fault roughness results

Fault Name & Displacement*	Lithology	Sense	Fault Patches	Scanner	Resolution δx	Spatial precision	Noise on the data δz	$H_{//}$ (±0.05)	$H_{\perp}$ (±0.05)	Average $H_{//}$	Average $H_{\perp}$
Vuache-Sillingy 45°57' 14.5"N 6°2' 56"E	Limestone 10-30 m	Strike slip	Surf-1	GS 100 (Trimble)	20mm	± 5 mm	4.5mm	0.59	0.79	0.60 ± 0.07	0.82 ± 0.04
			Surf-7	GS 100 (Trimble)	20mm	± 5 mm	4.5mm	0.68	0.84		
			Surf-6	LMS Z420i (Riegl)	30mm	± 7.5 mm	10.2mm	0.50	0.81		
			Surf-JPG	S10 (Trimble)	1mm	± 0.25 mm	0.9mm	0.62	0.83		
			Small	Lab. profilometer	20µm	± 1 µm	<1µm	0.65	0.80	0.60 ± 0.05	0.79 ± 0.03
			Vu-1-G					0.56	0.79		
			Vu-A-1	WLI	2µm	± 0.025 µm	3nm	0.58	0.76	0.59 ± 0.05	0.79 ± 0.04
			Vu-A-2		2µm			0.55	0.79		
			Vu-A-7		1µm			0.64	0.83		
			Vu-A-8		1µm			0.60	0.78		
Corona Heights 37°45' 55"N 122°26' 14"W	Chert several m to >1 km	Strike slip	Corona-A	HDS3000 Leica	5 mm	± 1.25 mm	2 mm	0.57	0.85	0.65 ± 0.05	0.83 ± 0.04
			Corona-B					0.64	0.82		
			Corona-C					0.68	0.88		
			Corona-D					0.64	0.81		
			Corona-E					0.69	0.78		
			Corona-F					0.68	0.84		
			P3	Lab. profilometer	20µm	± 1 µm	<1µm	0.66	0.86	0.62 ± 0.05	0.85 ± 0.03
			Co-AGU					0.58	0.85		
			Co-A-4	WLI	2µm	± 0.025 µm	3nm	0.62	0.82	0.62 ± 0.03	0.84 ± 0.04
			Co-A-9		1µm			0.63	0.86		
Bolu 40°41' 07"N 31°34' 04"E	Limestone 20 m to >1 km	Strike slip	Stack2345	Ilris-3D Optech	20mm	± 5 mm	20mm	0.47	0.79	0.49 ± 0.07	0.77 ± 0.04
			Stack67					0.50	0.77		
			Stack12					0.43	0.77		
			W-detail-2					0.44	0.76		
			E-detail-3					0.48	0.81		
			E-detail-2					0.45	0.79		
			E-detail-1					0.64	0.73		
			Bolu-1	Lab. profilometer	20µm	± 1 µm	<1µm	0.58	0.77	0.55 ± 0.05	0.75 ± 0.04
			Bolu-2					0.51	0.72		

Fault Name & Displacement*	Lithology	Sense	Fault Patches	Scanner	Resolution δx	Spatial precision	Noise on the data δz	$H_{//}$ (±0.05)	$H_{\perp}$ (±0.05)	Average $H_{//}$	Average $H_{\perp}$
Dixie Valley 39°56' 48"N 117°56' 43"E	Rhyolites	Normal	Dixie-1	HDS3000 Leica	5 mm	± 1.25 mm	2 mm	0.66	0.78	0.59 ± 0.08	0.81 ± 0.04
			Dixie-2					0.63	0.79		
			Dixie-3					0.60	0.83		
			Dixie-4					0.46	0.84		
			Map-1	Lab. profilometer	20µm	±1 µm	<1µm	0.56	0.82	0.58 ± 0.04	0.81 ± 0.03
			Map-2					0.60	0.81		
	several m to 3-6 km		Dixie-D	WLI	2µm	± 0.025 µm	3nm	0.56	0.88	0.56 ± 0.05	0.88 ± 0.03
			Dixie-H		1µm			0.50	0.87		
			Dixie-E		2µm			0.60	0.90		
			Dixie-C		2µm			0.59	0.89		
Magnola 42° 7'N 13°28' 31"E	Limestone	Normal	A32	Ilris-3D Optech	20mm	± 5 mm	20mm	0.58	0.76		
			M2	Lab. profilometer	20µm	±1 µm	<1µm	0.59	0.83		
	several m to >500m										

** Except for the Vuache-Sillingy fault surface, a lower and upper bound of the displacement is given. Indeed, although total geological cumulated slip for the fault zone as a whole can be kilometric (i.e. the upper bound), scanned individual surfaces within the fault zone may have experienced considerably less slip (i.e. the lower bound).*

The other three faults offset limestone rocks (Vuache-Sillingy in the French Alps, Magnola in the Appenines, and Bolu in Turkey). The Vuache-Sillingy fault is an active strike-slip fault system in the western part of the French Alps (Thouvenot, 1998). The fault surface (Renard *et al.*, 2006; Candela *et al.*, 2009) lies on a short segment of this fault system, where the accumulated slip was small, in the range $10-30$ meters (estimated on aerial photographs). The fault plane was exhumed ten years ago by the activity of a quarry and as a consequence, the LiDAR measurements could be performed on vegetation free fresh surfaces, where weathering was minimum. The Magnola fault (Candela *et al.*, 2009), in the Fuccineo area, is part of the extensive fault system in central Appenines (Italy). This 15 km long normal fault shows microseismic activity and presents an average vertical displacement larger than 500 meters.

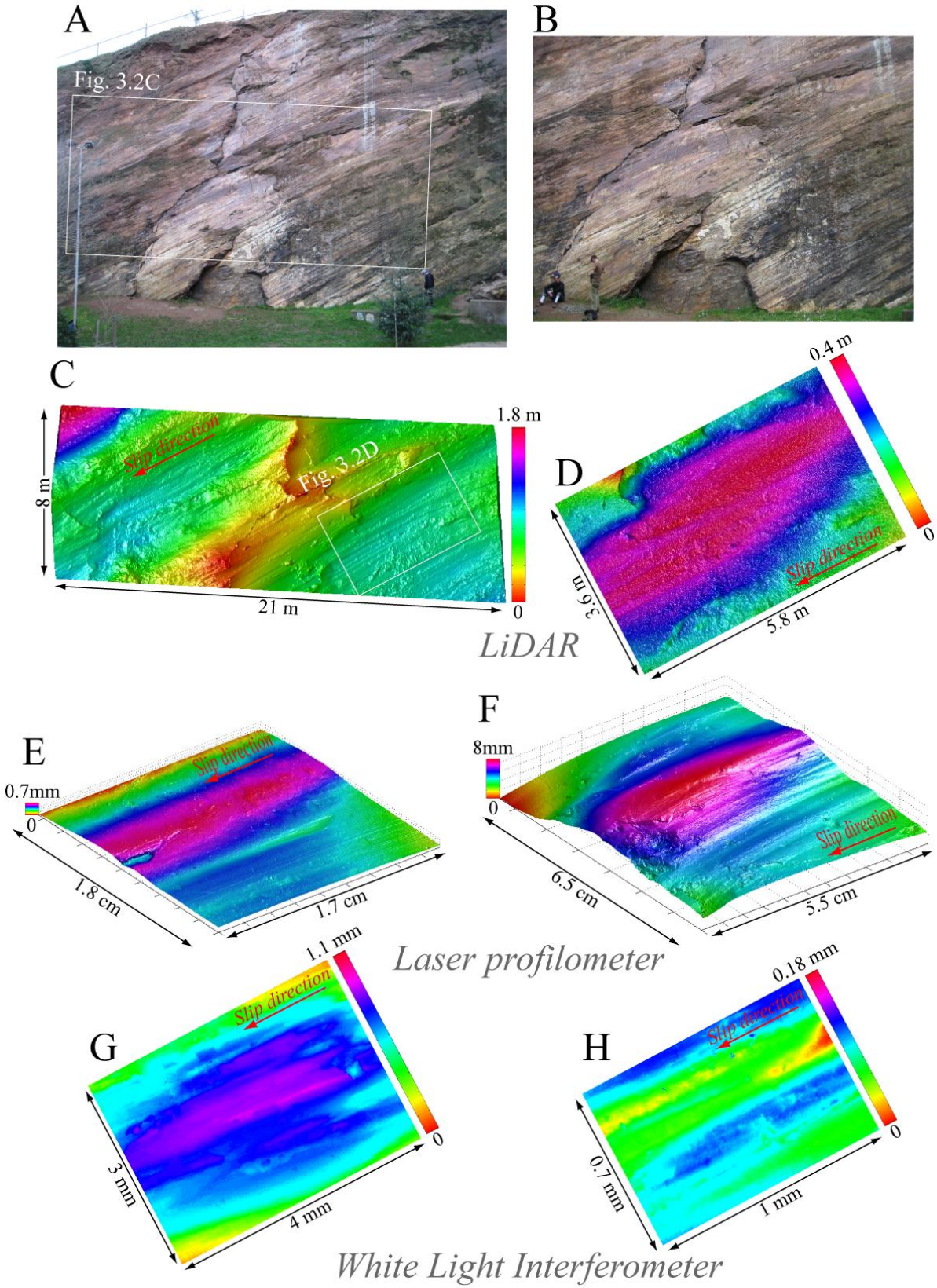
A
Fig. 3.2C
B
C
Slip direction
Fig. 3.2D
1.8 m
0
8 m
21 m
D
0.4 m
0
3.6 m
5.8 m
Slip direction
LiDAR
E
Slip direction
0.7mm
0
1.8 cm
1.7 cm
F
8mm
0
6.5 cm
5.5 cm
Slip direction
Laser profilometer
G
Slip direction
1.1 mm
0
3 mm
4 mm
H
Slip direction
0.18 mm
0
0.7 mm
1 mm
White Light Interferometer

Figure 3.2. *Corona Heights fault. Multiple bumpy discrete slip surfaces constituting lenses and striations can be detected at all scales up to the measurement resolution of each scanner device. A: Whole outcrop view. The inset corresponds to the surface shown on Figure 3.2C. B: Zoom on the fault showing different segments constituting the surface. C&D: Map of fault surfaces scanned with a LiDAR topography. The inset in C corresponds to the patch shown on Figure 3.2D. E and F: Maps of fault surfaces scanned with the laser profilometer. G and H: Zoom on the Figure 3.2E-F scanned with the white light interferometer.*

The site we study has been recently exhumed (Palumbo *et al.*, 2004; Carcaillet *et al.*, 2008) with less alteration by weathering than older exhumed portions of the fault. The Bolu fault is part of the North Anatolian strike-slip fault system. The study area (Figure 3.3) is a part of the section that ruptured during the 1944 earthquake (Kondo *et al.*, 2005; Kondo *et al.*, 2010; Barka, 1996). The small vertical component of the motion (~1m), compared to the dominant horizontal strike-slip motion (~3.5), was responsible for the partial exhumation of the fault plane (Figure 3.3) during the 1944 earthquake (Barka, 1996). More recently, anthropic activity (excavation for a garbage dump) also contributed to the exhumation of the outcrop. As for the Corona Heights fault, even if the total geological offset can be multi-kilometer in the region of the Bolu segment (Hubert-Ferrari *et al.*, 2002), it is not easy to define the slip accommodated specifically on each individual slip surface constituting the fault zone of the Bolu segment. Paleosismological investigations on the Bolu segment give a lower bound of approximately 20 m.

The five faults studied were exhumed from shallow depths ($< 5\,km$ depths), and their topography has recorded both the propagation and termination of major earthquakes rupture that initiate at greater depths. Even if it is difficult to accurately determinate under what conditions at depth (confining pressure, temperature, strain rate and chemical environment) fault surfaces were built, our set of faults clearly samples a large range of different parameters (accumulated displacement, lithology, tectonic regime) which possibly could control fault surface roughness.

3.2.2. B. Scanner devices and digital elevation models of fault roughness

Fault surface topography was scanned in the field using five independent $3D$ portable laser scanners (also called LiDAR, Light Detection And Ranging apparatus) that use the time of flight

of a light beam to accurately measure distances. The laser scanner records the topography of each exposed fault surface by collecting a cloud of points whose three dimensional coordinates correspond to points on the fault surface (Renard *et al.*, 2006; Sagy *et al.*, 2007; Candela *et al.*, 2009; Resor and Meer, 2009; Zhanyu *et al.*, 2010).

The actual point spacing depends on the distance between the target and the scanner and a chosen angular spacing. Different techniques were used to scan fault surfaces. Either, the entire fault outcrop was scanned or fresh sub-surfaces were selected for higher resolution acquisition (Figure 3.2, 3.3). Up to five scans of the same sub-surface have been also realized and the raw data of each scans have been stacked together to decrease the level of noise.

Our data sets cover surface scales from $1\,m^2$ to $800\,m^2$ at a spatial length scale resolution δx from $1\,mm$ to $30\,mm$. This spatial length scale resolution δx corresponds to the point spacing after the data processing (see section 3.2.3), and is systematically taken twice as large as the average irregular spacing one, that is from $0.5\,mm$ to $15\,mm$. The actual precision in the spatial positioning is estimated to be at the maximum equal to half the original average spacing, that is $\pm 0.25\,mm$ to $\pm 7.5\,mm$.

The height precision achievable depends on scanning conditions and is closely related to the spatial length scale resolution and to the roughness amplitude of the surface. In Table 3.1, δz represents the estimated amplitude of the instrumental noise.

The scans were combined with digital photographs to distinguish clear slip surfaces from eroded areas. This manual cleaning of the extremely large datasets (several tens of millions of points) was completed using $3D$ Reshaper software, a point cloud editor and visualization tool. Once all non-fault features such as trees, grass or anthropogenic structures, were removed, the whole fault scarp or selected smaller patches were analyzed (Figure 3.2, 3.3). Typically, in our data sets less than 5% of spurious points were removed from the raw scanner data. As pointed out by Candela *et al.* (2009) the estimation of the fault surface properties was not significantly biased by the presence of randomly distributed holes and missing data in the cloud of points (see Appendix 3.A for a quantitative analysis of the bias inherent to data acquisition in the estimation of the geometrical properties of fault surfaces).

In the laboratory, we used a home-made laser profilometer (Méheust, 2002), to measure a sample of the fault surface (between $20\,cm^2$ and $100\,cm^2$, Figure 3.2 and 3.3), set on a $2-axis$ moving table. The sample is scanned by geometric triangulation, measuring the distance between the sample and a laser head (Schmittbuhl *et al.*, 2006; Candela *et al.*, 2009). A difference with the LiDAR is that the data are regularly spaced with the laser profilometer. The spatial length scale resolution δx is equal here to the horizontal step, that is $20\,\mu m$. The actual precision in the spatial positioning is $\pm 1\,\mu m$ and the vertical resolution (δz) is better than $1\,\mu m$. The reliability and accuracy of the cloud of points obtained with this laser profilometer required that only few spurious points were removed (less than 0.01%).

At the millimeter scale, the topography of several slip surfaces (between $0.5\,mm^2$ and $40\,mm^2$, Figure 3.2 and 3.3) was measured using White Light Interferometry (WLI) microphotography (Dysthe *et al.*, 2002). This is done by a microscope that uses a broad-band white light source and that is coupled to a Michelson interferometer. A reference arm creates interference fringes with maximum intensity at equal optical path lengths of the imaging beam and reference beam. By vertical movement of the sample and simultaneous image capturing the interference, intensity envelope and thereby the relative height of the imaged surface at each pixel is determined with a resolution of $\delta z = 3\,nm$. The horizontal resolution depends on the lens used and with the highest magnification it is at the diffraction limit of white light, of about 0.5 micrometers. In the present study, we have selected horizontal steps (δz) between 1 and 2 micrometers (Table 3.1). The actual precision in the spatial positioning is estimated to be $\pm 0.025\,\mu m$. As for data acquired with the laser profilometer the cloud of points obtained are regularly spaced and only some spurious points have been manually removed. The whole suite of characteristics of the scanners devices and digital elevation models (spatial precision, resolution δx, noise on the data δz) used in this study are shown in Table 3.1.

As examples, two fault surfaces (Corona Heights fault, Figure 3.2 and Bolu fault, Figure 3.3) have been selected to illustrate the topographic data acquired at all scales with the three techniques presented. These fault surfaces are constituted of many discrete slip surfaces delimiting bumpy lenses elongated in the slip direction (Figure 3.2). These multi-scale bumpy

lenses give the wavy aspect of the fault surfaces that are overprinted by fine linear polished striations and coarser corrugations generated by abrasions (Figures 3.2 and 3.3).

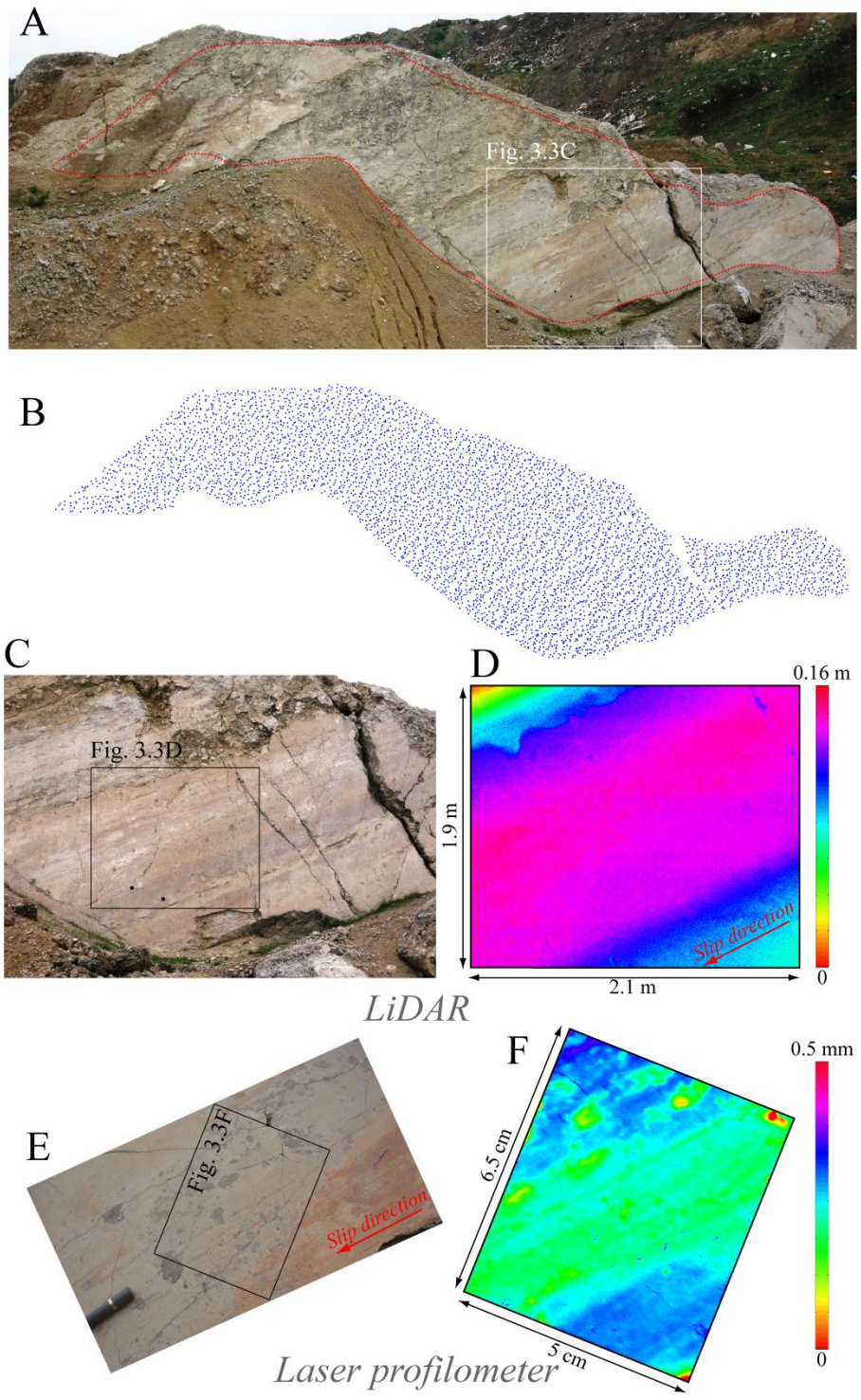

Figure 3.3. *Bolu Fault. A: Photograph of the fault zone in the Bolu limestone. Dashed red contour corresponds to the limits of the cloud of points shown in B. C: Photograph of a well-preserved slip surface constituting the fault zone. D: LiDAR data of surface in C. E and F: Zoom on the fault surface and the corresponding topographic map acquired with the laser profilometer, which still includes anisotropic roughness features in the slip direction.*

3.2.2. C. Surface rupture data

Fault trace roughness has been previously analyzed (Scholz and Aviles, 1986; Power *et al.*, 1987; Lee and Bruhn, 1996; Wechsler *et al.*, 2010). Most of the previous work focused on the San Andreas system and some studies wrestled with precision issues. In the present study, high resolution geological maps of large continental strike-slip earthquakes surfaces ruptures, in various geological setting, were analyzed, using the dataset of Klinger (2010) (See for example Figure 3.5 in Klinger (2010)). For each event, the surface ruptures length, earthquake magnitude, and total geological offset are provided in Table 3.2.

In a first approximation, we consider that the surface rupture trace of strike-slip earthquake is representative of the fault roughness along the slip direction. These rupture traces have been acquired using field cartography that allowed mapping the geomorphologic traces of the rupture coupled to slip distributions, and to high resolution satellite images (Klinger *et al.*, 2005, 2006; Klinger, 2010). The actual point spacing is irregular and its average is comprised between 200 m and 1300 m. However, it is worth to note that the precision of the position of each point is close to the meter scale by coupling the field observations with high resolution satellite images (Klinger *et al.*, 2005). This last information is crucial to have access to a multi-meter fine description of the roughness of the rupture trace.

First of all, we emphasize that to avoid bias due to local wiggles of the digitized rupture trace, the data set are re-sampled to ensure consistent spatial sampling, independent of the length of each rupture (Klinger, 2010). This re-sampling procedure does not affect the Fourier transform computation and makes it possible to keep the scaling information of the rupture traces (see Appendix 3.A).

Table 3.2. Characteristics and roughness results of earthquake rupture maps used in this study. (References for each earthquakes and detailed descriptions of their surface rupture traces could be found in Klinger (2010))

Name	Year	Magnitude	Length (km)	Total geological offset (km)	*H*
Owens Valley (USA)	1872	Mw 7.5-7.8	81	20	0.6 ± 0.1
Segment 1			18.5		
Haiyuan (China)	1920	Ms 8	240	125	0.8 ± 0.1
Segment 1			70		
Gobi-Altay Mongolia	1957	M 8.3	235	<20	0.7 ± 0.1
Segment 1			52		
Superstition Hills (USA)	1987	M 6.6	18	⩽24	0.7 ± 0.1
Segment 1			18		
Luzon (Philippine)	1990	Mw 7.8	107	<200	0.8 ± 0.1
Segment 1			107		
Landers (USA)	1992	Mw 7.2	65	>40	0.8 ± 0.1
Segment 1			15.3		
Zirkuh (Iran)	1997	Mw 7.2	104	70-90	0.9 ± 0.1
Segment 1			31		
Hector mine (USA)	1999	Mw 7.1	39	⩽10	0.7 ± 0.1
Segment 1			39		

Typical geometric discontinuities that are commonly observed on the eight high resolution maps of large continental strike-slip earthquake surface ruptures are fault azimuth changes or bends, relay zones which are also referred as jogs.

These discontinuities reflect the multi-scale en-echelon pattern of the fault system, in the range from a few hundred meters to several kilometers in size. Due to the presence of abrupt steps associated with relay zones, which influence the Fourier transform and therefore bias the roughness analysis, the ruptures traces are divided into individual segments (Figure 3.4). A "reconstruction" of the entire rupture trace can still be made when removing steps but the information contained in the first order large scale segmentation has been removed. Note that for some earthquake surface traces (Luzon, Superstition Hills, Hector Mine) no abrupt step was detected and the whole rupture trace can be directly analyzed.

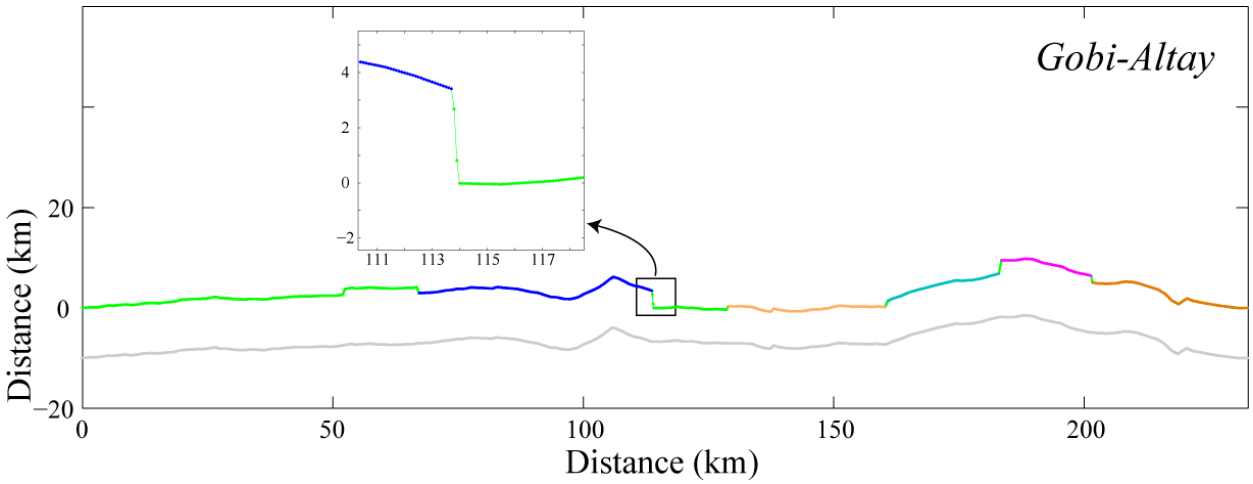

Figure 3.4. *Digitized surface rupture trace of the Gobi-Altay earthquake. The inset zooms on one of the steps removed for the Fourier transform analysis. Each segment individualized and bounded by steps have different colors and the whole profile is represented in green. The reconstructed trace by removing steps is displayed in gray.*

3.2.3. Analysis of scaling properties of roughness data

In this section we detail the procedure to characterize the scaling properties of the scanned fault surface topography. The same approach was followed for the digitized earthquake surfaces ruptures since they are considered as rough profiles extracted from the fault surface. In Appendix 3.A, the potential biases inherent to roughness data acquisition have been quantitatively defined in order to demonstrate that they do not significantly affect the Fourier transform computation.

First the original cloud of points (Figure 3.3) with irregularly spaced points was rotated, so that the mean rupture surface is horizontal and parallel to major axis (X, Y), and in this case the $3D$ set of points was transformed in two data set: (X,Y) + 1D (Z) (Renard *et al.*, 2006; Sagy *et al.*, 2007; Candela *et al.*, 2009; Zhanyu *et al.*, 2010). A set of parallel cuts was taken through the cloud of points to obtain a series of thin bands of points striking at an angle θ from the X axis. Then, each band of points was projected to obtain a series of profiles with irregularly spaced points. The thickness of the bands of points is closely related to the average spacing (X, Y) of the original raw data. Linear interpolation on a regular spacing and linear detrending are performed independently on all profiles to yield a set of heights $h(X_i)$, function of the coordinate X_i along the cut. The regular spacing taken for the linear interpolation has been systematically chosen as twice as large as the average irregular spacing of the original profiles. In the linear detrending procedure, any trends or undulations with wavelengths longer than the profile length were removed by referencing all heights along the profile to a line forced to go through the first and last points. The trend removal procedure causes an apparent decrease in power at wavelengths close to the profile length. This can be corrected by considering a variety of profile lengths from each surface (Power *et al.*, 1988).

To describe the scaling properties of these rough profiles (Figure 3.1), we search for possible spatial correlations of the height fluctuations. Along each profile, we computed the auto-correlation functions. If the auto-correlation function of a rough profile is a power law and scales as $< h(x), h(x+\delta x) > \propto \delta x^{2H}$, then the rough profile is self-affine with H the Hurst exponent, if multi-affinity is excluded. One way to estimate the auto-correlation function is to compute the power spectrum which is the Fourier Transform. This method is well-suited and robust to recognize and characterize self-affine roughness, as suggested by Candela *et al.* (2009).

The Hurst exponent H can be estimated from the Fourier power spectrum, which has a power law form for a $1D$ self-affine profile (Barabasi and Stanley, 1995; Meakin, 1998). For each profile, the Fourier power spectrum $P(k)$, i.e., the square of the modulus of the Fourier transform, is calculated as a function of wavenumber k. Then, after having verified the stationarity behavior of the statistical properties of each profile in one direction, each cloud of points is computed as a whole by stacking and averaging all $1D$ Fourier transforms to reduce the noise associated with individual profiles. When plotting the average power spectrum as a function of wavenumber in a log-log space, a self-affine function reveals a linear slope, which is itself a function of H through $P(k) = C\,k^{-1-2H}$. The power-law exponent of the spectrum, $-1-2H$, describes how the roughness changes with scale, while the intercept or pre-factor C fixes the steepness or roughness of the surface at a reference scale (Mandelbrot, 1983, p. 350), and both parameters are necessary and sufficient to describe a self-affine geometry. As an example, the computed Fourier power spectrum along the slip direction of one patch of the Corona Heights fault surface (Corona-B) acquired with a LiDAR is displayed on Figure 3.5. Taking into account one standard deviation compared to the best linear regression fit (least square method), we estimate the error bar on the calculated Hurst exponent. For our entire data set of fault surface patches acquired with three independent scanner devices (LiDAR, Laser profilometer, WLI), the upper bound limit of the error bar on the estimated Hurst exponent is equal to ± 0.05. Due to the fact that only one rough profile for each rupture trace is analyzed (Figure 3.4), the noise in the spectrum is higher compared to fault surface patch (constituted by an average of a multitude of profile). For a single power spectral estimate, the standard deviation is equal to the mean (Press *et al.*, 2007). So that the upper bound limit of the error bar in the estimated Hurst exponent of the eight rupture traces analyzed is equal to ± 0.1.

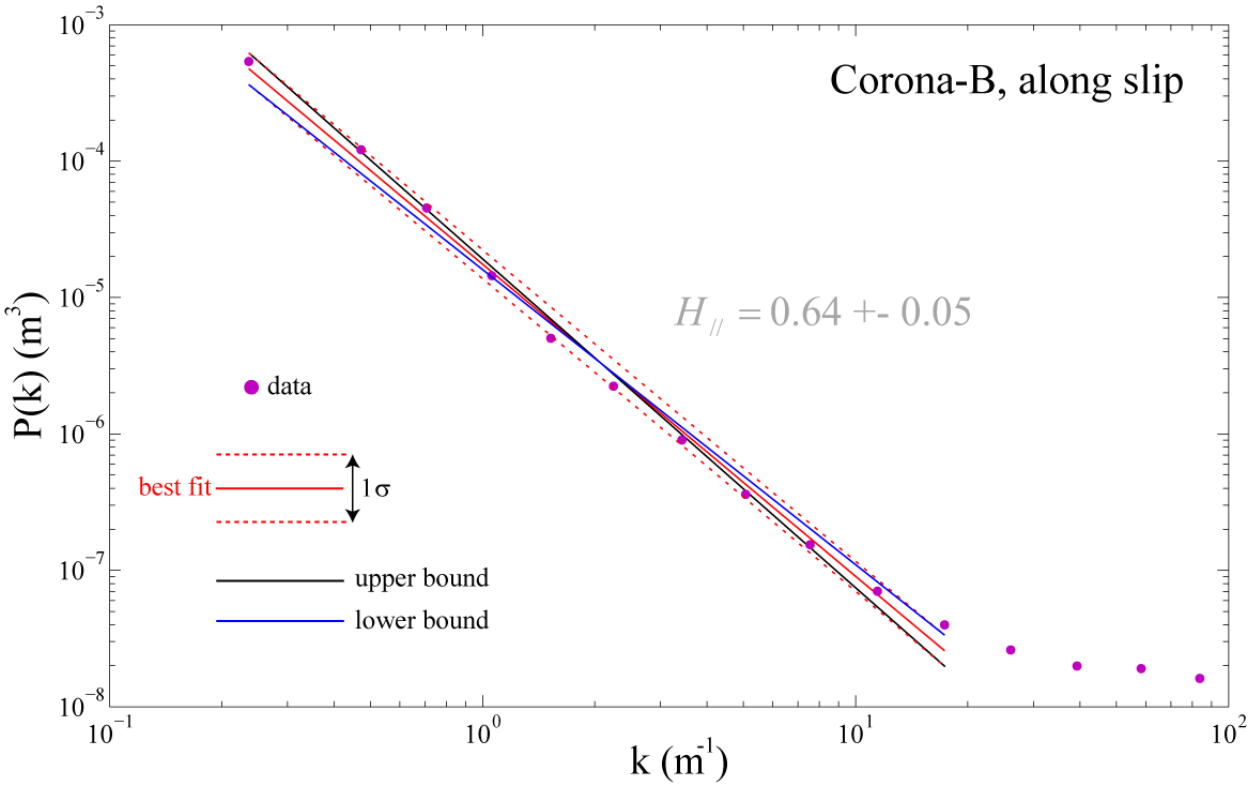

Figure 3.5. *Estimation of the Hurst exponent and the associated error on each Fourier power spectrum. Taking as example the Corona-B fault patch (see Table 3.1), a linear fit regression (least square method) is performed on the linear portion of its spectrum. The flattening at small scales (or large wavenumbers) is a consequence of the electronical noise inherent to LiDAR data acquisition. We consider one standard deviation from the best linear regression to estimate both the upper and lower bound of the acceptable fits and therefore the error bar on the estimated Hurst exponent.*

3.2.4. Fault roughness results

3.2.4. A. Anisotropic self-affine regime

First, the Figure 3.6 compiles all roughness values calculated on the five fault surfaces, bringing together LiDAR, laser profilometer, and WLI measurements. Fourier power spectra, underlining the scaling properties of each fault patch analyzed (41 sub-surfaces in total), are displayed along and normal to the slip direction.

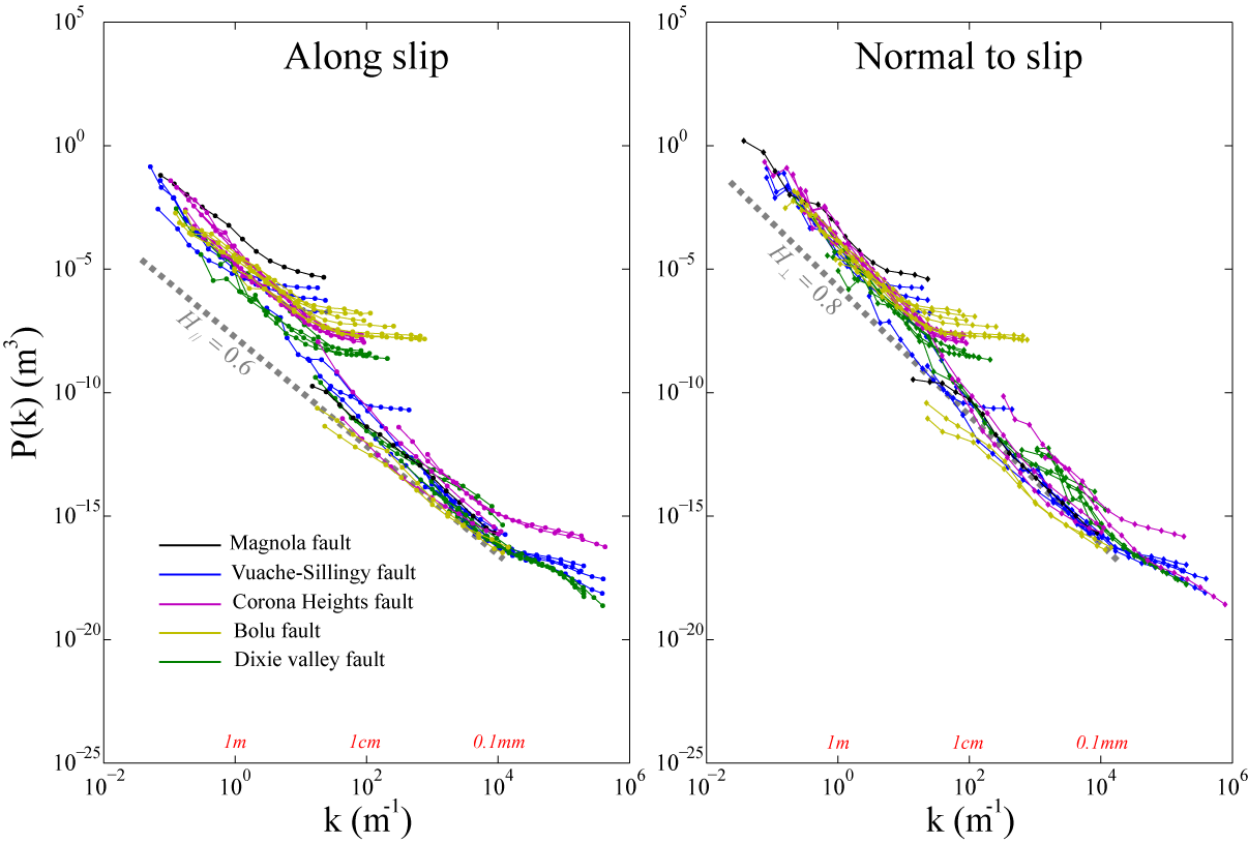

Figure 3.6. *Fourier power spectrum of the 41 surfaces analyzed along slip direction (left) and perpendicular to it (right). The computed curves of all the fault patches scanned with the 3 independent scanner devices (LiDAR, laser profilometer, WLI) are represented together on each of these two log-log graphs. We emphasize that the linear regressions have been computed on the linear part of each individuals Fourier power spectrum (see Figures 5 and 8). A large variability in the pre-factor is highlighted between scanned fault patches of the same fault surface and also between the five faults. The slight variability of the estimated slope of the curves (i.e. on the estimated Hurst exponent) is depicted in Figure 8. Two power-laws fit with prescribed Hurst exponent of 0.6 in the slip direction and 0.8 perpendicular to it, are displayed one each graphs for eye guidance.*

In order to highlight the specific trend of each fault, we have averaged the similar spectra (that means spectra with an approximately identical slope but with a slightly different vertical position) obtained from each scanner devices. Each curve on Figure 3.7 represents therefore an average of similar spectra obtained for multiple fault patches. In this way, this technique gives a smoother spectrum that represents the average self-affine character of the entire fault surface

while preserving good wavelength resolution. Our results show an identical directional morphological self-affine anisotropy for the five faults, characterized by two different global Hurst exponents (see Table 3.1): $H_{//} = 0.58 \pm 0.07$ in the direction of slip and $H_{\perp} = 0.81 \pm 0.04$ perpendicularly to the slip. We will refer to $H_{//} = 0.6$ and $H_{\perp} = 0.8$ afterwards. We emphasize that the slip direction underlined by striations and the direction perpendicular to it correspond roughly to the direction where the estimated self-affine exponents are respectively the smallest and the largest.

The Fourier power spectrum technique indicates that the power-laws are similar for field data and laboratory data, demonstrating the robustness of the self-affine behavior over approximately 6 decades of length scales (between $0.05\,mm$ and $30\,m$). Hence, it excludes several self-affine regimes, with different roughness exponents, bounded by characteristic scales.

A systematic bending of the Fourier power spectra (along both the parallel and the perpendicular slip directions) at the length scale $0.05\,mm$ is observed on the WLI data. This change of regime occurs at large length scale relatively to the expected WLI resolution, and we suspect that it could be the hallmark of the transition between two physical processes appearing at the grain scale. Indeed, Chen and Spetzler (1993) suggest that a characteristic length scale appearing at the grain scale is due to a change in the dominant mode of deformation from small scale intergranular cracking to intraganular cracking at large scale. The same observation and interpretation was made by Meheust (2002) on tensile cracks. However, it is beyond the scope of this work to quantitatively characterize this possible characteristic length scale and we limit our scaling analysis down to $0.05\,mm$.

Slight deviations (natural variation) of the Fourier power spectra from the general trend can be observed, for example between $0.05\,mm$ and $30\,m$, for the Bolu fault surface roughness data; the Hurst exponent is slightly lower than 0.6 along the direction of slip. We propose, however, that the global anisotropic self-affine behavior is consistent when taking into account the typical fluctuations indicated in Table 3.1. Indeed, fault surface with a Hurst exponent smaller or larger than one standard deviation of their distribution (± 0.07 in slip direction and ± 0.04 normal to slip) exist, but all Hurst exponents fall within two standard deviations interval (Figure 3.8).

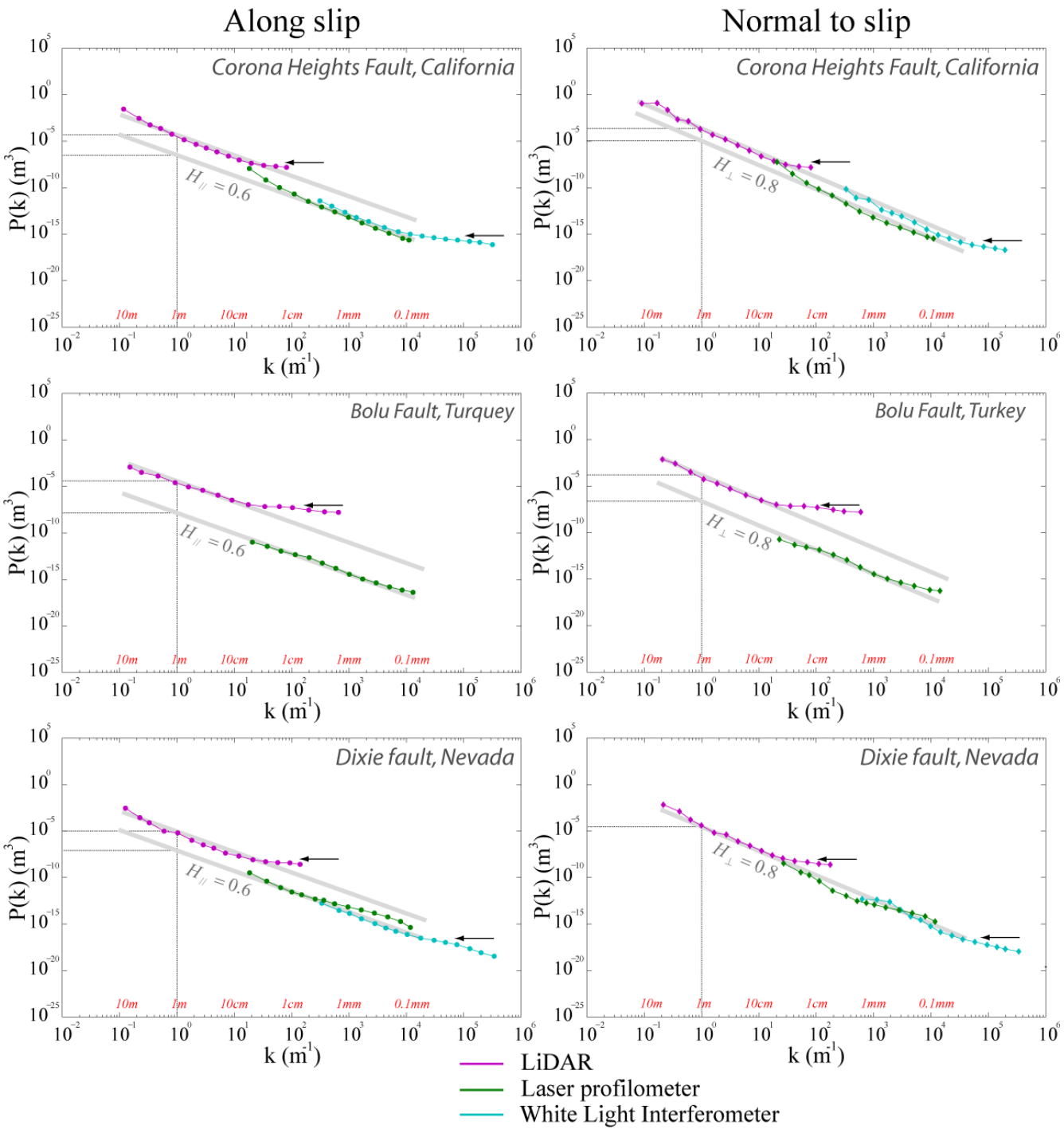
Along slip
Normal to slip
Corona Heights Fault, California
Bolu Fault, Turquey
Bolu Fault, Turkey
Dixie fault, Nevada
$H_{//} = 0.6$
$H_{\perp} = 0.8$
P(k) (m^3)
k (m^{-1})
10m
1m
10cm
1cm
1mm
0.1mm
LiDAR
Laser profilometer
White Light Interferometer

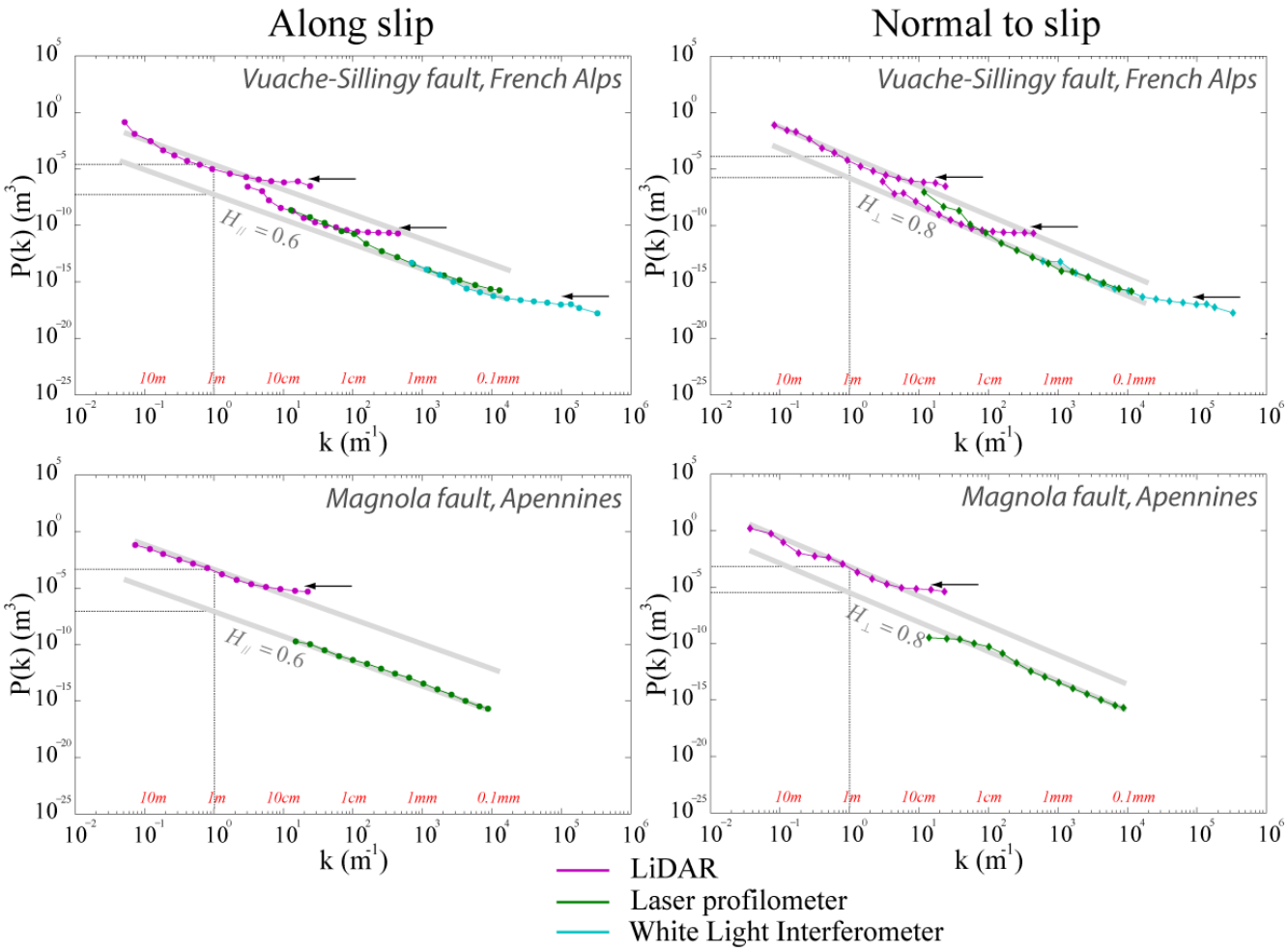

Figure 3.7. *Fourier power spectra from the five faults analyzed along the slip direction (left) and perpendicular to it (right). Each curve at each scale (LiDAR, laser profilometer, white light interferometer) includes together the average spectra of several sub-surfaces (or fault patches in Table 3.1). Power-law fits (thick gray lines) with a roughness exponent of* $H_{//} = 0.6$ *and* $H_{\perp} = 0.8$*, connecting the field and laboratory data in both directions, are shown on plot for eye guidance. Dotted black lines indicate the range of pre-factors,* $C_{//,\perp}$*,* $(P(k) = C_{//,\perp}\, k^{-1-2H_{//,\perp}}$*, extracted from the power-law fits at* $k = 1\,m$*. For each curve at large scale the deviation from the global linear trend is due to finite size effects. Black arrows (at the bending of spectra) indicate the level of noise of the LiDAR and the lower limit for the fit performed at the WLI scale.*

For each scanned fault patch, the profiles parallel to slip are smoother (i.e. lower power spectrum modules at each scale and more precisely the power-law relationships between $P(k)$ and k have both lower power-law exponents and pre-factors) than profiles normal to slip.

Some surfaces show vertical shifts between the spectra obtained by each device. These shifts might be due partly to their various resolutions, and partly to the fact that the surfaces are statistically heterogeneous, i.e., different pre-factors may be calculated from different parts of the same surface. This latter observation is discussed in more details in the section 3.2.4.C.

Finally, the compiled results of the present data and previous works (Schmittbuhl *et al.* 1993; Lee and Bruhn, 1996; Renard *et al.*, 2006; Candela *et al.*, 2009) clearly show that a universal anisotropic self-affine model accurately describes fault surfaces roughness. In addition, this description of the fault surfaces is independent of the geological context, i.e. lithology, accommodated displacement, tectonic regime.

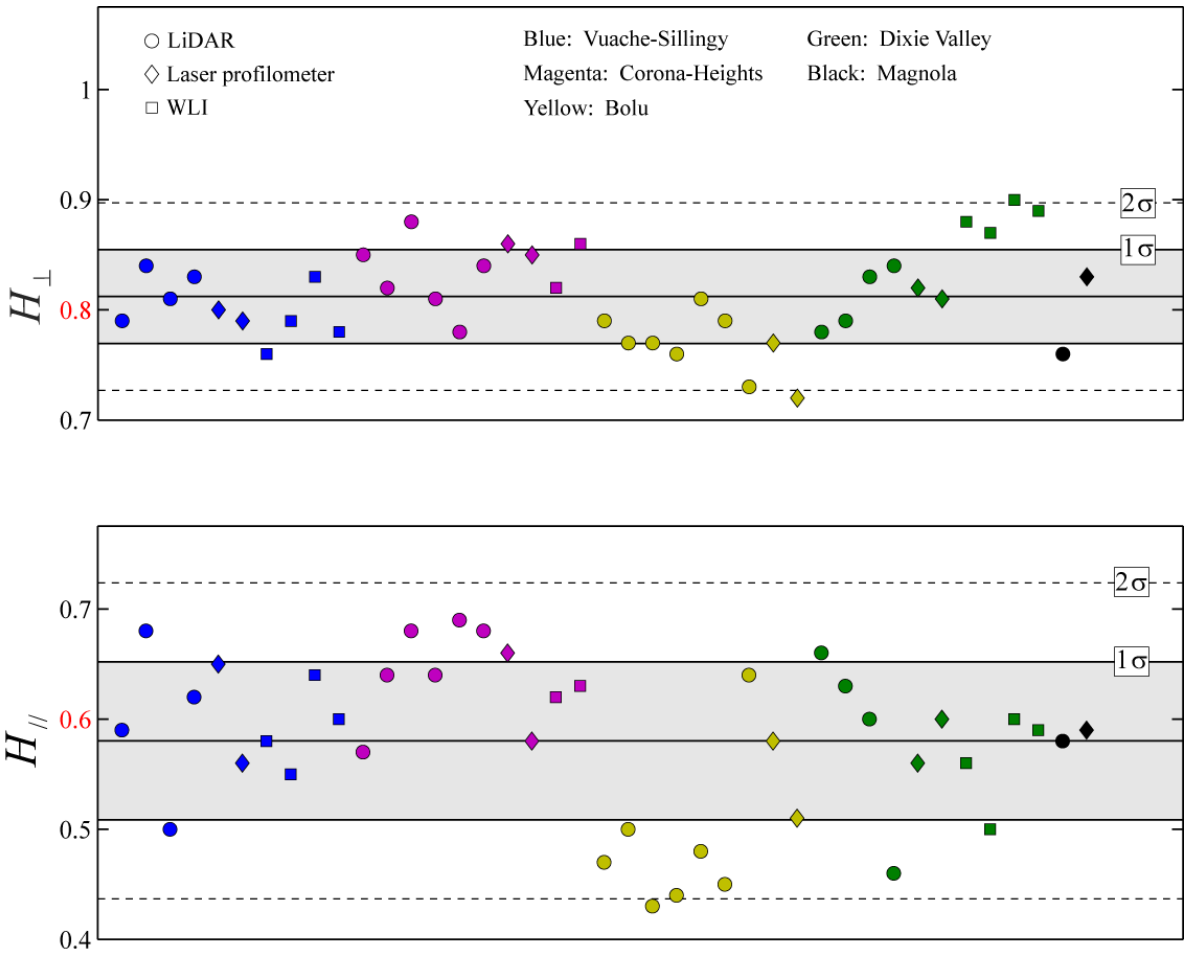

Figure 3.8. *Plot of the Hurst exponents (see Table 3.1) in slip direction (down) and normal to it (up). To differentiate the five faults, the same color code of Figure 3.6 has been used. The average Hurst exponent is equal to* 0.58 *along the direction of slip and* 0.81 *perpendicular to it. The shaded area and dashed lines indicates the* 1σ *and* 2σ *confidence intervals, respectively.*

3.2.4. B. Pre-factor variability

In section 3.2.4.A, we have focused on the analysis on the slope of the power-law, which appear to be constant along slip and perpendicular to it for the whole set of fault surfaces. This observation highlights the fact that, for one direction (parallel or perpendicular to slip), the relative amplitude of short and large wavelengths remains identical for the whole data set. However, a significant variability of the pre-factor (the vertical position of the Fourier power spectra) is observed for each fault surface and at each scale (LiDAR, Laser profilometer, WLI). Here we illustrate this variability on the data acquired with the LiDAR on the Corona Heights fault, along the slip direction. A significant vertical shift is observed on the Fourier power spectra corresponding to the six different patches of the Corona Heights fault (Table 3.1). The slope, however, seems similar (Figure 3.9). As it is observed on profiles extracted from each of the six fault patches (Figure 3.9), this vertical shift is correlated to the roughness amplitude of the profiles at all scales. Indeed, sections of the fault surface with a large relative pre-factor (or Fourier power spectrum relatively higher in Figure 3.9), include profiles with larger roughness amplitude but keep the same self-affine scaling properties of amplitude versus length scales. In other words, on the Corona Heights fault surface, individual patches show differences in Fourier power spectrum at all scales but the Hurst exponent i.e. the relative amplitude of the modes of short and large wavelengths remains identical.

In order to validate this observation, we have performed a test on two synthetic anisotropic self-affine surfaces computed by a Fourier based method (Candela *et al*., 2009) for which the Hurst exponents are identical but the pre-factors of the power-law vary by a factor 10 (Figure 3.10). These synthetic simulations mimic $5\times5\,m$ fault patches on the Corona Heights fault and show that a decrease of the pre-factor shifts vertically downwards the position of the spectra in the log-log, whereas the slope (or the Hurst exponent) remains constant (Figure 3.10). These

simulations can explain the variability in the pre-factor observed in natural fault surface and illustrated on Figure 3.9.

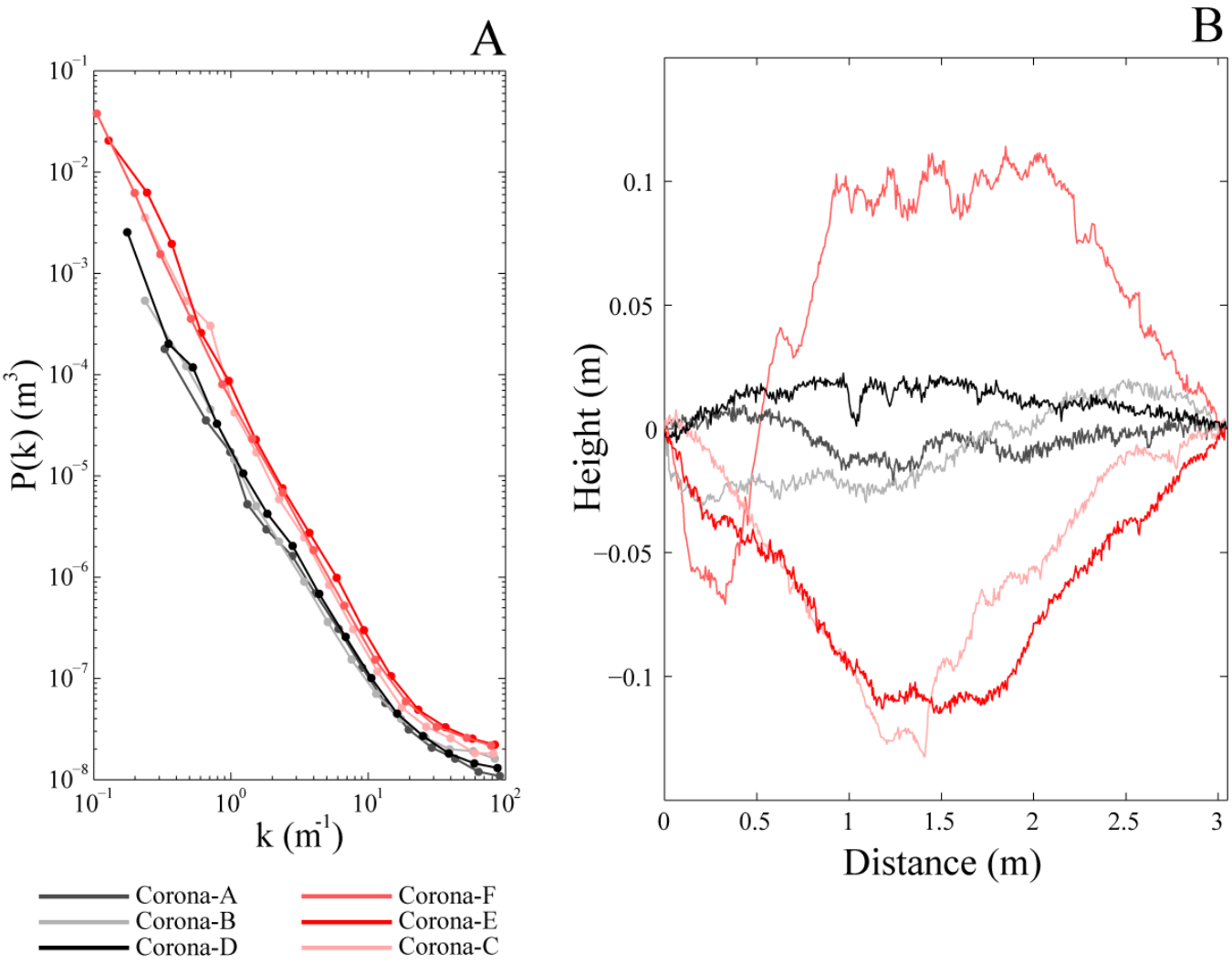

Figure 3.9. *Variability of the pre-factor on the Corona Height fault surface. A: Fourier power spectra calculated in the slip direction from the six patches of the Corona Heights fault surface measured with a LiDAR and showing a significant vertical shift between the spectra whereas they keep a roughly similar slope. B: Example of 1D profiles extracted along slip direction. The vertical shift of the spectra is correlated with the roughness amplitude of the profiles at all scales.*

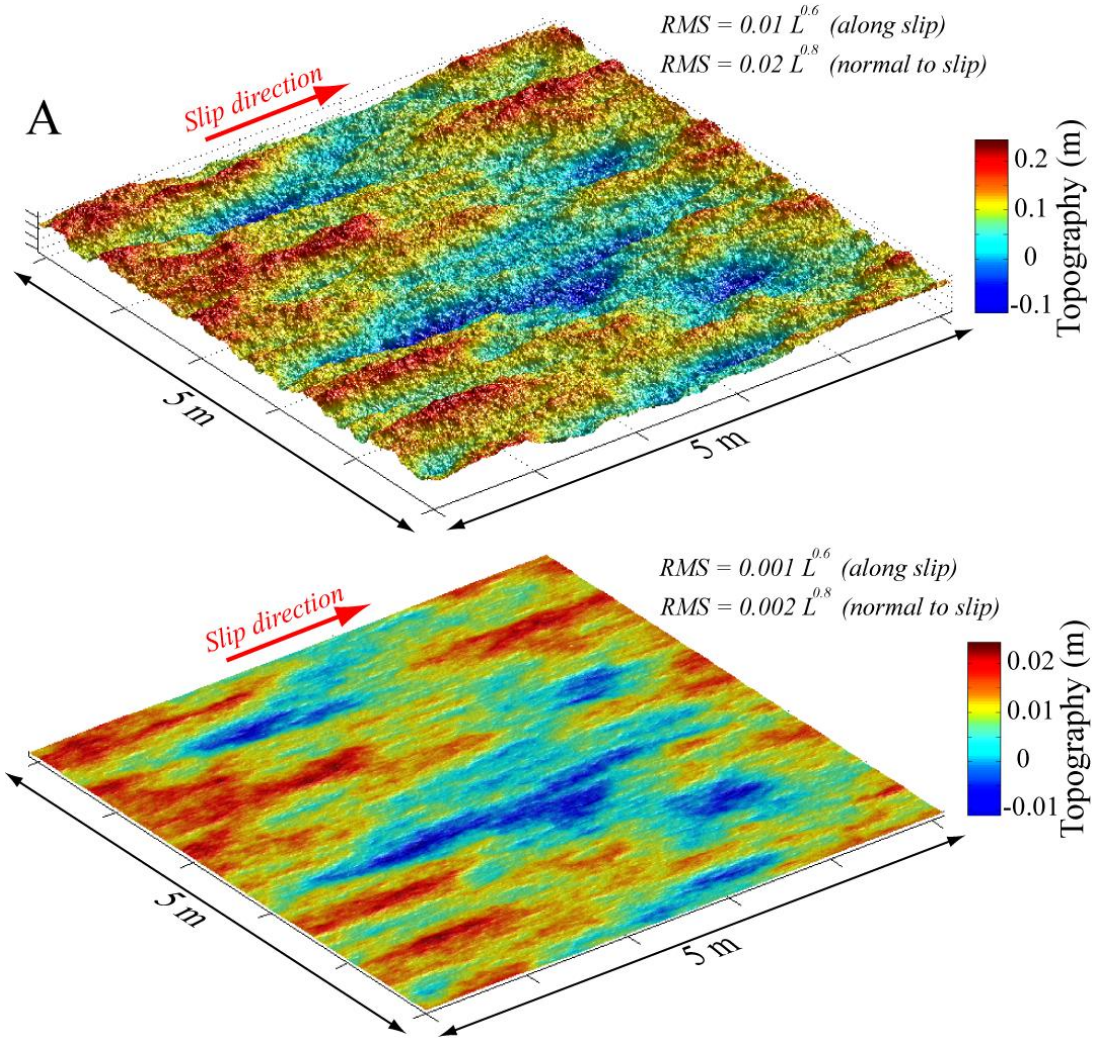
A
Slip direction
RMS = 0.01 L^0.6 (along slip)
RMS = 0.02 L^0.8 (normal to slip)
0.2
0.1
0
-0.1
Topography (m)
5 m
5 m
Slip direction
RMS = 0.001 L^0.6 (along slip)
RMS = 0.002 L^0.8 (normal to slip)
0.02
0.01
0
-0.01
Topography (m)
5 m
5 m

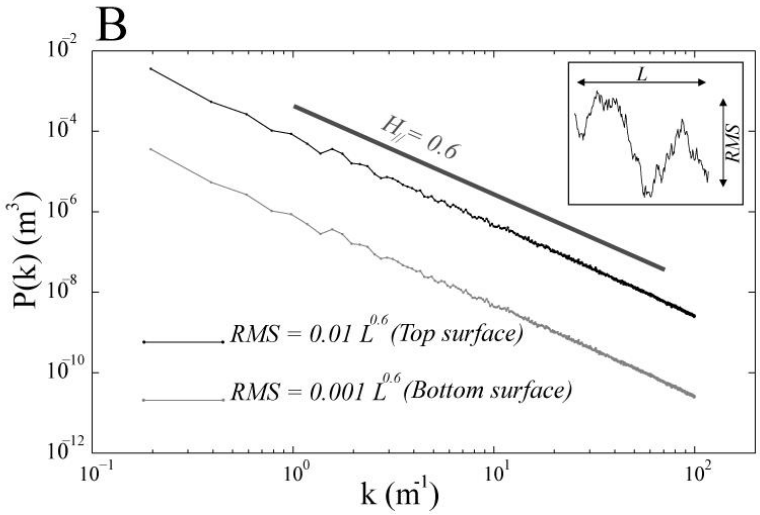
B
P(k) (m^3)
k (m^-1)
H// = 0.6
L
RMS
RMS = 0.01 L^0.6 (Top surface)
RMS = 0.001 L^0.6 (Bottom surface)

Figure 3.10. *RMS roughness amplitude and variability of the pre-factor on synthetic fault surface. A: Map view of synthetic anisotropic self-affine surface. The* RMS *standard deviation at the length scale* L *follows a power law* $RMS = 0.01L^{0.6}$ *(top) and* $RMS = 0.001L^{0.6}$ *(bottom) along slip direction, and* $RMS = 0.02L^{0.8}$ *(top) and* $RMS = 0.002L^{0.8}$ *(bottom) perpendicular to it. B: Fourier power spectra performed in slip direction for both synthetic fault surfaces shown in A. The inset displays an example of the* RMS *and* L *for a rough profile extracted from these surfaces.*

3.2.4. C. Geometrical model of slip surfaces

In this section we give a full description of fault surface geometry that includes all the roughness scaling information included in the Figure 3.7, that is the Hurst exponents and the range of pre-factors of the scaling functions along and normal to the slip direction for each fault surfaces. The second order moment of the heights distribution, which corresponds to the root-mean-square (RMS) roughness amplitude, is related to the power spectrum module. Using Parseval's theorem (Sagy *et al.*, 2007), if $0 < H_{//,\perp} < 1$, for a profile of length L, the integration of $P(k) = C_{//,\perp}\, k^{-1-2H_{//,\perp}}$ over the wavelength λ (with $\lambda = 1/k$) yields that the RMS roughness correlates as $RMS = \left(C_{//,\perp} \Big/ 2H_{//,\perp} \right)^{0.5} L^{H_{//,\perp}}$. Therefore, we use the range of pre-factors and the average value of $H_{//} = 0.6$ and $H_{\perp} = 0.8$ for each fault surface, which represent the global trends observed in Figures 3.7, 3.8, to infer the RMS roughness amplitude as a function of scale (Figure 3.11).

For each fault surface and both along and normal to the slip direction (except for the Dixie Valley fault in the slip direction), the variability of the pre-factor $C_{//,\perp}$ implies a range of values. In both directions (along slip and perpendicular to it), the maximum and minimum pre-factors are extracted from the data set shown in Figure 3.7 and indicated in Table 3.3. Finally, we obtain for each faults two power-laws relationships between RMS and L, which bound the slip parallel and slip perpendicular roughness (Figure 3.11). These anisotropic self-affine geometrical models do not show any characteristic length scale and are valid over a restricted range of wavelengths between approximately $0.05\ mm$ and $30\ m$.

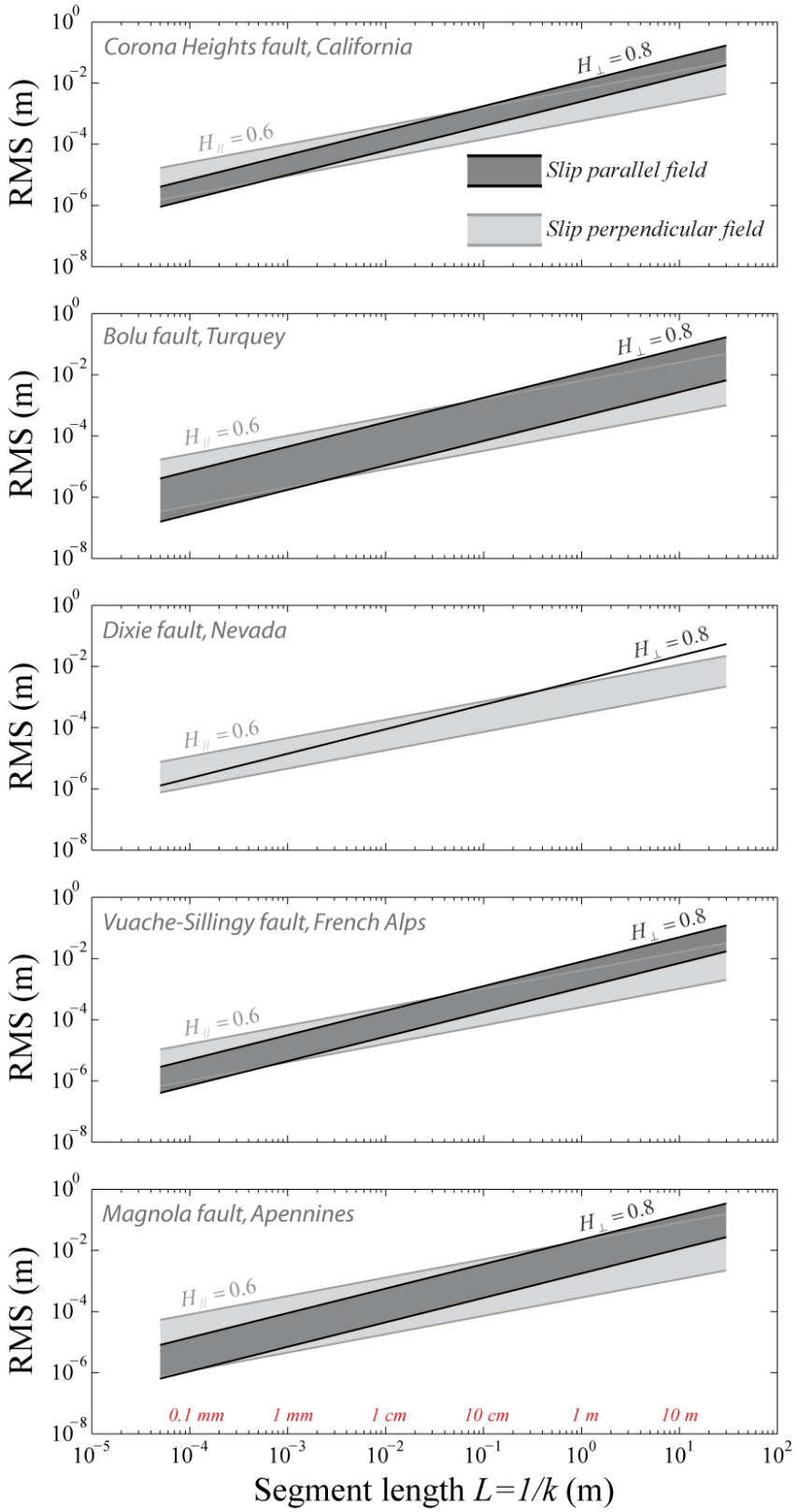
Corona Heights fault, California
Bolu fault, Turquey
Dixie fault, Nevada
Vuache-Sillingy fault, French Alps
Magnola fault, Apennines
$H_{\perp} = 0.8$
$H_{//} = 0.6$
Slip parallel field
Slip perpendicular field
RMS (m)
10^{0}
10^{-2}
10^{-4}
10^{-6}
10^{-8}
0.1 mm
1 mm
1 cm
10 cm
1 m
10 m
10^{-5}
10^{-4}
10^{-3}
10^{-2}
10^{-1}
10^{0}
10^{1}
10^{2}
Segment length $L=1/k$ (m)

Figure 3.11. *Anisotropic self-affine geometrical models of fault surfaces inferred by* RMS *roughness amplitude as a function of scale. Taking into account the close relationship of the power spectrum module with the moment of order* 2 *of the heights distribution (which is the* RMS *roughness amplitude), and using the two global Hurst exponents (*$H_{//} = 0.6$ *and* $H_{\perp} = 0.8$*) and the range of pre-factor between* $P(k)$ *and* k *shown in Figure 3.7 and Table 3.3, we propose a geometrical model for each fault surface valid over the range of wavelengths sampled by the five fault studied, i.e. between approximately* $30\ m$ *and* $0.05\ mm$.

As a consequence of the large range of pre-factors (Figure 3.7 and Table 3.3), it is difficult to point out a characteristic length scale where the roughness would not depend on the orientation relative to the surface, i.e. where the surface could be considered as isotropic.

We also extract directly from these limit cases, the pre-factor $l_{r(//,\perp)}$ of the scaling relationship $RMS\,(L) = l_{r(//,\perp)}^{1-H_{//,\perp}}\ L^{H_{//,\perp}}$, which defines the topothesy of the surface (Simonsen *et al.*, 2000; Schmittbuhl *et al.*, 2006, 2008; Candela *et al.*, 2009). The topothesy corresponds physically to a length scale, for which typical fluctuations of the roughness are of the same order as the wavelength considered, that is $RMS\,(l_{r(//,\perp)}) = l_{r(//,\perp)}$. In other words, $l_{r(//,\perp)}$ is the length scale at which the profiles shows an average slope of 45^{o}. The topothesy is complementary to the Fourier pre-factor $C_{//,\perp}$, but in contrast with this latter it is homogeneous at a length scale whatever the value of the exponent. The smaller $l_{r(//,\perp)}$, the flatter the surfaces appears on a macroscopic scale (Table 3.3). Note that for each fault, given that their surface appears relatively more rough or jagged in the slip direction compared to the perpendicular direction (as a direct consequence of the difference in their scaling exponents), the along slip topothesy is always larger than perpendicular to it. Given the extremely small values of estimated topothesy along slip and normal to it (see Table 3.3), the local slope of the surface is always significantly smaller than 45^{o} for the range of scales that we explored, i.e. from $30\ m$ to $0.05\ mm$, meaning that fault surfaces are rather smooth macroscopically.

Table 3.3. Pre-factor and Topothesy

			Parallel to slip	Perpendicular to slip
Vuache-Sillingy	Pre-factor (m^3)	min	8×10^{-8}	2×10^{-6}
		max	2×10^{-5}	1×10^{-4}
	Topothesy (m)	min	1×10^{-9}	2×10^{-15}
		max	1×10^{-6}	3×10^{-11}
Corona Heights	Pre-factor (m^3)	min	4×10^{-7}	1×10^{-5}
		max	5×10^{-5}	2×10^{-4}
	Topothesy (m)	min	8×10^{-9}	1×10^{-13}
		max	3×10^{-6}	2×10^{-10}
Bolu	Pre-factor (m^3)	min	2×10^{-8}	3×10^{-7}
		max	5×10^{-5}	2×10^{-4}
	Topothesy (m)	min	2×10^{-10}	2×10^{-17}
		max	3×10^{-6}	2×10^{-10}
Dixie Valley	Pre-factor (m^3)	min	1×10^{-7}	2×10^{-5}
		max	1×10^{-5}	
	Topothesy (m)	min	1×10^{-9}	6×10^{-13}
		max	4×10^{-7}	
Magnola	Pre-factor (m^3)	min	1×10^{-7}	5×10^{-6}
		max	5×10^{-4}	8×10^{-4}
	Topothesy (m)	min	1×10^{-9}	2×10^{-14}
		max	6×10^{-5}	6×10^{-9}

The minimum and maximum pre-factor, $C_{//,\perp}$, $(P(k) = C_{//,\perp}\, k^{-1-2H_{//,\perp}})$ *are extracted from the power-law fits performed on Figure 3.7 along the slip direction and normal to it for each fault surface. Then, using* $RMS = \left(C_{//,\perp} \Big/ 2H_{//,\perp} \right)^{0.5} L^{H_{//,\perp}}$ *with* $L = 1/k$, *we can plot the RMS roughness amplitude as a*

function of scale, as displayed on Figure 3.11. On Figure 3.11, the minimum and maximum topothesy, $RMS\ (l_{r(//,\perp)}) = l_{r(//,\perp)}$ *for the five fault surfaces is extracted for the slip direction and perpendicualr to it.*

3.2.4. D. Roughness of large continental earthquakes surface ruptures

The Gobi-Altay earthquake rupture shows an example of how we have segmented surface rupture traces each time we encountered a relay zone formed by two non co-planar faults (Figure 3.4). As already mentioned in section 3.2.2.C, these disruptions in fault traces diffract the Fourier transform and, therefore bias the roughness analysis. The Fourier transform analysis performed on individual segments (Figure 3.12) indicates that each of them has a roughly identical self-affine regime characterized by a Hurst exponent of 0.7 ± 0.1 (see also Table 3.2). Moreover, the profile obtained for the entire "reconstructed" rupture trace represents an average of the roughness over all the individual segments and keeps an approximately identical self-affine exponent (Figure 3.12). To summarize, the self-affine regime is maintained constant along the rupture trace, characterized both by stable self-affine exponent and pre-factor.

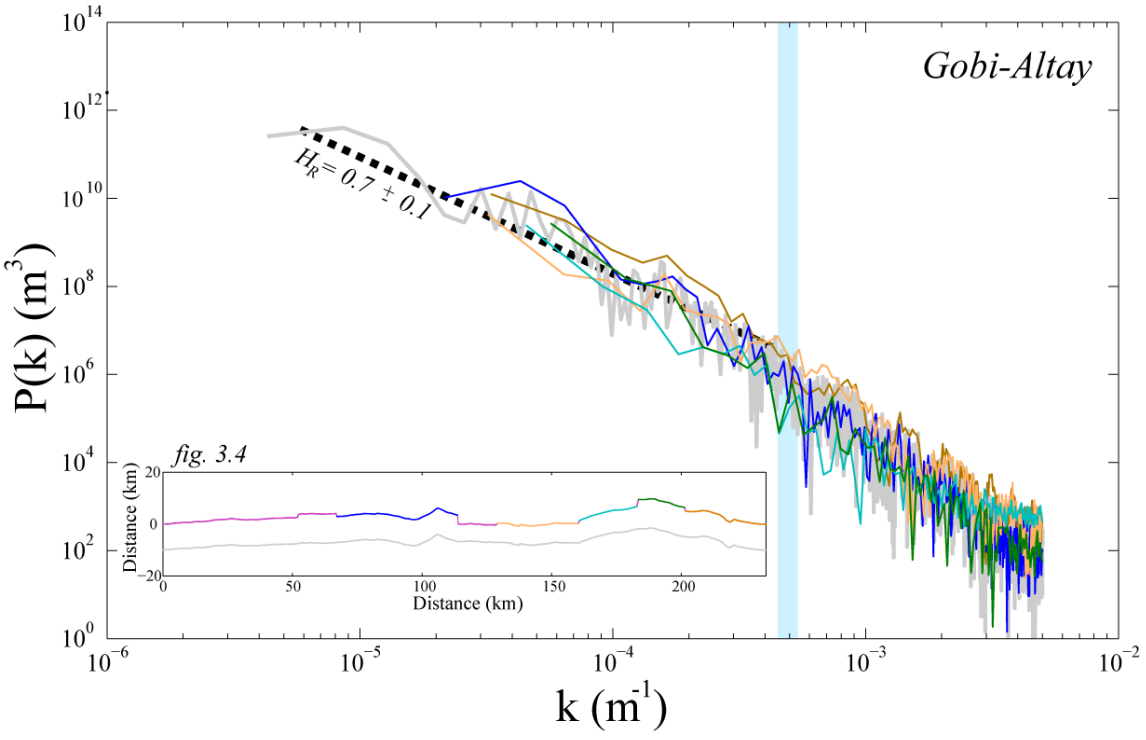

Figure 3.12. *Roughness analysis of the Gobi-Altay earthquake surface rupture. Fourier power spectra of each segment of the Gobi-Altay earthquake surface rupture and the whole reconstructed trace shown in Figure 3.4 (inset). Colors for each curve follow the same code used for the profiles in Figure 3.4 (inset). Above the cross-over length scale, indicated by the blue vertical bar and marking the beginning of the regime controlled by data re-sampling, all the curves follow a power-law behavior with a similar slope giving an average Hurst exponent of* 0.7 ± 0.1 *(see also Table 3.2).*

In Figure 3.13, a compilation of the roughness results is provided for the eight surface ruptures. Results of the Fourier power spectrum analysis are shown for one selected segment (bounded by abrupt steps), and the whole rupture trace. Power-laws fits and inferred Hurst exponents on the linear part of the curves at large scales show a consistent similar slope for selected individual segments and the whole rupture trace (Figure 3.13). Note that except for short segments (i.e. with a frequency content not large enough for a Fourier analysis) an identical scaling behavior is observed for all individual segments, but for clarity of the Figure 3.13 we focus here on the comparison between one segment and the whole rupture trace.

On the same log-log graph (Figure 3.14) a stack of all the spectra performed on individual segments (called “Segment 1” in Table 3.2) complements the Figure 3.13 and underlines that the totality of our rupture data can be described by a unique global self-affine exponent with an average Hurst exponent of 0.8 ± 0.1. Another interesting result highlighted in the Figure 3.14 it is that even if the eight rupture traces analyzed clearly sample variable geological settings, a unique global self-affine regime best fits the data and, in particular, no trend is observed with the finite geological offset accumulated by the fault zone hosting the earthquake ruptures. Indeed, even if the surface rupture traces are related to fault zone which have accumulated a large range of finite geological offset (see Table 3.2), the variability of the pre-factors highlighted in Figure 3.14 seems to be uncorrelated with the geological offset. Hence, no smoothing related to fault maturity is observed. This last observation is also supported by the fact that a unique global self-affine exponent characterizes the whole rupture traces analyzed. It is important to point here that rupture traces actually individualize the active portions of the fault zone, which should possibly have recorded a signal of geometrical regularization with the slip accumulated. Such a signal of fault maturity (Ben-Zion and Sammis, 2003) is not observed here.

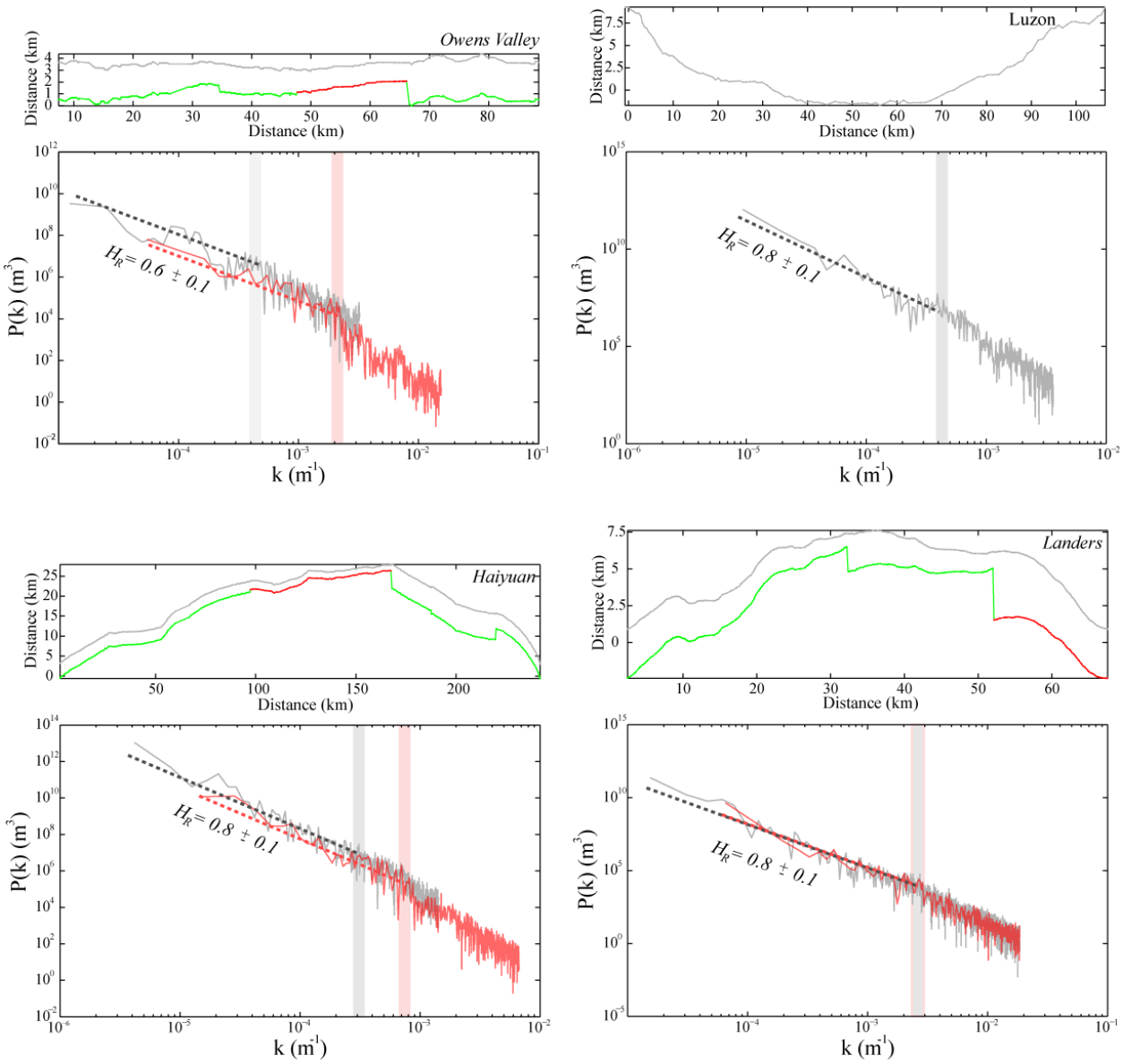
Owens Valley
Distance (km)
Distance (km)
P(k) (m³)
$H_R = 0.6 \pm 0.1$
k (m⁻¹)
Luzon
Distance (km)
Distance (km)
P(k) (m³)
$H_R = 0.8 \pm 0.1$
k (m⁻¹)
Haiyuan
Distance (km)
Distance (km)
P(k) (m³)
$H_R = 0.8 \pm 0.1$
k (m⁻¹)
Landers
Distance (km)
Distance (km)
P(k) (m³)
$H_R = 0.8 \pm 0.1$
k (m⁻¹)

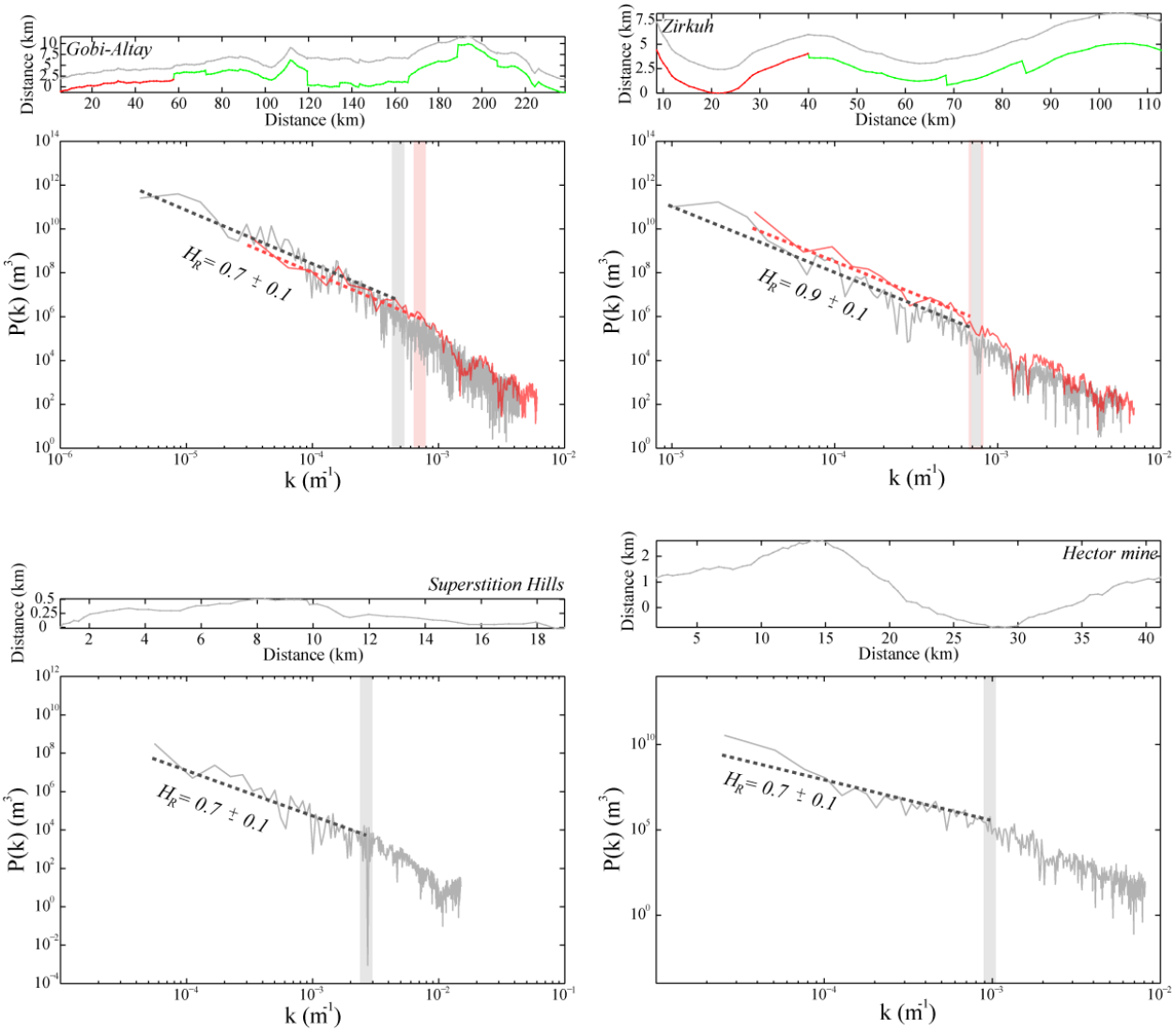

Figure 3.13. *Compilation of the surface rupture roughness results: Digitized rupture traces (top) and corresponding Fourier power spectrum (bottom). Because of the abrupt steps biasing the Fourier transform computation, we have performed this roughness analysis on one segment (colored in red) between two steps of the whole profile (in green). In addition, the gray profile and the gray Fourier power spectrum corresponding represent a reconstruction of the entire profile. Power-law fits and the inferred Hurst exponents on the linear part of each curves at large scale (above the cross-over length scale) are represented on each graph. Note here that for each rupture trace, the curves corresponding respectively to the selected segments and the reconstructed profiles both follow a similar self-affine regime as seen on Figure 3.12.*

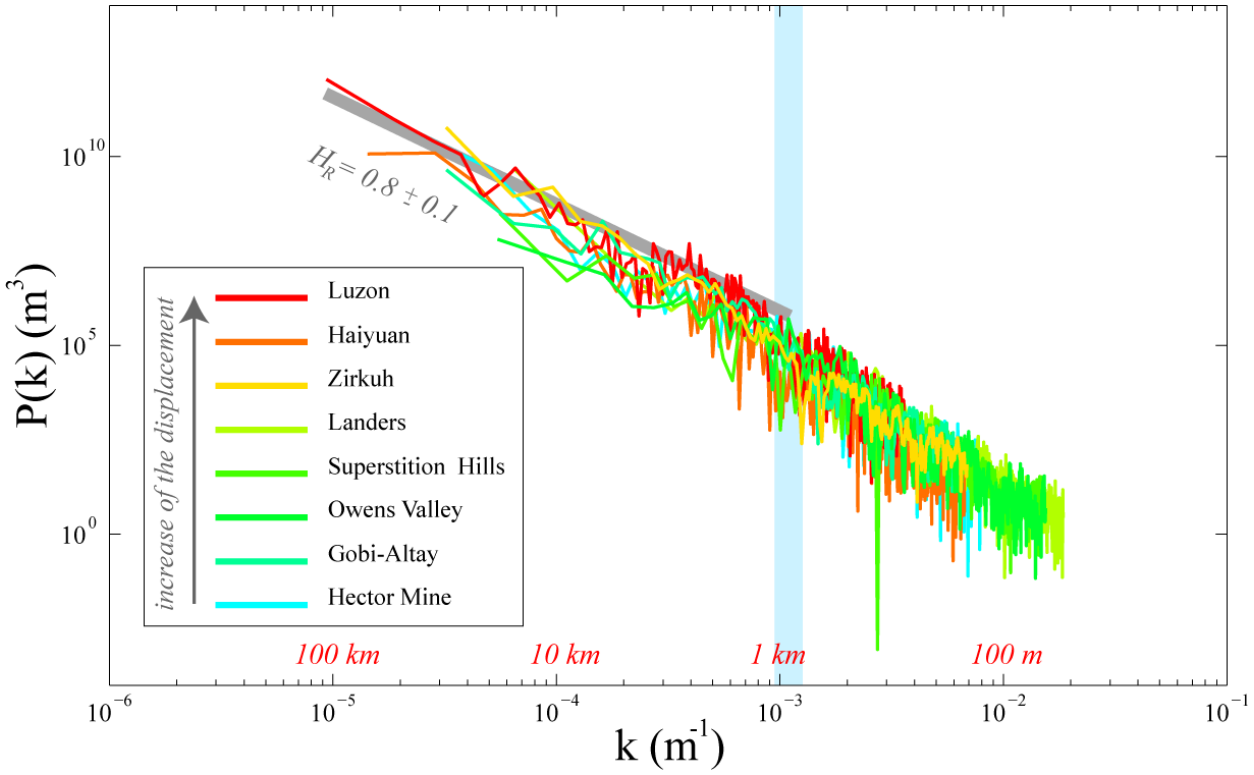

Figure 3.14. *Variability of the pre-factor and roughness amplitude. A: Stack of all the Fourier power spectra of selected segments or the whole surface ruptures stacked (called "Segment 1" in Table 3.2), underlining the global trend of the self-affine behavior at large scale. Power-law fit giving an average Hurst exponent of* 0.8 ± 0.1 *is indicated. Variability of the vertical position, i.e. the pre-factor, between each curve is not correlated with the slip accumulated.*

3.2.5. Discussion

3.2.5. A. No evidence of characteristic length scale

In self-affine models only two parameters are needed, the Hurst exponent and the pre-factor, to describe how the *RMS* of the fault surface roughness scales in one direction. In this section, we focus on the Hurst exponent, directly related to the slope of the Fourier spectrum.

Previous studies on natural fault surfaces have shown that the slope of the Fourier spectrum could change from large to small scales (e.g. Lee and Bruhn, 1996) highlighting that different processes may be involved during the generation of surface fault textures at different spatial scales. In fact, any inflexion of the spectrum would correspond to a characteristic scale and

would often be interpreted as the transition between physical processes. Lee and Bruhn (1996) observed several characteristic length scales between $1\,mm$ and several meters and attributed them to a combination of frictional ploughing, secondary fracturing, and intersections between anastomosing fractures along sliding surfaces. At length scales greater than several meters, roughness would reflect the process of lateral growth and linking of several fault surfaces. However, such conclusions were based on $1D$ profilometry data that sampled only punctual information along the whole fault.

In the present study, five fault surfaces in different geological settings have been scanned with three independent scanner apparatuses. Our analysis of the spatial correlations of the fault surface roughness is based on robust and consistent data, providing a global geometrical model for the five fault surfaces scanned. An unique anisotropic mono-affine geometric model, for the five faults, characterized by two different global Hurst exponents $H_{//} = 0.6$ and $H_{\perp} = 0.8$ best fits the entire data set between $30\,m$ and $0.05\,mm$. No significant deviation from this global trend could be determined for each cloud of points (see Table 3.1 and Figure 3.7, 3.8). All Hurst exponents extracted from the whole set of fault surfaces fall within a two standard deviations of their distribution. This last observation demonstrates that this simple geometrical model is robust and the existence of several regimes bounded by characteristic scales could be excluded between $30\,m$ to $0.05\,mm$.

3.2.5. B. Variability of the Hurst exponent between scanned fault surfaces and rupture traces

The rupture trace geometry of strike-slip earthquakes should correspond to the continuity at the kilometer scale of the fault surface roughness sampled on fault scarps along the slip direction. However, our results highlight a small difference in the Hurst exponents of the eight ruptures traces compared to the average trend in slip direction of the five fault surfaces scanned. The spatial correlations of the rupture trace irregularities are characterized by a roughness exponent value of 0.8 ± 0.1, close to that in the direction perpendicular to slip, collected on the five fault surfaces scanned. We propose that the roughness increase at the rupture trace scale is due to the fact that the slip direction is not strictly sampled as it is the case for fault surfaces scanned. Slip

distributions of strike-slip earthquakes show that at some locations a vertical component could be significant (as for example the Gobi-Altay earthquake, Florensov and Solenko, 1965; Kurushin *et al.*, 1997). Therefore, at the surface rupture scale, a slight vertical slip component along the whole rupture trace of the strike-slip earthquake would explain that we sample a roughness oblique to the slip direction. This assumption is verified on Figure 3.15. The Hurst exponents of synthetic anisotropic self-affine surface ($RMS = 0.01L^{0.6}$ in slip direction and $RMS = 0.02L^{0.8}$ normal to it) were calculated on series of 1D profiles extracted at an angle θ from the slip direction. The same procedure was performed on a patch of the Corona Heights fault scanned (Corona-A in Table 3.1). A clear similarity is observed in the angular variability of the roughness exponent computed for the synthetic surface and the natural fault patch (considered as representative of our set of fault surfaces). Both surfaces expose the same non-linear dependence of the Hurst exponent with the azimuthal direction of profile extraction (θ). When departing a few degrees from the direction of the smallest exponent, i.e. the slip direction, the Hurst exponent sampled is already very close to the largest exponent, i.e. the direction normal to slip (Figure 3.15). This effect could explain the slight difference in the roughness exponents observed between the surfaces ruptures and along slip fault surface scanned.

Moreover, the traces of the ruptures show a structural complexity underlined by relay zones (compressive and extensive jogs), and bends, which could locally accommodate a significant vertical component at many locations along the fault (Klinger et al., 2006). In this case, the ruptures traces morphology would correspond to a combination of topography along slip direction and normal to it, which might partially explain the increase of the measured Hurst exponent compared to that of along slip fault surface scanned.

Finally, we suspect that no characteristic length scale is present in the gap of explored length scales between fault surfaces scanned and ruptures traces. We therefore propose that the global self-affine regime observed at the outcrop scale is maintained at the kilometer scale of earthquakes ruptures traces.

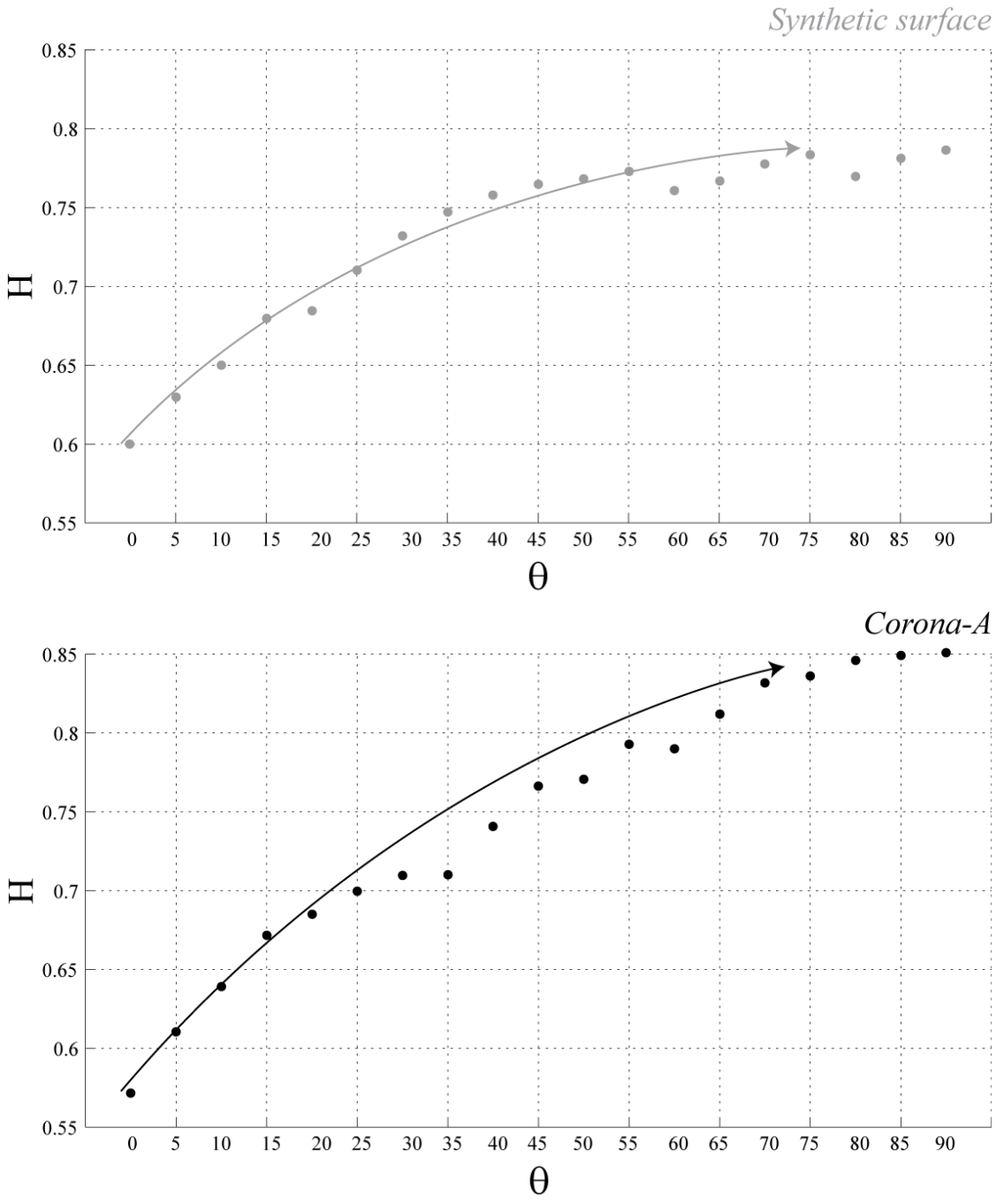

Figure 3.15. *Angular dependence of the Hurst exponent. Top: Hurst exponents computed on a synthetic anisotropic self-affine surface with two input exponents in perpendicular directions ($H_{//} = 0.6$ and $H_{\perp} = 0.8$). The Hurst exponents were calculated on series of $1D$ profiles extracted at an angle θ between the slip direction ($\theta = 0$) and the perpendicular direction ($\theta = 90$). Bottom: Angular variability*

of the roughness exponent computed for a patch (Corona-A, see Table 3.1) scanned with the LiDAR on the Corona Heights fault surface. Both surfaces expose the same non-linear dependence of the Hurst exponent with the azimuthal direction of profiles (θ).

3.2.5. C. Pre-factor variability independent of displacement

Even if our results illustrate that the spatial correlations of fault surface topography can be described by a unique self-affine exponent along the slip direction and perpendicular to it, a large variability in the pre-factor is observed in both data sets, fault surfaces and ruptures traces. In this paragraph, we attempt to decipher if this variability could be related to difference in the total slip accommodated.

Faults surfaces scanned

Faults zone are constituted by several multi-scale discrete slip segments. A tempting explanation of the variability of the pre-factor within a same fault surface is that the finite displacement accumulated by rougher fault patches (or segments) is smaller than for the smoother fault patches (Power *et al.*, 1987, Power and Tullis, 1989). For this assumption, abrasion process could explain the polishing of individual fault patch roughness in order to maintain a spatially stable Hurst exponent but various pre-factors (Figure 3.9). Following this reasoning, it is likely that the spatial heterogeneities on the pre-factor illustrated in Figure 3.9 highlights variable accumulated displacement (probably much less important than the total offset recorded by the fault zone) on each individual segments (or fault patches) constituting the whole fault zone. However as underlined by Power and Tullis (1989), this possibility is difficult to quantify because the total displacement for subparallel individual surfaces (which represent a part of the total offset of the fault zone) cannot be observed with certainty in the field. Alternate explanations for the difference in surface characteristics (Figure 3.9) would include formation of the individual fault patches at different depths, confining pressure, temperatures, or strain rate.

Sagy *et al.* (2007), selecting systematically the smoothest fault patches from each fault, have observed an evolution of its geometry in function of the slip accumulated for the whole fault zone. However, the range of pre-factor estimated in the work of Sagy *et al.* (2007) to discriminate between a large-slip and small-slip fault falls in the range of variability observed in

our study for the individual fault patches scanned on one individual fault surface (Figure 3.9). In addition, in Figure 3.7, each spectrum at each scale (LiDAR, Laser profilometer, WLI) represents an average of the spectra computed from multiple fault patches with different pre-factors but similar slope. Consequently, each spectrum provides an average of the roughness over the whole surface, and no clear relationship is observed between this last global roughness and the total slip estimated for the whole fault zone.

Other recent studies have noted changes in fault roughness and damage parameters as a function of maturity for faults spanning a range of offsets shifted from the dataset here (Sagy *et al*., 2007; Mitchell and Faulkner, 2009; Savage and Brodsky, 2011; Brodsky *et al*., 2011). Sagy *et al.* (2007) noted a difference in faults that slip more than 10 m versus those that slip less than 1 m. The fault roughness data presented here is for offsets that are within the mature population by these criteria. The lack of a discernible evolution signal is consistent with the suite of data in Brodsky *et al.* (2011) that also shows that smoothing is a very weak process.

Earthquakes rupture traces

Another important information of our roughness scaling analysis is that no correlation was observed between the finite displacement by the whole fault zone hosting the rupture trace and the roughness of this last one (see section 3.2.4.D). This observation is consistent with the work of Klinger (2010), who showed that the correlation between the characteristic fault segment length and the thickness of the seismogenic crust, is maintained, independently of the total slip accumulated. In addition, we suggest in this study that a coherent spatial organization persists over the entire range of length scales accessible (i.e. from hundred meters to ~ 50 km, see Figure 3.14), independently of the total geological offset. Note here that in following the reasoning of Klinger (2010), a specific length scale should appear at approximately 20 km (i.e. the thickness of the seismogenic crust). However, because of the lack of sufficient frequency content between 20 km and 50 km, this probable characteristic length scale is not clearly revealed by our analysis. Similarly, rupture trace data presented here covers an even greater scale of offsets that are well within the mature zone based on both the roughness and damage studies see a change in behavior about ~150 m offset (Savage and Brodsky, 2010).

Smoothing of fault geometry has been suggested by other studies (Wesnousky, 1988; Manighetti *et al.*, 2007), and is thought to result from surface roughness of faults being inversely related to their total displacement. Such smoothing of a fault trace, however, is mainly concerned for large scale geometrical asperities, such as step-overs of several kilometers. In our study, given that we remove these first-orders geometric discontinuities to perform our Fourier transform analysis, we lose these hallmarks of the fault maturity.

The notion of "geometric regularization" or "maturity" refers to the intuitive idea that the fault zone simplifies itself by abandoning or smoothing the complexity of the initial structures (segments) during the successive slip. Ben-Zion and Sammis (2003) recommend that it is necessary to separate the abandoned structural units of those which actively participate in the accommodation of the slip to reveal a possible regularization of the geometry of the fault zone with slip. It is therefore necessary to emphasize that both the fault scarps scanned on the field and the rupture traces are markers of the morphology of the actives structures of fault zone. Our results thus demonstrate that the active portions of faults from the spatial scale of microns up to at least the thickness of the seismogenic crust preserve a complex geometry during successive displacements. In other words, the complexity of active fault surface is maintained regardless of the accumulated displacement, and more precisely it is spatially organize following a simple self-affine geometrical model independently to the lithology and to the tectonic regime. Our observations suggest that a re-roughening mechanism is active in the fault zone to maintain the geometrical complexity during the successive slips (Brodsky *et al.*, 2011). As suggested by Klinger (2010), during the rupture propagation, processes related to branching and preexisting secondary faults (Poliakov *et al.*, 2002; Bhat *et al.*, 2004), could explain the persistent of some level of complexity and prevent the complete smoothing of the fault geometry.

3.2.6. Conclusion

The roughness properties of fault surfaces over nine decades of length scales (between $0.05\,mm$ and at least the thickness of the seismogenic crust, i.e. ~20 km) is displayed on Figure 3.16, where the Fourier power spectra of the Corona Heights fault surfaces along the slip direction and the spectra obtained for the continental earthquake surface ruptures are plotted together.

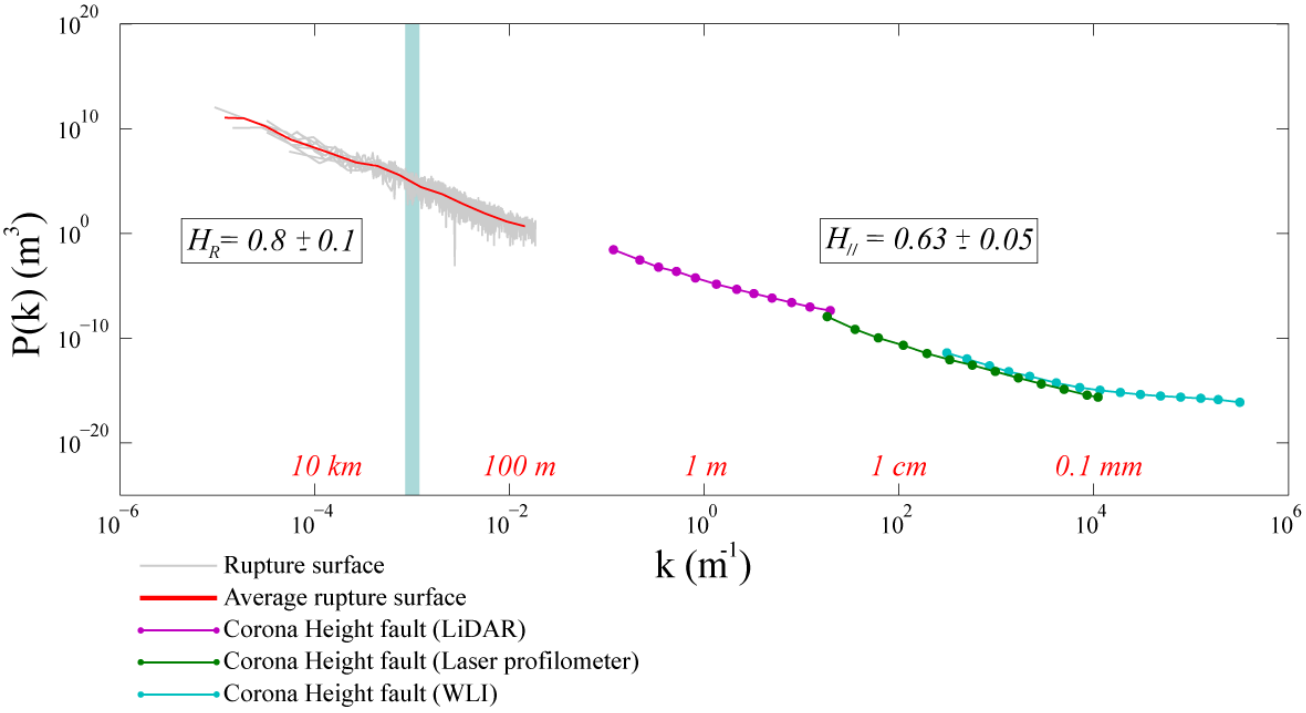

Figure 3.16. *Comparison of the roughness of the earthquakes surface ruptures with the Corona Heights fault topography. The Fourier power spectra along the slip direction of the Corona Heights fault surface are plotted on a log-log graph together with those obtained for the eight continental strike-slip earthquakes surface rupture traces. The Corona Heights fault data (purple, green, blue curves) are identical to those plotted on Figure 3.7, and those of the surface ruptures (gray curves) correspond to that of Figure 3.14. The red curve is an average of the spectra calculated for all data presented in Figure 3.14. Both Hurst exponents defining the self-affine regime in the range of scales sampled by the rupture traces (between* $50\,km$ *and approximately* $1\,km$*, i.e. above the blue vertical bar marking the beginning of the regime controlled by the data re-sampling) and that in the range of scales (between* $30\,m$ *and* $0.05\,mm$*) sampled by the scanners devices, are indicated.*

The overall picture indicates that a single anisotropic self-affine model ($H_{//} = 0.6$ and $H_{\perp} = 0.8$) is maintained over nine decades of length scales whatever the geological setting. In addition, even if in both cases, for the scanned fault surfaces and the ruptures traces, we have focused our analysis on the active portion of the fault zone, it appears that once a small amount of offset has been achieved, their geometric complexity is maintained regardless of whatever further slip is accommodated.

Acknowledgments: This study was supported by the *Agence Nationale pour la Recherche* grant ANR-JCJC-0011-01. Field work was supported in part by NSF Grant EAR-0711575. The authors are very grateful to Michel Bouchon for encouragements and scientific stimulations. The first authors gratefully acknowledge Andy Rathbun for his constructive comments that helped to improve the content and clarity of the manuscript.

3.2.7. Appendix 3.A

3.2.7. A. Potential bias in the roughness data

Reliability of the roughness results at the LiDAR scale: effect on the noise in the acquisition system

Before analyzing the main biases inherent to LiDAR data acquisition, we emphasize that raw scanner data acquired with the home-made laser profilometer are considered as quasi-ideal and noise free (a detailed description of the conditions in which measurements with this scanner device departs from the reality is given by Méheust, 2002), given access to an accurate estimation of the roughness scaling properties of the fault plane in the whole large range of length scales accessible with this scanner device (between $20\,\mu m$ and $10\,cm$). In addition, the slope of the spectra computed on WLI scans at scales higher than $0.05\,mm$, are consistent with those of laser profilometry for the same range of length scales (see Figure 3.5). This observation shows that an anisotropic mono-affine geometric model describes consistently both field and laboratory measurements over range of scales from 0.05 mm to 30 m and demonstrates the consistency of measurements carried out with these different devices.

In the spirit of the work of Schmittbuhl *et al.* (1995) on the reliability of a self-affine measurement on $1D$ rough profile, Candela *et al.* (2009) have reviewed different statistical methodologies which allowed the assessment and characterization of the anisotropic self-affine behavior of fault topography. This work was mainly devoted to precisely define the intrinsic error of the statistical methods (as the Fourier power spectrum) to estimate the scaling properties of fault surface roughness.

Here, a new test is performed by taking into account the error encountered in the spatial position (X,Y,Z) of each points measured by the $3D$ laser scanner. We used a synthetic anisotropic self-affine surface (Figure 3.A1) of $5\times5\,m$ with an original regular point spacing of $0.5\,cm$, and with two different Hurst exponents in perpendicular direction ($H_{//}=0.6$ and $H_{\perp}=0.8$). In order to simulate the error inherent to LiDAR data acquisition on the spatial position of each points (X,Y,Z), we added a Gaussian white noise with a distribution $[0, 0.25cm]$ on the original position of each points, to obtain the disturbed grid (X^1,Y^1,Z).

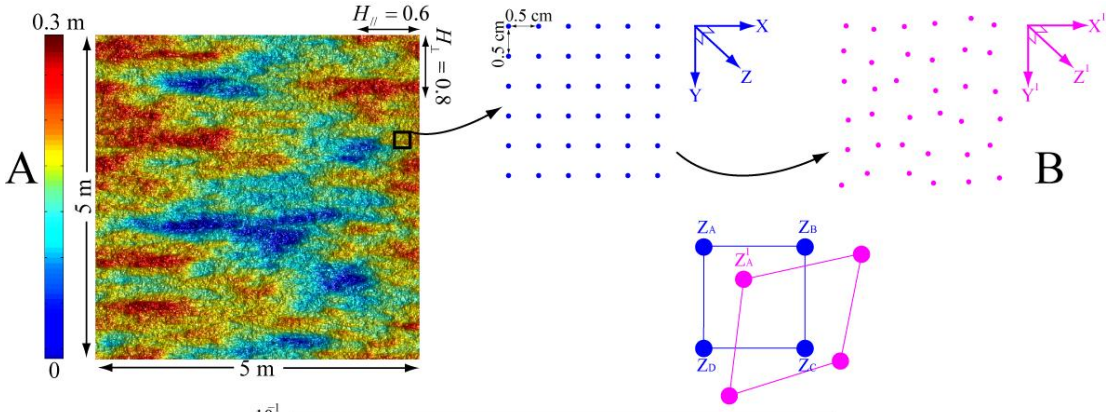
A
0.3 m
0
5 m
5 m
$H_{//} = 0.6$
$H_{\perp} = 0.8$
0.5 cm
0.5 cm
X
Z
Y
X^1
Z^1
Y^1
B
Z_A
Z_B
Z_A^1
Z_D
Z_C

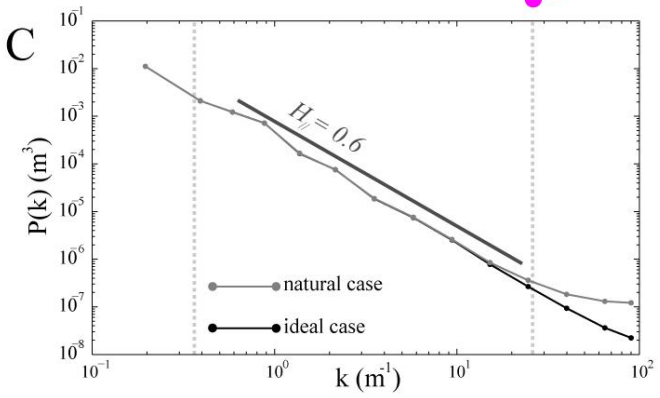
C
P(k) (m^3)
k (m^{-1})
$H_{//} = 0.6$
natural case
ideal case

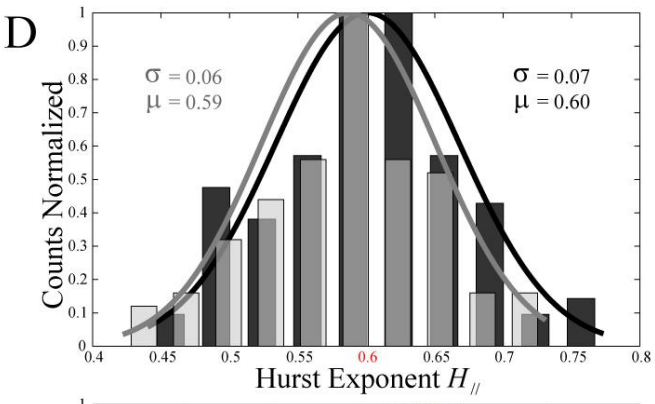
D
σ = 0.06
μ = 0.59
σ = 0.07
μ = 0.60
Counts Normalized
Hurst Exponent $H_{//}$

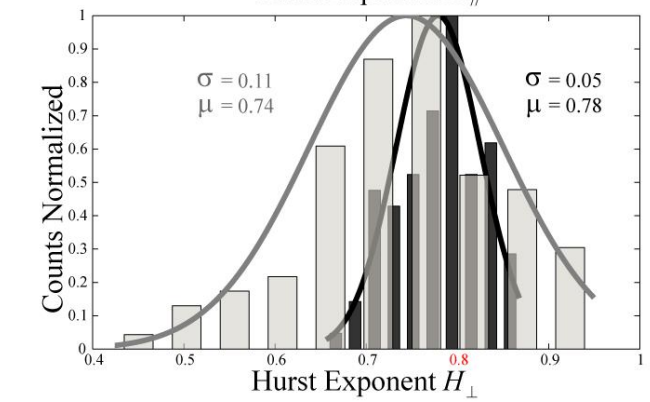
σ = 0.11
μ = 0.74
σ = 0.05
μ = 0.78
Counts Normalized
Hurst Exponent $H_{\perp}$

Figure 3.A1. *Effect of noise inherent to LiDAR data acquisition. A: Ideal synthetic* $5\times5\,m$ *self-affine surface with an original regular point spacing of* $0.5\,cm$. *B: Illustration of the addition of a noise in the regularly spaced original grid* (X,Y,Z). *To obtain the disturbed grid* (X^1,Y^1,Z^1). *A Gaussian white noise with a distribution* $[0,0.25cm]$ *was added to the X and Y coordinates. The new height of each points, for example* $Z^1{}_A$, *is computed by interpolating with the original height of the four nearest points* (Z_A,Z_B,Z_C,Z_D). *Finally, we add a Gaussian white noise with a standard deviation of* $0.5cm$ *to Z coordinates. C: Comparison of the Fourier power spectra in direction of slip obtained for the ideal synthetic surface and the noisy synthetic surface. Both vertical dashed grey lines indicate limits taken for fitting the Hurst exponent. D: Distribution of measured Hurst exponents, on* 100 *simulations, for the direction of slip and perpendicular to it. Black bars show the ideal simulated fault surface models, and the gray ones correspond to the noisy simulated fault surface models. The solid lines (black for the ideal case and gray for the natural case) represent the fits of the measurements to a normal distribution with mean* μ *and standard deviation* σ *given at the top left for the noisy natural case and the top right for the noise-free case.*

Then the height Z^1 of each points at these new positions (X^1,Y^1) are computed by interpolating (bilinear interpolation) the four nearest points of each of these new positions on the original ideal model (Figure 3.A1). In a final step, a Gaussian white noise, with a standard deviation equal to $0.5\,cm$, is randomly added on the interpolated heights Z^1, to yield the error of the LiDAR data in the vertical position.

After generated this noisy cloud of points (X^1,Y^1,Z^1), we extracted profiles oriented along slip direction and perpendicular to it as done for the measurements, and estimated both Hurst exponents. The results are then averaged over 100 realizations of synthetic surfaces. Due to the noise, the Fourier power spectra flatten at short length scales (as for examples in the slip direction shown in Figure 3.A1), which results into a slight underestimation of the Hurst exponents. For both directions, along slip and perpendicular to it, we find that the median estimates of $H_{//}$ and $H_{\perp}$ of the biased synthetic surfaces are 0.59 ± 0.06 and 0.74 ± 0.11 respectively, compared to the noise-free data where the Hurst exponents were 0.6 ± 0.07 and 0.78 ± 0.05, respectively. Note that the error bar of the estimated Hurst exponent of the biased

synthetic surfaces is approximately twice larger in direction perpendicular to slip relatively to that in the slip direction. In both directions, even if the Hurst is slightly underestimated for the noisy data, its value is still included in the range given by the standard deviation of the noise-free data. Therefore, the noise in the LiDAR data could be estimated as well as the reliability of Hurst exponent values.

Reliability of the roughness results at surface rupture scale: effect of re-sampling

For each earthquake, once the surface rupture map has been digitized, the data set are re-sampled to a regular spacing to ensure consistent spatial sampling, independent of the length of each rupture. This re-sampling is performed to avoid bias due to local wiggles of the rupture trace (Klinger, 2010). We verified here how this re-sampling process affects the Fourier transform. The original digitized rupture trace of the Hector mine earthquake, taken as example is re-sampled with various constant values of δx in the range 60-620 m (Figure 3.A2). On the Fourier power spectra of this set of digitized rupture traces, two regimes can be observed. At small scales, i.e., large wave numbers, (between approximately $120\,m$ and $1200\,m$) the behavior can be attributed to data re-sampling. At large scales, i.e. small wave numbers (above $1200\,m$), a power law giving a Hurst exponent $H_R = 0.74$ represents the best fit. The cross-over length scale of the two regimes corresponds to the maximum spacing between two points in the original data. Whatever the value of δx taken for re-sampling the data, the cross-over length scale remains at the same position. The regime at large scales, characterizing roughness properties of the digitized ruptures traces is therefore not affected by data re-sampling; both the slope and the pre-factor of each spectrum being identical (Figure 3.A2).

The same re-sampling procedure has been performed on ideal synthetic self-affine profiles in order to precisely define if the scaling property could be modified (Figure 3.A3). An original self-affine profile ($RMS = 0.01 L^{0.6}$) with regular spacing point of $500\,m$ and a total length of $100\,km$ (extracted from a synthetic surface as previously presented), is disturbed by adding to the X coordinates a Gaussian white noise with a distribution $[0,250\,m]$ (Figure 3.A3). This altered profile is re-sampled with different values of δx in the range [40-350] m. The Fourier spectra (Figure 3.A3) indicates that for the different values of δx, the large scale regime (above

750 m) characterizing the input self-affine behavior with a Hurst exponent of 0.6 is not biased. This test validates that the re-sampling procedure makes it possible to keep the scaling information of the rupture traces at spatial scales above 1200 m.

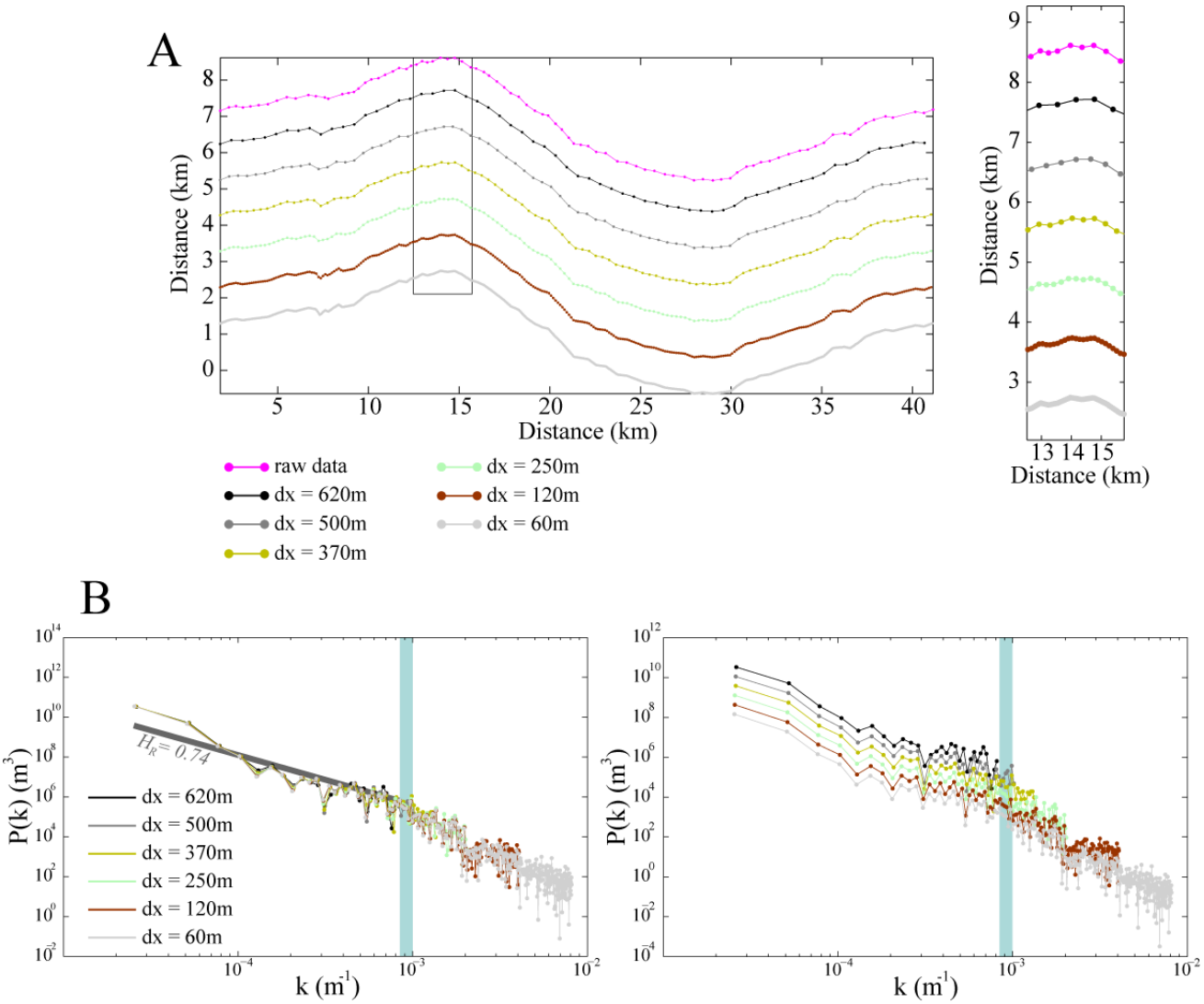

Figure 3.A2. *Effect of re-sampling on surface rupture roughness: example of Hector Mine earthquake. A: Digitized surface rupture traces of the Hector Mine earthquake. The original rupture map with an irregular point spacing (pink profile) is re-sampled in order to ensure consistent spatial sampling with a regular spacing* (δx). *The inset indicate the position of the zoom located on the right, showing the irregular point spacing on the top and the gradual increase of the re-sampling (or decreasing of* δx*) with*

a regular point spacing of profiles downwards. B: Fourier power spectra of the digitized rupture traces shown in A. Spectra colors are the same than in A. On the right: the spectra have been shifted vertically to improve the visibility. The blue vertical bar on both graphs highlights the cross-over length scale, at approximately $1200\,m$*, between both regimes, one below, attributed to data re-sampling, and that above, characterizing roughness properties of the digitized with a Hurst exponent* $H_R = 0.74$.

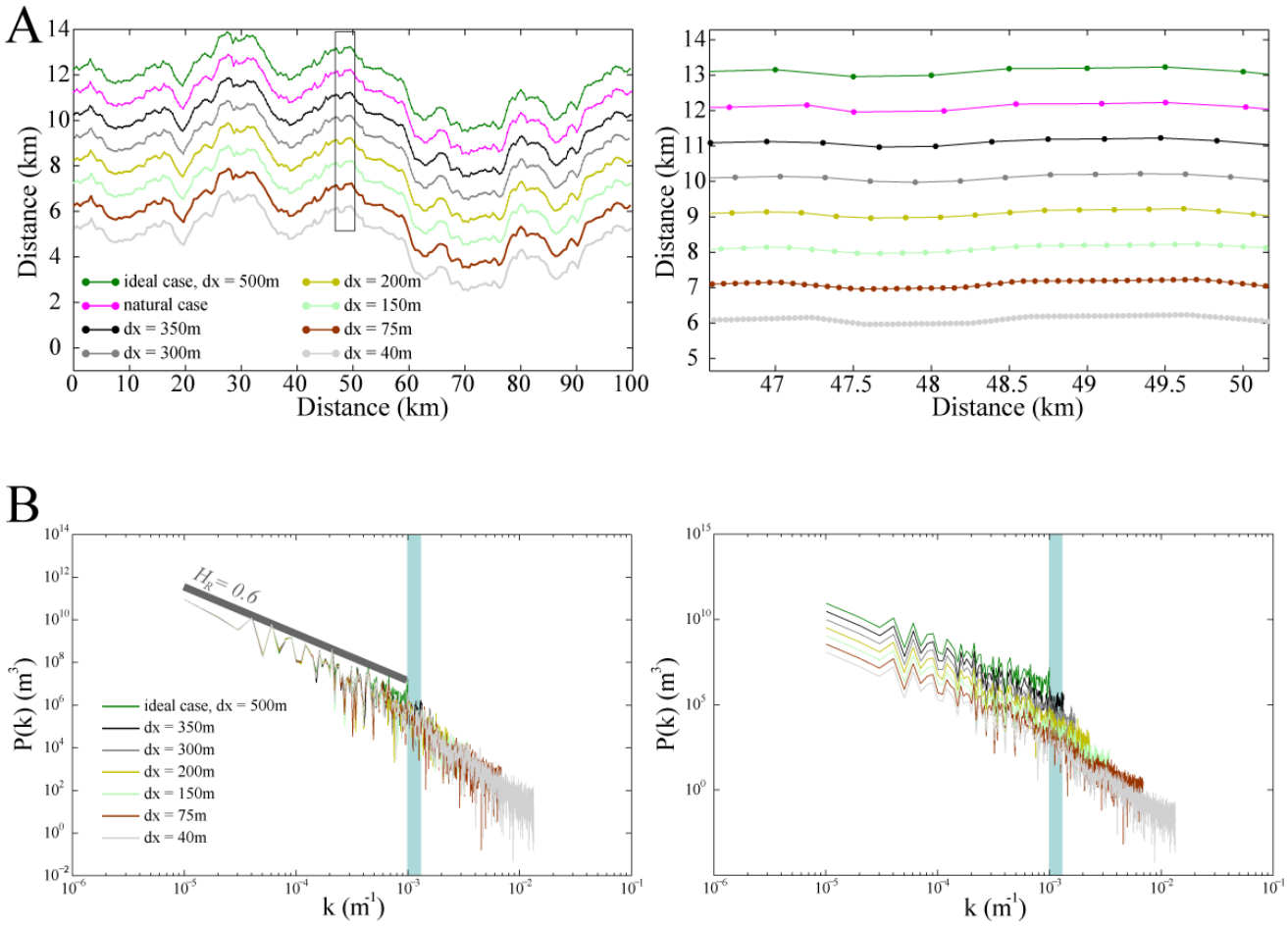

Figure 3.A3. *Effect of re-sampling on synthetic self-affine profiles. A: Example of synthetic rough profiles with a standard deviation that scales as* $RMS = 0.01\,L^{0.6}$*, analogue of digitized surface rupture traces. The green profile at the top of the left figure is the original ideal synthetic profile with a regular point spacing* δx *of* $500\,m$*. A Gaussian white noise with a distribution* $[0, 250\,m]$ *is added randomly on the original regular spacing to obtain a noisy profile (pink curve) similar to that of original ruptures*

maps. This noisy synthetic profile with irregular point spacing is re-sampled with a regular spacing δx. *The inset zooms on the synthetic profiles located on the right. B: Fourier power spectra of the synthetic self-affine profiles shown in A. Colors of each curves correspond to those of profiles. On the right: the spectra have been shifted vertically to improve the visibility.*

Chapter 4:

Fault slip distribution and fault roughness

4.1. Chapter 4 overview (Présentation du Chapitre 4)

4.1.1. Introduction

Dans ce chapitre, je présente un article soumis à la revue *Geophysical Journal Internationale*. Cette étude vise à démontrer le lien, souvent pressenti mais jamais clairement établi, entre la rugosité 3-D des failles et la distribution spatiale 2-D du glissement après un tremblement de terre.

4.1.2. Presentations at international meetings

2010, American Geophysical Union, Fall meeting, San Francisco (USA):

Candela, T., Renard, F., Bouchon, M., Schmittbuhl, J., and Brodsky, E., Self-affine fault surface roughness: implications for the slip distribution and the amount of static stress drop after an earthquake. Abstract S54A-03.

4.1.3. Contributors to Chapter 4

J'ai personnellement mis en place la conception de l'approche suivie dans cette étude. Le modèle numérique de propagation quasi-statique d'une rupture a été initialement élaboré par Perfettini *et al.* (2001), puis adapté pour cette étude par J. Schmittbuhl. Les mesures topographiques de la faille de Corona Height (San Francisco) ont été acquises sur le terrain par E.E. Brodsky, F. Renard et moi-même. En laboratoire, l'acquisition des mesures de rugosité des échantillons des surfaces de failles ont été effectués par moi-même en collaboration avec J. Schmittbuhl (à l'institut de physique du globe de Strasbourg) et K. Mair (au laboratoire de « Physics of Geological Processes »).

4.2. Fault slip distribution and fault roughness

Thibault Candela,[1] François Renard,[1,2] Jean Schmittbuhl,[3] Michel Bouchon,[1] and Emily E. Brodsky [4]

[1]ISTerre, CNRS, University Joseph Fourier - Grenoble I, OSUG, BP 53, 38041 Grenoble, France. E-mail: Thibault.Candela@ujf-grenoble.fr; francois.renard@ujf-grenoble.fr

[2]Physics of Geological Processes, University of Oslo, Oslo, Norway.

[3]UMR 7516, Institut de Physique du Globe de Strasbourg, Strasbourg, France. E-mail: Jean.Schmittbuhl@eost.u-strasbg.fr

Grenoble I, Grenoble, France. E-mail: Michel.Bouchon@ujf-grenoble.fr

[4]Department of Earth and Planetary Sciences, University of California–Santa Cruz, Santa Cruz, California 95064, USA. E-mail: ebrodsky@es.usc.edu

Abstract

We present analysis of the spatial correlations of seismological slip maps and fault topography roughness, illuminating their identical self-affine property. Though the complexity of the coseismic spatial slip distribution can be intuitively associated with geometrical or stress heterogeneities along the fault surface, this has never been demonstrated. Based on new measurements of fault surface topography and on statistical analyses of kinematic inversions of slip maps, we propose a model which quantitatively characterizes the link between slip distribution and fault surface roughness. Our approach can be divided into two complementary steps: (i) Using a numerical computation, we estimate the influence of fault roughness on the frictional strength (pre-stress). We model a fault as a rough interface where elastic asperities are squeezed. Our results suggest that pre-stress dominates the dynamical stress produced during earthquakes. The Hurst exponent H_τ, characterizing the self-affinity of the frictional strength field, approaches $H_\tau = H_{//} - 1$, where $H_{//}$ is the roughness exponent of the fault surface in the direction of slip. (ii) Using a quasi-static model of fault propagation, which includes the effect of

long range elastic interactions and spatial correlations in the frictional strength, the spatial slip correlation is observed to scale as $H_s = H_\tau + 1$, where H_s represents the Hurst exponent of the slip distribution. Under the assumption that the origin of the spatial fluctuations in frictional strength along faults is the elastic squeeze of fault asperities, we show that self-affine geometrical properties of fault surface roughness control slip correlations and that $H_s = H_{//}$. Given that $H_{//} = 0.6$ for a wide range of faults (various accumulated displacement, host rock, and slip movement), we predict that $H_s = 0.6$. Even if our quasi-static fault model is more relevant for creeping faults, the spatial slip correlations observed are consistent with those of seismological slip maps. A consequence is that the self-affinity property of slip roughness may be explained by fault geometry without considering dynamical effects produced during an earthquake.

4.2.1. Introduction

The increasing resolution of near field strong ground motion records gives now a clear evidence of the spatio-temporal complexity of the rupture process. Even if different kinematic inversions for the same earthquake show discrepancies, images of the spatial and temporal evolution of coseismic slip on fault planes provide compelling evidence that fault displacement is spatially variable at all resolvable scales (Mai and Beroza, 2002; Lavallee and Archuleta, 2005). Seismic sources have been shown to present large heterogeneities in the coseismic slip and the rupture velocity (Archuleta, 1984; Brune, 1991; Cotton and Campillo, 1995). The origin of this complexity is still poorly understood and often explained as generated by a combination of incorrect mapping of rupture variability into the slip distribution as well as the geometric irregularity of the fault surface or compositional heterogeneities (Mai and Beroza, 2002).

In addition, in their extended analysis of spatial correlations of slip maps for 44 earthquakes, Mai and Beroza (2002) found that the heterogeneous slip distribution follows a self-affine regime characterized by an average value of the slip roughness exponent close to those of recent statistical scaling analyses of high resolution topography measurements of natural fault surfaces (Renard *et al.*, 2006; Candela *et al.*, 2009). Even if this similar geometrical complexity between slip maps and natural fault surfaces may suggest that both are associated, whether the observed

slip patterns may reflect the underlying frictional or geometrical properties of the fault, or whether these are separate effects, remains to be addressed. The aim of this work is to propose an approach which demonstrates that a controlling parameter of the spatial slip correlations is related to the scaling properties of the topography of the slip surface (*i.e.* fault roughness).

In the following, we present new analysis of the spatial correlations of seismological slip maps (section 4.2.2) and new data of fault surface roughness (section 4.2.3), illuminating their identical self-affine property. In section 4.2.4, we present our model which can be divided in two parts. Firstly we link the shear strength field distribution (pre-stress) to the roughness of the fault plane using a numerical computation of the transformation of fault asperities (including the broad range of asperity size as suggested by the self-affine property of natural fault surfaces) when submitted to a normal load. Only elastic deformation of the topography is considered, which is dominant at large scales, while the friction coefficient is held constant (i.e. Coulomb criterion). Secondly, using a quasi-static numerical model of fault propagation, which includes the effects of long range elastic interactions, we study the influence of the shear strength field distribution, provided by the first step of our model, on the resulting slip distribution. Finally, we compare our numerical slip distribution with that of seismological slip maps on active faults.

4.2.2. Self-affine correlations of seismological slip fields

Let first recall some definitions related to the scaling properties of a rough signal. A self-affine 1-D profile (Figure 4.1) remains unchanged under the scaling transformation $\delta x \to \lambda \delta x, \delta z \to \lambda^H \delta z$ (Meakin, 1998). Here, δx is the coordinate along the 1D profile and δz is the slip or roughness amplitude in the framework of our study. For a self-affine profile, the scaling exponent H, also called Hurst exponent (or roughness exponent), lies in the range $0 \le H \le 1$. In the particular case where $H = 1$, the profile is called self-similar. Accordingly, if a profile obeys to a self-similar description, a small portion of the profile, when magnified isotropically, has a statistically identical appearance to a larger part of the profile. Conversely, if a profile is best fit with a self-affine model, different magnification factors will be needed for the directions parallel and perpendicular to the profile for a small portion of the profile to appear statistically similar to the entire profile (Figure 4.1). As a consequence the large-scale slope

along a profile scales as $s = \delta z / \delta x \propto \delta x^{H-1}$ (Schmittbuhl *et al*, 1995). Accordingly, as opposed to self-similar surfaces, a self-affine profile is flatter at large scales but still includes a large variety of amplitudes of small scale asperities.

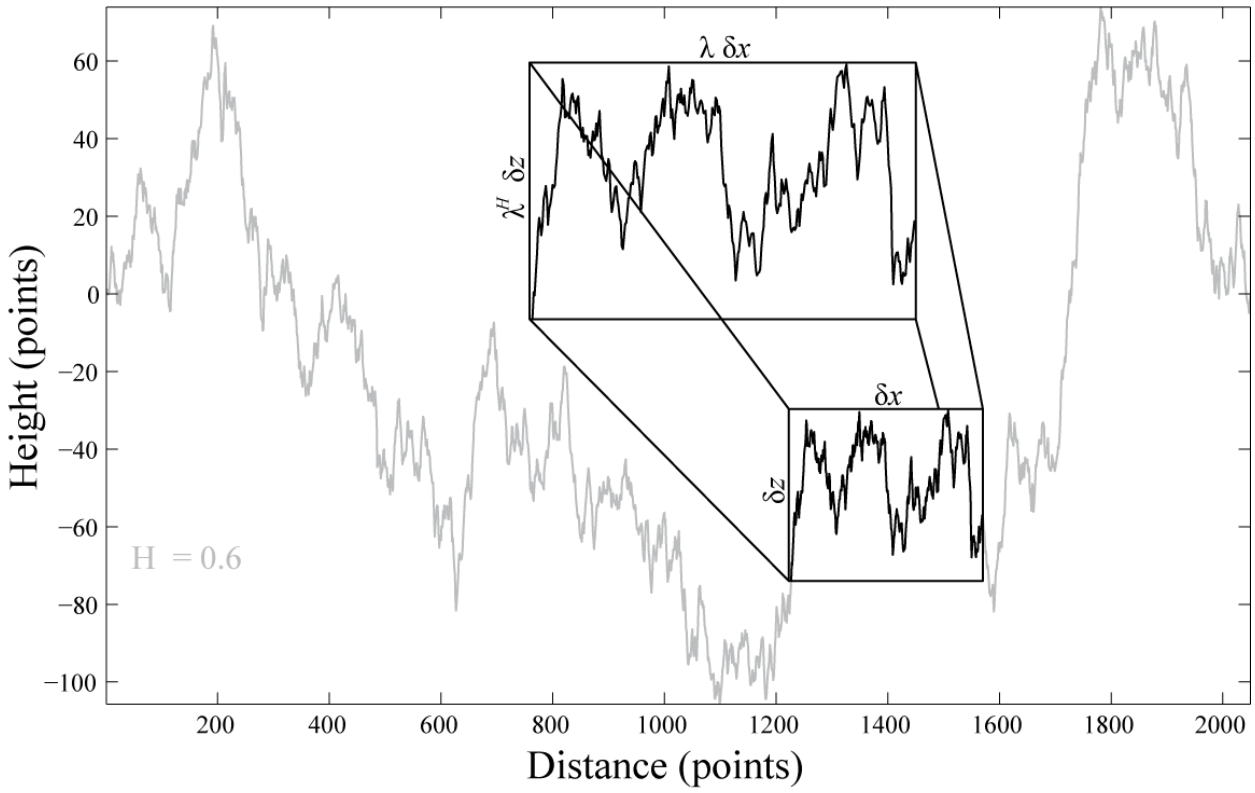

Figure 4.1. *Representative 1-D synthetic self-affine profile computed with a Hurst exponent equal to* 0.6. *We used a Fourier based method to simulate the self-affine profile, as performed by Candela et al. (2009). Inset: magnified portion of the profile, which has a statistically similar appearance to the entire profile when using the rescaling transformation* $\delta x \to \lambda \delta x, \delta z \to \lambda^H \delta z$.

Theoretical studies of extended source earthquake models describe heterogeneous slip distributions on fault planes (Andrews, 1980; Frankel, 1991; Herrero and Bernard, 1994) following a self-similar behavior characterized by $H_s = 1$, with H_s the Hurst exponent of the spatial distribution. However, in their extended analysis of spatial correlations of slip maps for 44 earthquakes, Mai and Beroza (2002) found that the heterogeneous slip distribution follows a

self-affine regime characterized by an average value $H_s = 0.71 \pm 0.23$, independently of moment magnitude or source dimensions. In support of these findings, Causse et al. (2010) have recently shown that kinematic inversions methods are a relevant tool to retrieve the slip roughness even if the smoothing constraints used to stabilize the inversion lead to a slight under-estimation of the slip spectrum corner wave number. The observation that $H_s < 1$ implies a larger short-scale variability of slip than for the self-similar model, and indicates that this model may not apply to explain the current knowledge on slip maps.

In the spirit of the analysis of Mai and Beroza (2002), we have examined the scaling heterogeneities of several slip fields extracted from finite-source rupture models (http://www.seismo.ethz.ch/srcmod), and selected ten of them with a frequency content sufficiently large for a Fourier analysis (see also Table 4.1).

The Hurst exponent H_s can be estimated from the Fourier power spectrum, which follows a power law for a 1-D self-affine profile (Barabasi and Stanley, 1995; Meakin, 1998). For each parallel profile extracted in the horizontal direction (or strike direction) of a slip map, the Fourier power spectrum $P(k)$, i.e., the square of the modulus of the Fourier transform, is calculated as a function of the wavenumber k. Then the spectrum of the entire surface is calculated by stacking and averaging all 1-D Fourier transforms to reduce the noise associated with individual profiles. When plotting the power spectrum as a function of wavenumber in a log-log space, a self-affine function reveals a linear slope, which is itself a function of H_s through $P(k) \propto k^{-1-2H_s}$.

Since we focus our analysis on the slope of the spectrum and to allow a better comparison of each power spectrum, Figure 4.2 displays the normalized power spectra of the 10 slip fields selected along strike direction (Table 4.1). In this figure, each Fourier spectrum is normalized by its maximum power. Even if the direction normal to strike corresponds to the average slip direction for normal or reverse faults, this direction is less extended than along strike and contains most of the time insufficient frequency content for a Fourier spectral analysis. However, as suggested by Mai and Beroza (2002) and our analysis on the Northridge earthquake slip map (inset on Figure 4.2), which contains a sufficient frequency content in the direction normal to strike, both directions have identical self-affine properties (i.e. an isotropic spatial distribution).

Finally, at large scales (above approximately $3\,km$), *i.e.*, above the effect of the spatial smoothing applied in the slip inversion, we find a self-affine behavior characterized by an average value of $H_s = 0.6 \pm 0.1$ which is very close to the average roughness exponent calculated by Mai and Beroza (2002) for these ten selected slip maps (Table 4.1) and falls within their range proposed in their extended analysis of spatial correlations of 44 slip maps.

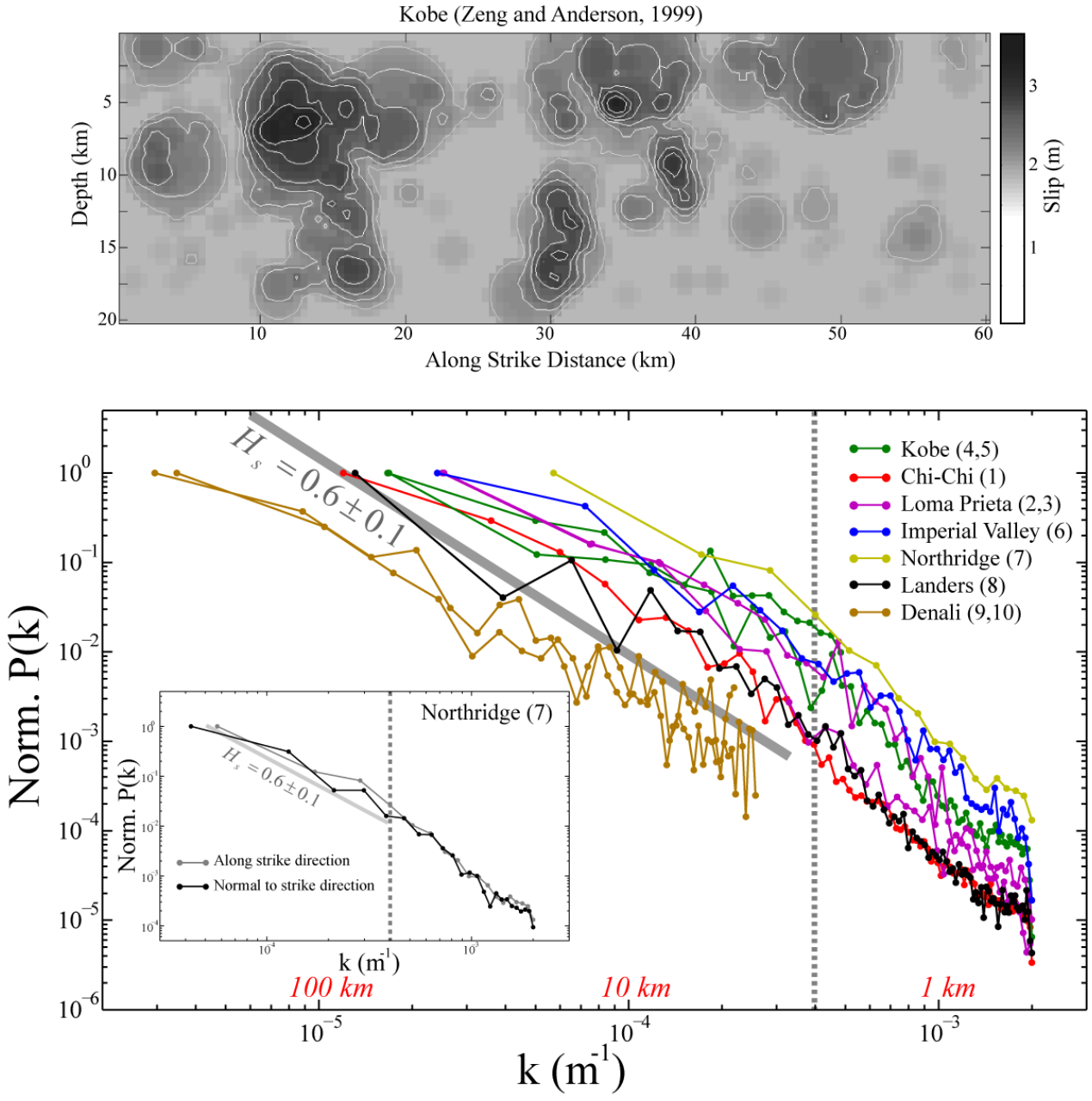

Figure 4.2. *Analyses of the roughness of several seismological slip distributions. Top: example of one of the ten slip maps analyzed (Table 4.1) derived by Zeng and Anderson (1999) for the Kobe earthquake, and illustrating the spatial variability of slip on the rupture plane. Bottom: Normalized Fourier power spectra of the horizontal (or strike direction) slip profiles of the ten slip maps analyzed. Inset: illustration on the Northridge earthquake of the identical self-affine regime in the strike direction and perpendicular to it.*

Table 4.1. Selected Slip Models

No.	Location	Date	#Frequency range (m^{-1})	H_s	H_s*	M_w	Reference
1	Chi-Chi (Taiwan)	09/20/1999	$[10^{-5} - 4.10^{-4}]$	0.54	0.66	7.61	*Zeng and Chen (2001)*
2	Loma Prieta	10/18/1989	$[2.10^{-5} - 4.10^{-4}]$	0.74	0.72	6.98	*Zeng and Anderson (2000)*
3	Loma Prieta	10/18/1989	$[2.10^{-5} - 4.10^{-4}]$	0.56	0.50	6.95	*Beroza (1991)*
4	Kobe	01/17/1995	$[10^{-5} - 4.10^{-4}]$	0.64	0.22	6.90	*Zeng and Anderson (2000)*
5	Kobe	01/17/1995	$[10^{-5} - 4.10^{-4}]$	0.59	0.40	6.99	*Sekiguchi et al. (2000)*
6	Imperial Valley	15/10/1979	$[2.10^{-5} - 4.10^{-4}]$	0.51	0.66	6.35	*Zeng and Anderson (2000)*
7	Northridge	17/01/1994	$[4.10^{-5} - 4.10^{-4}]$	0.59	0.73	6.71	*Zeng and Anderson (2000)*
8	Landers	28/06/1992	$[10^{-5} - 4.10^{-4}]$	0.65	0.72	7.20	*Zeng and Anderson (2000)*
9	Denali (Alaska)	03/11/2002	$[2.10^{-6} - 4.10^{-4}]$	0.54		7.91	*Oglesby et al. (2004)*
10	Denali (Alaska)	03/11/2002	$[2.10^{-6} - 4.10^{-4}]$	0.52		7.87	*Asano et al. (2005)*
Average				0.59	0.58		

 # The frequency range corresponds to upper and lower limits of wavenumbers used for fitting in Figure 4.2.

** Roughness exponents of slip maps obtained by Mai and Beroza (2002).*

4.2.3. Fault surface roughness

4.2.3. A. Self-affine properties of fault surfaces

High-resolution relocations of earthquakes using the multiplet technique have shown streaks of earthquake along several faults in California (Rubin *et al.*, 1999). This pattern has been interpreted as resulting from the presence of an organized large scale fault roughness (asperities) resisting slip (Schaff *et al.*, 2002). However, despite recent progress in seismology, the imaging of fault planes over a large range of scales at depth is not yet available. A quasi-unique access to high resolution description of the fault plane comes from exhumed fault scarp observations. This requires, of course, that the main morphological patterns of faults mapped at the surface of the Earth persist at least across the seismogenic zone.

Owing to technical limitations, the roughness of several fault planes has been studied mainly using 1D profilometry (Power *et al*. 1987). From these pioneer measurements, fault roughness has been shown to be scale invariant with a self-similar (Power *et al.*, 1987, 1988; Power and Tullis, 1991; Power and Durham, 1997) or self-affine character (Schmittbuhl *et al.*, 1993; Lee and Bruhn, 1996).

As pointed out by Power *et al.* (1987), there is a significant limitation in studying such roughness profiles, both because of intrinsic heterogeneity of the fault surfaces that may have existed at the time of faulting, and because later degradation of the surface by weathering may introduce variability and errors in the determination of the slope of the spectrum. This may explain why their studies i) did not have access to slight variations of the slopes, and ii) concluded on the presence of an "average" self-similar regime.

With the recent development of high resolution distancemeters, it is now possible to use accurate statistical approaches to quantify fault roughness. Indeed, portable 3-D laser scanners (also called LiDAR, Light Detection And Ranging) allow mapping fault surface outcrops over scales of millimeter to several tens of meters (Renard *et al.*, 2006; Sagy *et al.*, 2007; Candela *et al.*, 2009). The accuracy of the measurements enables a reliable quantification of the data. Renard *et al*. (2006) and Candela *et al*. (2009) demonstrated precisely the self-affine properties of fault topography using ground based LiDAR and laboratory profilometers. These studies, using two different and independent signal processing tools, validate the preliminary results of Schmittbuhl *et al.* (1993) and Lee and Bruhn (1996), and indicate that the various faults are characterized by an approximately identical self-affine geometry.

In the following paragraph, we use a technique based on Fourier power spectrum, as previously presented for slip correlations analysis and whose reliability and accuracy has been previously tested (Schmittbuhl *et al*, 1995, Candela *et al*., 2009) to investigate the scaling properties of fault surfaces, and confirm the self-affine model.

4.2.3. B. Scaling properties of the Corona Heights Fault, California

We present new roughness data obtained on a fault localized in the Castro Area of San Francisco (Corona Heights, 37.76°N, 122.43°W), that cross-cuts the brown Franciscan cherts, and where a post-1906 earthquake aggregate quarry has been transformed into a playground and

pet cemetery. The relatively recent exposure of the fault (Figure 4.3a) and the high resistance of cherts to weathering allow excellent preservation of the slip surface itself. This fault has a mainly strike-slip component, witnessed by large elongated bumps and depressions, associated with linear striations of smaller size observed at all scales down to the resolution of the measurement devices. We emphasize that the fault surface is characterized by an anastomosing network of highly polished, slickenlined surfaces, which might have been active during different episodes of faulting and might have accumulated various displacements.

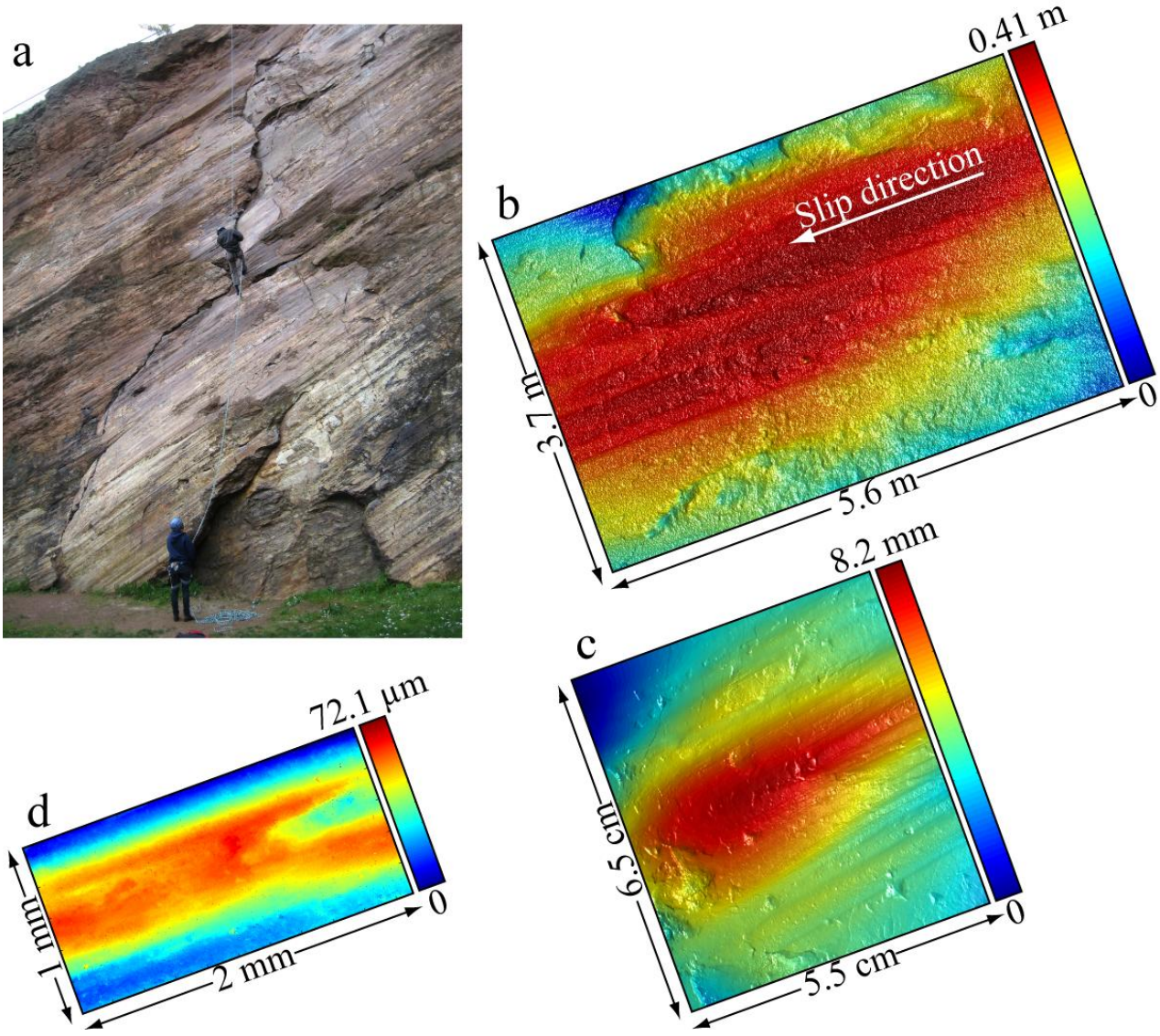

Figure 4.3. *Surface topography of the Castro Area fault (Corona Heights, San Francisco). (a) The fault surface consists of many discrete slip surfaces at all scales. (b) Example of fault surface topography measured using a LiDAR, and represented as a color-scale digital elevation model (DEM). The measurements were performed on a roughly regular grid with spatial resolution* $\sim 0.5cm \times 0{,}5cm$*, which contains* $\sim 2{,}000{,}000$ *points, and then averaged (bilinear interpolation) on a coarser grid to obtain the final model. The resolution of the elevation is less than one centimeter. (c) DEM of a hand sample, scanned with a laboratory laser profilometer. The surface contains* 4000×4000 *points on a regular grid with spatial resolution* $20 \times 20 \mu m^2$ *and elevation resolution less than* $10 \mu m$*. (d) Example of a DEM obtained with white light interferometry, that contains* 3000×3000 *points on a regular grid and gives access to a micrometer height resolution.*

At the field scale, a LiDAR apparatus (Leica HDS3000) was used to acquire digital elevation models (DEM) of the fault roughness at a spatial length scale resolution of 5 mm and with a height resolution of approximately 2 mm (Figure 4.3b). At the laboratory scale, the roughness of several slip planes was characterized using a laser profilometer (Méheust, 2002, Figure 4.3c, Schmittbuhl *et al*, 2008) with horizontal increments of $20 \mu m$ and a vertical resolution better than $1 \mu m$. We used also a White Light Interferometer (WLI, from Veeco©) giving access to a micrometer spatial length scale resolution for an estimated height resolution close to $3 nm$ (Figure 4.3d). Each measurement produces a matrix of millions of points from which 1D profiles in any direction can be extracted (insets on Figure 4.4).

To compare fault surface spatial correlations with that of the seismological slip maps, we focus our Fourier transform analysis along the slip direction even if the fault surface roughness shows a slightly anisotropic morphology (see Renard *et al.*, 2006; Candela *et al.*, 2009). On Figure 4.4, the spectrum in each structural direction (the slip direction and normal to it) is obtained by averaging several spectra with variable pre-factors but with roughly identical slopes at every scale (LiDAR, laser profilometer, WLI). In other words, each curve represents an average of similar spectra obtained for multiple fault patches. In this way, this technique gives a smoother spectrum that represents the average self-affine character of the entire fault surface while preserving good wavelength resolution.

Our results highlight a self-affine regime in the slip direction characterized by $H_{//} = 0.63 \pm 0.05$ (refered to $H_{//} = 0.6$ afterwards), over approximately 6 decades of length scales (Figure 4.4), similar to what was observed by Renard *et al*. (2006) and Candela *et al*.

(2009) for other faults. This roughness exponent corresponds to an average of those calculated at every scale and given for the LiDAR, laser profilometer, and the WLI scales, respectively: 0.65 ± 0.05, 0.62 ± 0.05, and 0.62 ± 0.03. The Fourier power spectrum technique indicates that the power laws can easily be connected for the field and laboratory data, demonstrating the robustness of the self-affine behavior and excluding several regimes (with different roughness exponents) bounded by characteristic scales. One has to note that the slight vertical shift between the spectra obtained by each device used in this study might be due partly to their various resolutions, and partly to the fact that we have preferentially selected surfaces with ridges and grooves (*i.e.* larger amplitude) at the laboratory scales (Figure 4.3c, d).

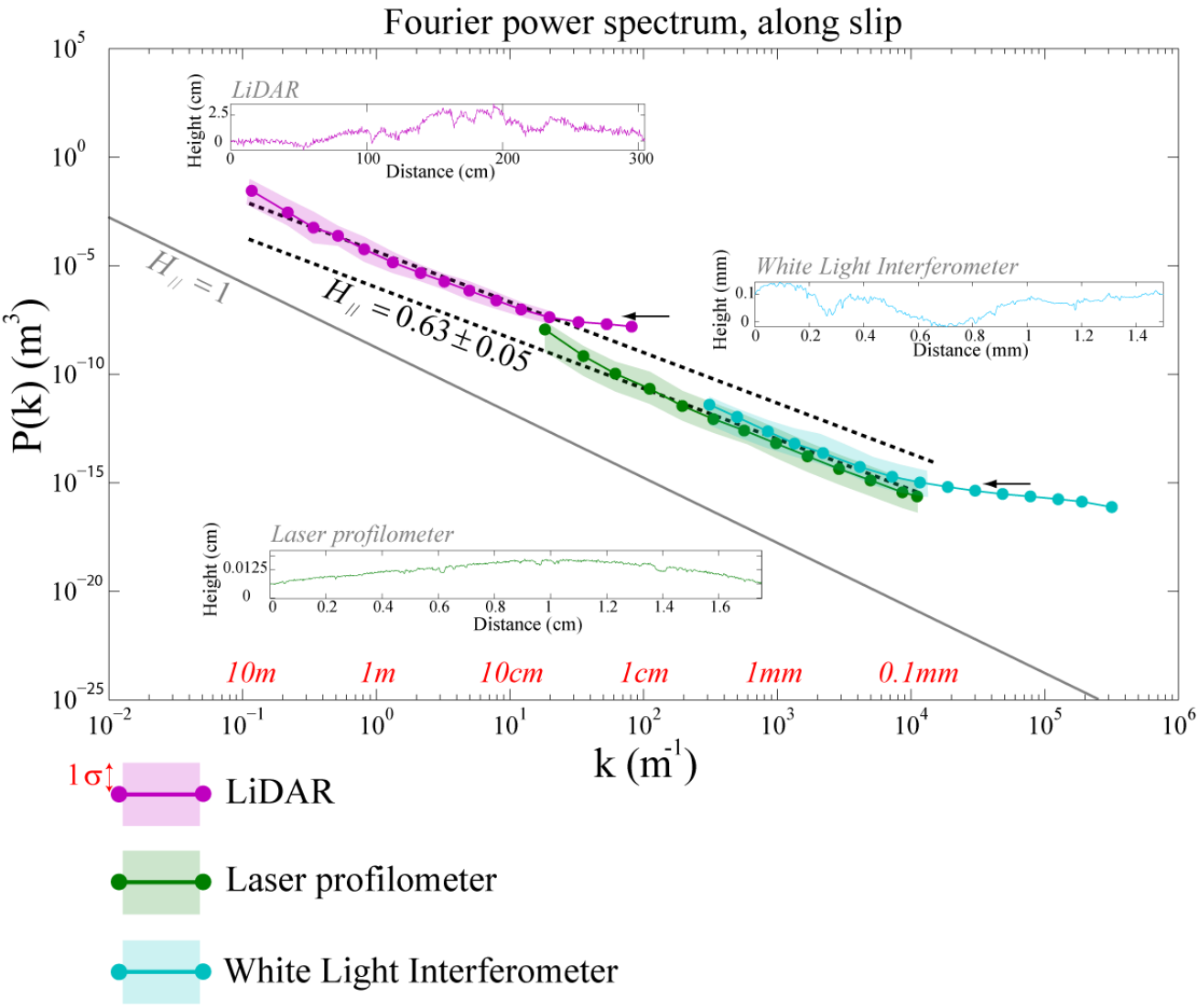

Figure 4.4. *Fourier power spectra and their respective standard deviations calculated for the Castro Area Corona Heights fault surface along slip and covering 6 decades of spatial wavelengths. The data collected contain five sections of the fault, that have been scanned using ground based LiDAR (magenta curve), two hand samples measured by laboratory profilometer (green curve), and two surfaces scanned using white light interferometry (blue curve). Each curve is an average over a large set of parallel profiles extracted from several DEM as shown for example on Figure 4.3. Each DEM gives one spectrum. For the LiDAR scale, five similar spectrums computed from five DEM have been averaged, and for both the laboratory profilometer and the white light interferometer scale two similar spectrums have been averaged. Power-law fits (dashed dark lines) with a roughness exponent* $H_{//} = 0.63 \pm 0.05$*, connecting the field and laboratory data, are shown on plot for eye guidance. Both black arrows indicate the level noise of the LiDAR and the lower limit for the fit performed at the white light interferometer scale. The insets display examples of rough profiles at all scales extracted in the direction of slip from each DEM shown in Figure 4.3.*

The compiled results of this analysis and previous works (Schmittbuhl *et al*., 1993; Lee and Bruhn, 1996; Renard *et al*., 2006; Candela *et al*., 2009) clearly show that, despite different geological settings (various accumulated displacement, host rock, and slip movement) a unique self-affine model may describe accurately the geometry of fault roughness along the slip direction. The fact that the fault studied was exhumed from shallow depth (< 5 *km*), implies that (i) its topography has only recorded the propagation and termination of hypothetic major earthquakes ruptures that initiate at greater depths, and (ii) it is difficult to identify irrefutable coseismic slip markers (as melt products). However, it is worth to note that in a recent work (Bistacchi *et al.*, 2011), the same self-affine regime was found for the Gole Larghe fault zone (Italian Alps) where the conditions of seismogenic nucleation depths have been sampled and where pseudotachylytes were found (Di Toro and Pennacchioni, 2005). One may conclude that the presented self-affine geometrical model represent a global feature of natural fault surfaces and might be preserved in depth.

4.2.4. From fault geometry to the spatial distribution of slip

4.2.4. A. Correlation between the pre-stress field and fault roughness (asperity squeeze model)

Schmittbuhl *et al*. (2006) have proposed that heterogeneities of the stress field are quenched along the fault plane, i.e. dominated by intrinsic fault properties and weakly sensitive to

dynamical stress fluctuations due to earthquake propagation since spatially persistent before and after the rupture event (at least at large scales). Their model, based on the studies of Hansen *et al.* (2000) and Batrouni *et al*. (2002), consists of a boundary element method that describes the full normal contact between two facing elastic self-affine rough surfaces mated with spatially correlated asperities. This model disregards plastic processes like rock fragmentation, and focuses on elastic deformation of the topography which is the dominant mode at large scales. It follows that when the loading is sufficient to suppress the fault morphology roughness and transform it in a normal stress roughness along a smooth plane, the Hurst exponent H_σ, characterizing the self-affinity of the normal stress field (the initial or pre-stress field before a rupture event), approaches: $H_\sigma = H_{//} - 1$, where $H_{//}$ represents the Hurst exponent of the fault surface morphology under exposure condition (no normal stress). This relationship arises from the fact that, for an elastic material, the stress field is related to the first derivative of the displacement field.

If we use our estimate of the Hurst exponent of the fault morphology $H_{//} = 0.6$, we obtain that the Hurst exponent of the normal stress field is: $H_\sigma = -0.4$.

4.2.4. B. A quasi-static heterogeneous slip distribution model

We use a quasi-static three dimensional fault model, detailed by Perfettini *et al.* (2001), which accounts for long range elastic interactions. Perfettini *et al.* (2001) have examined the influence of spatial heterogeneities of frictional strength on the slip distribution along a creeping fault. In this model, slip fluctuates spatially because of pinning on local asperities (heterogeneities of frictional strength). Depinning from these asperities involves local instabilities. When the elastic coupling is small, the motion is controlled by individual asperities. Conversely, for strong elastic coupling, *i.e.* weak pinning, asperities interact because of elasticity and the dynamics becomes global.

In distinction to the study of Perfettini *et al.* (2001), where a uniform random distribution of quenched frictional strength was used to characterize an heterogeneous static pre-stress field, we consider here, also a quenched disorder of the frictional strength (or shear strength) but spatially correlated and controlled by a self-affine exponent H_τ. We propose to link the Hurst exponent

of the shear strength H_τ to that of the normal stress H_σ on the basis of a local Byerlee criterion: $\tau_c = \mu\sigma_n$ with $\mu = 0.6$. Because of the linearity between the shear strength and the normal stress, both are expected to exhibit the same scaling leading to: $H_\tau = H_\sigma = H_{//} - 1$. With our estimate of $H_{//} = 0.6$, we obtain $H_\tau = -0.4$.

Numerical model

In this paragraph we briefly list the main characteristics and assumptions of the quasi-static numerical fault model, based on the study of Perfettini *et al.* (2001). We consider a simple elastic model of rupture along a fault plane located at $z = 0$ through an unbounded homogeneous elastic solid. The rupture propagates along the y direction.

The problem is then governed by a quasi-static scalar wave equation involving a two-dimensional displacement field $U(x,z;t)$, and the related shear traction across planes parallel to the crack is $\sigma(x,z;t)$. The actual slip $u(x;t) = U(x,0^+;t) - U(x,0^-;t)$ is the slip discontinuity across the fault plane and $\tau(x;t)$ denotes the associated perturbation of traction. We assume that slip occurs quasi-statically and neglect any dynamical effects. In that case, elastic waves are neglected, and the stress change $\tau(x;t)$, located at $y = 0$, and due to variations of slip discontinuity along the fault is given by (e. g. Cochard and Rice, 1997)

$$\tau(x;t) = \frac{G}{2\pi} PV \int_L J(x-\xi)[u(\xi;t) - u(x;t)]\, d\xi \qquad (4.1)$$

where integration takes place over the fault of size L and PV indicates the principal value. The elastic kernel $J(x) = 1/x^2$ accounts for the long range elastic interactions and G is the shear modulus. To avoid edge effects, we assume an L-periodic interface in the x direction such that the $1/x^2$ kernel in (4.1) transforms in $J_L(x) = (\pi/L)^2 / \sin^2(\pi x/L)$.

In order to characterize locally the heterogeneous frictional properties along the interface, we balance $\tau(x;t)$ with a quenched frictional strength that does not evolve with time $\eta_p(x;u(x;t))$. To mimic the spatial heterogeneities of the frictional strength previously described, their fluctuations are assumed to be spatially correlated with long range correlations,

i.e. the frictional strength are controlled by a negative self-affine exponent $H_\tau = -0.4$. A uniform random distribution of the frictional strength (Perfettini *et al.*, 2001) would correspond to $H_\tau = -1$ in two dimensions (Hansen *et al.*, 2001). The correlation function of the frictional strength is assumed to behave as $\Gamma(x-x') \propto \left|(x-x')\right|^{2H_\tau}$ and in Fourier space $P(k) \propto k^{-2-2H_\tau}$.

At any time, the quasi-static motion of the fault has to satisfy: $\eta_p(x;u(x;t)) \geq \tau(x;t)$ for all points of the interface. The evolution of the system may be regarded as purely dissipative, i.e. all the released energy being dissipated by frictional work (Fisher, 1998).

The loading results from an imposed displacement. The system is discretized both in time and space. An elementary step (*i.e.*, a time step) corresponds to the motion of only one segment for which a frictional strength $\eta_p(x;u(x;t))$ has been defined. At each step, the weakest segment is searched for (i.e., event driven dynamics) by assuming that its location corresponds to the least shear traction required to advance the crack. At each step of the calculation, only the weakest point slips by an elementary distance which is a fraction of the discretization length. The local driving force is locally updated according to the adopted self-affine distribution to follow the quenched imposed disorder of the frictional strength. At that stage, the rupture front is locally unloaded and all the forces along the front line are modified according to a discretized form of equation (4.1). The procedure is then repeated. The behavior of the system is controlled by the competition between local fluctuations of the frictional strength and the effects of long-range elastics interactions.

Perfettini *et al.* (2001) have shown that three regimes of slip correlations exist depending on the ratio of the stress drop of a point that just slipped by an elementary distance and the root-mean-square (rms) of the frictional strength fluctuations. In the first regime, when the stress drop is much greater than the rms of the frictional strength fluctuations, the heterogeneities are not strong enough to pin the front, thus crack advance can never be arrested. Conversely, slip in the second regime is expected to have the same statistical distribution as the fluctuation of the frictional strength, because the magnitude of the elastic interactions (due to a small stress drop) is much smaller than the frictional strength heterogeneities. The third regime, on which we focus our study, is intermediate and the magnitude of the elastic interactions is comparable to the

frictional strength variations. The interactions between frictional strength heterogeneities and elastic stress transfers lead to non trivial spatio-temporal correlations of slips.

Results

In the numerical model, we let the initially flat slip front evolve with increasing displacement. In Figure 4.5, the evolution of the crack front line geometry during the transient regime is displayed, and corresponds to the spreading of slip over the whole length of the model, until slip correlations reach a stationary regime. For small increment of slip, the profile appears essentially flat (only correlated at small wavelengths), showing that the spatial correlations between successive slip distribution occur at small wavelengths. As slip increases, the activity zone spreads, and the profile appears correlated at all length scales when it reaches the system size. In other words, during the transient regime, the spreading of the activity is emphasized by the increase of the fluctuations of the crack-front line which becomes rougher and rougher until is stationary geometry is reach. The spreading of the activity with increasing displacement results from two competing effects: long range elastic interactions and frictional strength heterogeneities. The former tends to strongly correlate slip laterally while the latter tends to pin the slip at one site.

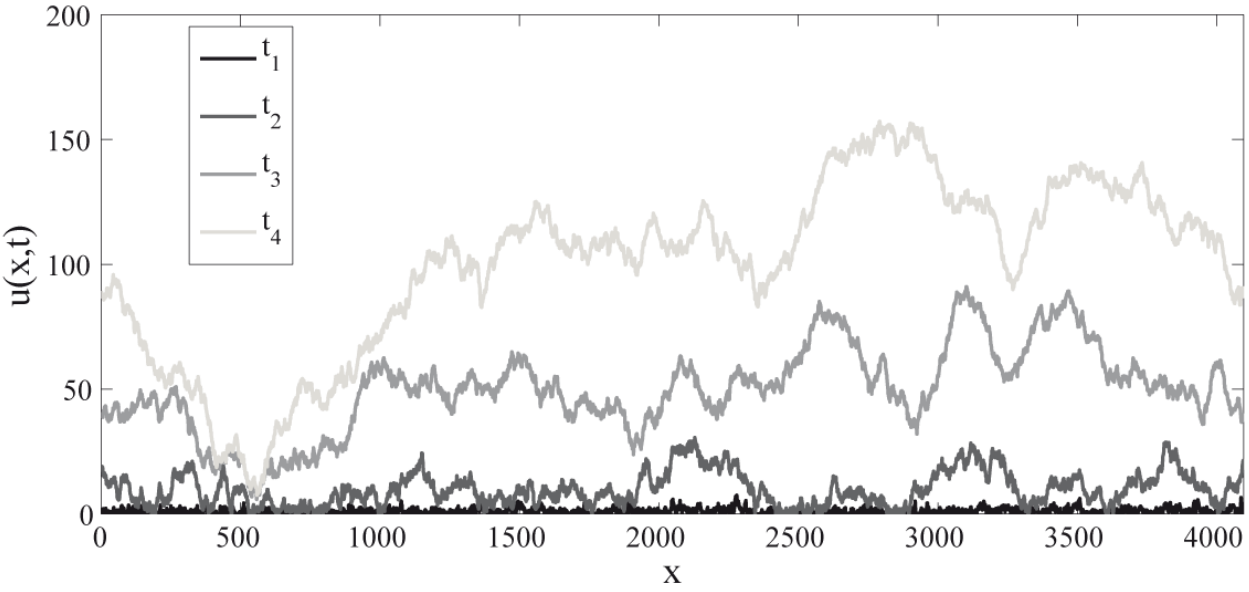

Figure 4.5. *Evolution (bottom to the top) of the crack-front line geometry during the transient regime until the stationary state. The system size is* 4096. *Elementary slip of broken segment is taken in a uniform distribution* $[0.09;0.11]$. *The shear modulus is set to* $30\,GPa$. *The average shear strength is* $100\,MPa$ *with a rms of* $30\,MPa$. *The Hurst exponent of the shear strength distribution is* $H_\tau = -0.4$.

The power spectrum of the slip distribution in the statistically stationary regime, averaged over many realizations of the rupture front, is shown in Figure 4.6. As previously indicated, we have considered the case where frictional strength correlations are controlled by a self-affine exponent $H_\tau = -0.4$, which mimics the initial strength field along a fault. The Fourier power spectrum of the modeled fronts exhibits a power law behavior with a power exponent $\alpha = -2.2$, which indicates a self-affine behavior with a Hurst exponent $H_s = 0.6$ ($\alpha = -2H_s - 1$, see Meakin 1998).

This result is consistent with that obtained for mode I ruptures by Schmittbuhl and Villote (1999), who studied the slow propagation of an interfacial mode I crack, including the effects of long range elasticity and those of spatial correlations in the toughness of the interface. They obtained that the crack-front line correlations scale as $H_s = H_\tau + 1$ for any value of H_τ, which extends our particular case, $H_s = 0.6$ and $H_\tau = -0.4$, using the analogy between mode I fracture and shear rupture discussed in Schmittbuhl *et al.* (2003).

Finally, combining $H_\tau = H_{//} - 1$, that comes from the elastic squeeze of fault asperities, and $H_s = H_\tau + 1$, given by our numerical fault model, we obtain that $H_s = H_{//}$. In other words the origin of the spatio-temporal complexity of the slip distribution could be related to geometrical properties of the fault. Considering two self-affine surfaces pressed together elastically and sheared, we have made the link between the 3-D fault roughness, which is perpendicular to the fault plane, and the 2-D slip roughness included in the fault plane.

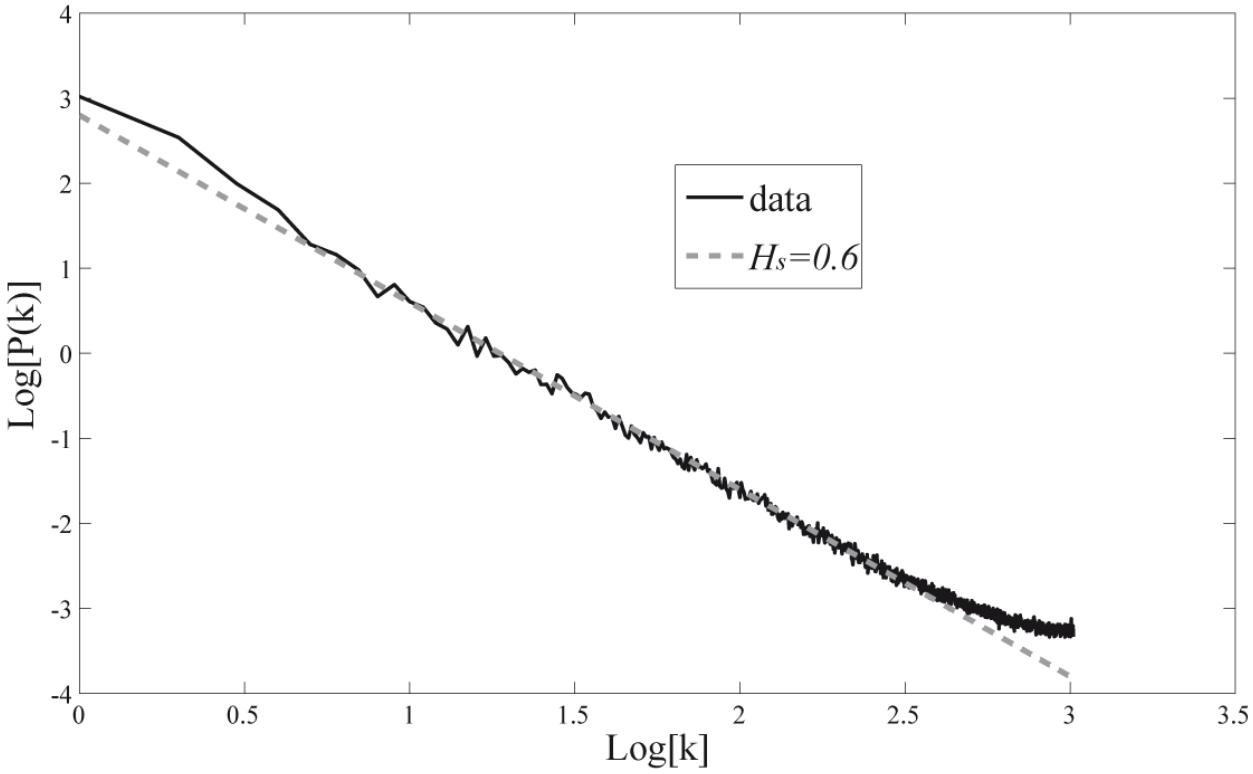

Figure 4.6. *Power spectrum of the slip distribution in the statistically stationary regime, averaged over* 7322 *fronts taken each after* 4096 *iterations (*$3\ 10^7$ *iterations in total). The power law fit provides an estimate of the Hurst exponent of the slip distribution:* $H_s = 0.6$.

4.2.5. Discussion and Conclusion

Considering the two main assumptions made in our study (fluctuations of the stress field along the fault are dominated by quenched fault properties and slip occurs quasi-statically), our results shed some lights on the influence of the fault surface roughness on the spatial slip distribution for creeping faults. Indeed, our work proposes a direct link between correlations in shear strength and slip distribution along the fault plane. Given that the origin of the spatial fluctuations of the shear strength (or initial stress) along faults is possibly the elastic squeeze of fault asperities, we therefore demonstrate that self-affine geometrical properties of fault surface roughness may control slip correlations.

Even if our quasi-static fault model is more adapted to creeping faults since inertia and wave effects, are neglected, it is worth to note that the self-affine spatial slip correlations observed in

our quasi-static model are consistent with that of seismological slip maps. Even if we still have to evaluate a complete elastodynamic description of this problem (Ramanathan and Fisher, 1998), this last observation leads us to propose that dynamical effects produced during an earthquake represent only a second-order effect as assumed by the asperity squeeze model. This line of thoughts seems to be validated by strong similarities in the spatial correlations of initial and final shear stresses along the Nojima fault for the Kobe earthquake (Schmittbuhl *et al.*, 2006). Finally, as pointed out by Sammis *et al.* (1999), our results support the hypothesis that the continuous slip of a creeping fault may results from a series of micro-events related to breakage of asperities (such as the ones in the numerical model), and has the advantage of collectively gathering seismically active and creeping faults.

Acknowledgments: This study was supported by the *Agence Nationale pour la Recherche* grants ANR-JCJC-0011-01 and ANR-SUPNAF. We thank Fabrice Cotton for fruitful discussions.

Chapter 5:

Stress drop during earthquakes: effect of fault roughness scaling

5.1. Chapter 5 overview (Présentation du Chapitre 5)

5.1.1. Introduction

Dans ce chapitre, je présente un article soumis à la revue *Bulletin of the Seismological Society of America*. Cette étude se situe dans la continuité du chapitre 4, et vise à estimer les implications probables des propriétés géométriques auto-affines des surfaces de failles sur la chute de contrainte après un tremblement de terre.

5.1.2. Presentations at international meetings

2010, American Geophysical Union, Fall meeting, San Francisco (USA):

Candela, T., Renard, F., Bouchon, M., Schmittbuhl, J., and Brodsky, E., Self-affine fault surface roughness: implications for the slip distribution and the amount of static stress drop after an earthquake. Abstract S54A-03.

5.1.3. Contributors to Chapter 5

J'ai personnellement mis en place la conception de l'approche suivie dans cette étude. Les mesures topographiques de la faille de Corona Height (San Francisco) ont été acquises sur le terrain par E.E. Brodsky, F. Renard et moi-même. Les scans de la faille de la Vuache-Sillingy ont été effectués par F. Renard et C. Voisin.

5.2. Stress drop during earthquakes: effect of fault roughness scaling

Thibault Candela,[1] François Renard,[1,2] Michel Bouchon,[1] Jean Schmittbuhl,[3] and Emily E. Brodsky [4]

[1]ISTerre, CNRS & University Joseph Fourier - Grenoble I, OSUG, BP 53, 38041 Grenoble, France. E-mail: thibault.candela@ujf-grenoble.fr; francois.renard@ujf-grenoble.fr

[2]Physics of Geological Processes, University of Oslo, Oslo, Norway

[3]UMR 7516, Institut de Physique du Globe de Strasbourg, Strasbourg, France. E-mail: Jean.Schmittbuhl@eost.u-strasbg.fr

[4]Department of Earth and Planetary Sciences, University of California–Santa Cruz, Santa Cruz, California 95064, USA. E-mail: ebrodsky@es.usc.edu

Abstract

We propose that a controlling parameter of static stress drop during an earthquake is related to the scaling properties of the fault surface topography. Using high resolution laser distancemeters, we have accurately measured the roughness scaling properties of two fault surfaces in different geological settings (French Alps, Nevada). The data show that a fault surface topography is scale dependent and may be accurately described by a self-affine geometry with a slight anisotropy, characterized by two extreme roughness exponents (H_R) in direction of slip and perpendicular to it $(H_{//} = 0.6, H_{\perp} = 0.8)$.

Assuming that a fault zone is elastic at large scales, the stress drop is proportional to the deformation, which is a spatial derivative of the slip. One can derive directly from the self-affine property of the fault surface, the evolution of stress drop fluctuations on the fault plane with the length-scale λ as $std_{\Delta\sigma}(\lambda) \propto \lambda^{H_R - 1}$.

Assuming no characteristic length scales in fault roughness and a rupture cascade model, we show that, as the rupture grows, the average stress drop and its variability should decrease with

increasing source dimension, that is for the average stress drop: $\Delta\sigma(r) \propto r^{H_R-1}$, where r is the radius of a circular rupture. This result is a direct consequence of the elastic squeeze of fault asperities which induces that the largest spatial fluctuations of the shear strength before and after the earthquake show at local (small) scales peculiar spatial correlations.

5.2.1. Introduction

One of the most commonly used source parameters in the interpretation of earthquakes is the static stress drop $(\Delta\sigma)$, which measures the stress decrease after an earthquake, averaged over the rupture surface area (Aki, 1967; Scholz, 2002). A controversial question about stress drop is its dependence or independence with respect to the seismic moment (M_0). Self-similar models of earthquakes, *i.e.*, scale invariance property of earthquake source mechanics, imply that small and large earthquakes are similar in terms of their rupture physics, and, as a consequence, stress drop should be independent of earthquake size. This has been proposed in many studies where earthquake stress drop is generally described as independent of source dimension and seismic moment (Aki, 1967; Hanks, 1977; Kanamori and Brodsky, 2004; Kanamori and Anderson, 1975; Abercrombie, 1995; Ide *et al.*, 2003; Imanishi and Ellsworth, 2006; Abercrombie and Rice, 2005; Prieto *et al.*, 2004; Shearer *et al.*, 2006).

The wide dispersion of commonly accepted values of static stress drop, however, calls into question the assumption of whether earthquake source properties are in fact scale invariant. The scatter of static stress drop values versus seismic moment originates partly from unmodeled sources of error such as directivity effect (Bernard *et al.*, 1996; Imanishi and Ellsworth, 2006) or near-surface attenuation (Hanks, 1982; Anderson and Hough, 1984; Anderson, 1986). Indeed, corrections for path and site response effects need to be applied before determining the source radius and the stress drop (Frankel and Wenneberg, 1989; Boatwright *et al.*, 1991). However, other studies suggest that heterogeneous properties in faulting influence the value of static stress drop, and propose that source factors do account for the observed variability (Venkataraman and Kanamori, 2004; Choy and Kirby, 2004). Singh and Suárez (1988) report a correlation between low stress drops and smaller number of aftershocks in the Cocos subduction zone in Central America compared to a global average. They proposed that variations in the smoothness of the

seafloor topography may be a possible cause. Harrington and Brodsky (2011) have observed that small earthquakes on immature faults obey the energy scaling expected for constant stress drop (self-similar model), while those of mature faults do not. Based on the estimations of source parameters from spectra of 42367 earthquakes between 1984 and 2005, Allmann and Shearer (2007) indicate that the patterns of high and low stress drop regions on the San Andreas Fault (California) remain largely unchanged by the occurrence of the 2004 M6.0 Parkfield earthquake. These authors suggest that stress drops are mainly controlled by rock properties and that strong heterogeneities of the stress field persist along the fault over the seismic cycle. This picture is also supported by the observation that the aftershocks of the Parkfield earthquake are distributed along the same streaks and display the same seismicity holes as the background before the main shock (Allmann and Shearer, 2007).

In the present study, we propose that a controlling parameter of the static stress drop is related to the scaling properties of the topography of the fault surface, i.e. fault roughness. Combining new fault roughness measurements with a recent study (Schmittbuhl *et al.*, 2006) that links the fault surface morphology with the shear strength along the fault plane, and using a numerical model of fault propagation (Schmittbuhl and Vilotte, 1999; Candela *et al.*, 2011), we deduce that fault geometry controls slip fluctuations on the fault plane. Given the close relationship between slip and stress drop, we infer the evolution of the spatial fluctuations of the stress drop on the fault plane as a function of the length scale. Then, considering that an earthquake is constituted of a hierarchical set of smaller earthquakes, we propose in the framework of a rupture cascade model, a theoretical scaling model for the average static stress drop and its variability directly associated with the scaling property of the fault surface.

In section 5.2.2, we present new analysis of fault roughness illustrating a unique identical self-affine property whatever the geological setting (various accumulated displacement, host rock, and slip movement). In section 5.2.3, we present the scaling of the spatial variability of the stress drop along the rupture surface. In section 5.2.4, we infer the evolution of the average stress drop and its variability as a function of the earthquake size by applying a rupture cascade model. Our scaling relationships are applied on the Nojima fault plane (Kobe earthquake, M7, 1995) for which the stress pattern along the fault plane could be imaged before and after the earthquake (Bouchon et al. 1998). We extrapolate the spatial fluctuations of the stress drop after the Kobe

earthquake towards small scales and infer the average stress drop and its variability for small earthquakes nucleating on this fault.

5.2.2. Roughness of natural fault surfaces

5.2.2. A. Definition of scaling properties and the Hurst exponent

Let first recall some definitions related to the scaling properties of a rough signal. A self-affine 1-D signal (Figure 5.1) remains unchanged under the scaling transformation $\delta x \to \lambda \delta x, \delta z \to \lambda^{H_R} \delta z$ (Meakin, 1998). Here, δx is the coordinate along the 1D profile and δz is the roughness amplitude. For a self-affine profile, the scaling exponent H_R, also called Hurst exponent (or roughness exponent), lies in the range $0 \le H_R \le 1$. In the particular case where $H_R = 1$, the profile obeys a self-similar description: a small portion of it, when magnified isotropically, has a statistically identical appearance than a larger part of the profile. Conversely, if a profile is best fitted with a self-affine model ($0 \le H_R < 1$), different magnification factors will be needed for the directions parallel and perpendicular to the profile for a small portion of it to appear statistically similar to the entire profile (Figure 5.1). As a consequence the slope along a self-affine profile follows a scaling such that $s = \delta z / \delta x \ \alpha \ \delta x^{H_R - 1}$, and tends to flatten for long wavelengths (Figure 5.1). Accordingly, as opposed to self-similar surfaces, this shows that the profile roughness is flatter at large scales but still includes a large variety of pattern of small amplitude asperities.

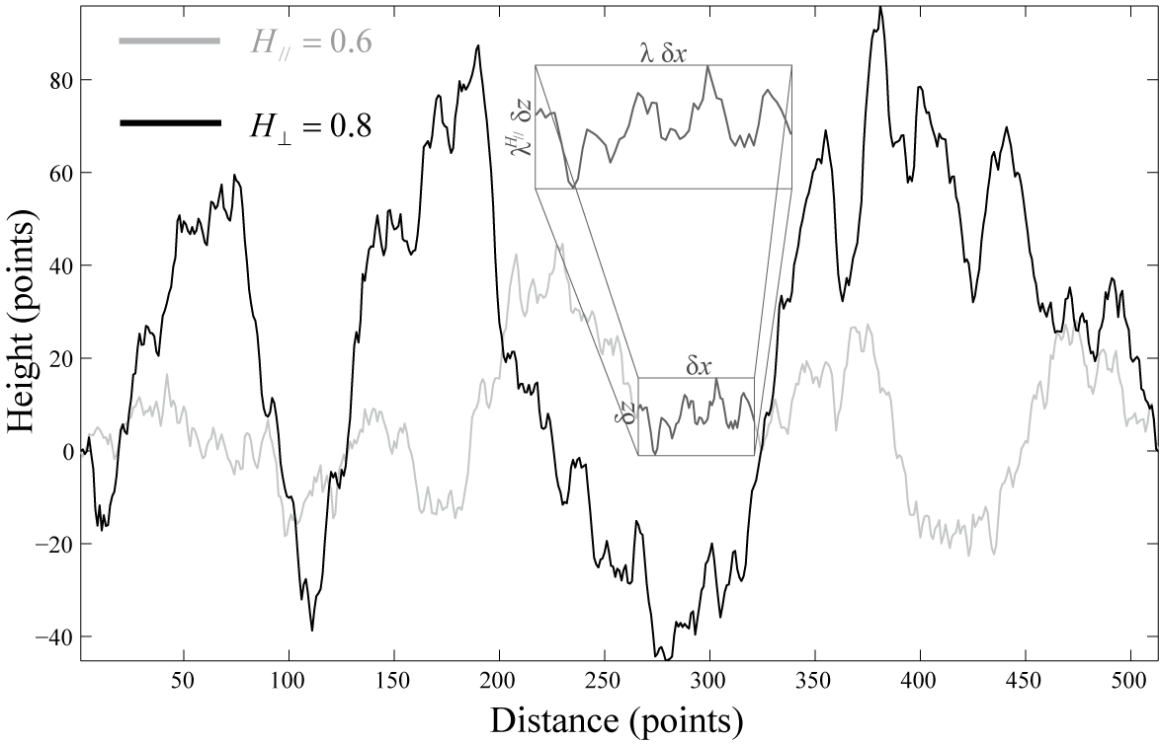

Figure 5.1. *Representative 1-D synthetic self-affine profiles computed with Hurst exponents* $H_{//} = 0.6, H_{\perp} = 0.8$. *We use a Fourier based method to simulate both self-affine profiles (Candela et al., 2009). The profile parallel to slip (with the smallest Hurst exponent) appears jagged at small scales and smooth at large scales, compared to the profile normal to slip. Inset: magnified portion of the profile along slip, which has a statistically similar appearance to the entire profile when using the rescaling transformation* $\delta x \to \lambda \delta x, \delta z \to \lambda^{H_{//}} \delta z$.

5.2.2. B. Fault roughness scaling

Despite recent progress in seismology, the imaging of fault planes over a large range of scales at depth is not yet available. A quasi-unique access to high resolution description of the fault plane comes from exhumed fault scarp observations. From pioneer measurements of fault surface topography using a mechanical profilometer, it has been shown that fault roughness is scale invariant with a self-similar character (Power *et al.*, 1987, 1988; Power and Tullis, 1991; Power and Durham, 1997). Two parameters are required to describe a self-similar or self-affine model in the spectral domain: The slope of the power spectrum and its intercept on a log-log plot of power spectral density versus frequency. The slope of the spectrum (directly proportional

to H_R) describes how the roughness changes with scale, while the intercept determines the amplitude of surface elevation at a given scale (Power and Tullis, 1991).

Owing to technical limitations, as pointed out by Power *et al.* (1987), these pioneer analyses, performed mainly with 1-D profilometer, did not give access to slight variations of the slope of the spectrum because of the large variability and errors introduced by the sporadic sampling of the whole fault scarp. Consequently, these studies have focused their efforts on the intercept and concluded that an obvious and expected consequence of slip related striations on fault planes is that profiles parallel to slip have lower spectral densities than those normal to slip, whereas the slope is roughly identical in both directions and follows an "average" self-similar regime (Power *et al.*, 1987, 1988; Power and Tullis, 1991; Power and Durham, 1997).

With the recent development of high resolution distancemeters, it is now possible to use accurate statistical approaches to quantify fault roughness. Indeed, portable 3-D laser scanners (also called LiDAR, Light Detection And Ranging) allow mapping the whole fault surface outcrops over scales from millimeter to several tens of meters (Renard *et al.*, 2006; Sagy *et al.*, 2007; Candela *et al.*, 2009). The accuracy of the measurements enables a reliable quantification of the data. Renard *et al*. (2006) and Candela *et al*. (2009) demonstrated precisely the anisotropic self-affine properties of fault topography using ground based LiDAR and laboratory profilometers. They showed that both slope and intercept are lower in direction of slip than perpendicular to it.

5.2.2. C. Self-affine geometry of the Vuache and Dixie fault scarps

In addition to previously published data acquired on the Vuache fault (Renard et *al.*, 2006; Candela et *al.*, 2009), we include new measurements performed on the Dixie Valley fault surface (Table 5.1) where a neighboring fault scarp has been studied by Power *et al.* (1987) and Power and Tullis (1992). The aim of this section is to compare two faults in different geological settings and to quantify their roughness properties.

The Vuache fault is an active strike-slip fault system in the western part of the French Alps (Thouvenot, 1998) which offsets meter-scale beds of limestones. We consider here a satellite branch of this fault system, where the cumulated slip was small, in the range $10-30$ meters. The

fault plane was exhumed ten years ago by the activity of a quarry. As a consequence, the LiDAR measurements could be performed on fresh surfaces, where weathering was minimum and vegetation free.

The Dixie valley (Nevada) fault surface has a mainly normal slip component and cross-cuts through rhyolites. The high resistance of rhyolite (composed mainly of quartz) to weathering and the dry climate of the Nevada desert allow excellent preservation of the slip surfaces (Figure 5.2a). These latter consists of many discrete slip surfaces at all scales separating lenses of variably deformed fault rock. Although normal cumulated slip for the fault zone as a whole in the study area is $3-6\,km$ (Okaya and Thompson, 1985; Fonseca, 1988; Power and Tullis, 1989), individual surfaces within the fault zone have experienced considerably less slip.

Three different models of LiDAR apparatus were used to acquire digital elevation models (DEM) of the fault roughness with a height resolution down to one centimeter, respectively the Leica HDS3000 for the Dixie fault and both the Riegl LMS Z420i and Trimble GS100 for the Vuache fault (Table 5.1). For each fault, several patches of the surface were scanned at a resolution from 5 mm to 30 mm, coarser than the precision of the scanner, and constituted individual DEM whose size lies between $1\,m^2$ and $170\,m^2$. In Figure 5.2b, we show one example of a DEM extracted from the Dixie fault surface, whereas DEMs of the Vuache fault surface are presented in Candela *et al.* (2009).

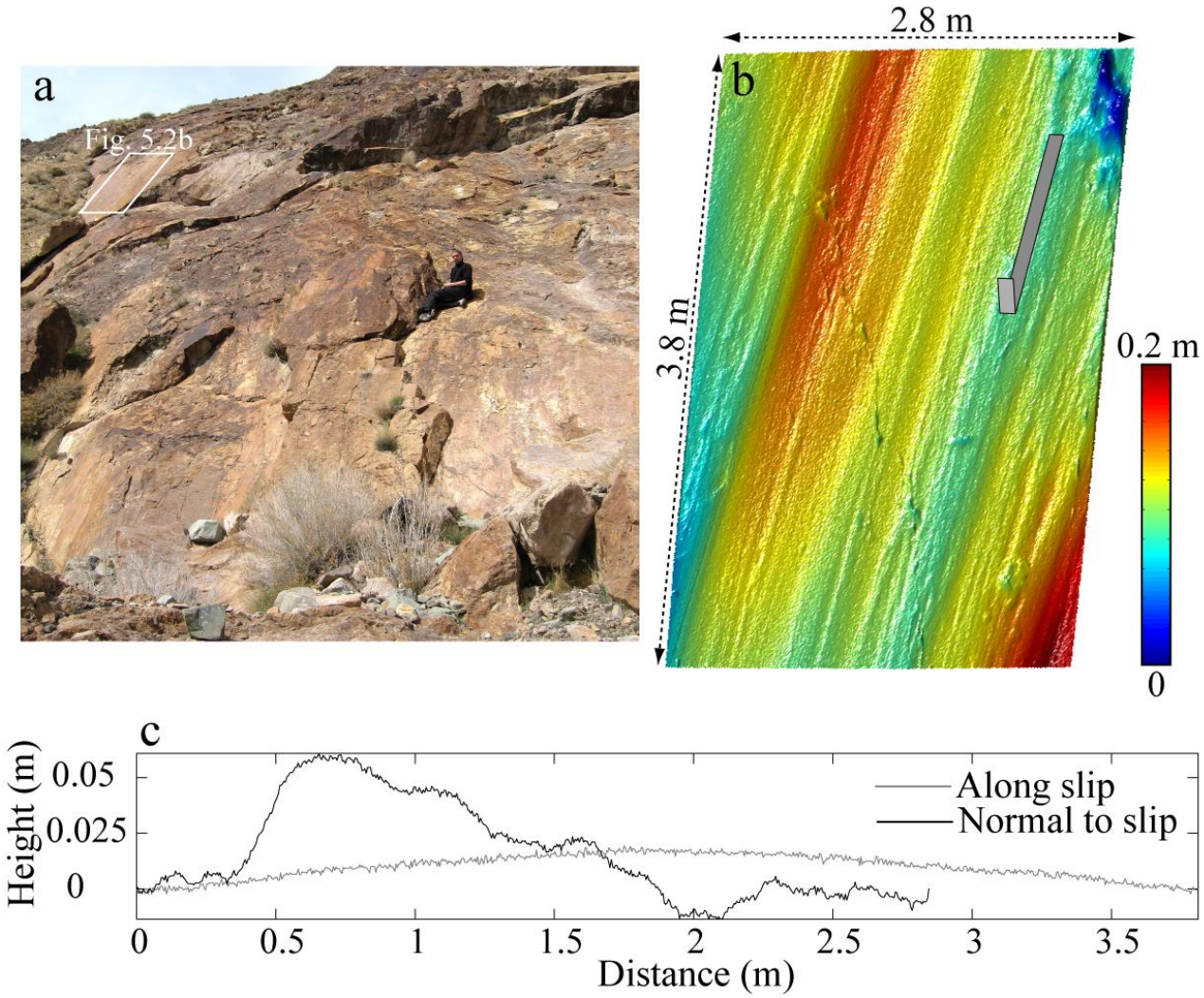

Figure 5.2. *Dixie Valley fault surface topography. (a) Whole outcrop constituted by many discrete slip surfaces. The inset corresponds to the surface shown on (b). (b) Zoom on the fault which corresponds to the digital elevation model (DEM) labeled Dixie-2 in Table 5.1. (c) Representative 1-D self-affine profiles of the slip surface extracted from the DEM (b) in the direction of slip and perpendicular to it.*

The Hurst exponent H_R can be estimated from the Fourier power spectrum which has a power law form for a 1-D self-affine profile (Barabasi and Stanley, 1995; Meakin, 1998). First, linear detrending is performed independently on all the profiles selected in a given direction from a DEM (Figure 5.2c). Then, for each parallel detrended profile in direction of slip and perpendicular to it (Figure 5.1), the Fourier power spectrum $P(k)$, i.e., the square of the modulus

of the Fourier transform, is calculated as a function of wavenumber k. Then the spectrum of each DEM is calculated by stacking and averaging all 1-D Fourier transforms to reduce the noise associated with individual profiles. Each DEM gives one spectrum. Three and four similar spectra were computed from three and four DEM for the Vuache and Dixie fault surfaces, respectively. These spectra were then coarse-grained and averaged to recover the general trend of each surface (Figure 5.3 and Table 5.1).

When representing the Fourier power spectrum as a function of wavenumber in a log-log plot, a self-affine function reveals a linear slope, which is itself a function of H through $P(k) \propto k^{-1-2H_R}$. In Figure 5.3, Fourier power spectra are displayed for the slip direction and normal to it, showing the two extreme self-affine regimes characterizing fault topography, as suggested by Candela *et al.* (2009). Note that these scaling relationships flatten at length-scales below $\sim 10\,cm$ for the Vuache and $\sim 2\,cm$ for the Dixie fault. This is due to the noise inherent to the measurement using LiDAR apparatus. This noise level varies between the three instruments we used and was in the range $2-10\,mm$ (see Table 5.1).

Table 5.1. Laser Scanner Characteristics and fault roughness results

Fault name	Location	DEM	Scanner	Resolution	Noise on the data	$H_{//}$ (±0.05)	$H_{\perp}$ (±0.05)	*Average* $H_{//}$	*Average* $H_{\perp}$
Vuache	45°57' 14.5"N 6°2' 56"E	Surf-1	GS 100 (Trimble)	20 mm	4.5 mm	0.59	0.79	0.59 ± 0.09	0.81 ± 0.02
		Surf-7	GS 100 (Trimble)	20 mm	4.5 mm	0.68	0.84		
		Surf-6	LMS Z420i (Riegl)	30 mm	10.2 mm	0.5	0.81		
Dixie Valley	39°56' 48"N 117°56' 43"E	Dixie-1	HDS3000 Leica	5 mm	2 mm	0.66	0.78	0.59 ± 0.08	0.81 ± 0.04
		Dixie-2	HDS3000 Leica	5 mm	2 mm	0.63	0.79		
		Dixie-3	HDS3000 Leica	5 mm	2 mm	0.60	0.83		
		Dixie-4	HDS3000 Leica	5 mm	2 mm	0.46	0.84		

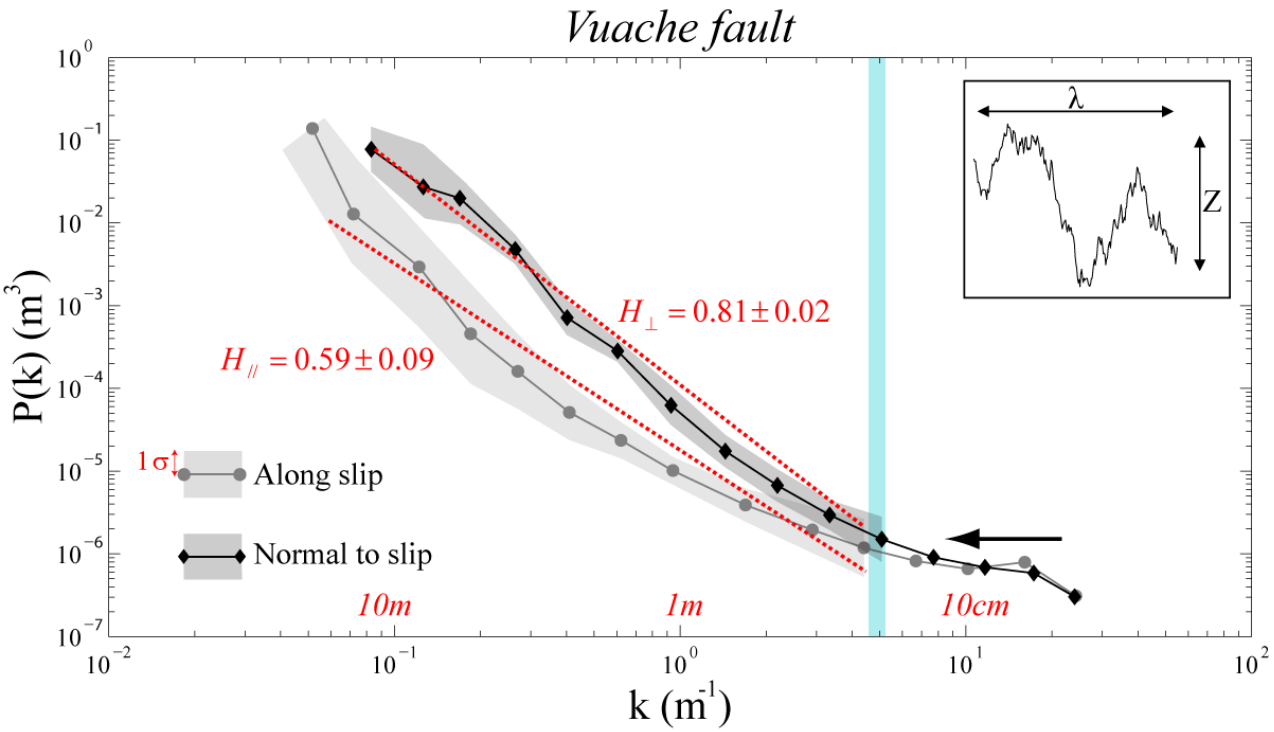
Vuache fault
P(k) (m³)
k (m⁻¹)
λ
Z
H⊥ = 0.81 ± 0.02
H// = 0.59 ± 0.09
1σ
Along slip
Normal to slip
10m
1m
10cm

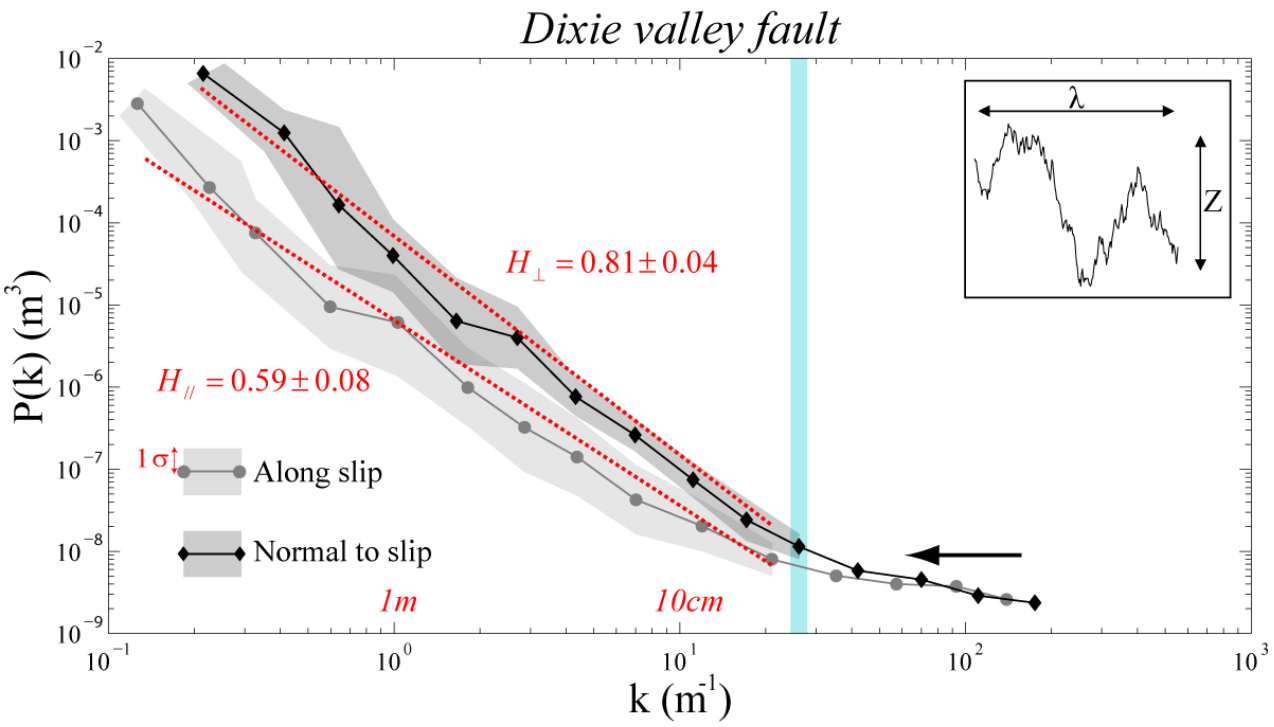
Dixie valley fault
P(k) (m³)
k (m⁻¹)
λ
Z
H⊥ = 0.81 ± 0.04
H// = 0.59 ± 0.08
1σ
Along slip
Normal to slip
1m
10cm

Figure 5.3. *Fourier power spectrum calculated for the Vuache fault and Dixie fault surfaces in directions (along and perpendicular to slip) and their respective standard deviations. The data collected contain respectively three and four surfaces of the Vuache and Dixie fault surfaces, that have been scanned using ground based LiDAR. Power-law fits (dashed red lines) are shown on plots for eye guidance. The blue vertical bars display the upper limits of wavenumber used for fitting. The insets display an example of the height elevation Z (~ y-axis) vs. wavelength λ=1/k (~ x-axis) of a rough profile. The level of noise is indicated by the arrows.*

Our results clearly highlight an identical directional morphological self-affine anisotropy for both fault surface geometries (Figure 5.3). All the power-law fits performed for each sub-surface (or DEM) to extract each roughness exponents are presented in Table 5.1. The Vuache and Dixie fault surface geometry can be accurately described by two scaling roughness Hurst exponents H_R in both structural directions, which are: $H_{//} = 0.59 \pm 0.09, H_{\perp} = 0.81 \pm 0.02$ and $H_{//} = 0.59 \pm 0.08, H_{\perp} = 0.81 \pm 0.04$, respectively. The structural slip direction, highlighted by linear striations at small scales, and the direction perpendicular to it correspond roughly to the two directions where the estimated self-affine exponents are the smallest and the largest, respectively.

The compiled results of this analysis and previous works (Schmittbuhl *et al*., 1993; Lee and Bruhn, 1996; Renard *et al*., 2006; Candela *et al*., 2009) show that, despite different geological settings (various accumulated displacement, host rock, and slip movement), an anisotropic self-affine model may describe accurately fault asperity geometry. The roughness exponents H_R are in the range 0.6-0.8 (*i.e*. self-affine case), and always smaller than 1 (*i.e*. self-similar case) in both structural directions.

The two faults studied were exhumed from shallow depths (i.e. < 5 *km*). Their topography has recorded both the propagation and termination of major earthquakes ruptures that initiate at greater depths. It is worth noting that in a recent work (Bistacchi *et al.*, 2011) the same self-affine regime was measured on the Gole Larghe fault zone (Italian Alps). This fault has recorded slip processes at the depth of seismogenic nucleation. One may conclude that the self-affine geometrical model may represent a global feature of natural fault surfaces.

5.2.3. Spatial variability of the stress drop on the fault plane

5.2.3. A. Relationship between slip and fault roughness

In their "asperity squeeze model" Schmittbuhl *et al*. (2006) have proposed that fluctuations of the frictional shear strength field can be understood as the expression of two self-affine fault planes pressed together elastically and sheared with frictional sliding (i.e. at Coulomb threshold). Within their approximations (full contact, elastic deformation of the topography), frictional shear strength distribution constitutes an intrinsic property of the fault plane, and is only slightly affected by dynamical stress fluctuations produced during the earthquake. Accordingly, the Hurst exponent H_{τ_i}, characterizing the self-affinity of the shear strength field before the earthquake, approaches

$$H_{\tau_i} = H_R - 1 \tag{5.1}$$

In addition, Schmittbuhl and Vilotte (1999), using a numerical model of quasi-static tensile crack propagation have demonstrated that the interactions between toughness heterogeneities and elastic stress transfers lead to non trivial spatio-temporal correlations of slip. Indeed, neglecting any dynamical effects due to stress overshoots, inertia or wave effects, they show that for long-range correlations of toughness heterogeneities, characterized by a self-affine exponent H_t, the roughness exponent of the slip distribution follows the scaling $H_s = H_t + 1$ for a wide range of values of H_t between -1 and $+1$. The results obtained with this numerical model developed for mode I cracks can be extended to mode II or III ruptures, which are relevant for the description of shear fault rupture during earthquakes (Schmittbuhl *et al*., 2003; Candela *et al*., 2011). The toughness disorder in the case of mode I rupture propagation is then converted into frictional disorder for mode II or III cracks and

$$H_s = H_{\tau_i} + 1 \tag{5.2}$$

with H_{τ_i}, characterizing the long-range correlations of the frictional shear strength (such as due to asperities) along the fault plane before the rupture. Finally, combining (5.1) and (5.2), it follows that

$$H_R = H_s \tag{5.3}$$

showing that self-affine geometrical properties of fault surface roughness may control slip correlations. Even if the quasi-static model of fault propagation discussed here neglects any dynamical effect inherent to rapid coseismic slip, we emphasize that the spatial slip correlations observed (Equation 5.3) are consistent with those of seismological slip maps (Mai and Beroza, 2002).

5.2.3. B. Scaling of the standard deviation of the stress drop after an earthquake

Fault slip distribution and stress drop variability

For a two-dimensional scale-invariant model of slip, the Fourier transform of the slip distribution $u(k)$ follows $k^{-1-H_s}\gamma(k)$, with γ a Gaussian white noise (Marsan, 2006). By definition, for an elastic body the stress drop is proportional to the deformation, which is a spatial derivative of the slip. Therefore, the stress drop scales as $\Delta\sigma(k) \propto k.u(k) \propto k^{-H_s}\gamma(k)$ for a wavenumber *k* (Marsan, 2006), and the scaling of the standard deviation $std_{\Delta\sigma}(\lambda)$ of the stress drop at scale λ is given by

$$std^2{}_{\Delta\sigma}(\lambda) \propto \int_{1/L}^{1/\lambda} dk\ k\left|\Delta\sigma(k)\right|^2 \Rightarrow std_{\Delta\sigma}(\lambda) \propto \left[\left(\frac{L}{\lambda}\right)^{2-2H_s} - 1\right]^{1/2} \qquad (\text{for } H_s < 1) \quad (5.4)$$

where L is the size (total length) of the coseismic rupture. In the limit $\lambda \to 0$,

$$std_{\Delta\sigma}(\lambda) \propto \lambda^{H_s - 1} \quad (5.5)$$

Note that, when reaching small wavelengths, the standard deviation of the stress drop should diverge. There, the elastic assumption is not relevant anymore because plastic deformation must take place to dissipate the largest stress concentrations (Dieterich and Smith, 2009).

As suggested by the previous paragraph, spatial slip correlations are directly linked to the distribution of fault asperities and combining (5.4) and (5.5) with (5.3) we obtain for H_R <1:

$$std_{\Delta\sigma}(\lambda) \propto \left[\left(\frac{L}{\lambda}\right)^{2-2H_R} - 1\right]^{1/2} \quad (5.6)$$

and in the limit $\lambda \to 0$,

$$std_{\Delta\sigma}(\lambda) \propto \lambda^{H_R - 1} \quad (5.7)$$

indicating that the evolution of the stress drop standard deviation with the length-scale λ may be controlled by fault geometrical properties. In other words, the variability of the stress drop along the fault plane after an earthquake should increase towards small scales because of the self-affine character of the fault surface ($H_R < 1$). Note that, in the case of a self-similar fault roughness, stress fluctuations would be of the same intensity at all scales. Figure 5.4 displays this standard deviation $std_{\Delta\sigma}(\lambda)$ for H_R ranging from 0.6 to 0.8, as given by equation (5.6). Considering the two end-members H_R obtained in the fault roughness analysis ($H_{//} = 0.6, H_{\perp} = 0.8$), we illustrate the scaling of the standard deviation of the stress drop on a rupture surface of total length $L = 60\,km$, when the stress drop variability is known down to the scale of $4\,km$ as generally obtained by seismological slip inversions. In other words, we extrapolate at small scales the stress drop variability on a fault surface caused by a magnitude ~ 7 earthquake (analogue to the Kobe earthquake).

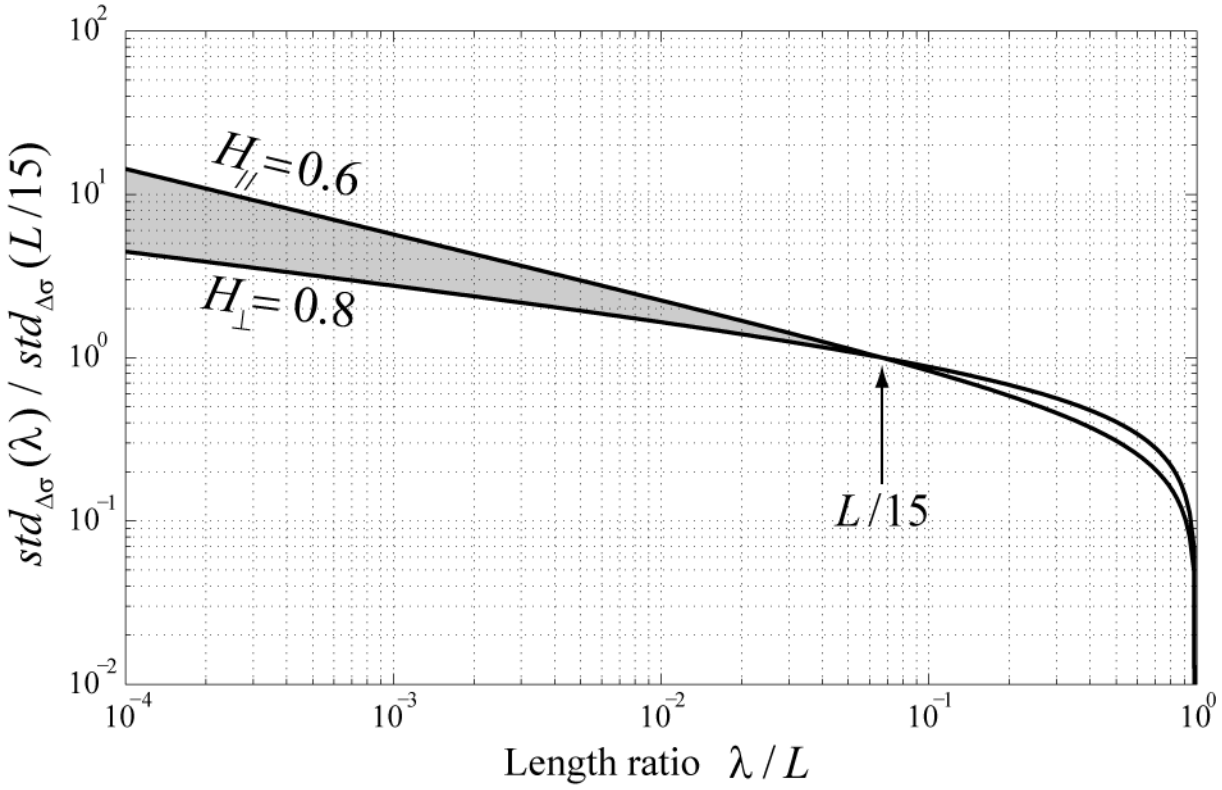

Figure 5.4. *Increase of* $std_{\Delta\sigma}(\lambda)$*, the stress drop variability (standard deviation) at scale* λ*, with the decrease of* λ*, for the range of Hurst exponents* H_R *given by fault roughness analyses*

($H_{//} = 0.6, H_{\perp} = 0.8$). This graph represents the generic case of a rupture of total length L, for which the stress drop variability is known from seismological slip inversions down to scale $L/15$. Such a scale is generally close to $\sim 4\,km$, corresponding to a $\sim 60\,km$ long rupture (i.e., a magnitude ~ 7 event, analogue to the 1995 Kobe earthquake).

Absolute shear stress and stress drop variability

a. Analogy between the stress drop and the fracture aperture scaling

In section 5.2.3.A, the shear strength field before the rupture is directly linked to fault topography by the "asperity squeeze model" Schmittbuhl *et al*. (2006). In the same way, this model implies that the state of stress after an earthquake is controlled by fault roughness and is only slightly affected by the dynamical effects during the rupture propagation, at least when considering its scaling properties. In this framework, the only way to alter the final strength distribution is to modify the fault morphology during the slip event. Therefore, the relationship (5.1) could be applied for both the initial and final shear strength and the scaling of their standard deviations at a given length scale λ evolves as:

$$std_{\tau_i,\tau_f}(\lambda) \propto \lambda^{H_R - 1} \tag{5.8}$$

where τ_f corresponds to the final shear strength. If one assumes that the stress drop quasi-statically from the initial shear strength τ_i (which can be interpreted as the yield stress) to the final shear strength (i.e. the final loading stress), therefore the static stress drop after an earthquake can be defined as $\Delta\sigma = \tau_i - \tau_f$. To derive the scaling of its variability we make the analogy with the scaling of fracture aperture (Méheust and Schmittbuhl, 2003). Indeed, in our case, each facing fracture surface mimicks the initial and final shear strength. Two situations are possible: (i) both self-affine surfaces display fluctuations uncorrelated with each other at all scales, or (ii) they are matched at large scales but uncorrelated at small scales. In (i) the difference of the two self-affine surfaces (the fracture aperture or the stress drop) is also self-affine with an identical Hurst exponent, but for the case (ii) at large scales where both surfaces are matched, their difference appears smooth and does not preserve the self-affine regime still present at smaller scales.

b. Application to the 1995 Kobe earthquake

The 1995 Kobe, Japan, earthquake (Nojima fault) for which it has been possible to reconstruct not only the stress drop, but also the absolute stress field (Bouchon *et al.*, 1998), is a unique case which gives the opportunity to test both previous possibilities and infer the scaling of the stress drop variability in a different and independent way of the one previously proposed in (3.2.1). In Figure 5.5a, the shear stress maps before and after the Kobe earthquake show persistent spatial fluctuations (Bouchon *et al.*, 1998): relative maxima are located at similar positions along the fault plane, except at large depths.

Before precisely analyzing the spatial distributions and more especially the possible spatial correlations of the absolute stress field and the stress drop of the Kobe earthquake, it is important to clarify some points on the reliability of a model derived from an inversion. Indeed, even if inversions of the same rupture event show discrepancies, Mai and Beroza (2002) in their extended analysis of spatial correlations of slip maps for 44 earthquakes found that they follow a self-affine regime characterized by an average value $H_s = 0.71 \pm 0.23$. This result even if it is accompanied by a large standard deviation demonstrates that the very heterogeneous patterns of slip maps is better fit by a self-affine model (i.e. H <1) rather than a self-similar one (i.e. H = 1). In addition, Causse *et al.* (2010) have recently shown that kinematic inversions methods represent a relevant tool to retrieve the slip roughness even if the smoothing constraints used to stabilize the inversion lead to a slight under-estimation of the slip spectrum corner wave number.

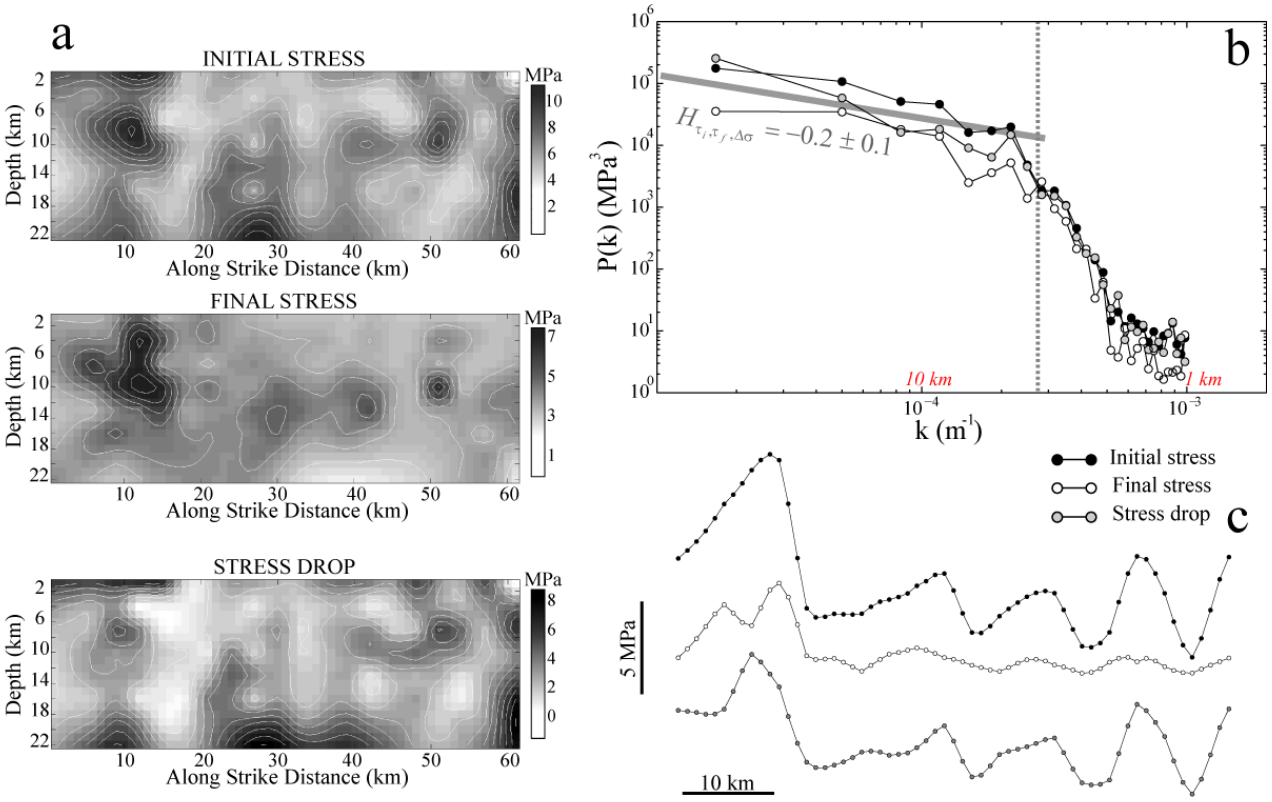

Figure 5.5. *Investigation of the absolute shear strength and the stress drop variability inferred for the Kobe earthquake. (a) Absolute shear strength and stress drop inferred for the Kobe earthquake (after Bouchon et al., 1998). Above 10 km of depth, these distributions show persistent spatial fluctuations: relative maxima (dark gray areas) are located at similar positions along the fault plane.*

(b) Fourier power spectrum of the absolute shear strength and stress drop profiles averaged over the ten first kilometers of depth in the maps shown in (a). Note that the vertical dashed gray line displays the smallest length scale at which the spatial fluctuations of the stresses are accessible by the seismological inversions, i.e. ~ 4 km.

(c) Profiles extracted at the same position (7 km of depth) for each stress maps displayed in (a) showing that fluctuations are larger at small scales than at larger scales where they appear nearly linear. In addition, persistent spatial fluctuations of relative maxima are clearly identifiable between the initial stress profile and the final one even if the overall roughness amplitude of this latter is considerably reduced. The resulting difference of these unmatched initial and final stress profiles, i.e. the stress drop profile, displays identical fluctuations at all scales conserving the same self-affine regime.

In the same way performed for the roughness analysis of fault surfaces, we have therefore searched for possible spatial correlations of the absolute stress field and the stress drop on each map which can be considered reliable despite the small range of resolution. The Fourier power spectrum of each stress map is obtained by averaging the spectra of the individual profiles of the ten first kilometers of depth (i.e. the region of highest resolution). The power spectra of the initial and final stress profiles along strike direction (Figure 5.5b) show an identical self-affine behavior with a negative Hurst exponent $H_{\tau_i,\tau_f} = -0.2 \pm 0.1$ at scales larger than $\sim 4\ km$, the scale below which spatial smoothing applied for the inversions has an effect. This self-affine behavior is in qualitative agreement with the range of values predicted by the asperity squeeze model. This confirms that an elastic squeeze of fault asperities could explain the spatial distributions of the shear strength along the fault, both before and after the rupture event.

Another important result is that the stress drop spatial distribution follows the same self-affine regime as that for the initial and final stress. This later observation suggests that even if the initial and final strength maps show persistent spatial fluctuations, they are also uncorrelated with each other at all scales, explaining that their difference, i.e. the stress drop, is also self-affine with an identical negative self-affine Hurst exponent. Indeed, the vertical shift downward of the final shear stress spectrum compared to the initial one, while keeping the same log-log slope, indicates that the roughness amplitude was decreased at all scales but the relative amplitude of the modes of short and large wavelengths remains identical. In other words, and illustrated by profiles extracted from the stress field maps (Figure 5.5c), the position of relative maxima (largest asperities) have been conserved, keeping the spatial fluctuations persistent even if at all scales the roughness amplitude has decreased.

Finally, given that in the framework of the asperity squeeze model, the stress field before and after the earthquake are the fingerprints of the fault surface roughness, we suspect that this difference in both stress fields is directly linked to slight change in fault morphology caused by the rupture event. As suggested by Schmittbuhl *et al.* (2006), it is conceivable that a slight decrease of the roughness amplitude at all scales (while keeping a similar Hurst exponent) caused by the earthquake, could contribute to the decreasing of the pre-factor observed for the Kobe final strength. This hypothesis is illustrated on Figure 5.6 using three synthetic self-affine

profiles defined by an identical negative Hurst exponent of -0.2 and three different prefactors as visualized for the distributions of the shear strength and the stress drop along the Nojima fault plane before and after the Kobe earthquake.

In summary, our analysis of the spatial variability of the strength before and after the Kobe earthquake demonstrates that they are uncorrelated mutually at all scales even if large scale fluctuations are persistent, and confirms that their difference, i.e. the stress drop, scales also with λ as provided by the scaling relationship (5.7).

5.2.4. Evolution of the stress drop with rupture size

5.2.4. A. Implication of a rupture cascade model on the variability of the stress drop

In the previous section, we have demonstrated that, as a consequence of $H_R < 1$, the variability of the stress drop after an earthquake increases towards the small scales and large stress drops could be attained at small scales along the fault plane hosting the rupture. Here we propose to deduce the dependence of the average stress drop with rupture size.

In a slip pulse model of earthquake on a fault with a spatially varying strength, once slip initiates at a point, the fault continues to slide until it encounters a strong barrier (e.g. Brodsky and Mori, 2007). In a different point of view, but not incompatible with the slip pulse model, an earthquake can be conceptualized as a hierarchical cascade of ruptures: an earthquake would be composed of subevents with different sizes and these subevents are themselves composed of subevents, and so on (Frankel, 1991). Note that the propagation of each small earthquake or subevent can follow the slip pulse theory. Based on our analysis of fault surface morphology, we use a self-affine model of fault roughness on which a cascade rupture propagation occurs. For such model, Andrews (1980) and Frankel (1991), have suggested that the stress drop could be independent of event size. However, in both works, the initial shear strength was implicitly independent of scale ($H_{\tau_i} = 0$).

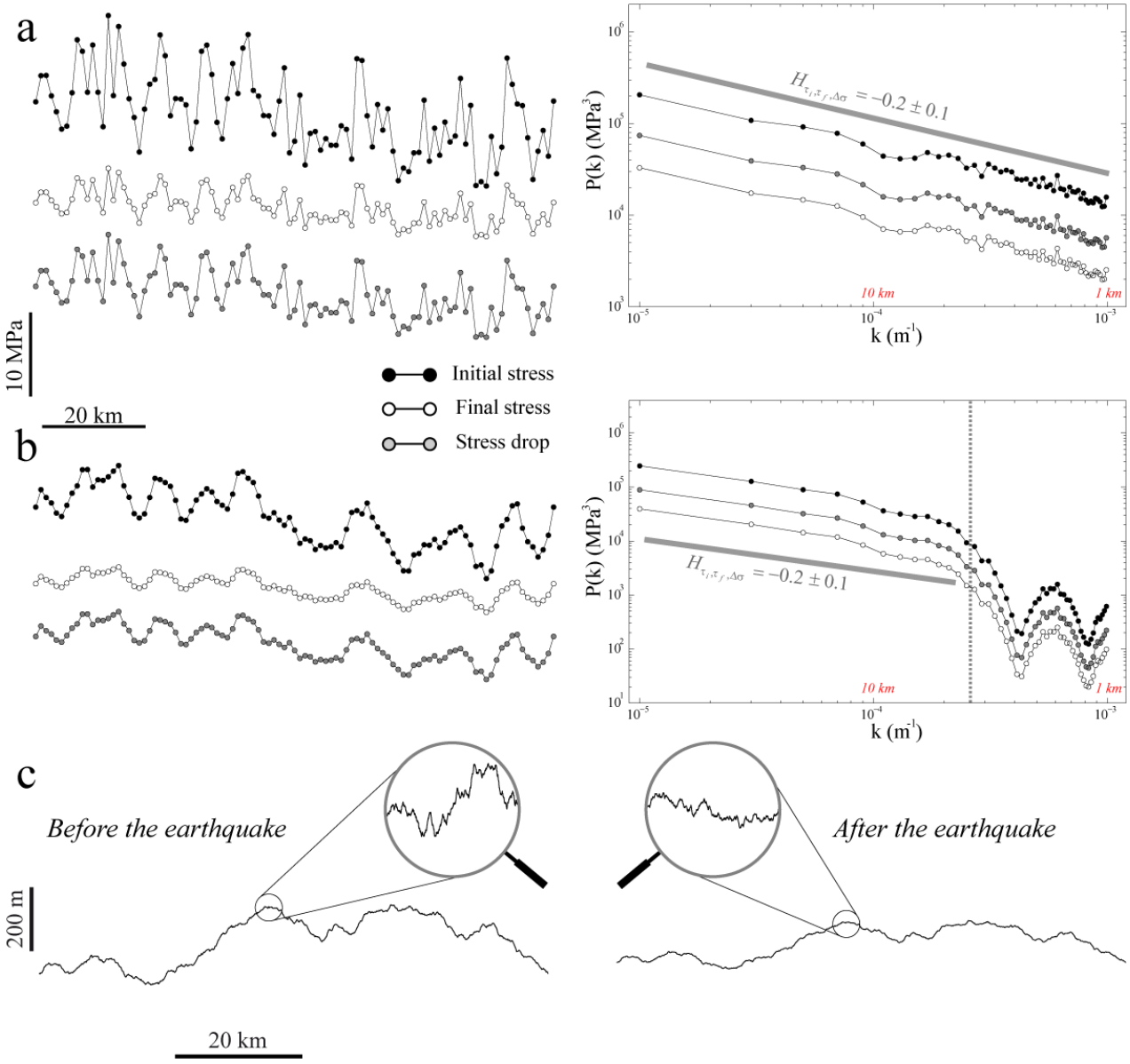

Figure 5.6. *Conceptual model of the difference in the variability of the shear strength before and after the Kobe earthquake. (a) Ideal synthetic self-affine profiles with a prescribed Hurst exponent of -0.2 analogue to the stress field of the Kobe earthquake (shown in Figure 5.5) without smoothing inherent to inversion procedure. The difference between the synthetic initial and final stresses shows a decrease of the roughness amplitude at all scales preserving the relative importance between large and small scale fluctuations. Persistent spatial fluctuations at large scale are preserved. The stress drop synthetic profile is also self-affine with an identical negative scaling exponent. At the right, the Fourier power spectra of each profiles show a similar pattern as observed for the Kobe earthquake stress maps (displayed in*

Figure 5.5). (b) Same graph as in (a), except that the ideal synthetic self-affine profiles have been smoothed as observed on seismological slip inversions. Large scale fluctuations are not affected by the smoothing procedure. (c) Difference in the pre-factors of the respective Fourier spectra is directly related to slight variations in fault morphology caused by the rupture event. Two examples of synthetic rough profiles with a prescribed Hurst exponent of 0.8 (analogue to that sampled on natural fault surface).

Consequently, in their analysis, the average stress drop over a given surface area was independent of the size of this area since the standard deviation of the spatial variations of the initial shear strength was considered constant on the fault plane. In other words, as the rupture propagates, rupture of an asperity (or subevent) removes the spatial fluctuations in shear strength over the dimension of the asperity. Thus the stress drop remains proportional to the standard deviation of the initial shear strength. As in their model the shear strength was scale independent, therefore each subevents of different sizes released an equal stress.

In the present study, we have constraints on the stress state before and after the mainshock, directly given by the asperity squeeze model and applied for the absolute stress distributions visualized on the Kobe earthquake. The power spectrum modules of the shear stress distribution of the Kobe earthquake are related to their spatial variability (standard deviation) in order to visualize the two "boundary conditions" of our problem. Considering that $std_{\tau_i,\tau_f}(\lambda) = \theta\, \lambda^{H_{\tau_i,\tau_f}}$ and $P_{\tau_i,\tau_f}(k) = \beta\, k^{-1-2H_{\tau_i,\tau_f}}$, we directly deduce that $\theta = \beta^{1/2}$, with $\lambda = 1/k$. In Figure 5.7, after extracting the pre-factors of the power laws fits performed on the Fourier spectrum of the initial and final shear strength of the Kobe earthquake, we deduce the scaling of the variability of the initial and final shear strengths as a function of the length scale.

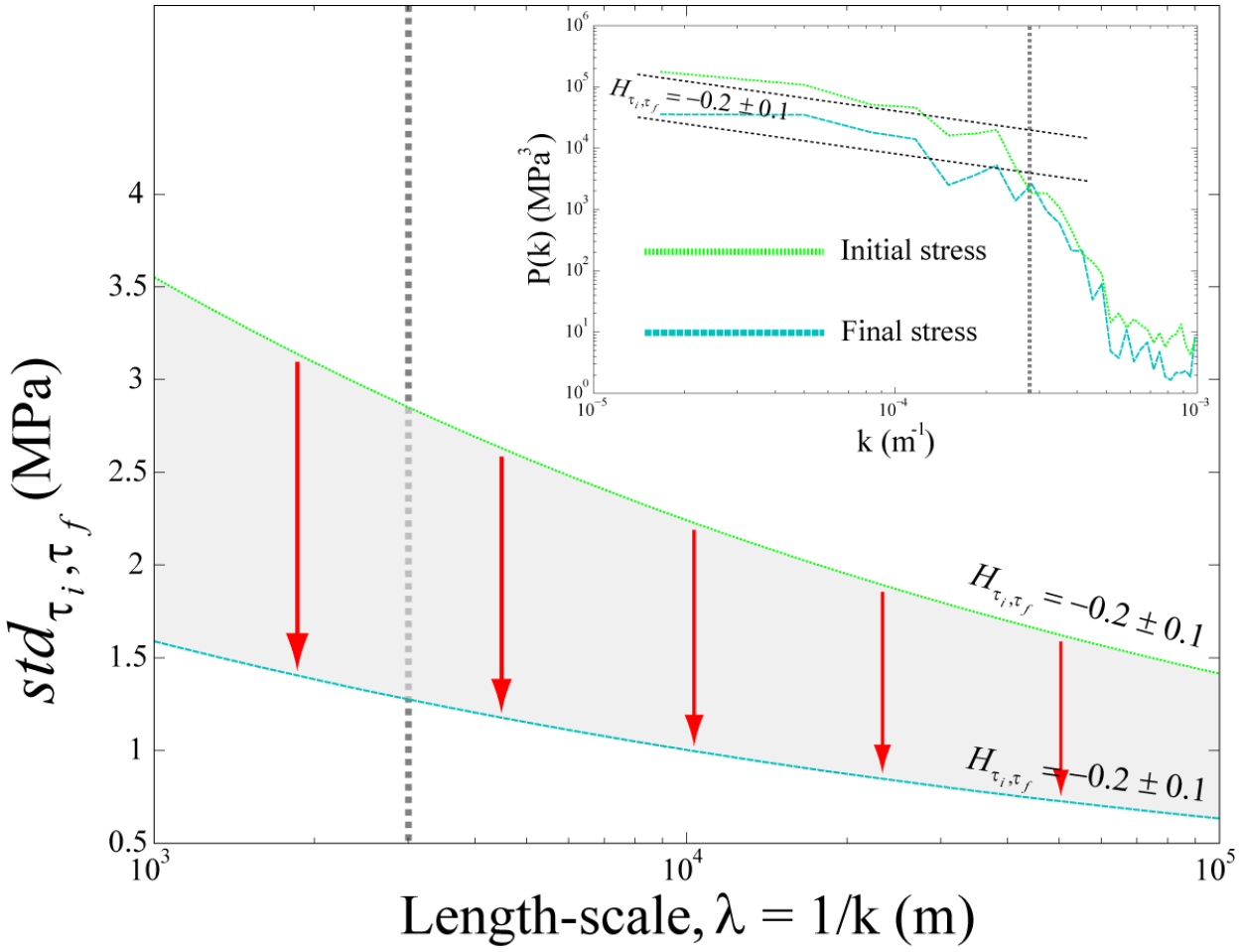

Figure 5.7. *Standard deviation scaling of the initial and final shear strengths of the Kobe earthquake deduced from Fourier power spectra (data from Bouchon et al. 1998). The second order moment of the shear strength distributions, which corresponds to the standard deviation of their spatial fluctuations, is related to the power spectra modules. Each length scales are treated as subevents of hierarchical size constituting the whole earthquake rupture, consequently the evolution of the stress release as a function of the subevent size is conceptualized by the red arrows. On both graphs, the vertical dashed gray lines indicate the smallest length scale at which the stresses variability is known by the seismological inversions (i.e. ~ 4 km).*

Considering that each length scale corresponds to subevents of hierarchical size, it is possible to visualize the evolution of the stress drop as a function of the subevents size. In the framework of a rupture cascade model, the unique way to obtain the spatial distribution of the initial and final shear strength on the Nojima fault plane is to release the condition of stress proportionality to the

initial shear strength at each scale. Indeed, to obtain the final shear strength from the initial one, the stress release is proportional to the initial stress state in order to maintain an identical self-affine regime between the two distributions. Following the same reasoning of Frankel (1991), the stress drop is proportional to the standard deviation of the initial shear strength. As a consequence, the final stress state is still rough and heterogeneous after the rupture propagation on the entire fault plane and could explain the occurrence of aftershocks just after the mainshock. This differs from the model suggested by Frankel (1991), where a homogenous, smooth final stress state is assumed.

A schematic model is presented on Figure 5.8 to describe the relationship between the initial shear strength on the fault plane and the stress drop of each subevent constituting the mainshock in a rupture cascade propagation. The negative Hurst exponent characterizes spatial correlations of both the initial and final shear stress. These correlations have an antipersistent property, which is conceptualized as a sum of sine waves of amplitude to wavelength ratios more important at small scale than at larger scales. As the rupture propagates, the rupture fronts will encounter the small-scale stress variations that will form subevents and their own subevents. When each subevent fails, the stress over its rupture area drops from the solid line in Figure 5.8 to the level of dashed line. Given that this stress drop is proportional to the initial stress state, the smallest subevents bear a larger magnitude of stress change.

Finally, based on a cascade rupture model of earthquake, and constrained by both the initial and final shear strength of the Kobe earthquake, we suggest that the stress drop averaged over the rupture area could be dependent to the size of this rupture. Given the proportionality between the initial shear strength and the stress drop, the scaling relationship reads:

$$\Delta\sigma(l) \propto l^{H_R-1} \tag{5.9}$$

where l corresponds to the size of the events. Note this relationship also implies that the stress drop variability averaged over the rupture area should scale in the same way and therefore increase when decreasing of the rupture area, that is:

$$std_{\Delta\sigma}(l) \propto l^{H_R-1} \tag{5.10}$$

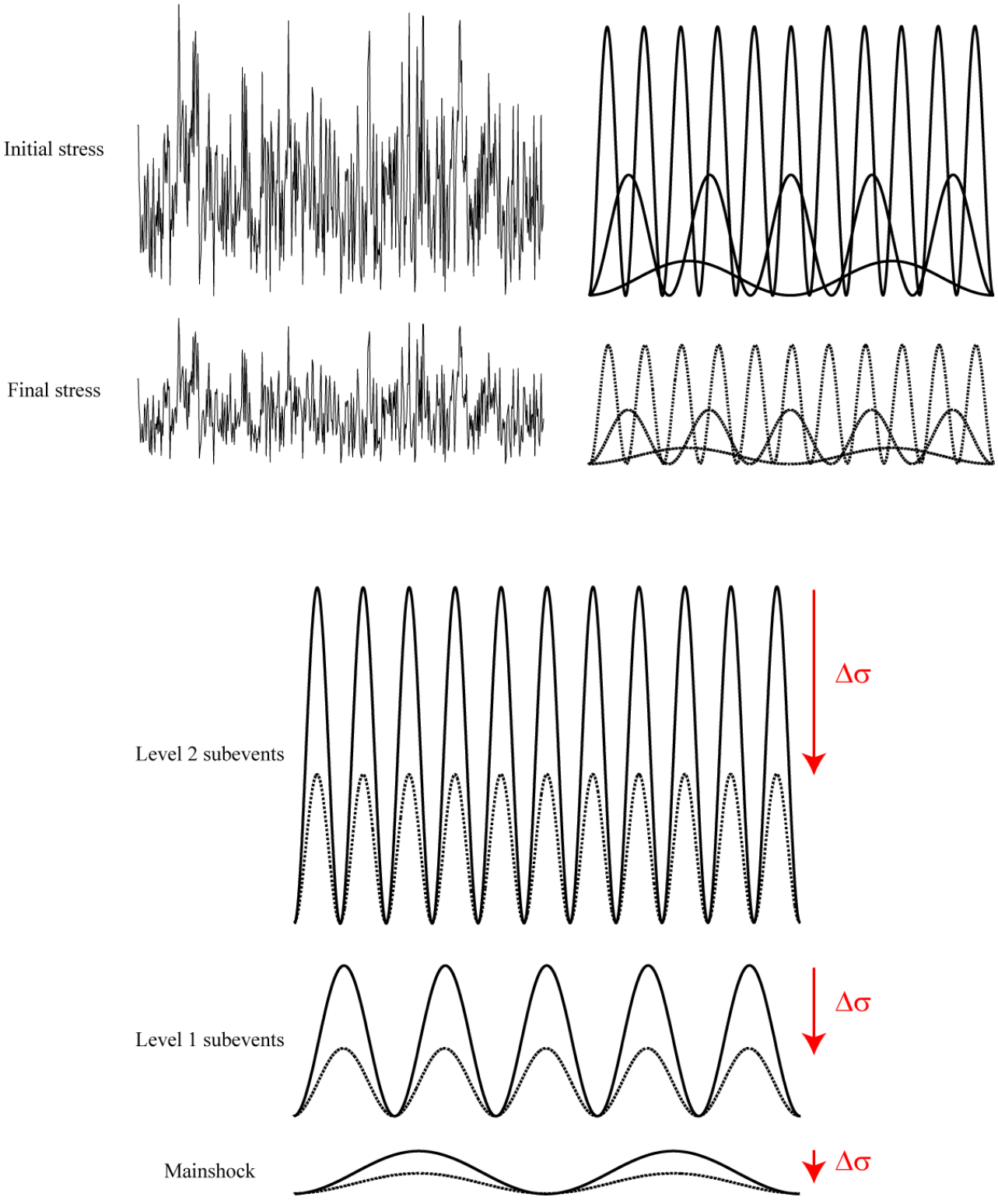
Initial stress
Final stress
Level 2 subevents
Level 1 subevents
Mainshock
Δσ
Δσ
Δσ

Figure 5.8. *Schematic model explaining the relationship between the initial shear strength on the fault plane and the stress drop of each subevents constituting the mainshock in a rupture cascade propagation. The sine waves of amplitude to wavelength ratios are more important at small scales and depict initial and final shear stress profiles characterized by anti-persistent spatial correlations (i.e. negative Hurst exponent). Each wavelength is assimilated to a subevent constituting the mainshock. As the rupture propagates, the smallest subevents fail, and the stress over their rupture area changes (marked by the vertical red arrows) from the solid line (initial shear strength) to the dashed line (final shear strength). When the rupture continues to expand on the whole fault surface, subevent of increasing sizes are activated until the long and smooth wavelength shear strength constituting the mainshock is released.*

5.2.4. B. Implications for earthquake sources parameters: application to Kobe earthquake

To illustrate the theoretical scaling relationships (5.9) and (5.10), we consider the case of the M_L 7.2 Kobe earthquake in 1995 where the stress drop and its standard deviation averaged over the 60x20 km inversion region are rather low and equal to 1.7 MPa and 0.7 MPa, respectively (Bouchon *et al*., 1998). Approximating the rupture surface area as a disk, these two values would correspond to the average stress drop and its variability for a 20 km radius circular rupture. It would be more accurate to approximate the area of the surface rupture of the Kobe earthquake to an ellipse but we emphasize that this assumption of a circular rupture is reasonable since we will consider small events with magnitudes smaller than 6 nucleating on the Nojima fault plane. Given this assumption, we can infer the scaling of the stress drop and its variability as a function of the radius of events nucleating on the Nojima fault plane,

$$std_{\Delta\sigma} = 37\, r^{H_R - 1} \tag{5.11}$$

$$\Delta\sigma = 89\, r^{H_R - 1} \tag{5.12}$$

where r (m) is the radius of the rupture and the stresses are given in MPa.

Taking $H_R = H_{//} = 0.6$, from the roughness results of section 5.2.2, these scaling relationships become:

$$std_{\Delta\sigma} = 37\, r^{-0.4} \tag{5.13}$$

$$\Delta\sigma = 89\, r^{-0.4} \tag{5.14}$$

Figure 5.9 displays the average static stress drop and its variability as a function of the rupture radius. Whereas the average and standard deviation of the stress drop are independent of scale for a self-similar fault surface, it appears that the stress drop fluctuations should be larger at small scales and large stress drop values could be reached for small earthquakes. It is important to emphasize that the scaling relationships (5.13) and (5.14) have only been determined for the case of the Kobe earthquake and the pre-factors are implicitly conditioned by the values given by the seismological inversions of this event. We propose here that this behavior could be generic of earthquakes since the roughness Hurst exponents of fault surfaces and that of slip distribution are systematically measured below unity.

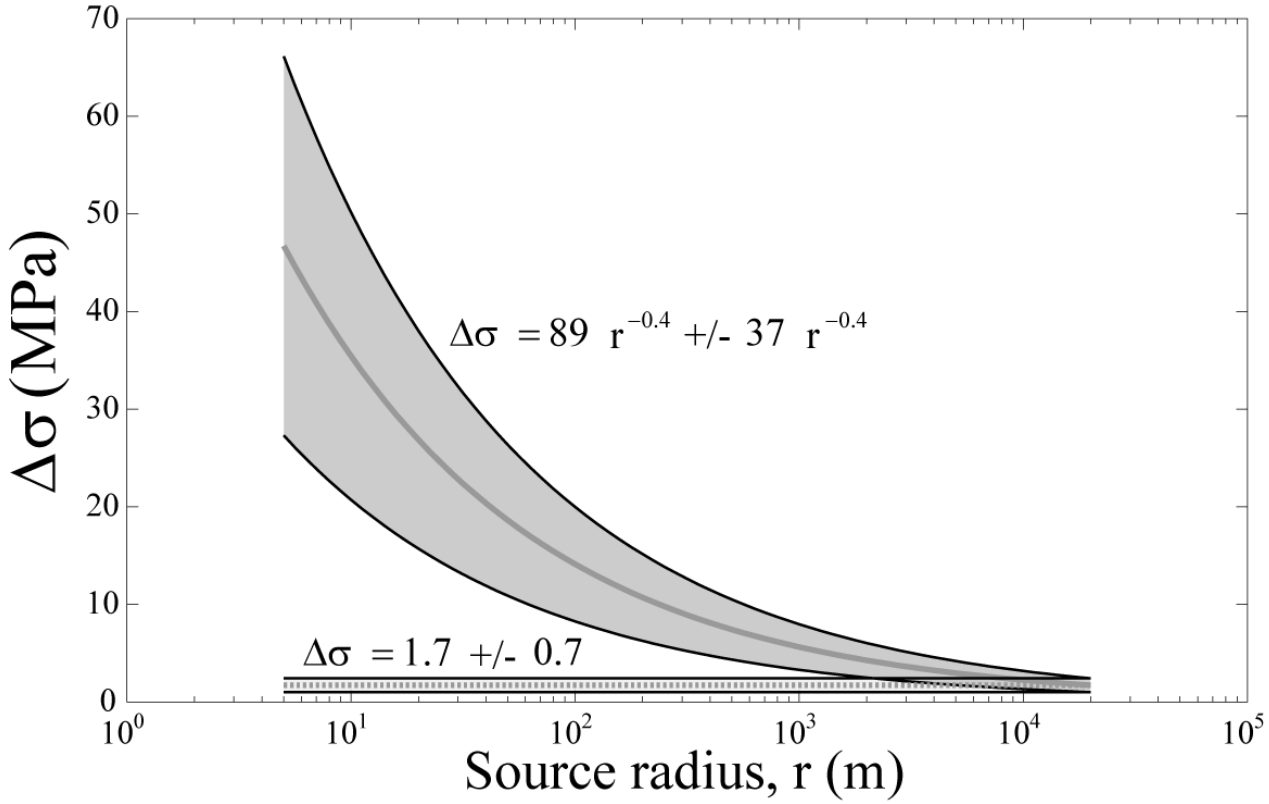

Figure 5.9. *Theoretical scaling model of the average stress drop and its variability, showing their respective evolution with the radius of ruptures nucleating on the Nojima fault plane hosting the Kobe earthquake. It is assumed that fault roughness is characterized by* $H_{//} = 0.6$. *The model of self-similar faulting* $(H_{//} = 1)$ *is also shown for comparison.*

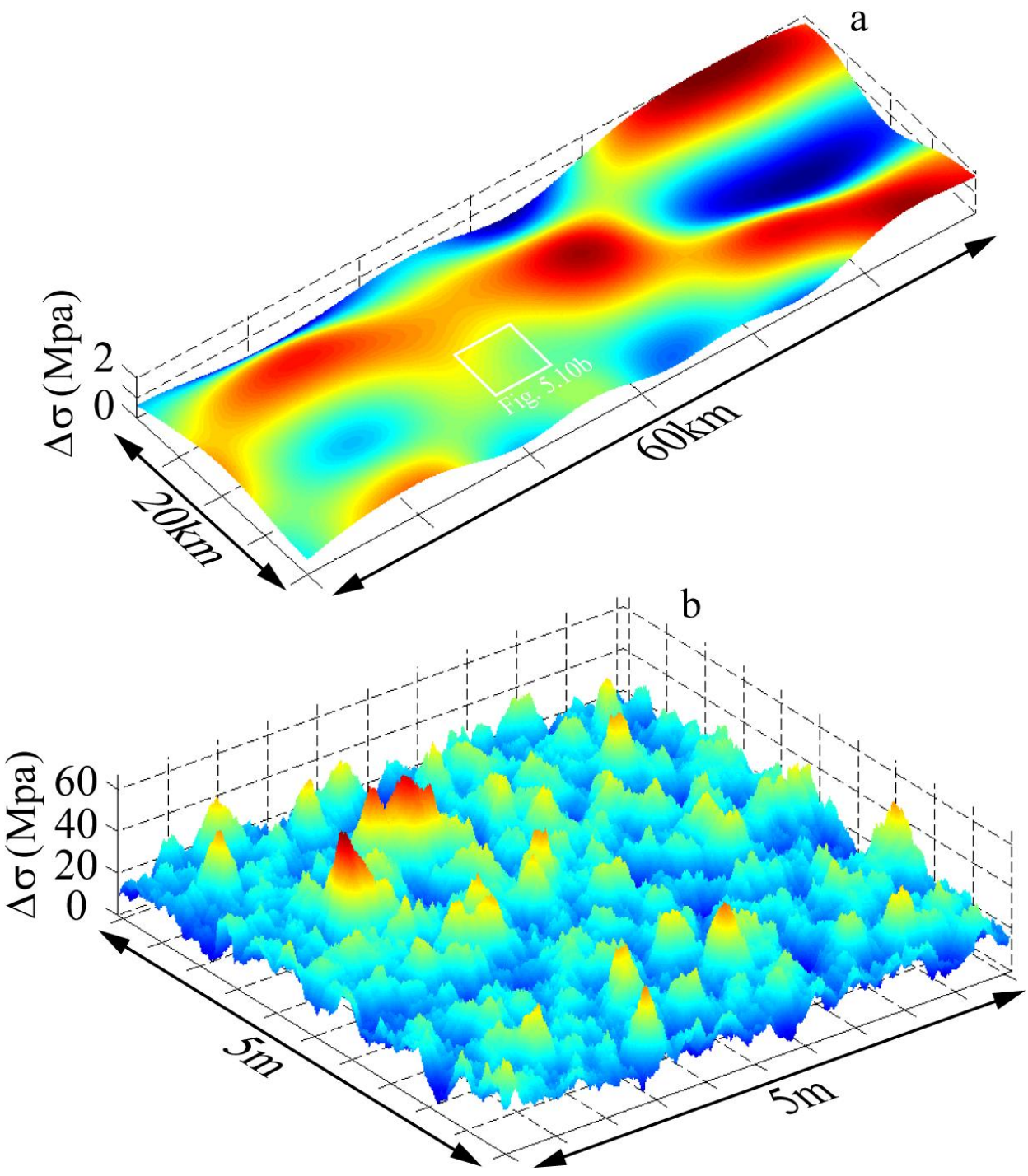
a
Δσ (Mpa)
2
0
20km
60km
Fig. 5.10b
b
Δσ (Mpa)
60
40
20
0
5m
5m

Figure 5.10. *Map views of synthetic self-affine stress drop distributions calculated using the theoretical scaling relationships (5.12) and (5.13). (a) Smooth synthetic stress drop field similar to the inversion results of the Kobe earthquake. The inset corresponds to the map shown on Figure 5.10b. (b) Magnified portion of the map (a) giving access to higher stress drop concentrations at small scales. This illustrates the stress drop distribution inferred for a small earthquake nucleating on the Nojima fault plane.*

Figure 5.10 displays map views of two realizations of synthetic stress drop fields computed with a Hurst exponent of -0.4 (corresponding to the stress drop field for $H_R = H_{//} = 0.6$). A Fourier based method is used to simulate the isotropic self-affine matrix (Candela *et al*., 2009). The synthetic stress drop fields are normalized to the peak amplitude of the field, which implies that areas of stress increase (negative stress drop) are not visible. Figure 5.10a illustrates a smooth stress drop field at large scales, with large correlated regions, similar to the inversion result of the Kobe earthquake. Because slip inversions only resolve the largest wavelengths of stress drop fluctuations, normalized stress concentrations between 0 and 2 MPa are appropriate for this resolution. The implication is that improved resolution of slip yields higher stress drop concentrations. This is shown on Figure 5.10b that highlights a magnified area of the stress drop field (Figure 5.10a) with no smoothing at small scales and that is representative of a small earthquake nucleating on the Nojima fault plane. These realizations illustrate that large-scale fluctuations of stress drop have high-amplitude small-scale variations within them. Given our assumptions, this spatial distribution of the stress drop field can be understood as the expression of two self-affine fault planes pressed together elastically and sheared with frictional sliding (*i. e.* at Coulomb threshold).

Still considering the case of the Kobe earthquake, we estimate some commonly calculated source parameters relationships, such as average static stress drop $(\Delta\sigma)$, average slip (a), area of rupture (A), vs. seismic moment (M_0). One can write the average stress drop in terms of average slip and source radius (Kanamori and Anderson, 1975),

$$\Delta\sigma = \frac{7\pi}{16} G \frac{a}{r} \tag{5.15}$$

and the corresponding moment as (Aki, 1966)

$$M_0 = G\,A\,a \tag{5.16}$$

where G is the shear modulus. Here $G = 30\,GPa$ is taken as a representative value. The average static stress drop $(\Delta\sigma)$, average slip (a), and area of rupture (A), vs. seismic moment (M_0) are shown in Figure 5.11. Combining (5.12) with (5.15), we obtain $a \propto r^{H_R}$ and combining this last relationship with (5.15) it appears that $M_0 \propto r^{H_R+2}$ (5.17). Finally, associating (5.17) with (5.12), as a consequence of the self-affine properties of the fault geometry, the faulting is not self-similar and the average strain associated with the earthquake, or equivalently the average stress, exhibits a weak dependence upon the seismic moment,

$$\Delta\sigma \propto M_0^{\frac{H_R-1}{H_R+2}} \tag{5.18}$$

Taking $H_R = H_{//} = 0.6$,

$$\Delta\sigma \propto M_0^{-0.15} \tag{5.19}$$

Note that in Figure 5.11, we inferred the evolution of the variability of the stress drop with the seismic moment. Compared with a self-similar faulting, our theoretical scaling model based on self-affine fault roughness with $H_{//} = 0.6$, suggests that the rupture surface area should scale strongly with slip and only weakly with seismic moment. In other words, in contrast with a self-similar faulting model where $A \propto M_0^{2/3}$ and $a \propto M_0^{1/3}$, the size of an earthquake, as measured by M_0, would be mainly controlled by the area of slip on the fault $(A \propto M_0^{0.77})$, with the amount of slip having only a weak dependence on M_0 $(a \propto M_0^{0.23})$.

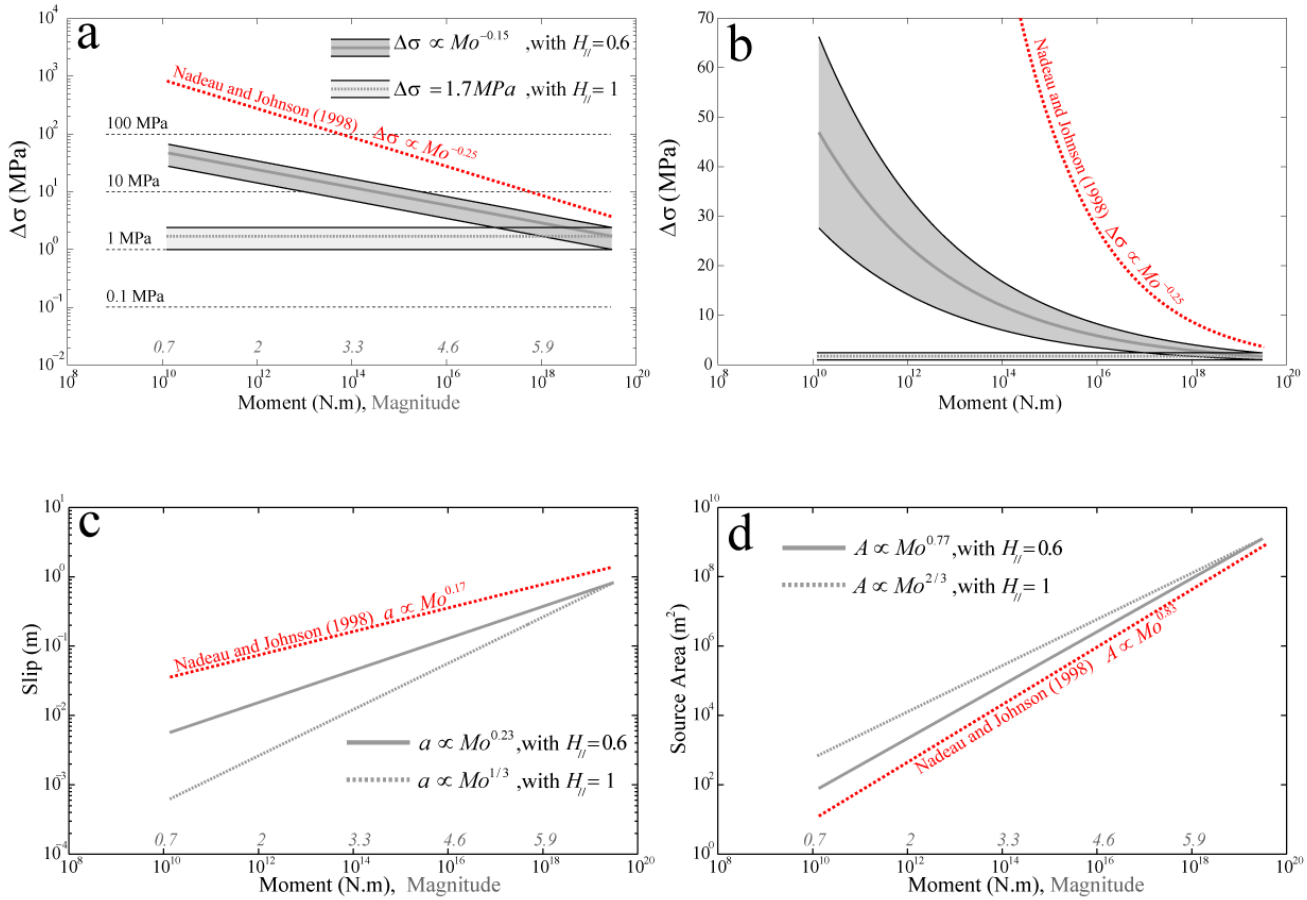

Figure 5.11. *Scaling relationships for the static stress drop (a-b), displacement (c), and source area (d) with seismic moment, inferred for the Nojima fault. In (a), the horizontal dashed black lines indicate the range of seismologically observed constant average stress drop, typically comprised between 0.1 and 100 MPa (e.g. Kanamori, 1994; Abercrombie, 1995). (b) is identical to (a) but plot in semi-log axis in order to highlight the increase of the variability of the stress drop with the decrease of the seismic moment. On each graph, the scaling behavior of these source parameters is displayed, if the Nojima fault roughness was self-similar* $(H_{//}=1)$ *or self-affine* $(H_{//}=0.6)$*. Dashed red lines are the scaling relationships proposed by Nadeau and Johnson (1998).*

5.2.5. Discussion

In this study we have studied the following still debated question: "Do earthquakes scale self-similarly or are large earthquakes dynamically different than small ones?'' In our approach, the squeezing followed by the shearing of two self-affine surfaces, as it would be the case for a fault interface at depth, supports the second hypothesis of this question. So that, the stress drop could be scale dependent and more important for small earthquakes compared to large ones. The aim of this last part is to replace our results with regard to the previous works which support most of the time a self-similar faulting, but also to highlight the observations corroborating our findings. The limitations of our approach and conclusions reached by our study will also be exhibited with respect to the main bias inherent in the estimation of the sources parameters by seismological observations.

5.2.5. A. Evidences of high stress drop for small events

Our scaling model implies only a slight dependence of the stress drop on the event size (Eq. 5.12) and predicts higher values of stress drop for small events (Figure 5.9) which are near the upper bound of the range of seismologically observed stress drops, typically comprised between 0.1 and 100 MPa (e.g. Kanamori, 1994; Abercrombie, 1995). Our scaling arguments (Eqs. 5.11-5.12) suggest that, if a small earthquake with a source radius of $5\,m$ (i.e., a magnitude ~ 0.75 earthquake) would nucleate on the Nojima fault, its average stress drop would approximately reach $50 \pm 20\ MPa$. This estimate is nevertheless conditioned by the low average stress drop (~ 1.7 MPa) over the inversion region of the Kobe earthquake (Bouchon *et al.*, 1998). Taking a rupture of similar size of the Kobe earthquake with a stress drop of 10 MPa given by the seismological inversions, our scaling model would predict a stress drop of nearly $200 \pm 80\ MPa$, which is still close to the upper limit of the large range of seismologically observed stress drops.

In addition, stress drops on the order of hundreds of MPa appear to be rare but have been observed. Munguia and Brune (1984) calculated stress drops in excess of 200 MPa for events in the Victoria, Baja California earthquake swarm of 1978. Kanamori *et al.* (1990, 1993) estimated stress drops for a small earthquake in Pasadena (California) between 30 and 200 MPa. Imanishi and Ellsworth (2006) studied 34 M0.2-M2.1 earthquakes near Parkfield (California) from the

SAFOD Pilot Hole Array and found that half had stress drops greater than 10 MPa, with some exceeding 50 MPa.

5.2.5. B. Experimental ruptures and field observations

On way to estimate if the rupture processes of small and large earthquakes are different, is to attempt to bridge the gap between experimental rupture performed in laboratory and natural large earthquake. The works of McGarr *et al.* (2003, 2010) suggest that stick-slip friction events observed in the laboratory and earthquakes in continental settings, even with large magnitudes, have similar rupture mechanisms. McGarr *et al.* (2003) have revealed that the maximum slips inferred for major earthquakes are consistent with those measured in the laboratory during large scale, biaxial stick-slip friction experiments (Lockner and Okubo, 1983), if differences in the state of stress and loading stiffness are taken into account. Nevertheless, it is important to note that directly due the fact that the friction experiments of Lockner and Okubo (1983) were conducted at low normal stress (i.e. 2.76 MPa for the rupture event analyzed by McGarr et al., 2003), accordingly the stress drop implied was also very low (~ 3 MPa) relatively to typical measurement performed in laboratory.

Stress drops measured in triaxial experiments of shear failure of intact rocks are typically on the order of hundreds of MPa to GPa (e.g., Brace and Byerlee, 1966). Triaxial experiments with sawcut samples have yielded slightly smaller stress drops in the range from tens to hundreds of MPa (Brace and Byerlee, 1966).

In the cascade rupture model (section 5.2.4.A), faults are highly inhomogeneous and large earthquakes are composed by a sum of small asperities with large stress drop within an average fault surface with small stress drop. Therefore, the laboratory failure experiments of Brace and Byerlee (1966) are consistent with this line of thinking, and suggest that stress drops during small earthquakes, constituted by single small asperities, would be relatively high.

Recently, Griffith *et al.* (2009) have proposed an alternative approach for studying the source of small earthquakes, to better characterize the source dimensions and geometry inherent to the seismological inverse problem. Using detailed field mapping of small subvertical strike-slip faults in the Lake Edison granodiorite of the central Sierra Nevada (California), they have measured the rupture length and the slip identified for eight unique events. Assuming elliptical

faults and using the equation (5.15), they calculated stress drops in the range 90-250 MPa for rupture radius of 8-12 m, i.e. in qualitative agreement with our theoretical estimate for earthquakes of similar size (see Figure 5.9). As emphasized Griffith *et al.* (2009), all of the coseismic slip occurred at an interface that may have represented an at least partially strong healed asperity. This support the argument that large earthquakes may be composed of multi-scales small asperities with large stress drop. The smaller the scale of an earthquake, the more likely a single, isolated asperity is sheared.

5.2.5. C. Evolution of the stress drop with the magnitude

Until now we have simply discussed the occurrence of high stress drop for small ruptures but not the dependence of the stress drop with the event sizes. In the case of the scaling of its variability, some seismological observations seems to be in aggreement with the theoretical model inferred by our study. Indeed, Cotton *et al.* (2008) and Akkar and Bommer (2010), observed in their set of seismological data that the ground-motion standard deviation increases when the magnitude decreases. These latter results are consistent with our results since, at first order, ground-motion variability is dependent on stress drop variability (Causse *et al.*, 2008).

In the case of the scaling of the average stress drop averaged over the rupture area, some studies have suggested a scale independent behavior (e.g. McGarr 1999; Ide and Beroza 2001; Ide *et al.*, 2003), finding no evidence of increasing stress drop or apparent stress with magnitude. In particular, the work of McGarr *et al.* (2003) points out that the maximum slip across a small patch within a larger earthquake fault zone scales as the cubic root of the seismic moment. This finding supports the expected relationship between the slip and the seismic moment for a constant stress drop scaling (e.g. Hanks, 1977) and departs from that proposed in our model (see section 5.2.4.B). As opposed, numerous authors (e.g. Abercrombie, 1995; Kanamori and Heaton, 2000; Brodsky and Kanamori, 2001; Prejean and Ellsworth, 2001) have presented evidence suggesting that the apparent stress drop increases with earthquake magnitude. These reported increases have been used to argue for a fundamental change in the earthquake physics above a threshold magnitude. For instance, formation of melt associated with large slip confined to a narrow rupture zone (e.g., Di Toro and Pennacchioni, 2005), thermal pressurization (e.g., Sibson, 1973; Lachenbruch, 1980), elastohydrodynamic lubrication (Brodsky and Kanamori, 2001) or

chemical decomposition (Han et al. 2010, di Paola et al., 2010) might be expected to reduce the resistance to slip and therefore increase the dynamic stress drop (and so the apparent stress). It is conceivable that this type of weakening processes alter the scaling model proposed in our study when a critical event size is reached. In other words, we suspect that the rupture physics is controlled mainly by the fault topography and more especially the stress drop of small earthquakes follows the scaling relationship depicted by the equation (5.9) up to critical size (which is difficult to precisely define).

This line of thought is also supported by Mayeda *et al.* (2007) which states that an abrupt change in stress parameter may take place between the Mw 7 Hector mine earthquake and its moderate-sized aftershocks. One of the conclusions of their study based on the coda spectral ratio method contradicts our theoretical scaling model, that is: the apparent stresses are systematically lower for the aftershocks than the mainshock. In other words, the data of Mayeda *et al.* (2007) show increasing stress drops for earthquake sizes comprise between 3.76 and 5.35 of magnitude where we propose a small decreasing trend.

However, there is some evidence that the stress drop of small events (partially covering the same range of magnitude as aftershocks studied by Mayeda *et al.*, 2007), especially studies that focus on micro earthquakes and repeating earthquakes, scale in the same way proposed by our theoretical model. Indeed, decrease of the stress drop as a power law of the seismic moment as suggested by equations (5.18) and (5.19), is in qualitative agreement with a study of repeating earthquakes on the San Andreas Fault (SAF) in California by Nadeau and Johnson (1998). Based on the recurrence interval of repeating microearthquakes in the magnitude range -0.7 to 1.4 in Parkfield area and an assumed fault slip rate, these authors derived a scaling relationship for displacement, source dimension, and static stress drop with seismic moment. They also estimated moments for eight repeating sequences of events having magnitudes between 3.5 and 4.9 from the Stone Canyon section of the SAF originally discussed by Ellsworth and Dietz (1990) and for repeating sequence of six magnitude 6 events that have occurred at Parkfield since 1857 (Bakun and McEvilly, 1984). The stress drop was observed to decrease as a power law of the seismic moment (Figure 5.11):

$$(\Delta\sigma \propto {M_0}^{-0.25}) \tag{5.20}$$

On Figure 5.11, our scaling relationships and those of Nadeau and Johnson (1998) are compared. The power law relationship (5.20) of Nadeau and Johnson (1998) implies a stress drop of ~ 2000 MPa for the smallest earthquakes with r ~ 0.5m, whereas our model inferred from the Kobe earthquake implies a stress drop of only ~ 100 MPa for an event of identical radius (see Figure 5.11). Although Sammis *et al.* (1999) argued that high stresses cannot be ruled out on physical grounds, they require perfect healing (no microscopic flaws) at the smallest asperities; therefore we suspect that the model of Nadeau and Johnson (1998) may significantly overestimate the actual stress drops associated with repeating earthquakes.

The study of Nadeau and Johnson (1998) was performed on a creeping fault where small repeating earthquakes reveal a weak variation in recurrence interval (T_r) with seismic moment, $T_r \propto M_o^{1/6}$, compared to the usually accepted relationship, $T_r \propto M_o^{1/3}$, which was derived from standard assumption of constant stress drop of self-similar faulting without aseismic slip taking place. Given $T_r \propto M_o^{1/6}$ and considering that the geodetically inferred slip rate on the fault plane at the surface is equal to the displacement on the smaller repeating patches at depth; Nadeau and Johnson (1998) have therefore proposed that the stress drop could decrease when the event size increases (5.20). Other possible explanations of the weakest variation in recurrence interval with seismic moment compared to expected for self-similar faulting have been proposed (Beeler *et al.*, 2001; Sammis and Rice, 2001; Chen and Lapusta, 2009): (i) aseismic slip occurs on repeating patches during the interseismic period, and (ii) geodetically inferred slip rate on the fault plane is greater than the displacement on the smaller repeating patches due to shielding by adjacent or surrounding locked faults. In both cases (i) and (ii), the scaling relation $T_r \propto M_o^{1/6}$ is conserved but the stress drop should remain constant.

The weak variation in recurrence interval with seismic moment proposed initially by Nadeau and Johnson (1998) on the SAF at Parkfield, was also observed by Chen *et al.* (2007) on repeating sequence in a oblique thrust fault zone in eastern Taiwan and in the Japan subduction zone, but with different pre-factors of the power law relationship. Chen *et al.* (2007) have demonstrated that when adjusted to account for differences in the geodetically derived slip rates for the three fault zone, the $T_r - M_0$ relationship is remarkably consistent among the three

regions. It is still being debated which process is responsible for the observed $1/6$ power law dependence of T_r on M_0, however, the consistency of this dependence among diverse tectonic environments suggests that a single process may be taking place in fault zones generally. Given that fault roughness seems to be independent of the geological context, it appears that the elastic squeezing of this last might be a good candidate in the framework of our study and could explain that the unexpected $T_r - M_0$ scaling is related to stress drop dependent on the earthquake size.

5.2.5. D. Numerical simulations and dynamical effects

Bailey and Ben-Zion (2009), using numerical simulation of evolving seismicity and stress field on a heterogeneous fault have higlighted a similar behavior as suggested by our study, that is the average stress drop and its variability increase when the rupture size decreases. Their simulations included fault heterogeneities modeled as heterogeneous initial shear strength, and took into account dynamic overshoots (which are not considered in our present analysis). Their model showed a reduction of both variability in stress drop and its average when the earthquake size decreases.

In an extended analysis of spatial correlations of slip maps for 44 earthquakes, Mai and Beroza (2002) found that the heterogeneous slip distribution follows a self-affine regime characterized by an average value $H_s = 0.71 \pm 0.23$, independent of moment magnitude or source dimensions, and which is in qualitative agreement with the scaling relationship (5.3). This latter observation suggests that dynamical effects produced during an earthquake might be neglected and that our scaling model highlighting the dependence of the average stress drop and its variability with the rupture size applies to seismically active faults.

5.2.5. E. Potential biases of the seismological observations

There is a general lack of data where the stress drop has been computed by consistent methods over a broad magnitude range in a similar region, and scatter in the results tends to be dominated by uncertainty involved in the computation method. In addition, it is important to bear in mind that, since earthquake seismology involves interpretations of elastodynamic waves, the wave field contains only indirect information about source processes (Beeler, 2006). Source

physics influence the radiated field through the magnitude of several dissipative processes, for instance heat dissipation, damage, and latent heat, that reduce the radiated energy and might bias a scaling relationship between sources properties and earthquake size. As pointed out by Allmann and Shearer (2009), the computed stress drop given by slip inversions depends strongly upon modeling assumptions, especially the inherent assumption of constant rupture velocity. For example, slower rupture velocities would imply smaller estimated source radii and larger stress drops.

Prieto *et al.* (2007) have revealed, in estimating source parameters from the seismic spectrum (using the idea of the jackknife variance), that it is important not only to obtain a measurement of the source parameters but also to quantify the uncertainties, by means of confidence intervals. They have shown that, unless the errors are kept small, a slight dependence of the stress drop with earthquake magnitude would pass unnoticed. In other words, given that uncertainty in source parameter estimation is large, any slight trend of the stress drop with the rupture size would remain unnoticed.

To sum up, the fact that the systematic decrease in the average stress drop with magnitude is not observed as an average property in most earthquake catalogs (expect for small repeating earthquakes sequences) could have two origins. Either, the way stress drops are computed may induce a large noise (as underlined by Prieto *et al.,* 2007). Or some physical processes, such as off-fault damage (Dieterich and Smith, 2009), rock fragmentation and comminution, and heat dissipation during rupture, may alter the scale dependence of the elastic stress field proposed in our study.

5.2.6. Conclusions

In the present study, we propose that fault surface geometry may explain the heterogeneous patterns of seismological images of stress drop inferred from slip inversion (Bouchon, 1997; Mai and Beroza, 2002; Lavallée and Archuleta, 2005; Tinti *et al*., 2005). We show that the spatial distribution of the stress drop field or fault strength on a fault plane may be explained by the presence of two self-affine surfaces pressed together elastically and sheared. Given that roughness Hurst exponents of fault surfaces, as measured from field observations, are

systematically below unity in different geological settings, as a consequence the variability of the stress drop (or its standard deviation) spatial fluctuations on the fault plane after the rupture event should increase toward small scales. Indeed, kinematic rupture models are restricted to long wavelength (typically < 1 Hz), and therefore the estimation of the stress drop fluctuations along the rupture surface is thus limited to the largest scales, hence ignoring the largest stress variations that are expected to characterize the small scales because of the large variety of patterns of fault asperities.

Our analysis supports that the initial stress field along the fault constitutes a strong guide for the development of the earthquake and more particularly the stress drop. Assuming no characteristic length scale in fault roughness, and a rupture cascade model of rupture propagation, we have extrapolated the average and standard deviation stress drop scaling behaviors towards the small earthquakes. As a direct consequence of the anti-persistent spatial correlations of the shear strength before and after the earthquake (both directly related to the elastic squeeze of fault asperities), we show that, as the rupture grows, the average stress drop and its variability should decrease with increasing source dimension or seismic moment. Therefore faults may be considered as highly inhomogeneous with large earthquakes composed by a sum of small asperities with large stress drop within an average fault surface with small stress drop. The proposed model addresses more particularly the small to moderate size earthquakes, i.e. that we consider the rupture physics is controlled mainly by the fault topography up to critical size where a fundamental change in the earthquake physics is expected to take place (e.g. formation of melt or other phenomena of dynamic lubrication).

Acknowledgments: This study was supported by the *Agence Nationale pour la Recherche* grant ANR-JCJC-0011-01. We thank Fabrice Cotton and David Marsan for fruitful discussions.

Chapter 6:

Effect of surface morphology on the dissipation during shear and slip along a rock-rock interface that contains a visco-elastic core

6.1. Chapter 6 overview (Présentation du Chapitre 6)

6.1.1. Introduction

Dans ce chapitre, je présente un article publié dans la revue *Pure and Applied Geophysics* (Angheluta *et al.*, 2011). Cet article se situe dans la continuité du chapitre 5, et présente une étude théorique et numérique de l'effet de la rugosité des lèvres de la faille sur la répartition des contraintes cisaillantes dans la couche visco-élastique de matériel endommagé.

6.1.2. Contributors to Chapter 6

Le modèle numérique et la description analytique du problème aborde dans cette étude ont été élaborés L. Angheluta, J. Mathiesen et F. Renard. Les observations de terrain ainsi que l'analyse de la rugosité de la faille de Vuache-Sillingy ont été effectués par F. Renard et moi-même.

6.2. Effect of surface morphology on the dissipation during shear and slip along a rock-rock interface that contains a visco-elastic core

Luiza Angheluta,[1] Thibault Candela,[2] Joachim Mathiesen,[1,3] and François Renard,[1,2]

[1]Physics of Geological Processes, University of Oslo, P.O. Box 1048 Blindern, N-0316 Oslo, Norway.

[2]ISTerre, CNRS, University Joseph Fourier - Grenoble I, OSUG, BP 53, 38041 Grenoble, France.

[3] Niels Bohr Institute, University of Copenhagen, Blegdamsvej 17, DK-2100 Copenhagen, Denmark.

Abstract

High resolution topography measurements of the Vuache-Sillingy fault (Alps, France) reveal a characteristic roughness of the fault zone. We investigate the effect of roughness on the rheology of a planar shear configuration by using a model system consisting of a visco-elastic layer embedded into a rigid solid. The model is discussed in the context of several geological cases: a damage fault zone, a fault smeared with a clay layer, and a shear zone with strain weakening. Using both analytical approaches and finite element simulations, we calculate to linear order the relation between wall roughness and the viscous dissipation in the fault zone as well as the average shear rate.

6.2.1. Introduction

In the Earth's crust, many systems involve deformation along pre-existing interfaces. The fact that these interfaces, loaded by normal or shear stress or a combination of both, locally alter

the stress transmission may lead to several important geological phenomena that occur on all scales. At the grain scale, stress is concentrated along grain boundaries where localized deformation may occur either by dissolution precipitation processes or by surface diffusion (Angheluta *et al.*, 2008; Rutter, 1976). At the outcrop scale, localized dissolution along existing planes leads to the formation of pressure solution seams or stylolites (Arthaud and Mattauer, 1969; Railsback and Andrews, 1995). At the lithospheric scale, shear displacement is also widely observed, along faults in the upper-crust, or in shear zones at greater depth - for a review, see for example Chester *et al.* (2004). In a recent work, we have shown that such mechanical interfaces can become morphologically unstable and roughen with time (Angheluta *et al.*, 2010). All these observations involve deformation past a mechanical discontinuity.

In the present study, we characterize the interaction between the morphology of the interface and the corresponding shear or sliding resistance in a set-up where a visco-elastic layer is embedded between two rigid bodies. For this, we use analytical approaches and finite element simulations in two dimensions to estimate how surface roughness affects the effective shear flow properties. We consider here two elastic solids, separated by a fluid layer of finite thickness H. The contact layer is approximated by a Maxwell visco-elastic rheology representing a core of a fault zone where dissipative processes occur (Chery *et al.*, 2004). The model could be applied to various geological cases: faults that contain a damage zone, faults smeared with a clay layer, shear zones with strain weakening, or stylolites with a clay interface. Note also that a similar approach has been applied in studies of basal flow of glaciers along rough surfaces (Kamb, 1970) and the formation of residual stresses due to slip on wavy faults (Chester and Chester, 2000; Saucier *et al.*, 1992). Here we consider a full visco-elastic rheology and extend on previous analyses by performing a numerical modelling in geometries sampled in the field.

The paper is divided into three sections. In section 6.2.2, we present geological observations of rough fault surfaces and how high resolution topography measurements can help characterizing the self-affine property of the slip surface. In section 6.2.3, we consider relations between this roughness and the rheology of the fault by introducing a simple model of a fault gouge. The effect of small perturbations of the fault surface on the fault dissipation is studied within the linear analysis. The analysis can be extended into the finite amplitude regime using numerical simulations. We compute numerically the stress distribution near a rough surface and

the average flow rate in the Newtonian limit and compare it with the linear theoretical analysis. Finally, section 6.2.4 offers concluding remarks.

6.2.2. Rough geological interfaces

6.2.2. A. Observations of rough faults

In the upper crust, many processes happen at interfaces which generally have mechanical properties different than the bulk. Often these interfaces are not at and have developed complex rough morphologies. Active fault surfaces are known to show corrugation at all scales (Power *et al.*, 1987), see Figure 6.1. Their complex geometry results from the interplay of abrasion processes, crack multi-branching and damage during rupture propagation (Power *et al.*, 1988; Sagy *et al.*, 2007), and healing processes during the interseismic periods (Renard *et al.*, 2000).

With the recent development of accurate Light Detection And Ranging (LiDAR) laser devices, it is possible to measure accurately the topography of such surfaces at all scales (Figure 6.2). These measurements show a non-flat topography from the micrometer scale to the scale of several tens of meters (Candela *et al.*, 2009). Moreover, detailed surface rupture mapping on the kilometer scale also reveals non planar geometry (Klinger, 2010). In several cases, the geometry of slip surfaces has been observed to scale with different power-law exponents in the direction of slip and perpendicular to it (Power *et al.*, 1987; Renard *et al.*, 2006).

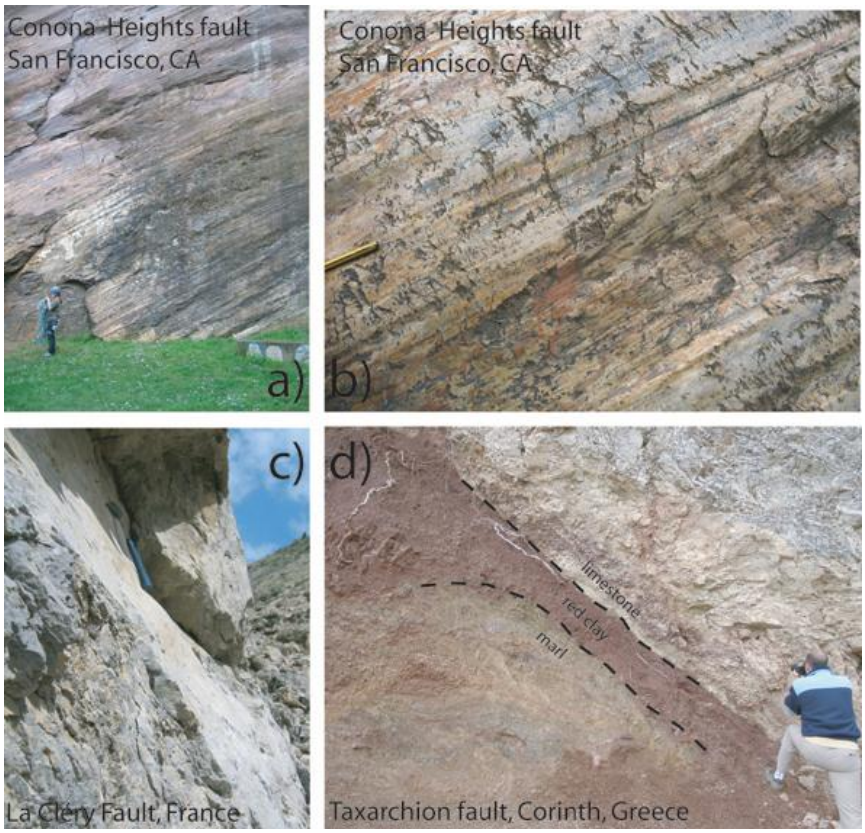

Figure 6.1. *Several fault zones in various geological environments show morphological corrugations at all scales. a) Strike-slip plane in silt rocks of the Corona Heights Fault (San Francisco, CA) showing corrugations at the meter scale. b) Zoom on the slip surface, showing striations and asperities at the centimeter scale (pencil for scale). c) Strike-slip plane of the La Clery Fault (Vercors, France), in limestones, show large wavelengths topographical variations (hammer for scale). d) Red clay layer drag along the Taxarchion Fault (Corinth, Greece) smear this normal fault plane.*

In such faults, a weaker layer or damage zone (from meters to tens of meters wide (Shipton *et al.*, 2006)) is sandwiched between less damaged rock bodies (Caine *et al.*, 1996; Chester and Logan, 1986). This zone may creep slowly, either permanently (i.e. the creeping segment of the San Andreas Fault, north of Parkfield, CA) or for a short period after a major earthquake, where afterslip is often measured (for a review on afterslip processes see, for example, Pritchard and Simons, 2006). These observations indicate that the motion along the fault is able to overcome the morphological roughness asperities, usually without any emission of seismic waves.

Therefore, some time-dependent dissipative deformation mechanisms are at work during aseismic slip.

At the outcrop scale, it is also common to observe, in faulted sedimentary basins, that clay layers smear a fault interface (Egholm, 2008) and lubricate it (see Figure 6.1d). In this case, the clay layer, with a visco-plastic behavior, is often strongly dragged, sheared and internally deformed during slip, as shown experimentally by Cuisiat *et al.* (2010). In general, the clay layer must deform along the interface such to overcome the possible roughness of fault interfaces.

6.2.2. B. Roughness of the Vuache-Sillingy strike-slip fault

The roughness of a slip surface of the Vuache-Sillingy has been measured for spatial wavelengths covering more than 6 decades. This fault is considered as a model system and the results could be extrapolated to other faults which show similar scaling properties (Power *et al.*, 1987; Sagy *et al.*, 2007). This strike-slip fault, with a small normal component, is located near Annecy in the French Alps (Renard *et al.*, 2006) and exposes well-preserved slip surfaces in carbonate rocks (Figure 6.2a). The fault surface has been measured at different scales using three high resolution devices. At the outcrop scale, the morphology of the slip surface was measured using a LiDAR device (see Renard *et al.* (2006) for more details).

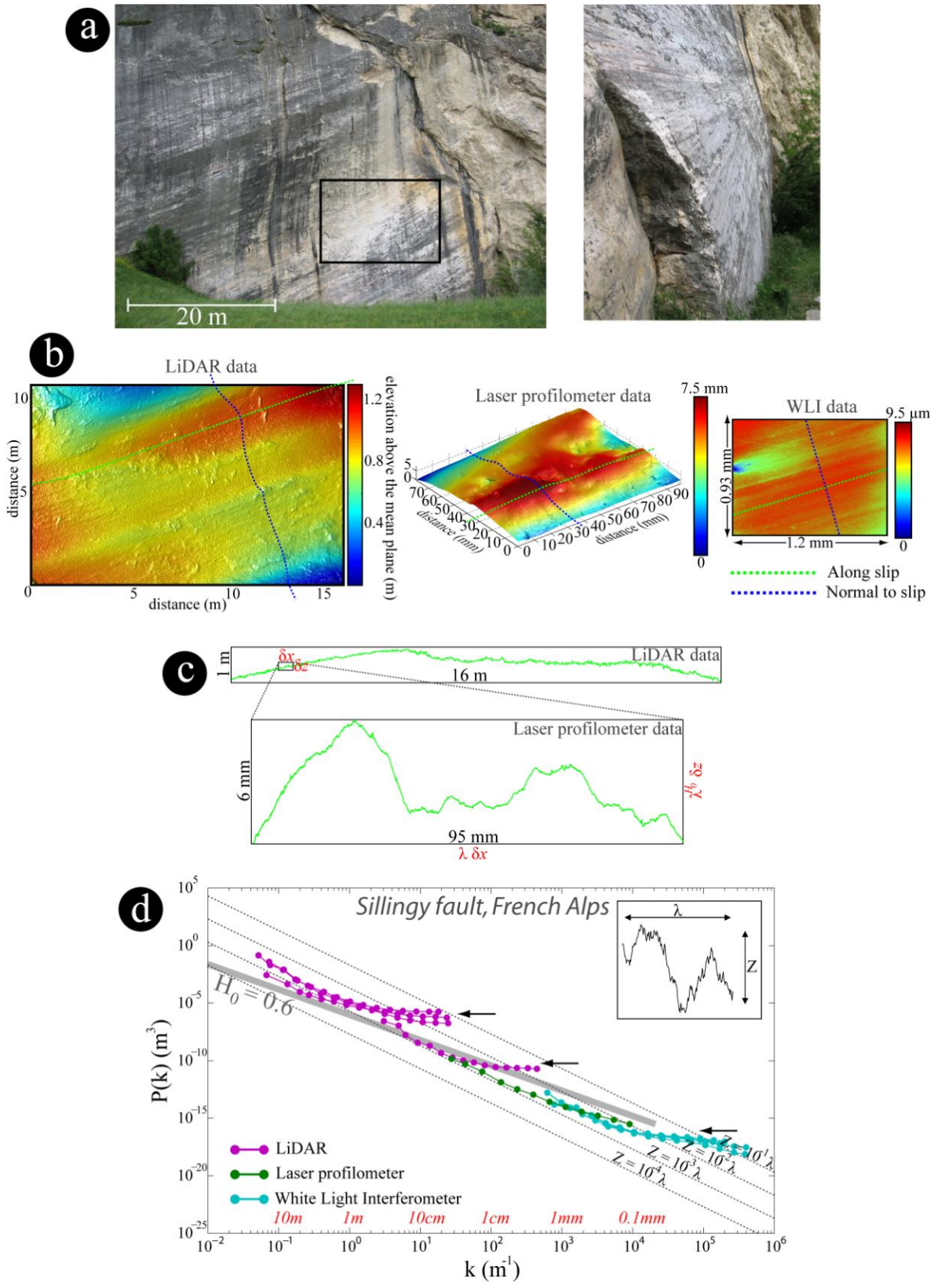
a
20 m
b
LiDAR data
distance (m)
elevation above the mean plane (m)
Laser profilometer data
distance (mm)
7.5 mm
WLI data
9.5 µm
0.93 mm
1.2 mm
Along slip
Normal to slip
c
1 m
δx
δz
LiDAR data
16 m
Laser profilometer data
6 mm
95 mm
λ δx
d
Sillingy fault, French Alps
H0 = 0.6
P(k) (m3)
k (m-1)
LiDAR
Laser profilometer
White Light Interferometer
10m
1m
10cm
1cm
1mm
0.1mm

Figure 6.2. *Surface roughness results of the Vuache-Sillingy strike-slip fault (French Alps). (a) The fault surface consists of many discrete slip surfaces at all scales separating lenses of variably deformed fault rock. The black rectangle corresponds to the surface shown on (b). (b) Examples of Digital Elevation Model (DEM) at the outcrop scale (LiDAR) and at the laboratory scale (laser profilometer, white light interferometer). (c) Representative 1-D self-affine profiles of the slip surface extracted and detrended from the DEM (b) along the direction of slip. Magnified portion of the profiles at the LiDAR scale (up) has a statistically similar appearance to the entire profile when using a self-affine transformation with a Hurst exponent equal to 0.6. (d) Fourier power spectrum calculated for the fault surface along slip, covering 6 orders of magnitude of spatial wavelengths. Power-law fit (thick gray line) with a prescribed roughness exponent ($H_0 = 0.6$), connecting the field and laboratory data, is shown on plot for eye guidance. The inset displays an example of the height elevation Z (y-axis) versus wavelength (x-axis) of a rough profile. Contours (black dotted line) representing constant elevation Z to wavelength ratio, reflecting a self-similar behavior, are provided to allow easier interpretation of the spectra. Black arrows (at the bending of spectra) indicate the level of noise of the LiDAR and the lower limit for the fit performed at the WLI scale.*

In the present study, we complement these outcrop data with laboratory scale measurements. We have measured the topography of several hand samples using a laser profilometer, with a height resolution down to 1 micrometer and spatial increments of 30 micrometers; and a white light interferometer, with a height resolution down to 1 nanometer and spatial increments of 0.5 micrometer. The results of each topography measurement is a Digital Elevation Model (DEM) of the slip surface (Figure 6.2b).

The slip surface shows corrugations at all scales and a slight anisotropy is observed, due to slip along a well-defined direction. We have extracted several hundred of profiles in this direction of slip to analyze the statistical properties of the fault roughness (Figure 6.2c). A Fourier power spectrum method was used, which has been shown to be robust and reliable, to characterize scaling properties of surfaces (Candela *et al.*, 2009). For all 2D DEM data, the topography of the slip surfaces shows a self-affine geometry, demonstrated by a linear relationship when plotting on log-log axes the Fourier Power spectrum versus the spatial wavenumber (Figure 6.2d). The different slip surfaces analyzed cover approximately 6 decades

of length scales and show a scaling relationship with a Hurst exponent H_0 close to 0.6 for profiles along the slip direction. These data confirm and extend previous studies of scaling properties of fault surfaces (Power *et al.*, 1987, Renard *et al.*, 2006).

6.2.3. Visco-elastic shear flow between rough walls

6.2.3. A. Setup

We now consider a simple model of a fault consisting of two undeformable plates separated by a fault gouge or fluid layer of thickness H as sketched in Figure 6.3. Either one or both of the plates are assumed to have a rough surface and the middle layer is assumed to satisfy a Maxwell visco-elastic rheology. Using this system, we analyze how the rough walls change the mean shear stress when the top plate moves with a fixed velocity. In other words, we study an effective rheology of a system where the roughness of the outer plates couple to the flow properties of the full system. In general, assuming that the average separation distance H is fixed, we find that, for a small amplitude roughness of the outer surfaces, the viscous dissipation increases while the flow rate decreases with the amplitude.

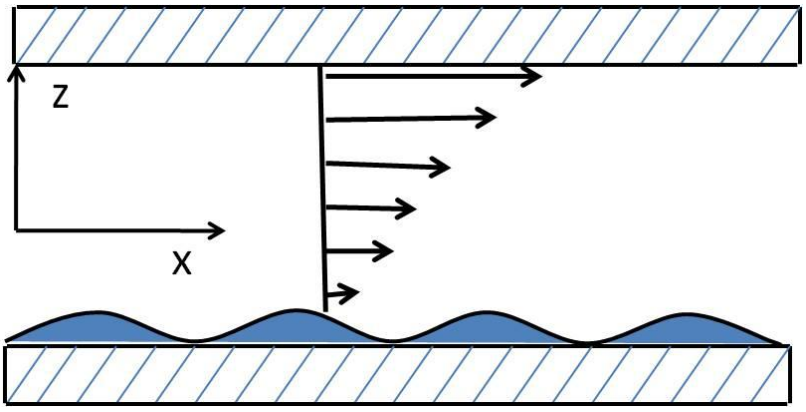

Figure 6.3. *Model system of a visco-elastic layer trapped between two rigid planes. The lower plane is assumed to have a rough surface and a simple shear is applied to the system by moving the upper plane at a constant velocity. This system is utilized in an analysis of the effective rheology of a fault system.*

The governing equations are given by the mass and momentum conservation laws supplemented by the rheological equation of state. Moreover, the visco-elastic layer is assumed to be incompressible with constant density, which implies that

$$\partial_i v_i = 0, \tag{6.1}$$

and the momentum conservation in the limit where fluid inertia can be neglected is satisfied by the relation

$$\partial_i T_{ij} = 0, \tag{6.2}$$

where T_{ij} is the fluid stress tensor. The stress components can be decomposed into a homogeneous isotropic part and deviatoric components $T_{ij} = -p\delta_{ij} + \tau_{ij}$, where the deviatoric components τ_{ij} can be related to the strain rate by the Oldroyd-type equations of state (Oldroyd, 1950; Shankar and Kumar, 2004) for a Maxwell visco-elastic fluid

$$\frac{\mu}{G}(\partial_t \tau_{ij} + v_k \partial_k \tau_{ij} - \partial_k v_i \tau_{kj} - \partial_k v_j \tau_{ki}) + \tau_{ij} = \mu(\partial_i v_j + \partial_j v_i), \tag{6.3}$$

where G is the elastic shear modulus and μ is the Newtonian viscosity. These equations are brought in a non-dimensional form by rescaling the spacial coordinates in units of the layer thickness H, the velocity in units of the upper boundary velocity V, time and stresses are given in units of H/V, $\mu V/H$ respectively. The rough bottom surface is positioned in dimensionless units at $z_b(x)$. With these rescalings, Eq. (6.3) is equivalent to

$$W(\partial_t \tau_{ij} + v_k \partial_k \tau_{ij} - \partial_k v_i \tau_{kj} - \partial_k v_j \tau_{ki}) + \tau_{ij} = \partial_i v_j + \partial_j v_i, \tag{6.4}$$

where the variables now are dimensionless and the $W = \dfrac{\mu V}{H G}$ is the Weissenberg number representing the ratio between the stress relaxation time and convective timescale. Newtonian rheology is obtained in the limit of instant stress relaxation, i.e. $W = 0$. To model the relative slip between plates, we assume that the top plate moves at a constant velocity, while the bottom plate is fixed, namely

$$v_x(x,1) = 1, \qquad v_z(x,1) = 0 \tag{6.5}$$

$$v_x(x, z_b) = 0, \qquad v_z(x, z_b) = 0. \tag{6.6}$$

In the case where the confining surfaces are flat, i.e. $z_b = 0$, the steady state solution of the flow is obtained by matching the boundary conditions, thus $v_x^{(0)} = z$, $v_z^{(0)} = 0$. Here we have introduced an upper index which refers to the solutions around a flat interface. If we now insert

the fluid velocity into the equations of state, Eq. (6.4), we determine the stress components, i.e. $\tau_{xz}^{(0)}=1,\ \tau_{xx}^{(0)}=2W$ and $\tau_{zz}^{(0)}=0$. Notice the jump in the normal stress components $\tau_{xx}^{(0)}-\tau_{zz}^{(0)}$, which vanishes in the Newtonian limit.

6.2.3. B. Small perturbations to a flat fault interface

While the flow field readily follows when the interfaces are at, the calculation for a system with rough interfaces becomes more involved. We now derive expressions for the steady state dynamics and the corresponding stress state in the limit where the interfaces are roughened by small amplitude perturbations. We restrict ourselves to consider perturbations of the lower interface only, which is assumed to have a height profile in the z-direction given by the expression $z_b=\sum_n A_n e^{inqx}+c.c.$, where A_n is the amplitude (in units of H), n is the Fourier mode and $q=2\pi/\lambda$ is the characteristic dimensionless wavenumber. The linear regime is set by the condition $nqA_n<<1$ for all n. In particular, we consider a sinusoidal perturbation, for which $A_1=const$ and $A_n=0$ for $n>1$.

For small morphological amplitudes $|A_n|<<1$, all the relevant fields (velocity and stress) are expanded around the unperturbed state as:

$$F(x,z)=F^{(0)}(x,z)+\sum_{n=1}^{\infty}(F^{(n)}(z)e^{inqx}+c.c.), \tag{6.7}$$

where the function $F(x,z)$ is introduced as a generic expression for the variable under consideration. The disturbance field is decomposed into Fourier modes denoted by $F^{(n)}(z)$, which are determined from the linearized governing equations. After substituting the Fourier modes for stress and velocity into Eqs. (6.1), (6.2) and (6.4), the subsequent equations can be reduced to a single equation in $v_z^{(n)}(z)$ which has a general solution given by (Gorodtsov and Leonov, 1967; Shankar and Kumar, 2004)

$$v_z^{(n)}=B_1\,z\,e^{nqz}+B_2\,z\,e^{-nqz}+B_3\,e^{nq(-iW+\sqrt{1+W^2})z}+B_4\,e^{-nq(iW+\sqrt{1+W^2})z}. \tag{6.8}$$

The other component $v_x^{(n)}(z)$ follows directly from Eq. (1), namely

$$v_x^{(n)}(z) = \frac{i}{qn}\frac{dv_z^{(n)}(z)}{dz}. \tag{6.9}$$

The coeffcients B_k, $k = 1,\ldots 4$, are obtained by inserting the expressions for $v_x^{(n)}(z)$ and $v_z^{(n)}(z)$ into the boundary conditions from Eqs. (6.5)-(6.6). To the first order in the surface amplitude, the velocity modes satisfy the following boundary conditions

$$v_x^{(n)}(0) + A_n = 0, \qquad v_z^{(n)}(0) = 0 \tag{6.10}$$

$$v_x^{(n)}(1) = 0, \qquad v_z^{(n)}(1) = 0, \tag{6.11}$$

where the nontrivial equation for $v_x^{(n)}$ follows from an expansion at the perturbed interface,

$$v_x(x, z_b) = v_x^{(0)}(x,0) + \sum_n [\partial_z v_x^{(0)}(x,0) A_n + v_x^{(n)}(0) + O(A_n^2)]\, e^{i n q x} + c.c., \tag{6.12}$$

and using the planar Couette solution, $\partial_z v_x^{(0)}(x, z) = 1$. Solving the system from Eqs. (6.10)-(6.11), we determine the coefficients B_k as a function of amplitudes A_n, Weissenberg number W and characteristic wavenumber q.

6.2.3. C. Effective flow and energy dissipation

In this section, we study the relation between wall roughness, mean flow rate and bulk energy dissipation. It is determined by the strain rate field given as the gradient of the velocity field, $e_{ij} = \partial_j v_i + \partial_i v_j$, where $\{i, j\} := \{x, y\}$. The shear rate, for instance, is reconstructed from the velocity Fourier modes and assumes the form

$$e_{xz}(x, z) = 1 + 2\sum_n \Re\left\{ [\partial_z v_x^{(n)}(z) + inq v_z^{(n)}(z)] e^{inqx} \right\}. \tag{6.13}$$

Similar expressions apply for the other strain rate components e_{zz} and e_{xx}. In general, the above expression depends on the detailed shape of the rough surface; however, we shall here consider an interface described by a single-mode profile $z_b = 2A_1 \cos(qx)$ .Then, the mean flow rate is obtained by the area average of the shear strain rate and given by

$$\langle e_{xz} \rangle = 1 + \frac{q}{2\pi}\int_0^{2\pi/q} dx \int_{z_b}^{1} dz\, e_{xz}(x, z) \approx 1 + f(q, W) A_1^2 \tag{6.14}$$

where $f(q,W)$ appears from the lowest order Taylor expansion in the roughness amplitude A_1. Similarly the mean energy dissipation rate in the bulk, $|\dot{E}|$, is computed as the area integral of $\left|\sum_{i,j}\partial_i v_j\right|^2$, thus

$$|\dot{E}| = \frac{1}{2}\left[1+\frac{q}{2\pi}\int_0^{2\pi/q} dx \int_0^1 dz(2e_{xz}^2 + e_{xx}^2 + e_{zz}^2)\right], \tag{6.15}$$

which to the lowest order in A_1 becomes

$$|\dot{E}| \approx \frac{1}{2}[1+g(q,W)A_1^2]. \tag{6.16}$$

The bulk energy dissipation depends both on the fluid rheology and the surface roughness. Although the function $g(q,W)$ follows directly from the linear expansion, it cannot be represented in a simple and short form.

6.2.3. D. Newtonian limit

Relatively simple expressions can be obtained in the Newtonian limit, i.e. when $W=0$. From Eq. (6.4), we observe that, in this case, the strain rate is the same as the deviatoric stress τ_{ij}. In particular, the shear strain rate equals to

$$\begin{aligned} e_{xz}(x,z) = 1 - \frac{4q\,A_1\cos(qx)}{\cosh(dq)-1-2q^2}[&q(2-z)\cosh(qz)+(2q^2z-2q^2-1)\sinh(qz) \\ &+ qz\cosh(qz-2q)+\sinh(qz-2q)]. \end{aligned} \tag{6.17}$$

Straightforwardly, we can determine the shear drag by evaluating the above expression on top and bottom surfaces, with the final result given by

$$\tau_{xz}(x,1) = 1 - 8qA_1\frac{q\cosh(q)-\sinh(q)}{\cosh(2q)-1-2q^2}\cos(qx) \tag{6.18}$$

$$\tau_{xz}(x,z_b) = 1 + 4qA_1\frac{\sinh(q)-2q}{\cosh(2q)-1-2q^2}\cos(qx). \tag{6.19}$$

The wall drag varies linearly with the roughness amplitude and frequency and, in a one mode approximation, alternates between regions of maximum and minimum resistance. These regions are located oppositely on the two plates. Namely, the maximum drag is set at protrusion of the

rough bottom surface, while the same point on the top at surface corresponds to a minimum drag. Also, inserting Eq. (6.17) into Eq. (6.14), we find that the effective shear flow depends on the amplitude to the lowest order,

$$\langle e_{xz} \rangle = 1 - 4q \frac{\sinh(2q) - 2q}{\cosh(2q) - 1 - 2q^2} A_1^2 . \tag{6.20}$$

We notice that in Eq. (6.20), the mean flow rate decreases monotonically with amplitude A_1 and wavenumber q and at some point will start having negative values corresponding to a change in the flow direction. This means that the linear prediction will break down at finite amplitudes and, one would expect that the mean shear will reach a minimum saturation value. To verify this, we resort to numerical simulations to study the steady state flow properties around a surface with a larger roughness amplitude.

A decrease in the mean flow rate is associated with an increase of the mean viscous dissipation, when $g(q,0) > 0$ as seen in Figure 6.6.

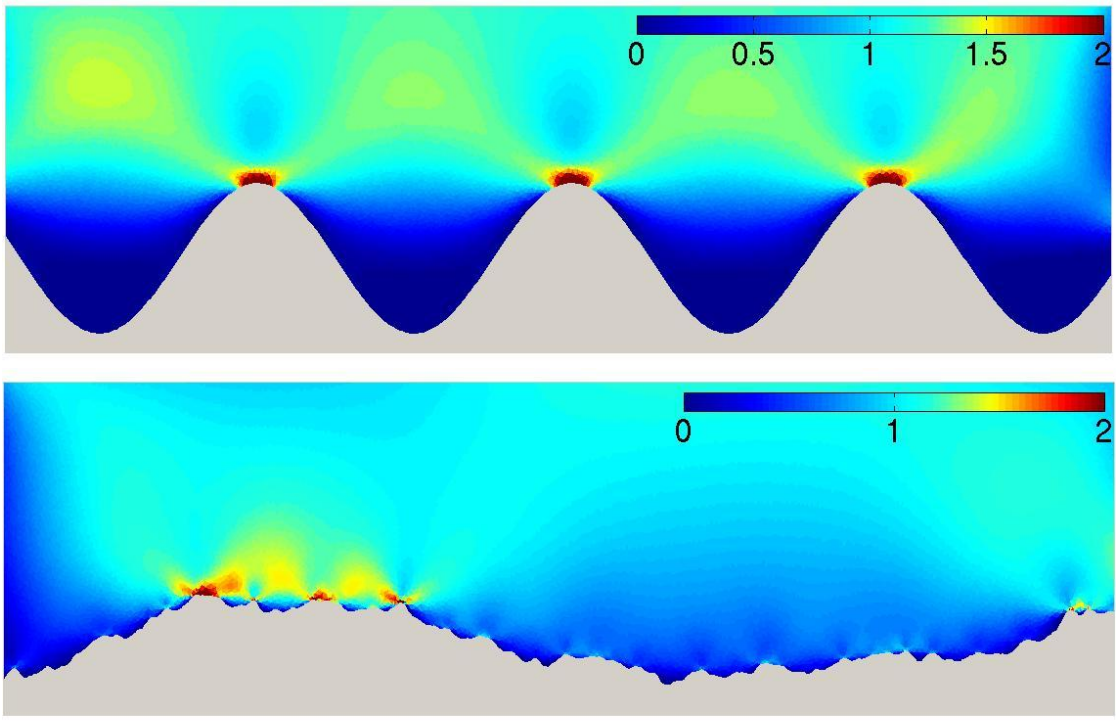

Figure 6.4. *Viscous shear flow along a lower rough surface. Left panel shows the flow profile in the case of a single harmonic perturbation. Right panel corresponds to a shear flow past a random surface with a Hurst exponent* $H_0 = 0.6$. *The color scale represents the magnitude of the dimensionless shear* τ_{xz} *and the velocity field is shown in the vicinity of the rough surface.*

6.2.3. E. Numerical approach

In order to simplify the analysis, we shall here assume that the embedded layer in our model configuration effectively behaves like a viscous fluid. That is, we consider the case where $W = 0$ for which the constitutive equations, Eqs. (6.1)-(6.4), reduce to those of an incompressible Stokes flow. We discretized the equations using a Galerkin finite element scheme on an unstructured triangular mesh. In general, the incompressibility condition is difficult to tackle numerically, since it leads to a singular matrix in the pressure equation. One way to resolve this problem is to use a mixed finite element formulation with quadratic velocity shape functions and a discontinuous linear interpolation for the pressure degrees of freedom. Our numerical implementation follows the algorithm proposed in Dabrowski *et al.* (2008).

A snapshot of the shear stress field for a finite amplitude roughness is illustrated in Figure 6.4. We observe that the presence of a rough interface locally disturbs the flow profile of the viscous layer. This in turn, will lead to changes in the overall shear resistance of the system and thereby increase the energy dissipation in the fault.

A comparison between the theoretical prediction given in Eq. (6.20) and the numerically computed mean shear stress is shown in Figure 6.5. In general, the increase in shear resistance becomes less pronounced as the roughness amplitude is increased. It might be speculated that in a real system the resistance might even start to decrease for large roughness amplitudes, since vortices may form and remain trapped in valleys of the surface morphology, e.g. Skjetne *et al.* (2009).

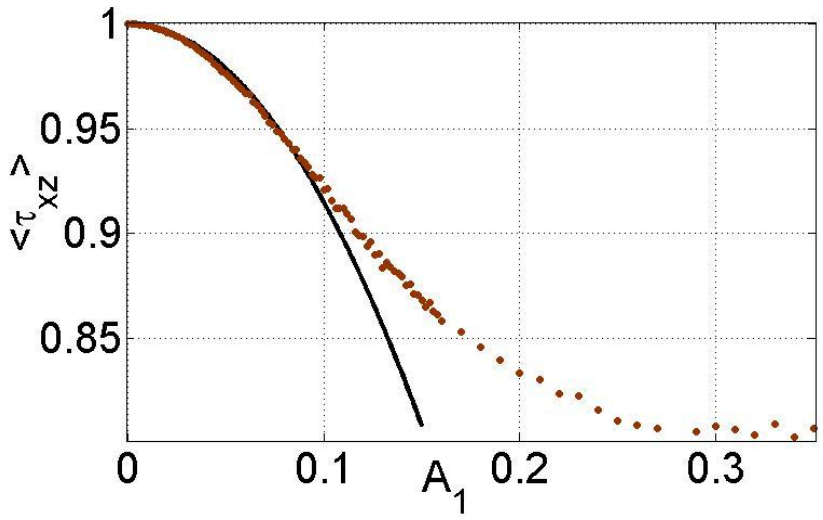

Figure 6.5. *Mean shear stress as a function of the roughness amplitude in the viscous limit* $W=0$ *and for a harmonic perturbation with* $q=1$. *Data from numerical simulations are shown by red dots and the black curve corresponds to the theoretical value obtained from the linear analysis, Eq. 6.20. It is observed that the linear analysis breaks down for a ratio between roughness amplitudes and layer thickness around 0.1.*

6.2.3. F. Effect of fluid elasticity

For a finite W number, we notice that, compared to the Newtonian limit, there is an extra contribution to the strain rate due to stress relaxation, as shown in Eq. (6.4).

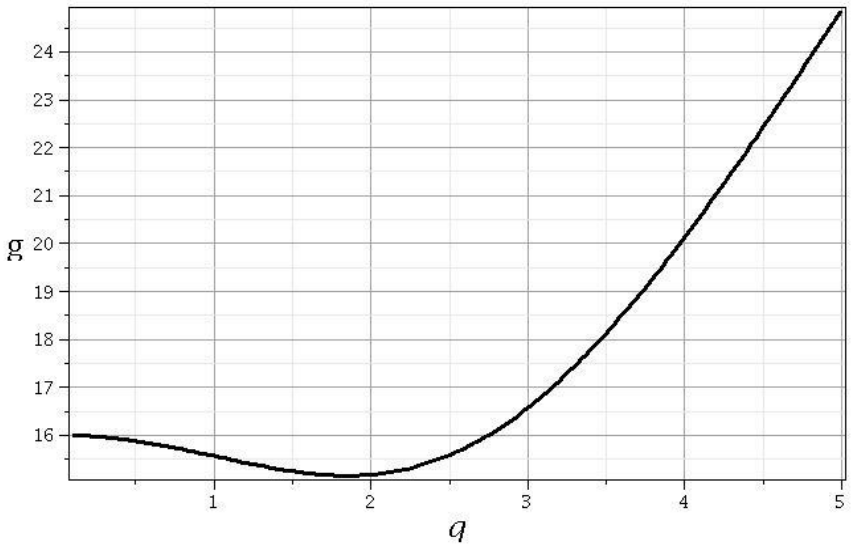

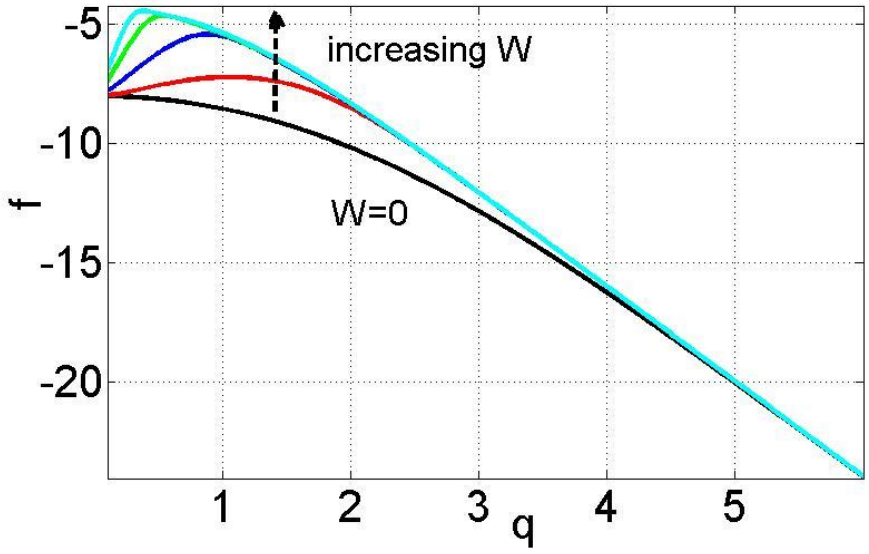

Figure 6.6. *(top panel)* $g(q,0)$ *showing the increase in the mean viscous dissipation with the amplitude and wavenumber. (bottom panel) The coefficient* $f(W,q)$ *from Eq. 6.14 as a function of wavenumber* W *and* q.

Thus, measuring the shear stress is not the same as measuring the strain rate. That being said, the mean flow rate also decreases with the amplitude for $W > 0$, as shown in Figure 6.6, albeit at a slower rate compared to the Newtonian limit. The fact that the shear flow rate at a given roughness is larger for a visco-elastic fluid than for a purely viscous one can be related to a positive contribution of the stress relaxation as suggested by Figure 6.6.

6.2.4. Concluding remarks

Recent measurements of fault slip surfaces have revealed a morphological roughness that spans a wide range of scales. For most active faults, it is likely that the roughness may develop on a time scale different than that introduced by the shear rate. The exact mechanisms leading to rough interfaces are largely unknown and may be related to both damage accumulation and recovery. On short time scales, rapid rupture can damage wall rocks and produce abrasive wear, while on a longer time scale, the branching of fractures or healing processes may corrugate the slip surface.

Here, we have considered the implications of this roughness on the dynamics of a fault by introducing a simple model consisting of a visco-elastic layer sandwiched between two rigid plates. The main result of our analysis is that the mean shear flow rate decreases with increasing roughness amplitude, while at the same time there is an increase in the mean bulk viscous dissipation. In the Newtonian limit, the maximum shear flow rate is attained when the interface is at and gradually decreases as the roughness amplitude is increased. Numerical simulations at finite amplitude suggest that the mean flow may approach a minimum value which is independent of the amplitude. At a finite stress relaxation, mean flow rate is relatively higher than in the viscous limit, suggesting that the elastic modes enhance the total deformation rate.

Chapter 7:

Perspectives : Origine de la rugosité des failles et développement des surfaces de glissements

7.1. Chapter 7 overview (Présentation du Chapitre 7)

7.1.1. Introduction

Dans ce chapitre, je présente mes résultats préliminaires mettant en avant l'organisation structurale des zones de failles observées sur le terrain, et visant à donner des pistes quant aux processus à l'origine de la rugosité des failles étudiées.

7.1.2. Presentations at international meetings

2009, American Geophysical Union, Fall meeting, San Francisco (USA):

Candela T., Renard F.,Brodsky E. E., Bouchon M., Correlation between slip surfaces roughness and the internal structures of active faults. Abstract T43A-2041.

7.2. Introduction

L'évolution des surfaces de failles à travers une série de processus physico-chimique complexes, agissant depuis la seconde aux millions d'années et sur des échelles spatiales de l'ordre du micron au kilomètre, pourrait laisser penser que leur géométrie est dominée par des processus stochastiques. Ces processus comprennent : la fragmentation des roches et la formation d'une gouge, la formation d'une zone endommagée et de fracturations secondaires, diverses transformations de phases qui ont lieu pendant le séisme ou durant la période intersismique, l'usure due au frottement, … Les mesures de rugosité de failles (Power *et al.*, 1987 ; Schmittbuhl *et al.*, 1993 ; Renard *et al.*, 2006, Candela *et al.*, 2009) montrent qu'aucune longueur caractéristique n'émerge sur 6 ordres de grandeurs (depuis l'échelle du grain jusqu'à des échelles de la dizaine de mètres), indiquant qu'un unique processus pourrait être à son origine. Le chapitre 3 de la thèse propose que cette loi d'échelle puisse être étendue sur 9 ordres de grandeur en y rajoutant la rugosité des ruptures de surface des grands séismes. Ces études montrent que la morphologie des surfaces de faille, le long et perpendiculairement à la direction du glissement, est décrite par deux lois puissance. En effet, une simple relation auto-affine anisotrope caractérisée par deux exposants de rugosité différents (H_R) dans la direction du glissement et perpendiculairement $(H_{//} = 0.6; H_{\perp} = 0.8)$ décrit la morphologie d'un ensemble de surfaces de failles qui se sont développées dans différents contextes géologiques (des lithologies, déplacements accumulés, régimes tectoniques variés). Cette description implique que l'amplitude de leur rugosité est dépendante de l'échelle, et, à la différence d'une surface auto-similaire $(H_R = 1)$, le rapport entre la rugosité et l'échelle spatiale évolue, c'est-à-dire augmente quand l'échelle diminue. Il existe donc un processus qui à la fois génère une absence d'échelle caractéristique dans l'ensemble du spectre de la rugosité du plan de faille, mais aussi contrôle le fait que la faille va apparaitre de plus en plus lisse aux grandes échelles car l'exposant H_R est inférieur à 1. Dans ce chapitre de perspective, je propose que ce processus soit la coalescence multi-échelle de segments de faille.

L'ensemble des zones de failles étudiées montre une structure d'endommagement semblable, caractérisée par un réseau anastomosé de surfaces de glissement individualisant des lentilles de matériel endommagé. En mesurant les axes de symétrie de ces lentilles sur la faille de Dixie, il apparait que leur géométrie évolue non linéairement avec l'échelle. Lorsque la taille des lentilles augmente, elles tendent à être de plus en plus fines et allongées dans la direction du glissement. Je cherche à démontrer que l'imbrication de ces lentilles multi-échelle est compatible avec le régime auto-affine de la morphologie des failles.

Mes observations de terrains sont complémentaires des travaux d'Otsuki et Dilov (2005) qui ont caractérisé expérimentalement le développement de zones de failles dans une roche calcaire. L'unique paramètre géométrique qui évolue de façon non linéaire dans la croissance de leurs zones de failles est la distance de séparation entre deux segments voisins. Cette dernière diminue avec l'augmentation de la taille des segments. De ce fait, leurs expériences montrent que le développement d'une surface de faille, par la coalescence de segment de tailles progressivement croissantes s'effectue de manière « allométrique ». Le terme « allometrique » signifie ici que lors de la croissance de la faille par imbrication et coalescence de segments, la surface de faille devient de plus en plus lisse du fait de la diminution du rapport entre la distance de séparation de deux segments voisins et leur longueur. La coalescence des deux segments voisins forme les lentilles observées sur les zones de failles naturelles, et il est probable que la géométrie auto-affine de leur surface marque la fossilisation de ce processus « allométrique » d'imbrication de lentilles mis en évidence par Otsuki et Dilov (2005). Néanmoins, ces observations convergentes n'expliquent pas l'origine de l'évolution de la forme des lentilles avec l'échelle qui semble intimement liée à la manière dont des segments voisins vont interagir pour finalement coalescer.

La manière dont deux failles se connectent a été étudiée pour des régimes tectoniques variés (Sibson, 1985; Deng *et al*., 1986; Knuepfer, 1989). Des modélisations numériques (Segall et Pollard, 1980 ; Pollard *et al.*, 1982; Pollard et Aydin, 1984; Willemse *et al.*, 1996; Maerten *et al.*, 1999) ou analogiques (Thomas et Pollard, 1993; Mauduit et Dauteuil, 1996; Acoccella *et al.*, 1999 ; Fender *et al.*, 2010) ont été conduites dans le but d'étudier les interactions mécaniques entre deux fractures. Elles ont montré que la coalescence de deux segments dépend de plusieurs paramètres, tels que le champ de contrainte lointain (Olson et Pollard, 1989), la configuration initiale des segments (Du et Aydin, 1991) et leur vitesse de propagation (Olson, 1993).

Cependant, si l'on considère le cas d'une roche avec des propriétés élastiques homogènes, le paramètre clé contrôlant la propagation d'une fracture et son interaction avec une fracture voisine, est le facteur d'intensité de contrainte critique K_c (rigidité de la fracture ou « fracture toughness ») caractérisant la magnitude de la concentration des contraintes à l'extrémité du crack (Cotterell et Rice, 1980 ; Schultz, 1988). En effet, ce paramètre semble le seul à pouvoir évoluer avec l'échelle du crack. Dans un modèle élastique non-linéaire de crack (e.g. Dugdale, 1960 ; Barenblatt, 1962), l'énergie de fracturation G_c dépensée en tête de la fracture pour sa propagation est donnée par:

$$G_c \propto K_c^2 \propto \left(\Delta\sigma \sqrt{\frac{l}{2\pi}} \right)^2 \tag{7.1}$$

où l correspond à la longueur du crack, et $\Delta\sigma$ est la chute de contrainte associée au glissement et à la propagation du crack. Etant donné qu'il est souvent admis que la chute de contrainte est constante et indépendante de la longueur de la faille (e.g. Scholz, 2007, 2010), l'équation (7.1) implique que G_c et par la même occasion l'intensité de la contrainte à l'extrémité du crack évoluent linéairement avec la longueur de la faille. Dans le cas d'une croissance progressive de la faille par coalescence de segments voisins de même taille, analogue aux expériences d'Otsuki et Dilov (2005), la distance d'interaction/coalescence entre deux segments devrait alors également évoluer linéairement, ce qui n'est pas le cas.

Dans le chapitre 5 de la thèse, il est proposé que la chute de contrainte est susceptible de diminuer avec l'augmentation de taille de la zone de rupture. Dans ce contexte, et en accord avec l'équation (7.1), il est probable que l'interaction mécanique entre deux segments voisins soit d'une intensité plus grande pour des segments de petites tailles. En d'autre terme, plus la longueur de deux segments voisins sera grande, plus la distance à laquelle ils vont interagir mécaniquement afin de coalescer sera importante par rapport à leur taille. De ce fait, la géométrie des lentilles résultant de la coalescence des cracks serait en accord avec nos observations de terrains et les modèles analogiques d'Otsuki et Dilov (2005).

Dans la section 7.3 ci-après, l'architecture et les principales textures des zones de failles sont présentées. Dans la section 7.4, la loi d'échelle du rapport de forme des lentilles qui constituent la zone de faille de Dixie est comparée avec celle des lentilles des zones de cisaillements expérimentales d'Otsuki et Dilov (2005). La section 7.5 est consacrée à la description mécanique de l'interaction/coalescence entre des segments voisins.

7.3. Architecture des zones de failles

Cette section a pour but de différencier les principales structures d'endommagement qui marquent l'architecture des zones de failles étudiées (voir Tableau 7.1). Les critères de différenciation entre les structures observées sont principalement basés sur des observations à grandes échelles effectuées sur le terrain. Les contextes géologiques des cinq failles étudiées sont détaillés dans le chapitre 3 de la thèse. Précisons que trois failles recoupent des roches calcaires (les failles décrochantes de Vuache-Sillingy et de Bolu ; et la faille normale de Magnola) et deux des roches silicatées (la faille décrochante de Corona Heights et la faille normale de Dixie).

Un aspect important de l'architecture des zones de failles étudiées est qu'elles sont toutes composées d'un réseau anastomosé de surfaces de glissements (~miroirs de failles) plus ou moins développées (Figure 7.1), entouré par une zone endommagée de part et d'autre de ce réseau. Au premier ordre, les zones de failles étudiées s'écartent d'un modèle de faille avec une unique zone de glissement principale d'intense déformation, bordée par des zones d'endommagement symétriques (Chester *et al.*, 1993 ; Sagy *et al.*, 2009). En effet, les zones de failles étudiées ici contiennent plusieurs surfaces principales de glissements à l'image de la faille de Carboneras étudiée par Faulkner *et al.* (2003).

Ces surfaces de glissement anastomosées segmentent les failles en individualisant des lentilles multi-échelles de matériel endommagé (Figure 7.1). Ces lentilles ont déjà été décrites dans les failles en compression (e.g. Boyer et Elliot 1982 ; Davison, 1994), les failles décrochantes (e.g., Woodcock et Schubert, 1994) et les failles en extension (e.g. Gibbs, 1983, 1984 ; Gabrielsen et Clausen, 2001, Lindanger *et al.*, 2004 ; Childs *et al.*, 1997). Elles sont observées à toutes les

échelles depuis l'échelle sismique (Gibbs 1983, 1984), jusqu'à l'échelle millimétrique (e.g. Gabrielsen et Clausen, 2001 ; Clausen *et al.*, 2003 ; Berg, 2004, Christensen, 2004).

Tableau 7.1. Zones de failles

Fault name	Location	Lithology	Displacement	Sense
Vuache - Sillingy	45°57' 14.5"N 6°2' 56"E	Limestone	10-30 m	Strike-slip
Corona Heights	37°45' 55"N 122°26' 14"W	Chert	several m to >1 km	Strike-slip
Bolu	40°41' 07"N 31°34' 04"E	Limestone	20 m to >1 km	Strike-slip
Dixie Valley	39°56' 48"N 117°56' 43"E	Rhyolites	several m to 3-6 km	Normal
Magnola	42° 7'N 13°28' 31"E	Limestone	several m to >500m	Normal

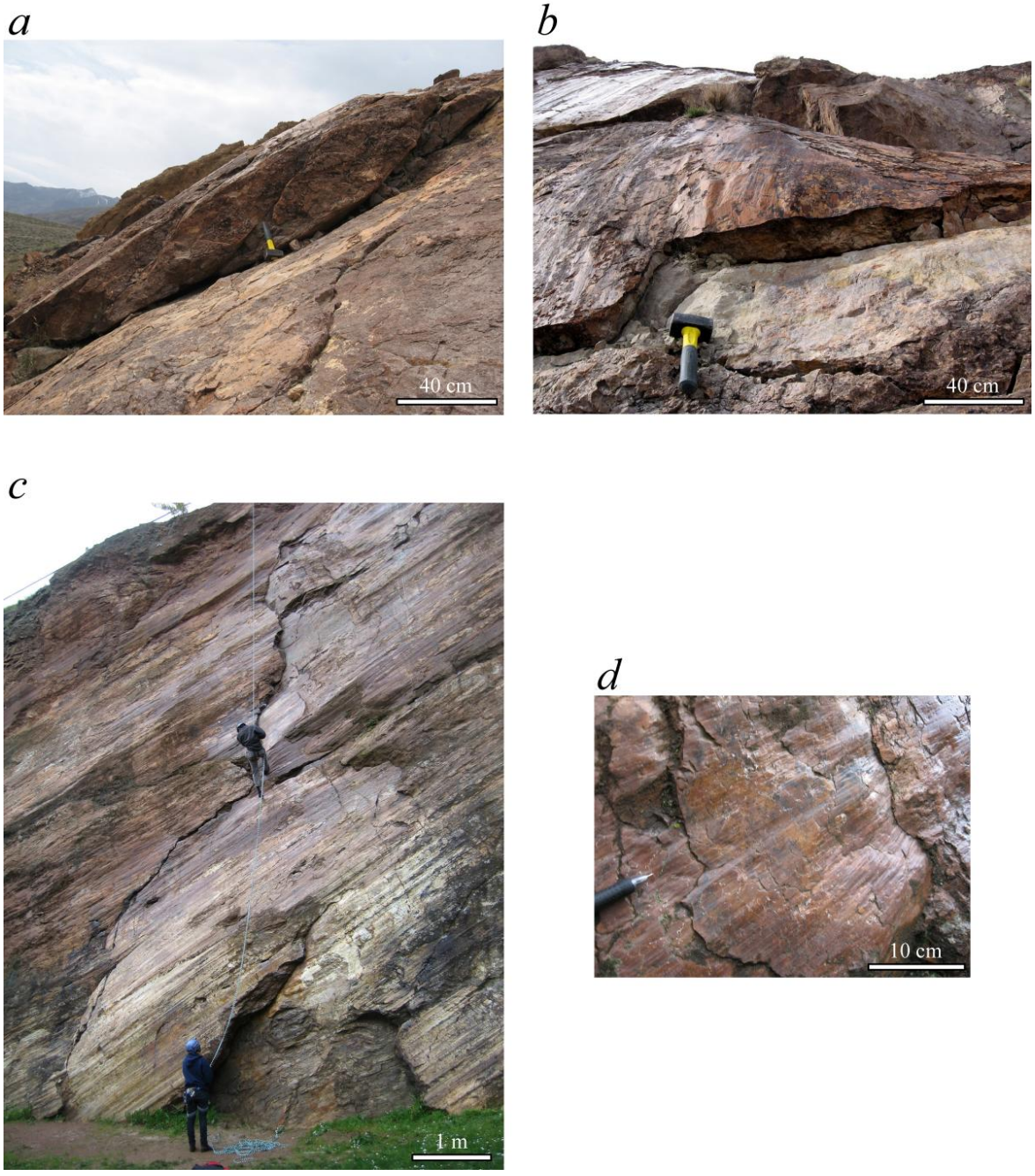

Figure 7.1. *Architecture des zones de failles de Dixie (a, b) et Corona Heights (c) montrant la structuration sous forme de segments anastomosés délimitant des lentilles à toutes les échelles. On note également en (c) les stries linéaires de friction, associées à la segmentation. (d) Zoom sur l'un des segments de la faille de Corona Heights, mettant en évidence la subdivision de sa surface en lentilles de plus petites tailles. On note aussi en (a), sur la section transverse de la zone de faille de Dixie, qu'une grande lentille (constituant l'essentiel de la photo) emballe trois lentilles de plus petite échelle.*

A l'échelle des lentilles bordées par des surfaces de glissement, trois textures sont clairement différenciables (Figure 7.2): (i) une bande de glissement principale d'épaisseur millimétrique à centimétrique composée souvent de plusieurs surfaces individuelles de localisation extrême du glissement, d'épaisseur pluri-micrométrique, et dont le sommet constitue les surfaces de glissement striées (~ miroir de failles scannées présentées dans le chapitre 3 de la thèse) ; (ii) une couche de cataclasites directement adjacente à la bande de glissement principale et d'épaisseur variable, centimétriques à pluri-centimétriques ; (ii) une zone d'intense fracturation d'épaisseur centimétrique à métrique, soit juxtaposée à la couche de cataclasites, soit directement en contact avec la bande de glissement principale lorsque la couche de cataclasites est absente. De façon générale, le corps des plus grandes lentilles est composé des trois textures (Figure 7.2), alors que les lentilles de petites tailles, ne contiennent pas toujours à la fois la couche de cataclasites et la zone fracturée. Ces dernières apparaissent généralement constituées uniquement du matériel fracturé. Ces trois textures rentrent dans la classification générale des structures des zones de failles (e.g. Sibson, 1977 ; Caine *et al.*, 1996 ; Woodcock et Mort, 2008).

Il est certain que les zones de failles étudiées couvrent une large gamme de déplacement total accumulé (depuis la dizaine de mètres jusqu'à plusieurs kilomètres, Tableau 7.1). Cependant, en prenant comme exemple la faille de Dixie, il faut souligner que même si le déplacement total accommodé par la zone de faille est de ~ 3 à 6 km (Power et Tullis, 1989), le glissement sur chaque segment de surfaces de failles, individualisant les lentilles, est probablement beaucoup moindre et distribué spatialement de façon hétérogène. La couche de cataclasite clairement distincte de la zone fracturée par son caractère granulaire (Sagy *et al.*, 2007 ; Chambon *et al.*, 2006), semble être nourrie par les produits d'usure générés par le glissement frictionnel préférentiellement localisé au niveau des surfaces de glissement bordant les lentilles. En effet, par exemple au niveau de la faille de Dixie, des fragments d'anciennes surfaces de glissement sont incorporés dans la couche granulaire (Figure 7.2), témoignant de ce processus d'usure mécanique.

Mon analyse de l'architecture des zones internes des failles étudiées, dégage deux processus principaux modelant la géométrie de leur surface : (i) le glissement frictionnel marqué par les corrugations et stries omniprésentes sur les surfaces de failles et à l'origine de l'usure mécanique

nourrissant la couche granulaire ; (ii) la coalescence de segments de failles multi échelles à l'origine d'un processus de fusion des lentilles les unes dans les autres.

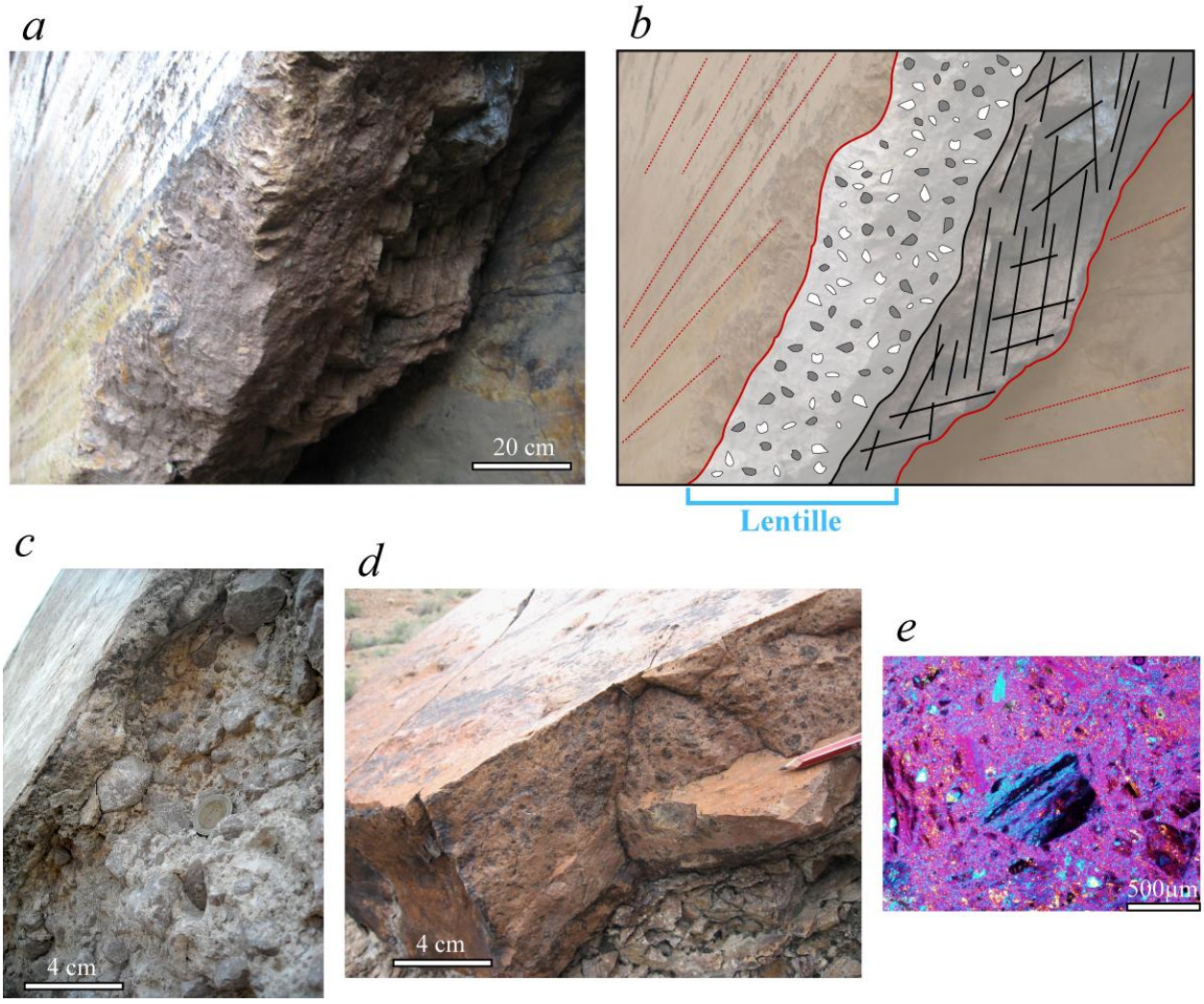

Figure 7.2. *Présentation des trois principales textures constituant les zones de failles à l'échelle des lentilles. (a) Zoom sur la Figure 7.1c et son croquis interprétatif (b), permettant de visualiser la structuration interne des lentilles de plus grandes échelles de l'affleurement de la faille de Corona Heights. Sur cette section transverse, on distingue deux segments de failles (à gauche et à droite) bordant une lentille. Juxtaposé au segment de gauche, on visualise la couche granulaire de cataclasite, contenant du matériel broyé, produit de l'usure durant le glissement frictionnel. A droite se trouve la zone fracturée, juxtaposée à la couche granulaire et située au-dessus du segment de gauche. (c) Zoom sur l'un des segments de la faille de Bolu, montrant la couche de matériel broyé en-dessous de la surface de*

glissement (à gauche). (d) Structuration interne d'une lentille de la faille de Dixie, équivalente à celle de la faille de Corona montré en (a, b). On retrouve en dessous de la surface de glissement (en haut), la couche granulaire, et en-dessous le matériel intensément fracturé. Sur cette photo, la surface de glissement symétrique de celle du haut n'est pas visible. On note également qu'une facture secondaire semble s'être localisée entre la couche granulaire et la zone fracturée. (d) Microphotographie de la couche granulaire au niveau de la faille de Dixie, prise sous polarisateurs croisés avec l'addition d'une lame de gypse. Des fragments de grains de quartz et d'anciennes cataclasites remaniées baignent dans une matrice à grains fins. On distingue au centre de la photo, un fragment d'une ancienne bande de glissement. Cette bande est constituée de plusieurs surfaces de glissement d'épaisseurs micrométriques.

7.4. Propriétés géométriques des lentilles

7.4.1. Evolution des lentilles de la faille de Dixie avec l'échelle

La faille de Dixie, du fait de nombreuses coupes transverses naturelles qui recoupent sa zone endommagée, offre l'opportunité de mesurer la géométrie 3D des lentilles multi-échelles bordées par les surfaces de glissement. La longueur des axes de symétrie des lentilles (Tableau 7.2 et Figure 7.3) a été mesurée de façon similaire aux travaux de Lindanger *et al.* (2007). Cette approche présente des contraintes méthodologiques car les lentilles ne sont que rarement exposées en totalité et les sections disponibles ont parfois un angle oblique par rapport au plan principal. J'ai choisi de sélectionner uniquement les lentilles exposées dans des conditions favorables (Cf. Tableau 7.2).

La forme des lentilles évolue avec leur taille. En effet, le rapport entre la longueur maximale l^* dans la direction du glissement et la largeur W dans la direction perpendiculaire au glissement diminue avec l'augmentation de la taille des lentilles (Figure 7.3). D'autre part, le rapport entre l'épaisseur maximale T^* et la longueur maximale l^* diminue également lorsqu'augmente leur taille (Figure 7.3). Ces deux précédents résultats combinés indiquent que les lentilles apparaissent de plus en plus fines et allongées dans la direction du glissement au fur et à mesure que leur taille augmente.

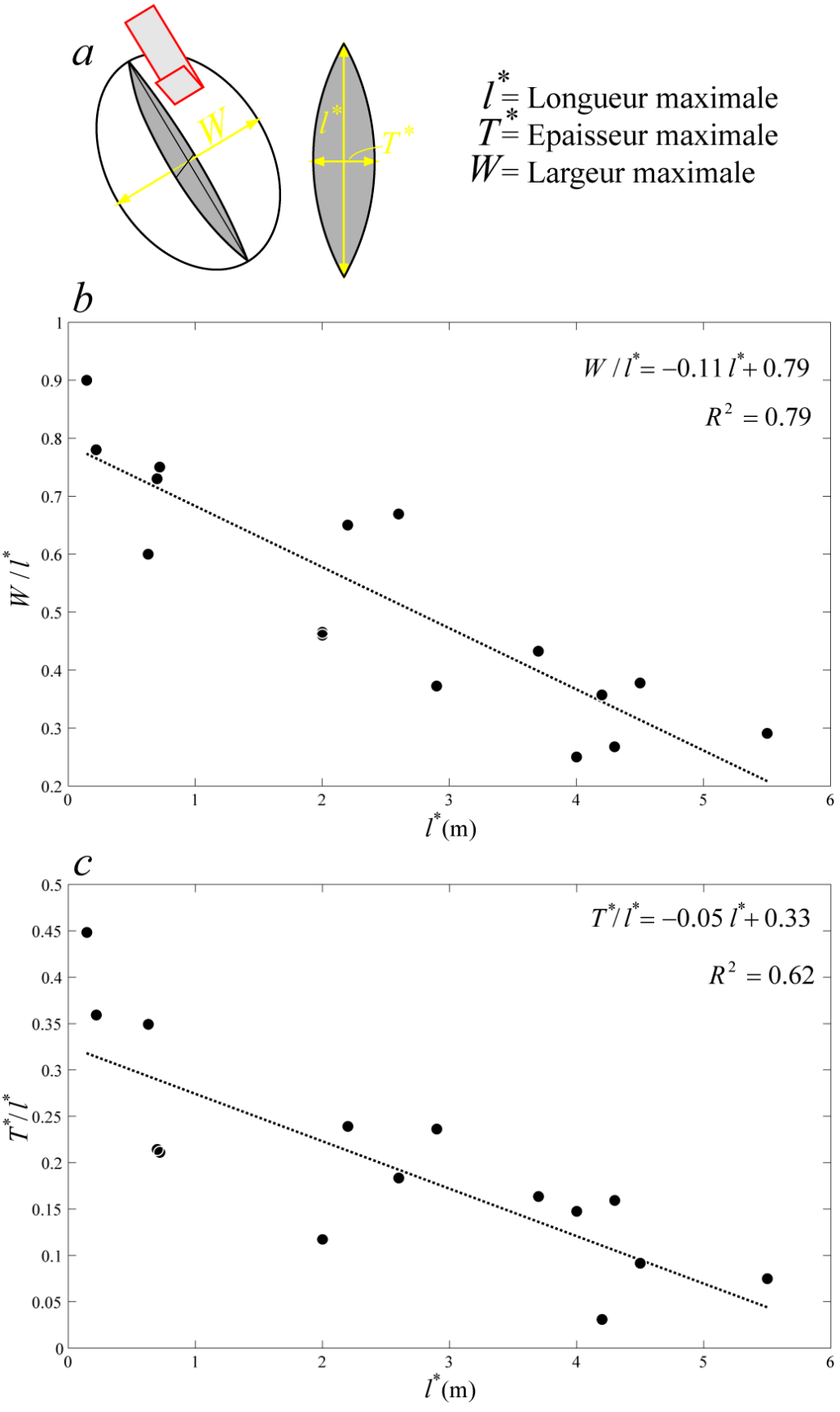
a
W
l*
T*
l* = Longueur maximale
T* = Epaisseur maximale
W = Largeur maximale
b
W / l* = –0.11 l* + 0.79
R² = 0.79
W / l*
l* (m)
c
T* / l* = –0.05 l* + 0.33
R² = 0.62
T* / l*
l* (m)

Figure 7.3. *Propriétés géométriques des lentilles de la zone de faille de Dixie. (a) Axes de symétrie des lentilles. (b) Rapport normalisé entre la longueur et la largeur des lentilles. (c) Rapport normalisé entre l'épaisseur et la longueur des lentilles.*

Tableau 7.2. Mesures des axes de symetrie des lentilles de la faille de Dixie

Max length, l^*(m)	Max width, W(m)	Max thickness, T^*(m)
4.0000	1.0000	0.5900
4.3000	1.1500	0.6850
2.9000	1.0800	0.6850
4.2000	1.5000	0.1300
5.5000	1.6000	0.4120
4.5000	1.7000	0.4120
2.0000	0.9200	0.2340
3.7000	1.6000	0.6050
2.0000	0.9300	0.2350
2.2000	1.4300	0.5260
2.6000	1.7400	0.4770
0.2200	0.1716	0.0790
0.1450	0.1305	0.0650
0.7000	0.5110	0.1500
0.6300	0.3780	0.2200
0.7200	0.5400	0.1520

7.4.2. Comparaison des lentilles naturelles avec une zone de faille expérimentale

En étudiant le développement d'une zone de faille expérimentale au sein d'une roche calcaire, Otsuki et Dilov (2005) ont mis en évidence que la distance de séparation de deux segments voisins en interaction (et sur le point de coalescer) évolue non linéairement avec leur longueur. En effet, le rapport entre la distance séparant deux segments voisins et leur longueur respective (ici équivalente) diminue lorsque leur taille augmente. D'autre part, tous les autres paramètres géométriques, tel que le rapport entre la distance de chevauchement des deux segments voisins et leur longueur, restent constant. Dans leurs expériences, les deux segments en interaction finissent par coalescer et définir alors une lentille analogue à nos observations de terrains. La distance de chevauchement des deux segments voisins, évoluant linéairement avec l'échelle, correspond alors à la longueur de la lentille dans la direction du glissement lorsque les

segments ont coalescé. Il en résulte que le rapport entre l'épaisseur de leurs lentilles et leurs longueurs va évoluer avec l'échelle dans le même sens que les lentilles observées sur le terrain. Dans l'expérience d'Otsuki et Dilov (2005), la faille croit progressivement par coalescence de segments de longueurs croissante, en imbriquant donc des lentilles de plus en plus fines. La croissance de la zone de faille est dite « allométrique ».

Sur la Figure 7.4, est comparée la loi d'échelle de l'épaisseur des lentilles proposée par Otsuki et Dilov (2005), $T^* = 0.09\, l^{*0.642}$ avec celles des lentilles de la faille de Dixie, $T^* = 0.2\, l^{*0.6}$. Même si ces données sont peu nombreuses, elles couvrent plus d'un ordre de grandeur, et sont donc considérées comme robustes. Les deux exposants de notre loi d'échelle et celle d'Otsuki et Dilov (2005) sont très proches, ce qui pourrait indiquer que le même processus d'imbrication de lentilles par coalescence de segments a été fossilisé durant la croissance de la faille de Dixie (Figure 7.5). La géométrie auto-affine des surfaces de faille serait alors le résultat direct de l'agrégation multi-échelle de lentilles (Figure 7.5). Les courtes longueurs d'ondes de la surface de faille seraient alors dominées par les lentilles épaisses, bombées, acquises lors des premiers stades de développement de la faille. Les grandes longueurs d'ondes, correspondraient aux grandes lentilles plus fines et lisses acquises lors du développement de la faille.

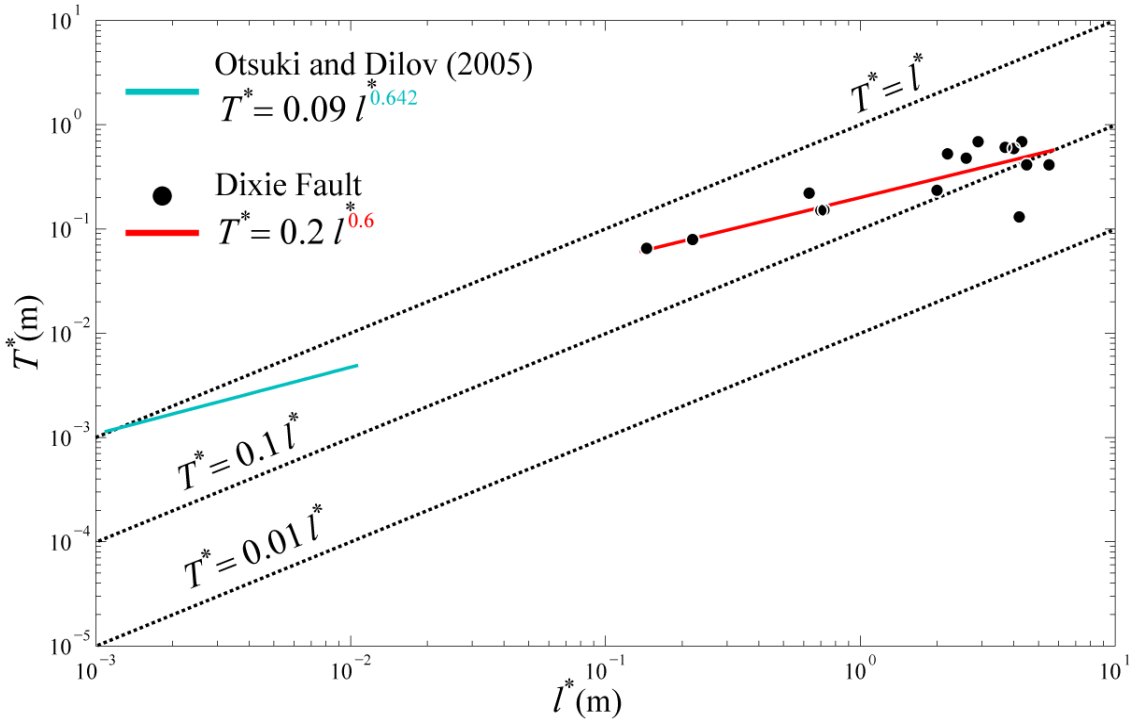

Figure 7.4. *Comparaison des lois d'échelle de l'épaisseur des lentilles du modèle analogue d'Otsuki et Dilov (2005) avec les lentilles de la faille de Dixie.*

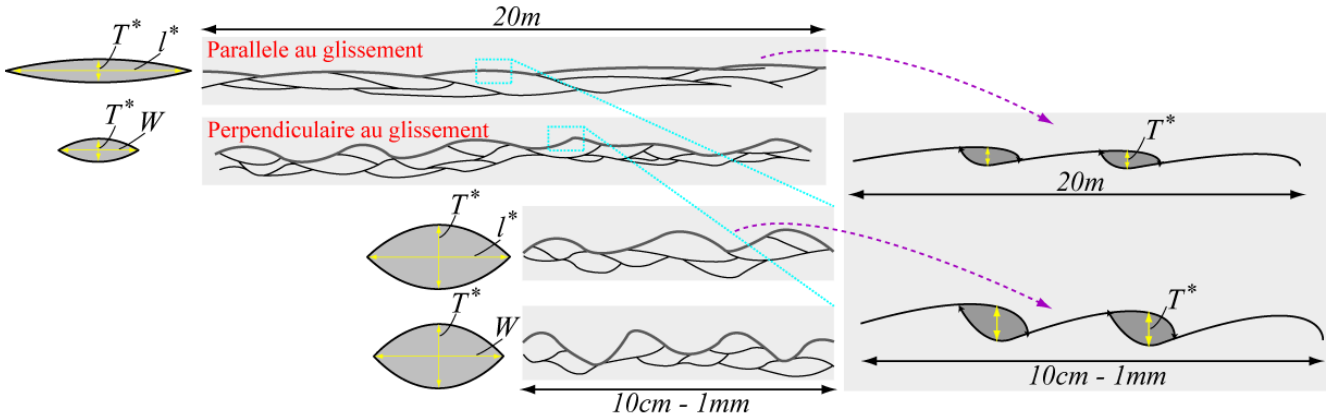

Figure 7.5. *Schéma conceptuel de la relation entre l'imbrication des lentilles dans la zone de faille et la rugosité auto-affine de sa surface.*

7.5. Modèle mécanique de la formation des lentilles

7.5.1. Distance caractéristique d'interaction/coalescence entre deux segments de faille

Dans un modèle élastique non-linéaire de crack (e.g. Dugdale, 1960 ; Barenblatt, 1962), la chute de contrainte $\Delta\sigma$ est spécifiée sur un crack à l'intérieur d'un solide sous contrainte et le déplacement résultant des murs du crack est calculé. Quand on applique un tel modèle aux failles, il est supposé que la chute de contrainte correspond à la contrainte cisaillante appliquée moins la contrainte de friction résiduelle sur la faille. Dans ce contexte et comme indiqué dans la partie introductive de ce chapitre 7, l'énergie de fracturation G_c dépensée en tête d'une faille de longueur l pour sa propagation est donnée par l'équation (7.1), ici ré-énoncé:

$$G_c \propto K_c^2 \propto \left(\Delta\sigma\sqrt{\frac{l}{2\pi}}\right)^2$$

Rappelons que K_c caractérise la magnitude de la concentration des contraintes à l'extrémité du crack (Cotterell et Rice, 1980 ; Schultz, 1988). Au premier ordre, la condition pour que deux

segments voisins coalescent est que les champs de contrainte à leurs extrémités respectives interagissent. Il est alors raisonnable d'admettre que la distance caractéristique d'interaction et donc de coalescence T entre deux segments voisins soit linéairement proportionnelle à G_c, i.e. :

$$T \propto G_c \tag{7.2}$$

Ici la distance caractéristique T est considérée dans cette analyse comme linéairement reliée à l'épaisseur des lentilles mesurées sur le terrain:

$$T \propto T^* \propto G_c \tag{7.3}$$

Il est généralement admis que la chute de contrainte $\Delta\sigma$ reste constante et n'est pas fonction de la longueur du crack (e.g. Scholz, 2007, 2010). De ce fait, en combinant les équations (7.1) et (7.3):

$$T \propto T^* \propto l \tag{7.4}$$

Par conséquent, la distance caractéristique d'interaction/coalescence entre deux segments de faille dans une roche élastique homogène évoluerait de façon linéaire avec leur longueur respective (ici équivalente). En considérant que le rapport entre la distance de chevauchement des deux segments voisins et leur longueur reste constant, comme observé par Otsuki et Dilov (2005), il s'en suit que l'épaisseur des lentilles évoluerait de façon linéaire avec leur longueur. En d'autre terme, le rapport de forme des lentilles issues de la coalescence des segments voisins serait alors constant quelle que soit leur taille. Lors de la croissance progressive de la zone de faille, en conséquence de l'imbrication de ces lentilles multi-échelles à rapport de forme stable, la rugosité de la surface de faille serait alors auto-similaire. Cette dernière remarque est donc en contradiction avec les mesures de rugosité présentées dans le chapitre 3 de la thèse et la géométrie des lentilles présentée dans la section 7.4.

7.5.2. Evolution de la distance d'interaction/coalescence à l'origine de la morphologie des lentilles

Au regard de l'équation (7.1), il est envisageable que la variabilité de la chute de contrainte puisse être l'unique alternative afin d'accorder nos observations de terrains et les travaux d'Otsuki et Dilov (2005) avec les mesures de rugosité des surfaces de failles. Le rapport entre le

déplacement et la longueur de la rupture, i.e. la chute de contrainte, est depuis longtemps considéré comme indépendant de l'échelle sur une large variété de tremblements de terre (Kanamori et Anderson, 1975; Abercrombie, 1995). Cependant, ces mêmes observations sismologiques montrent une grande variabilité de la chute de contrainte, $0.1 < \Delta\sigma < 100\ MPa$, supposée indépendante de la taille de la rupture. Cette grande dispersion des valeurs estimées par les observations sismologiques ne peut pas être due à des variations des constantes élastiques, qui ne varient pas de plus d'un facteur deux ou trois entre les différents types de roches. Dans le chapitre 5 de la thèse, il est proposé que la variabilité de la chute de contrainte est directement reliée aux propriétés géométriques de la longueur de la rupture:

$$\Delta\sigma \propto l^{H_R - 1} \propto l^{-0.2} \tag{7.5}$$

avec $H_R = H_\perp = 0.8$. En conséquence, pour un crack cisaillant naissant, la chute de contrainte serait de moins en moins importante au fur et à mesure de sa croissance. En combinant les équations (7.1) et (7.5), il vient:

$$G_c \propto l^{2H_R - 1} \propto l^{0.6} \tag{7.6}$$

et en associant les équations (7.3) et (7.6) :

$$T \propto T^* \propto l^{2H_R - 1} \propto l^{0.6} \tag{7.7}$$

avec $H_R = H_\perp = 0.8$. Ceci implique que la distance caractéristique d'interaction/coalescence entre deux segments de faille dans une roche homogène et isotrope évoluerait de façon non-linéaire avec leur longueur respective (ici équivalente). Plus précisément, lors de l'initiation de la faille, la distance caractéristique d'interaction/coalescence entre deux segments courts naissant, i.e. la distance maximum de coalescence (représentée sur la Figure 7.6 par l'addition des deux lobes de concentration de contraintes à l'extrémité des cracks voisins) sera grande relativement à leur longueur respective. Dans un stade plus avancé de la propagation de la faille, le rapport entre la distance maximum de coalescence et la taille croissante des segments voisins va diminuer.

D'autre part, en considérant que la distance du chevauchement entre deux segments voisins est linéairement proportionnelle à leur taille $(l^* \propto l)$ comme le suggère les expériences d'Otsuki

et Dilov (2005) et les observations de terrains d'Acoccela *et al.* (2000), il s'en suit que le rapport d'aspect des lentilles (T^*/l^*) issues de la coalescence des segments va diminuer durant la croissance de la faille (Figure 7.6). La géométrie auto-affine des surfaces de faille serait alors le résultat direct de l'agrégation multi-échelles de ces lentilles dont le rapport d'aspect diminue avec l'augmentation de leur taille.

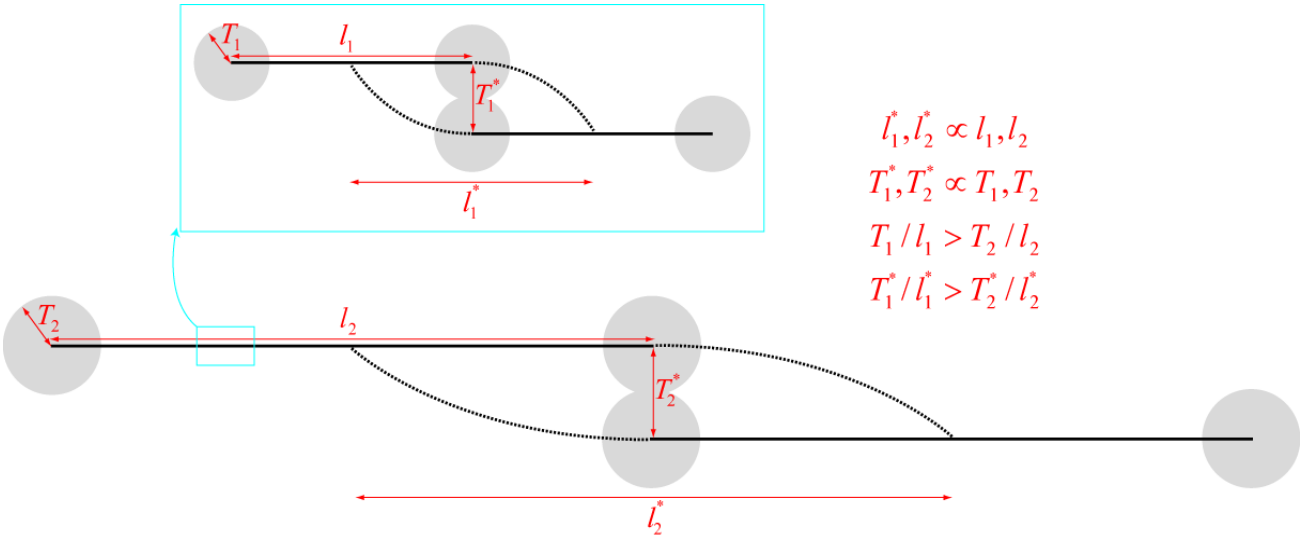

Figure 7.6. *Relations d'échelles des différents paramètres géométriques impliqués durant l'interaction et la coalescence de deux segments voisins.*

7.6. Perspectives

Dans ce chapitre 7, j'ai proposé que la propagation et la croissance d'une faille par interaction et coalescence progressive de segments pourrait être à l'origine de la géométrie des surfaces de faille. Lors du stade initial de propagation, la distance d'interaction/coalescence entre les premiers segments (qui naissent probablement au niveau d'hétérogénéités distribuées de manière aléatoire dans le matériel originel) est relativement grande par rapport à leur taille. Les lentilles générées par leur coalescence sont en conséquence relativement épaisses. Lors du développement progressif de la zone de faille par coalescence de segments de tailles croissantes, des lentilles relativement de plus en plus fines sont imbriquées par suite de l'évolution d'échelle

non linéaire de l'intensité de la concentration des contraintes à l'extrémité des segments. Ce modèle mécanique émerge directement du fait que la chute de contrainte évolue elle aussi non linéairement avec l'échelle. En effet, dans le contexte de la coalescence « allométrique » de segments multi-échelles, comme suggéré par nos observations de terrains, l'unique paramètre susceptible de contrôler ce mécanisme est la variation avec l'échelle de la chute de contrainte. Cette dernière émerge directement de la géométrie auto-affine des surfaces de faille, puisqu'étant dérivée principalement de la compression élastique des aspérités (voir chapitres 4 et 5 de la thèse). En conséquence, dès lors qu'un segment de faille nucléé, la propagation de ce segment par interaction et coalescence avec des segments voisins est auto-entretenue par sa propre morphologie.

7.6.1. Confrontation de l'hypothèse d'une chute de contrainte dépendante de l'échelle avec les observations de terrain

La stabilité du rapport entre le déplacement totale cumulé $(d_{\max})$ et la longueur totale de la faille (L) est souvent évoquée pour appuyer l'hypothèse de la chute de contrainte constante lors d'un événement individuel de rupture (e.g. Scholz, 2007, 2010). En effet, comme le souligne Scholz *et al.* (1993), la loi d'échelle entre le déplacement total cumulé et la longueur totale des failles est la mieux définie par les observations de terrain (Cowie et Scholz, 1992; Schlische *et al.*, 1996; Schultz *et al.*, 2006). De cette dernière sont déduites indirectement les lois d'échelles des autres paramètres, telles que l'énergie de fracture. Tout comme pour l'estimation de la chute de contrainte relâchée par un unique événement de rupture, la grande variabilité du pré-facteur du rapport entre $d_{\max}$ et L observée sur les données naturelles compilées $0.001 < d_{\max} / L < 0.1$, laisse croire à une dépendance de ce rapport avec l'échelle. En d'autres termes, cette variabilité du pré-facteur de la relation supposée linéaire entre $d_{\max}$ et L, ne serait pas uniquement liée à des variabilités des constantes élastiques des roches encaissantes traversées par les différentes failles compilées, mais pourrait aussi refléter l'évolution de la chute de contrainte avec la longueur de la rupture.

Modèle de croissance de faille

La relation d'échelle entre le déplacement (maximum) cumulé $d_{\max}$ et la longueur totale d'une faille L peut être décrite par (Scholz, 2010; Schulz *et al.*, 2006):

$$d_{\max} = \Delta\sigma \frac{2(1-\nu^2)}{E} L \tag{7.8}$$

avec E et ν le module de Young et le coefficient de Poisson de la roche encaissante. Dans l'équation (7.5), le déplacement moyen durant un séisme unique est relié à la longueur de la rupture par :

$$\Delta u = \alpha\, l^{H_R} \tag{7.9}$$

où α est une constante, alors que dans l'équation (7.8) nous avons accès au déplacement $d_{\max}$ total cumulé.

Dans cette section, un modèle géométrique de croissance de faille est utilisé afin de comparer ces deux relations en suivant un raisonnement similaire à celui de Cowie et Scholz, (1992). Le modèle de croissance est construit en supposant que le déplacement total $d_{\max}$ sur la faille est une somme d'incréments accumulés par une série de tremblements de terre. Si chaque séisme casse la longueur totale de la faille, alors le déplacement cumulé d_n après n tremblements de terre est donné par :

$$d_n = \sum_{i=1}^{n} \Delta u_i = \alpha \sum_{i=1}^{n} (L_{i-1})^{H_R} \tag{7.10}$$

où L_{i-1} est la longueur de la faille immédiatement avant le *i*-ème tremblement de terre. Si l'augmentation de la longueur de la faille ΔL_i produit par chaque tremblement de terre est fonction de la longueur de la rupture, comme proposé dans l'équation (7.7), alors :

$$\Delta L_i = r\, (L_{i-1})^{2H_R-1} \tag{7.11}$$

où r est une constante. L'équation (7.10) devient :

$$d_n = \frac{\alpha}{r^{\frac{H_R}{2H_R-1}}} \sum_{i=1}^{n} (\Delta L_i)^{\frac{H_R}{2H_R-1}} \qquad (7.12)$$

La Figure 7.7 montre les relations entre les paramètres relatifs à la croissance de la faille pour différentes valeurs de H_R. Quand $H_R = 1$, d_n est linéairement relié à L_n. Dans ce cas, la croissance de la faille durant chaque séisme est aussi linéairement reliée à la longueur de la faille juste avant le séisme, comme suggéré par l'équation (7.7), avec une chute de contrainte constante. Si $H_R < 1$, comme suggéré par nos données de rugosité de surface de faille, la relation entre d_n et L_n (la longueur de la faille après n tremblements de terre) est non linéaire; i.e. L croit plus rapidement pour des petits incréments d_n. Cette évolution non linéaire de la croissance de la faille en fonction du déplacement cumulé est le résultat du couplage de deux paramètres: (i) la vitesse d'accroissement de la faille à ses extrémités et (ii) la quantité de déplacement incrémenté à chaque rupture. Le bilan du couplage de ces deux paramètres résulte en un accroissement rapide de la longueur de la faille lors de son initiation.

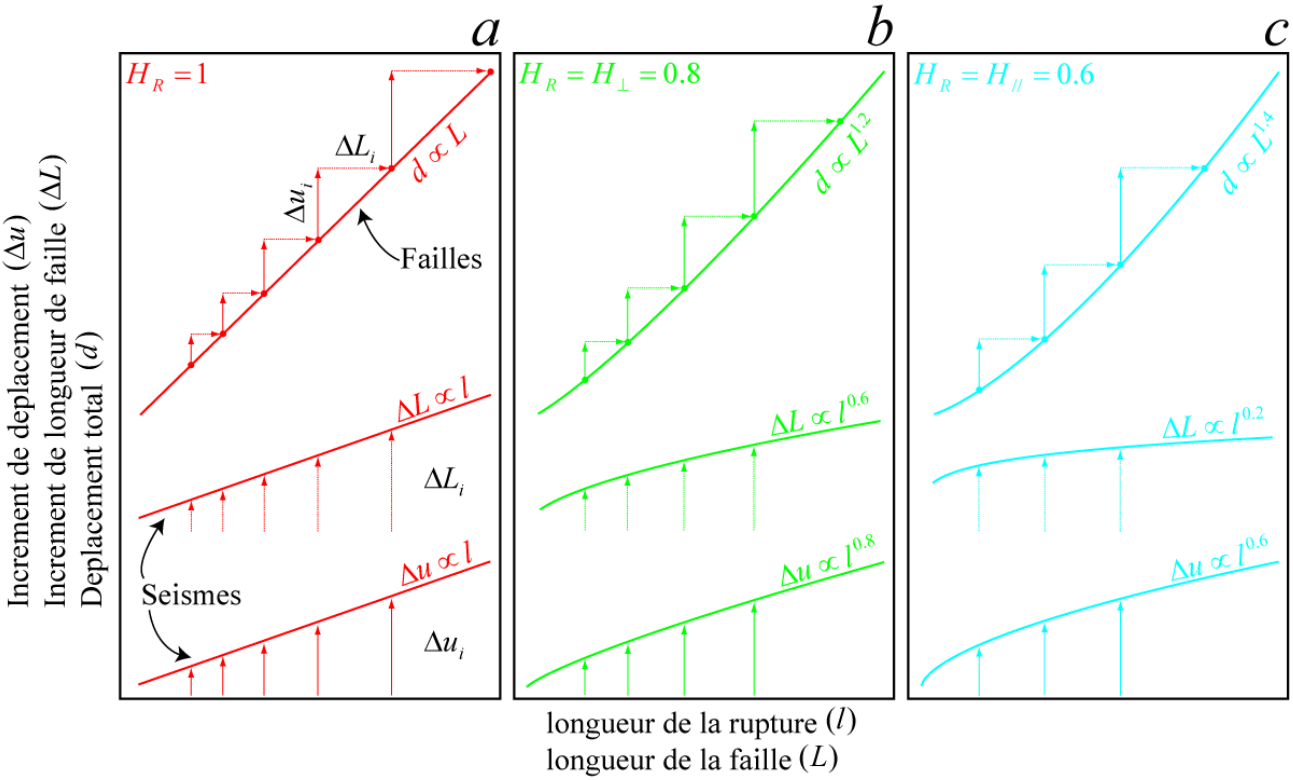

Figure 7.7. *Courbes de croissance pour une faille en suivant les équations (7.9), (7.11) et (7.12) du modèle de croissance géométrique. (a) Relations entre les paramètres* Δu , ΔL , d *vs.* l , L *pour le cas auto-similaire* $(H_R = 1)$ *considéré par Cowie et Scholz (1992). (b) et (c) sont respectivement les cas où* $H_R = H_\perp = 0.8$ *et* $H_R = H_{//} = 0.6$. *Dans chaque graphique, les deux lignes du bas, montrent la quantité de déplacement* (Δu) *et la longueur de la faille nouvellement créée* (ΔL) *si la faille casse dans sa totalité, i.e.,* $l = L$. *La ligne de haut indique le déplacement cumulé en fonction de la longueur de la faille* L *du fait des incréments graduels de glissement* (Δu_i) *et de croissance* (ΔL_i) .

Un résultat intéressant montré par ce modèle de croissance de faille, est qu'en utilisant $H_R = H_\perp = 0.8$, le déplacement total accumulé évolue en loi puissance avec la longueur de la faille, avec un exposant 1.2 (Figure 7.8). Cette observation, montre que, même si la chute de contrainte relâchée par chaque tremblement de terre n'est pas constante, la relation entre le déplacement maximum et la longueur de la faille suit une évolution quasi-linéaire comme suggéré par les observations de terrains compilées par Schulz *et al.* (2008), et représentées sur la Figure 7.8.

L'ensemble des données de déplacement maximum en fonction de la longueur totale, regroupe principalement des failles à composantes verticales (normales ou inverses; seulement deux failles sont décrochantes), et donc l'utilisation de $H_R = H_\perp = 0.8$ est bien adaptée. En prenant, $\alpha = 10^{-4}$ et $r = 0.006$, en accord avec la gamme de valeurs indiquée par Cowie et Scholz (1992), l'interpolation des données par une loi puissance avec un exposant de 1.2, semble ajuster au mieux les mesures de failles sur le terrain (Figure 7.8).

D'autre part, même si comme indiqué par Cowie et Scholz (1992) il est déconseillé d'ajuster les données de failles dans différentes lithologies et environnements tectoniques avec une loi puissance unique, il est important de noter que la loi d'échelle proposée (avec un exposant unique de 1.2 et des pré-facteurs variables) peut ajuster également chacune des failles prises individuellement.

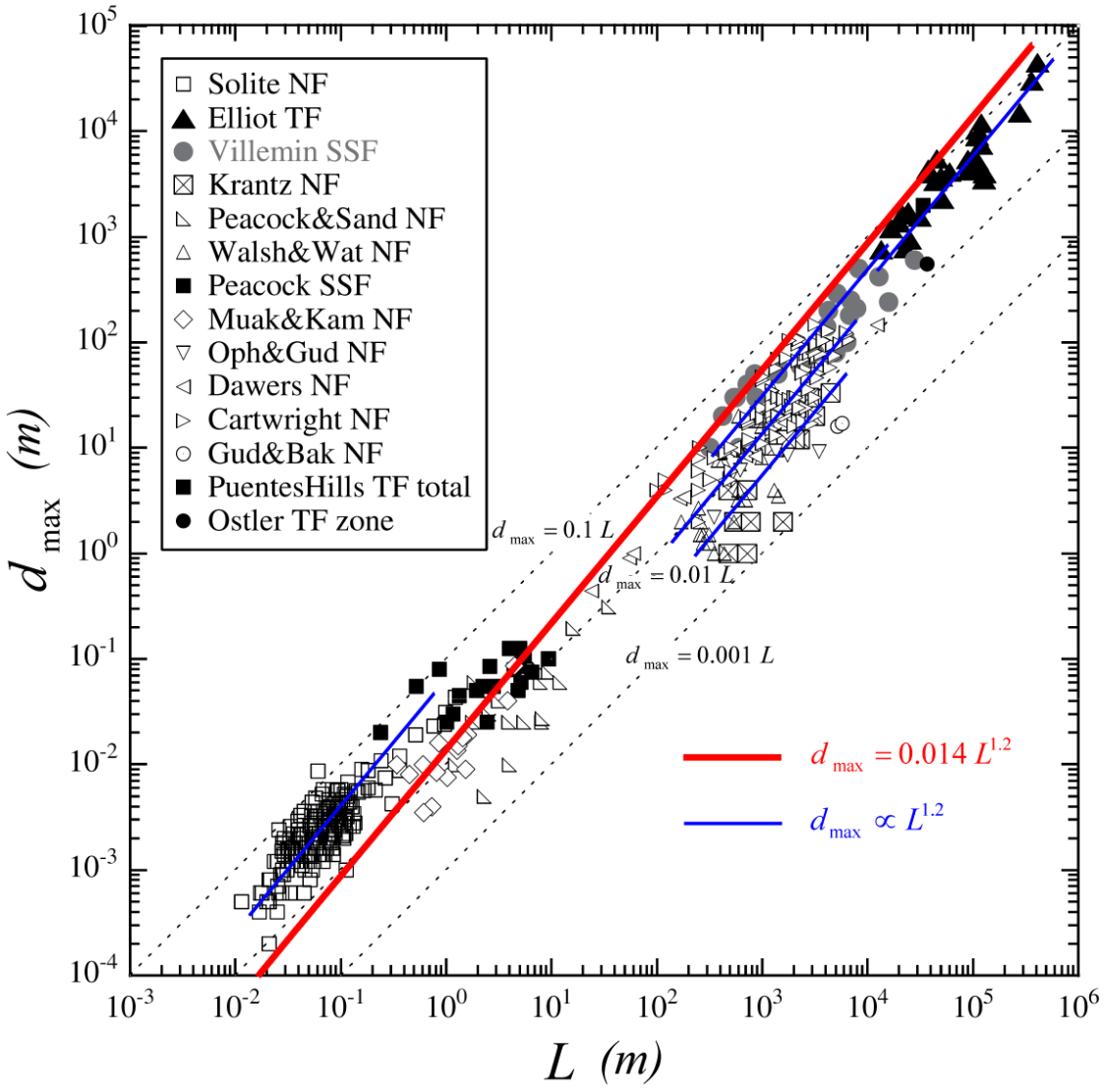

Figure 7.8. *Compilation des mesures de* d_{max} *vs.* L *(modifié d'après Schulz et al., 2008) sur des failles essentiellement avec composante verticale de déplacement: failles normales (NF); chevauchements (TF); failles décrochantes (SSF). L'approximation des données avec une loi puissance avec un exposant de 1.2, suggéré par le modèle de croissance de faille en prenant* $H_R = H_\perp = 0.8$*, est montrée par la ligne rouge. Les lignes bleues correspondent au modèle (avec un exposant 1.2 et des pré-facteurs variables) réalisé individuellement pour chacune des failles. Les lignes en pointillées de pentes constantes représentent le cas où* d_{max} *évolue linéairement avec* L*.*

Notons ici que les ajustements proposés en loi puissance avec un exposant de 1.2 restent à ce jour qualitatifs, et il nous reste à les justifier à l'aide d'une comparaison fine des coefficients de régression en récupérant les mesures compilées dans la Figure 7.8. Néanmoins, notre hypothèse d'une distance maximale de coalescence évoluant non linéairement avec la longueur de la faille du fait d'une chute de contrainte dépendante également de l'échelle, semble être en accord avec les observations de terrain. Il faut également rappeler ces mêmes observations de terrains forment la clé de voute de la relation supposée linéaire entre la distance maximale de coalescence et la longueur de la rupture (Scholz *et al.*, 1993; An, 1997).

7.6.2. Les hypothèses et limitations du modèle

Il faut préciser que dans cette analyse, nous n'avons accès qu'à la distance maximum d'interaction entre deux segments et donc à l'épaisseur maximum des lentilles. Il est probable que, dans un cas limite, des segments colinéaires de toutes tailles coalescent en ne laissant aucune structure sous forme de lentille. Cependant, les observations d'Otsuki et Dilov (2005) et d'autres expériences de développement de zones de cisaillements expérimentales (e.g. Tchalenko, 1970), montrent que les segments, avant leur coalescence, sont clairement décalés et donc non colinéaires. Il est probable qu'un même comportement émerge pour les failles observées sur le terrain, et donc puisse expliquer que les interactions mécaniques entre segments voisins à toutes les échelles se fassent préférentiellement sur des plans non colinéaires, tout en gardant une intensité évoluant avec l'échelle comme suggéré par l'équation (7.7).

Bien que les failles consistent en plusieurs segments individuels, notre analyse s'est focalisée sur l'interaction entre deux segments en considérant que la perturbation locale du champ de contrainte est dominée par les segments les plus proches (Segall et Pollard, 1980). En d'autre terme, la faille macroscopique se forme depuis la coalescence de sous-segments, lesquels eux-mêmes coalescent deux à deux en accord avec la théorie proposée. L'essence du principe suivi est que la propriété de l'ensemble (la faille) est une fonction des propriétés des sous parties (l'interaction mécanique, suivie de la coalescence multi-échelles de deux segments voisins). Cependant, une description plus complète et précise nécessiterait une quantification du

comportement collectif régissant la complexité des interactions mécaniques entre l'ensemble des cracks multi-échelles et les hétérogénéités préexistantes du milieu.

Cette analyse de la rugosité se situe dans le contexte d'une propagation quasi-statique et progressive des segments, et l'usure par glissement frictionnel n'est pas considérée. Au regard de nos observations de terrains (Cf. section 7.3), il parait évident que l'usure mécanique par glissement frictionnel joue aussi un rôle dans la création/destruction de la rugosité des failles. Néanmoins, les résultats du chapitre 3 de la thèse montrent qu'aucune corrélation nette n'émerge entre le déplacement accumulé et la morphologie des surfaces de failles. Une éventuelle « maturité » de failles par un processus de lissage progressif des aspérités directement lié au glissement frictionnel n'est donc pas observée. Il faut néanmoins préciser qu'à mon sens, un travail reste à faire quant à la compréhension exacte de l'impact joué par le glissement frictionnel sur la rugosité des failles. En effet, nous ne connaissons pas à ce jour qu'elle est l'influence joué par l'usure mécanique sur les lois d'échelles régissantes la rugosité des failles. En d'autres termes, l'usure mécanique par frottement de deux interfaces auto-affines affecte-t-elle l'ensemble des longueurs d'onde de la même manière, ou bien certaines sont-elles plus affectées que d'autres ? La réponse à cette question représente un nouveau challenge qui nécessitera de confronter données naturelles, expériences de laboratoire et simulations numériques de l'usure dans une gouge de faille.

Chapter 8:

Conclusion

Dans ce chapitre je vais synthétiser les points que je considère comme importants dans ce travail de thèse.

La surface de faille est la trace laissée derrière lui par le front de propagation de la rupture, et en retour les aspérités du plan de faille contrôlent la dynamique et la géométrie du glissement. Les aspérités de toutes tailles formées de manière mécanique lors du glissement jouent notamment un rôle crucial dans le développement de la rupture car elles concentrent les contraintes tectoniques et pourraient être le lieu de nucléation des séismes. Si l'on veut comprendre l'effet de la morphologie des failles dans la dynamique des tremblements de terre, une caractérisation fine de l'organisation spatiale des aspérités géométriques sur la large gamme d'échelles impliquées dans la rupture sismique (i.e. depuis l'échelle du grain jusqu'à l'épaisseur de la croute sismogenique) est nécessaire. La première partie de mon travail a donc consisté à répondre à la question suivante : est-il possible de définir un modèle universel de la géométrie des failles, ou au contraire des variabilités se dégagent suivant l'échelle d'observation et/ou le contexte tectonique ? Puis, dans un second temps, j'ai taché de comprendre comment cette rugosité participe à l'organisation spatiale multi-échelles des champs de glissement et de contrainte le long du plan ?

En combinant des méthodes de mesures topographiques indépendantes qui couvrent des gammes d'échelles complémentaires, une caractérisation fine de la morphologie des surfaces de failles a été apportée depuis le micromètre jusqu'à plusieurs dizaines de mètres. J'ai ainsi réalisé un travail méthodologique pour analyser, par différentes méthodes statistiques, la topographie de miroirs de failles et caractériser leurs propriétés de corrélation à toutes les échelles spatiales explorées. Un modèle cohérent se dégage de l'analyse des 5 surfaces de failles étudiées, à savoir l'amplitude de la rugosité peut être décrite par une ligne droite dans un graphique en log-log, où les axes sont la rugosité des surfaces et l'échelle spatiale. La rugosité des surfaces de failles est dépendante de l'échelle, avec un régime auto-affine légèrement anisotrope, qui peut être défini par deux paramètres, l'exposant de rugosité H_R, et le pré-facteur. Même si les zones de failles étudiées couvrent des contextes géologiques variés, à savoir des lithologies diverses, des

composantes principales de déplacement aussi bien verticales qu'horizontales, une large gamme de déplacements totales accumulés, l'exposant de rugosité est $H_{//} = 0.6$ dans la direction du glissement et $H_{\perp} = 0.8$ dans la direction perpendiculaire au glissement. Ces valeurs restent stables depuis le micromètre jusqu'à plusieurs dizaines de mètres. Néanmoins, le pré-facteur qui décrit l'amplitude moyenne de la rugosité à une échelle donnée varie localement au niveau d'une même surface de faille et entre les 5 failles étudiées. D'une part, pour la même faille, des sous parties avec des pré-facteurs différents peuvent être clairement observées ; et d'autre part le pré-facteur global, obtenu en moyennant les propriétés géométriques des sous parties, est également variable entre les 5 failles analysées. L'hétérogénéité spatiale du pré-facteur au sein d'une même surface de faille est attribuée au fait que les surfaces étudiées ne correspondent pas à un unique plan spatialement homogène, mais plutôt à un assemblage de surfaces de glissement discrètes avec une amplitude moyenne de leur topographie variable. En outre, la variabilité du pré-facteur global entre chacune des failles, ne semble pas imputable à des différences dans les contextes géologiques. Notamment, même si les zones de failles étudiées ont clairement accumulé des déplacements géologiques variables, aucune corrélation n'est observée entre ce paramètre et la variabilité du pré-facteur global de chacune des surfaces de failles. L'interprétation selon laquelle les zones de failles qui auraient accumulé un plus grand déplacement, seraient constituées par des surfaces de glissement globalement plus lisses du fait des processus abrasifs, semble donc inadaptée au regard de nos observations.

La détermination de la géométrie des traces de ruptures laissées à la surface par 8 tremblements de terre majeurs, a permis d'établir que les surfaces de failles restent probablement caractérisées par un unique régime auto-affine légèrement anisotropique et sans longueur caractéristique depuis le micromètre jusqu'à une échelle spatiale de 30 km. Il est à noter qu'aucune corrélation n'a été observée entre l'amplitude moyenne des fluctuations (i.e. le pré-facteur) des traces de ruptures et le déplacement total accumulé par les zones de failles accueillant la rupture sismique. Il faut souligner que dans les deux cas, à savoir les escarpements de failles actives scannées sur le terrain et les traces de ruptures, ces données ont enregistré la morphologie des structures actives de la zone de faille. Mes résultats mettent donc en évidence

que les portions actives des failles depuis l'échelle spatiale du micromètre jusqu'à la trentaine de kilomètres préservent une complexité géométrique au cours des déplacements successifs.

Par une approche numérique décomposée en deux étapes successives, la connexion pressentie entre les propriétés géométriques des surfaces de failles et l'hétérogénéité spatiale en glissement observées sur les modèles cinématiques de rupture durant un séisme a été clarifiée. Dans un premier temps les corrélations spatiales des aspérités géométriques ont étés traduites en terme de distribution spatiale de la résistance frictionnelle le long de la surface de faille en utilisant le modèle de poinçonnement initialement développé par Hansen *et al.* (2000). Ensuite, à l'aide d'un modèle numérique de rupture quasi-statique prenant en considération les interactions élastiques longue portée, les corrélations spatiales du glissement ont été connectées à l'hétérogénéité spatiale de la résistance frictionnelle précédemment déterminée. De cette manière, ma démarche permet de créer un lien direct entre la rugosité 3-D des failles, qui est perpendiculaire au plan de faille, et la distribution spatiale 2-D du glissement dans le plan. Malgré les hypothèses d'un modèle purement élastique lors du poinçonnement des aspérités et de l'absence d'effets dynamiques tel que l'inertie, les corrélations spatiales auto-affines observées sont en accord avec celles déterminées sur les modèles cinématiques de ruptures sismiques.

Dans la continuité de cette démarche numérique permettant de faire le lien entre la rugosité des failles et le glissement lors de la rupture, j'ai suivi une approche théorique afin de prédire l'évolution de la chute de contrainte avec l'échelle spatiale. Dans un premier temps, une implication directe du caractère auto-affine de la distribution spatiale du glissement observée à la fois dans le modèle numérique de rupture et dans les modèles cinématiques, est l'augmentation de la fluctuation spatiale de la chute de contrainte sur le plan de faille vers les petites échelles spatiales. Dans un second temps, en se plaçant dans modèle de propagation de la rupture en cascade, il apparait que la chute de contrainte moyenne ainsi que sa variabilité diminuent avec l'augmentation de la taille de l'événement.

L'ensemble des conclusions de mon approche à la fois numérique et théorique apporte un éclairage sur la relation étroite, souvent pressentie mais jamais clairement établie, entre la rugosité du plan de faille et deux paramètres clés : le glissement et la contrainte. En suivant ce raisonnement, le poinçonnement élastique et le cisaillement des lèvres à géométrie auto-affine de

la faille a plusieurs conséquences: (i) les corrélations spatiales de la rugosité du glissement obéissent également à un régime auto-affine, (ii) les fluctuations de la chute de contrainte le long de la rupture sont plus importantes aux petites échelles avec des corrélations anti-persistantes, (iii) la chute de contrainte moyenne et sa variabilité augmentent avec la diminution de la taille de l'événement de rupture. Le premier point est précisément en accord avec la distribution spatiale du champ de glissement mesuré sur les modèles cinématiques. Rappelons que ces images cinématiques sont restreintes aux grandes longueurs d'ondes, et ignorent probablement les plus grandes variations de la chute de contrainte mise en avant par la seconde conclusion de cette analyse. La troisième et dernière conséquence, à savoir les diminutions de la chute de contrainte moyenne et de sa variabilité avec l'augmentation de la magnitude de l'événement de rupture, n'est qu'en partie corroborée par les études sismologiques. En effet, alors que des données sismologiques récentes sur la déviation standard du mouvement fort du sol (elle-même reliée au premier ordre à la variabilité de la chute de contrainte) mettent en avant de plus grandes fluctuations vers les événements de faible magnitude, l'évolution avec l'échelle de la chute de contrainte moyenne n'est généralement pas observée dans les catalogues de séismicité actuels. Néanmoins, les valeurs de chutes de contraintes observées dans les expériences de ruptures menées en laboratoire, typiquement un à deux ordres de grandeurs supérieures à la gamme de valeurs estimées par les sismologues pour les grands tremblements de terre, confirment le raisonnement suivi. A savoir, du fait de la géométrie auto-affine des failles, les grands tremblements de terre sont probablement composés d'une somme d'aspérités multi-échelles, dont les plus petites (analogues aux ruptures expérimentales) sont susceptibles de supporter une forte chute de contrainte.

Motivés par mes mesures de rugosité qui montrent que les surfaces de faille peuvent être définies par un simple modèle géométrique auto-affine universel et qu'aucune longueur caractéristique n'émerge sur 9 ordres d'échelles spatiales, j'ai proposé qu'un unique processus puisse être à son origine. En mettant en avant l'organisation structurale ubiquiste des zones de failles sous forme de segments depuis l'échelle de l'affleurement jusqu'aux traces de ruptures, je suggère que la propagation et la croissance d'une faille par interactions et coalescence de segments puisse être à l'origine de la géométrie des surfaces de failles. L'approche proposée,

repose sur l'idée simple selon laquelle l'interaction mécanique entre deux segments est susceptible d'évoluer avec leur taille dans le même sens que la chute de contrainte, à savoir diminuer avec l'augmentation de la taille des segments. De cette façon, le processus de croissance de la faille par coalescence et imbrication de segments se fait de manière allométrique et la surface de faille apparait alors de plus en plus lisse aux grandes échelles, i.e. auto-affine.

Lors de ce travail sur la caractérisation de la rugosité des surfaces de failles, je n'ai pas cherché à l'avance à mettre en lumière des variabilités dans la morphologie des failles imputable à des différences dans la lithologie, de composante principale du déplacement, ou de déplacement accumulé. Les explications apportées sont nées des conséquences des analyses de rugosité, couplées aux observations de terrains. C'est la combinaison d'un très grand nombre de mesures indépendantes, à haute résolution, et surtout complémentaires les unes par rapport aux autres, qui a permis de mettre à jour une vision d'ensemble et spatialement continue de la rugosité des surfaces de failles sur 9 ordres de grandeur.

Le lien entre les hétérogénéités de glissement et de contraintes, et la géométrie du plan de faille a été étudié. Mon analyse démontre qu'il est probable qu'une grande partie des fluctuations en glissement et en contraintes le long du plan de faille est dominée par les complexités géométriques locales plutôt que par la dynamique du front de rupture lui-même. La prise en considération des petites échelles et l'intégration des corrélations spatiales des paramètres constitutifs de la rupture (comme le seuil de résistance initial et final, la chute de contrainte) mise en avant dans ce travail, apparait fondamental pour une meilleure compréhension de la mécanique des tremblements de terre.

Références Bibliographiques

Abercrombie, R.E., 1995. Earthquake source scaling relationships from -1 to 5 M(L) using seismograms recorded at 2.5-km depth. *J. Geophys. Res.* 100, 24,015-24,036.

Abercrombie, R.E., Rice, J.R., 2005. Can observations of earthquake scaling constrain slip weakening? *Geophys. J. Int.* 162, 406-424.

Acocella, V., Gudmundsson, A., Funiciello, R., 2000. Interaction and linkage of extension fractures and normal faults: examples from the rift zone of Iceland. *J. Struct.Geol.* 22, 1233.

Agosta, F., Aydin, A., 2006. Architecture and deformation mechanism of a basin-bounding normal fault in Mesozoic platform carbonates, Central Italy. *J. Struct. Geol.*, 28, 1445–1467, doi:10.1016/j.jsg.2006.04.006.

Akkar, S., Bommer, J.J., 2010. Empirical Equations for the Prediction of PGA, PGV, and Spectral Accelerations in Europe, the Mediterranean Region, and the Middle East. *Seism. Res. Lett.* 81, 2.

Aki, K., 1966. Generation and propagation of G waves from the Niigata earthquake of June 16, 1964. 2. Estimation of earthquake moment, release energy, and stress-strain drop from G wave spectrum. *Bull. Earthquake Res. Institute* 44, 23-88.

Aki, K., 1967. Scaling law of seismic spectrum. *Bull. Seism. Soc. Am.* 72, 1217-1231.

Aki, K., 1984. Asperities, barriers, characteristic earthquakes and strong motion prediction. *J. Geophys. Res.* 89, p. 5867–5872.

Allmann, B.P., Shearer, P.M., 2007. Spatial and temporal stress drop variations in small earthquakes near Parkfield, California. *J. Geophys. Res.* 112. B04305, doi:10.1029/2006JB004395.

Allmann, B.P., Shearer, P.M., 2009. Global variations of stress drop for moderate to large earthquakes. *J. Geophys. Res.* 114. B01310, doi:10.1029/2008JB005821.

Amitrano, D., Schmittbuhl, J., 2002. Fracture roughness and gouge distribution of a granite shear band. *J. Geophys. Res.* 107(B12), 2375, doi: 10.1029/2002JB001761.

Amontons, G., 1699. Memoire de l'Académie Royal des Sciences.

An, L.J., 1997. Maximum Link Distance between Strike-slip Faults: Observations and Constraints. *Pure appl. geophys.* 150, 19-36.

Anderson, J.G., 1986. Implication of attenuation for studies of the earthquake source, in Earthquake Source Mechanics. *Geophys. Monogr.* 37, Edited by S. Das et al., pp 311-318, AGU.

Anderson, J.G., Hough, S., 1984. A model for the shape of the Fourier amplitude spectrum of acceleration at high frequencies. *Bull. Seism. Soc. Am.* 74, 1969-1994.

Andrews, D.J., 1976. Rupture propagation with finite stress in antiplane strain. *J. Geophys. Res.* 85, 867-3877.

Andrews, D.J., 1980. A stochastic fault model: 1. Static case. *J. Geophys. Res.* 81, 3575-3582.

Angheluta, L., Jettestuen, E., Mathiesen, J., Renard, R., Jamtveit, B., 2008. Stress-driven phase transformation and the roughening of solid-solid interfaces. *Phys. Rev. Lett.*, 100:096106.

Angheluta, L., Mathiesen, J., Misbah, C., Renard, F., 2010. Morphological instabilities of stressed and reactive geological interfaces. *J. Geophys. Res.*115:doi:10.1029/2009JB006880.

Angheluta, L., Candela, T., Mathiesen, J., Renard, F., 2011. Effect of surface morphology on the dissipation during shear and slip along a rock-rock interface that contains a visco-elastic core. *Pure. Appl. Geophy.* in press.

Aochi, H., Madariaga, R., 2003. The 1999 Izmit, Turkey, Earthquake: Nonplanar fault structure, dynamic rupture process, and strong ground motion. *Bull. Seismol. Soc. Am.*, 93, 1249-1266.

Archard, J.F., 1957. Elastic deformation and the laws of friction. *Proc. R. Soc. London Ser. A.* 243, 190-205.

Archuleta, R., 1984. A faulting model for the 1979 Imperial Valley, California earthquake. *J. Geophys. Res.* 89, 4559-4585.

Arthaud, F., Mattauer, F., 1969. Exemples de stylolites d'origine tectonique dans le Languedoc, leur relation avec la tectonique cassante. *Bulletin de la Société Géologique de France*, 11:738-744.

Aviles, C.A., Scholz, C.H., Boatwright, J., 1987. Fractal Analysis Applied to Characteristic Segments of the San Andreas Fault. *J. Geophys. Res.* 92, 331–344.

Bailey, I.W., Ben-Zion, Y., 2009. Statistics of Earthquake Stress Drops on a Heterogeneous Fault in an Elastic Half-Space, *Bull. Seism. Soc. Am.* 99, 1786-1800, doi: 10.1785/0120080254.

Bakun, W.H., McEvilly, T.V., 1984. Recurrence models and Parkfield, California earthquakes. *J. Geophys. Res.* 89, 3051-3058, doi:10.1029/JB089iB05p03051.

Barabasi, A.-L., Stanley, H.E., 1995. Fractal Concepts in Surface Growth. Cambridge University Press.

Barenblat, G.I., 1962. The mathematical theory of equilibrium cracks in brittle fracture. *Adv. Appl. Mech.* 7, 55-80.

Barka, A., 1996. Slip Distribution along the North Anatolian Fault Associated with the Large Earthquakes of the Period 1939 to 1967. *Bull. Seismol. Soc. Am.*, 86, 1238-1254.

Batrouni, G., Hansen, A., Schmittbuhl, J., 2002. Elastic response of rough surfaces in partial contact. *Europhys. Lett.*, 60(5), 724– 730.

Beeler, N.M., Lockner, D.L., Hickman, S.H., 2001. A simple stick-slip and creep-slip model for repeating earthquakes and its implication for microearthquakes at Parkfield. *Bull. Seism. Soc. Am.* 91, 1797-1804.

Beeler, N.M., 2006. Inferring Earthquake Source Properties From Laboratory Observations and the Scope of Lab Contributions to Source Physics, in Eathquakes: Radiated Energy and the Physics of Faulting, edited by Abercrombie, R. E., McGarr, A., Kanamori, H., Di Toro, G., *Geophysical Monograph Series*, pp. 81-90, AGU.

Ben-Zion, Y., 2003. Key formulas in earthquake seismology, in International Handbook of Earthquake and Engineering Seismology, Part B, edited by W. H. K. Lee et al., appendix 2, pp. 1857–1875, Academic, Amsterdam.

Ben-Zion, Y., Okayada, D., Peng, Z., Michael, A.J., Seeber, L., Armbruster, J.G., Ozer, N., Baris, S., Aktar, M., 2000. High Resolution Imaging of the Geometry and Seismic Properties of the Karadere-Duzce Branch of the North Anatolian Fault at Depth, EOS Trans. Amer. Geophys. Union 81, F1172.

Ben-Zion, Y. and Sammis, C.G., 2003. Characterization of fault zones. *Pure Appl. Geophys.* 160, 677–715, doi: 10.1007/PL00012554.

Ben-Zion, Y., Katz, S., Leary, P., 1992. Joint Inversion of Fault Zone Head Waves and Direct P Arrivals for Crustal Structure near Major Faults. *J. Geophys. Res.* 97, 1943–1951.

Ben-Zion, Y., Malin, P., 1991. San Andreas Fault Zone Head Waves near Parkfield, California. *Science* 251, 1592–1594.

Berg, S.S., 2004. The architecture of normal fault zones in sedimentary rocks: Analysis of fault composition, damage zone asymmetry, and multi-phase flow properties. PhD-thesis, University of Bergen, 118 pp.

Bernard, P., Herrero, A., Berge, C., 1996. Modeling directivity of heterogeneous earthquake ruptures. *Bull. Seism. Soc. Am.* 86, 1149–1160.

Bhat, H., Dmowska, R., Rice, J., Kame, N., 2004. Dynamic slip transfer from the Denali to Totschunda faults, Alaska: Testing theory for fault branching. *Bull. Seismol. Soc. Am.*, 94(6B), S202–S213, doi: 10.1785/0120040601.

Bierme, H., Meerschaert, M.M., Scheffler, H.-P., 2007. Operator scaling stable random fields, *Stoch. Proc. Appl.* 117, 312-332.

Billi, A., Salvini, F., Storti, F., 2003. The damage zone-fault core transition in carbonate rocks: Implications for fault growth, structure and permeability. *J. Struct. Geol.*, 25, 1779–1794, doi:10.1016/S0191- 8141(03)00037-3.

Bistacchi, A., Griffith, W.A., Smith, S.A.F., Di Toro, G., Jones, R., Nielsen, S., 2011. Surface roughness of ancient seismic faults: a combined LIDAR and high-resolution photogrammetric analysis of fault trace profiles. *Pure. Appl. Geophys.* in press

Boatwright, J., Fletcher, J.B., Fumal, T.E., 1991. A general inversion scheme for source site, and propagation characteristics using multiply recorded sets of moderate-sized earthquakes. *Bull. Seism. Soc. Am.* 81, 1754- 1782.

Bouchaud, E., 1997. Scaling properties of cracks. *J. Phys. Condens. Matter*, 9, 4319–4344.

Bouchon, M., 1997. The state of stress on some faults of the San Andreas system as inferred from near field strong motion data. *J. Geophys. Res.* 102, 11731-11744, doi:10.1029/97JB00623.

Bouchon, M., Sekiguchi, H., Irikura, K., Iwata, T., 1998. Some characteristics of the stress field of the 1995 Hyogo-ken Nanbu (Kobe) earthquake. *J. Geophys. Res.* 103, 24271-24282, doi:10.1029/98JB02136.

Bouchon, M., Karabulut, H., Bouin, M.-P., Schmittbuhl, J., Vallée, M., Archuleta, R., Shamita, D., Renard, F., Marsan, D., 2010. Faulting characteristics of supershear earthquakes. *Tectonophysics*, doi:10.1016/j.tecto.2010.06.011.

Boullier, A.-M., Yeh, E.-C., Boutareaud, S., Song, S.-R., Tsai, C.-H., 2009. Microscale anatomy of the 1999 Chi-Chi earthquake fault zone. *Geochem. Geophys. Geosyst.*, 10, Q03016, doi:10.1029/2008GC002252.

Bowden, F.P., Tabor, D., 1950. The friction and lubrication of solids: Part 1. Oxford: Clarendon Press.

Bowden, F.P., Tabor, D., 1964. The friction and lubrication of solids: Part II. Oxford: Clarendon Press.

Boyer, S.E., Elliot, D., 1982. Thrust systems. *American Association of Petroleum Geologist Bulletin 66*, 1196-1230.

Brace, W.F., Byerlee, J., 1966. Stick-slip as a mechanism for earthquakes. *Science*. 153, 990–992, doi:10.1126/science.153.3739.990.

Brodsky, E.E., Kanamori, H., 2001. Elastohydrodynamic lubrication of faults. *J. Geophys. Res.* 106, 16,357–16,374.

Brodsky, E.E., Mori, J., 2007. Creep events slip less than ordinary earthquakes. *Geophys. Res. Lett.* 34, L16309, doi:10.1029/2007GL030917.

Brodsky, E.E., J.G. Gilchrist, A. Sagy and C. Colletini, Faults Smoothly Gradually as a Function of Slip, 2011. *Earth Planet. Sci. Lett.*, in press.

Brown, S.R., 1995. Measuring the dimension of self-affine fractals : Example of rough surfaces, in C. C. Barton et P. R. La Pointe, eds, "Fractals in the earth sciences", Plenum Publishing Corporation.

Brown, S.R., Scholz, C.H., 1985. Broad bandwidth study of the topography of natural rock surfaces. *J. Geophys. Res.* 90, 12575-12582.

Bruhn, R.L., Parry, W.L., Yonkee, W.A., Thompson, T., 1994. Fracturing and Hydrothermal Alteration in Normal Fault Zones. *Pure Appl. Geophys.* 142, 609–644.

Brune, J., 1991. Seismic source dynamics, radiation and stress. *Rev. Geophys.*, 29 Supplement, 688-699.

Byerlee, J.D., 1978. Friction of rocks. *Pure and appl. Geophys.* 116, 615-626.

Caine, J.S., Evans, J.P., Forster, C.B., 1996. Fault zone architecture and permeability structure. *J. Struct. Geol*. 24:1025-1028.

Campillo, M., Favreau, P., Ionescu, I.R., Voisin, C., 2001. On the effective friction law of an heterogeneous fault. *J. Geophys. Res.* 106, p.307-322.

Candela, T., Renard, F., Bouchon, M., Marsan, D., Schmittbuhl, J., Voisin, C., 2009. Characterization of fault roughness at various scales: implications of three-dimensional high resolution topography measurements. *Pure. Appl. Geophy.* 166, 1817-1851.

Candela, T., Renard, R., Schmittbuhl, J., Bouchon, M., Brodsky, E.E., 2011. Fault slip distribution and fault roughness. *Geophys. J. Int.* in review

Candela, T., Renard, R., Schmittbuhl, J., Bouchon, M., Brodsky, E.E., 2011. Stress drop during earthquakes: effect of fault roughness scaling. *Bull. Seism. Soc. Am.* in review

Candela, T., Renard, F., Klinger Y., Mair, K., Schmittbuhl, J., Brodsky, E.E., 2011. Roughness of fault surface over nine decade of length scales: self-affinity, variability, and absence of characteristic length scale. *J. Geophys. Res.* in prep.

Carcaillet, J., Manighetti, I., Chauvel, C., Schlagenhauf, A., Nicole, J.M., 2008. Identifying past earthquakes on an active normal fault (Magnola, Italy) from the chemical analysis of its exhumed carbonate fault plane. *Earth Planet. Sci. Lett.* 271, 145–158, doi:10.1016/j.epsl.2008.03.059.

Carlson, J.M., Langer, J.S., 1989. Mechanical model of an earthquake fault. *Phys. Rev. A* 40, 6470–6484.

Causse, M., Cotton, F., Cornou, C., Bard, P.-Y., 2008. Calibrating Median and Uncertainty Estimates for a Practical Use of Empirical Green's Functions Technique. *Bull. Seism. Soc. Am.* 98, 344-353, doi: 10.1785/0120070075.

Causse, M., Cotton F., Mai, P.M., 2010. Constraining the roughness degree of slip heterogeneity. *J. Geophys. Res.* 115, B05304, doi:10.1029/2009JB006747.

Chambon, G., Schmittbuhl, J., Corfdir, A., Orellana, N., Diraison, M., Geraud, Y., 2006. The thickness of faults: From laboratory experiments to field scale observations. *Tectonophysics*, 426, 77–94, doi:10.1016/j.tecto.2006.02.014.

Chen, G., Spetzler, H.A., 1993. Topographic characteristics of laboratory-induced shear fractures. *Pure Appl. Geophys.* 140, 123–135.

Chen, K.H., Nadeau, R.M., Rau R.-J., 2007. Towards a universal rule on the recurrence interval scaling of repeating earthquakes? *Geophys. Res. Lett*. 34, L16308, doi:10.1029/2007GL030554.

Chen, T., Lapusta, N., 2009. Scaling of small repeating earthquakes explained by interaction of seismic and aseismic slip in a rate and state fault model. *J. Geophys. Res.* 114, B01311, doi:10.1029/2008JB005749.

Chery, J., Zoback, M.D., Hickman, S., 2004. A mechanical model of the san andreas fault and safod pilot hole stress measurements. *Geophys. Res. Lett.* 31:L15S13, doi:10.1029/2004GL019521.

Chester, F.M., Chester, J.S., Kirschner, D.L., Schulz, S.E., Evans, J.P., 2004. Rheology and deformation of the lithosphere at continental margins, chapter Structure of large-displacement, strike-slip fault zones in the brittle continental crust, pp. 223. Columbia University Press, New York.

Chester, F.M., Logan, J.M., 1986. Implications for mechanical-properties of brittle faults from observations of the punchbowl fault zone, california. *Pure and appl. Geophys.* 124, 79-106.

Chester, F.M., Evans, J.P., Biegel, R.L., 1993. Internal structure and weakening mechanisms of the San-Andreas Fault. *J. Geophys. Res.*, 98, 771–786, doi:10.1029/92JB01866.

Chester, F.M., Chester, J.S., 2000. Stress and deformation along wavy frictional faults. *J. Geophys. Res.* 105(B10):23421.

Childs, C., Walsh, J.J., Watterson, J., 1997. Complexity in fault zone structure and implications for fault seal prediction. In Møller-Pedersen, P. and Koestler, A. G. (eds.), Hydrocarbon Seals: Importance for Exploration and Production. Norwegian Petroleum Society (NPF) Special Publications 7, 61-72.

Choy, G.L., Kirby, S.H., 2004. Apparent stress, fault maturity and seismic hazard for normal-fault earthquakes at subduction zones. *Geophys. J. Int.* 159, pp. 991 – 1012, doi:10.1111/j.1365-246X.2004.02449.x.

Christensen, M., 2004. Soft sediment faulting – Investigation of the 3D geometry and fault zone properties. Ph.D-thesis, University of Aarhus, 146 pp.

Clausel, M., Vedel, B., 2008. Explicit constructions of operator scaling stable random Gaussian fields. *Adv. Appl. Prob*.

Clausen, J.A., Gabrielsen, R.H., Johnsen, E., 2003. Fault architecture and clay smear distribution. Examples from field studies and drained ring-shear experiments. *Norwegian Journal of Geology* 83 (2), 131-146.

Cochard, A., Rice, J.R., 1997. A spectral method for numerical elastodynamic fracture analysis without spatial replication of the rupture event. *J. Mech. Phys. Solids*, 45, 1393-1418.

Cotterell, B., Rice, J.R., 1980. Slightly curved or kinked cracks. *lnt. J. Fracture*, 16, 155-169.

Cotton, F., Campillo, M., 1995. Inversion of strong ground motion in the frequency domain: Applications to 1992 Landers, California earthquake. *J. Geophys. Res.* 100, 3961-3975.

Cotton, F., Pousse, G., Bonilla, F., Scherbaum, F., 2008. On the discrepancy of recent European ground-motion observations and predictions from empirical models: analysis of KIK-net accelerometric data and point-sources stochastic simulations. *Bull. Seism. Soc. Am.* 98(5), 2244–2261.

Cowan, D.S., 1999. Do faults preserve a record of seismic slip? A field geologist's opinion. *J. Struct. Geol.* 21, 995-1001.

Cowie, P.A., Scholz, C.H., 1992. Displacement–length scaling relationships for faults: data synthesis and discussion. *J. Struct. Geol.* 14, 1149-115.

Cowie, P.A. Scholz, C.H., 1992. Growth of faults by accumulation of seismic slip. *J. Geophys. Res.* 97, 11085-11095.

Cowie, P.A., Scholz, C.H., 1992. Physical explanation for the displacement length relationship of faults using a post-yield fracture mechanics model. *J. Struct. Geol.* 14(10), 1133-1148.

Cuisiat, F., Skurtveit., S., 2010. An experimental investigation of the development and permeability of clay smears along faults in uncemented sediments. *J. Struct. Geol.* 1-14, doi:10.1016/j.jsg.2009.12.005.

Dabrowski, M., Krotkiewski, M., Schmid, D.W., 2008. Milamin: Matlab-based finite element method solver for large problems. *Geochem. Geophys. Geosyst.*, 9:Q04030, doi:10.1029/2007GC001719.

Davison, I., 1994. Linked fault systems; extensional, strike-slip and contractional. In: Hancock,P.L. (ed.): Continental deformation. Pergamon Press, Oxford, 121-142.

Dawers, N.H., Anders, M.H., Scholz, C.H., 1993. Growth of normal faults: displacement-length scaling. *Geology*, 21, 1107-1110.

Deng. Q., Wu, D., Zhang, P., Chen. S., 1986. Structure and deformational character of strike slip fault zones. *Pure Appl. Geophys.* 124, 204-223.

De Paola N., Hirose, T., Mitchell, T., Di Toro, G., Viti, C., Shimamoto, T., 2011. Fault lubrication and earthquake propagation in thermally unstable Rocks. *Geology*. 39, 35–38. doi: 10.1130/G31398.1.

Dieterich, J.H., 1979. Modeling of rock friction: 1.experimental results and constitutive equations. *J. Geophys. Res.*, 84, 2161–2168.

Dieterich, J.H., Kilgore, B.D., 1994. Direct observations of frictional contacts: new insights for state-dependent properties. in *Faulting, Friction, and Earthquake Mechanics*, Part II, eds. C.J. Marone and M.L. Blanpied, Basel: Birkhauser, pp. 283-302.

Dieterich, J.H., Kilgore, B., 1996. Implications of fault constitutive properties for earthquake prediction. *Proc. Natl Acad. Sci.* USA, 93, 3787-3794.

Dieterich, J.H., Smith, D.E., 2009. Nonplanar faults: mechanics of slip and off-fault damage. *Pure. Appl. Geophy.* 166, 1799-1815.

Di Toro, G., Pennacchioni G., 2005. Fault plane processes and mesoscopic structure of a strong-type seismogenic fault in tonalites (Adamello batholith, Southern Alps), *Tectonophysics* 402, 55-80.

Dozer, D.I., 1986. Earthquake processes in the Rainbow Mountain-Fairview Peak-Dixie Valley, Nevada, Region 1954-1969. *J. Geophys. Res.* 91, 12572-12586.

Du, Y., Aydin, A., 1991. Interaction of multiple cracks and formation of echelon crack arrays. *International Journal of Numerical and Analytical Methods in Geomechanics*, 15, 205-218.

Dugdale, D.S.J., 1960. Yielding of stress sheets containing slits. *Mech. Phys. Solids*, 8, 800-115.

Dysthe D.K., Podladchikov, Y., Renard, F., Feder, J., Jamtveit, B., 2002. Universal Scaling in Transient Creep. *Phys. Rev. Lett.*, DOI: 10.1103/PhysRevLett.89.246102.

Egholm, D.L., Clausen, O.R., Sandiford, M., Kirstensen, M.B., Korstgard, J.A., 2008. The mechanics of clay smearing along faults. *Geology*, 36:7877908.

Elliott, D., 1976. The energy balance and deformation mechanisms of thrust sheets. Philos. Trans. R. Soc. London, Ser. A, 283, 289-312.

Ellsworth, W.L., Dietz, L.D., 1990. Repeating earthquakes: Characteristics and implications, U.S Geol. Surv. Open File Rep. 90-98, 226-245.

Evans, J.P., Chester, F.M., 1995. Fluid-rock Interaction in Faults of the San Andreas System: Inferences from San Gabriel Fault Rock Geochemistry and Microstructures. *J. Geophys. Res.* 100, 13007-13020.

Faulkner, D.R., Lewis, A.C., Rutter, A.H., 2003. On the internal structure and mechanics of large strike-slip fault zones: field observations of the Carboneras fault in southeastern Spain. *Tectonophysics*, 367, 235-251.

Feder J., 1988. Fractals, Plenum, New York.

Fender, M.L., Lechenault, F., Daniels, K.E., 2010. Universal Shapes Formed by Two Interacting Cracks. *Phys. Rev. Lett.* DOI: 10.1103/PhysRevLett.105.125505.

Fisher, D., 1998. Collective Transport in Random Media: From Superconductors to Earthquakes. Physics Reports 301, 113–150.

Florensov, N.A., Solonenko, V.P., 1965. The Gobi-Altai Earthquake. 424 pp., U.S. Dep. of Commer., Washington, D. C.

Fonseca, J., 1988. The Sou Hills: a barrier to faulting in the Central Nevada Seismic Belt. *J. Geophys. Res.* 93, 475-489.

Frankel, A., 1991. High-frequency spectral fall-off of earthquakes, fractal dimension of complex rupture, b value, and the scaling of strength on faults. *J. Geophys. Res.* 96, pp. 6291-6302, doi:10.1029/91JB00237.

Frankel, A., Wennerberg, L., 1989. Microearthquake spectra from the Anza, California seismic network: Site response and source scaling. *Bull. Seism. Soc. Am.* 79, 581–609.

Gabrielsen, R.H., Clausen, J.A., 2001. Horses and duplexes in extensional regimes: A scale-modeling contribution. In: Koyi, H. A. and Mancktelow, N. (eds.), Tectonic models: A Volume in Honor of Hans Ramberg. Geological Society of America Memoir 193, 219-233.

Gibbs, A.D., 1983. Balanced cross-section construction from seismic sections in areas of extensional tectonics. *J. Struct. Geol.* 5, 153-160.

Gibbs, A.D., 1984. Structural evolution of extensional margins. *J. Geological Society of London*, 141, 609-620.

Goscombe, B.D., Passchier, C., Handa, M., 2004. Boudinage classification: end-member boudin types and modified boudin structures. *J. Struct. Geol.* 26, 739–763.

Gorodtsov, G.A., Leonov, A.I., 1967. On a linear instability of a plane parallel couette flow of viscoelastic fluid. *Journal of Applied Mathematics and Mechanics*, 31:310-319.

Greenwood, J.A., Williamson, 1966. Contact of nominally flat surfaces. *J. Proc. Roy. Soc. London*, 285, 300-319.

Griffith, A.A., 1920. The phenomena of rupture and flow in solids. *Trans. Roy. Soc. Phil. Ser. A* 221, 163-198.

Griffith, W.A., Di Toro, G., Pennacchioni, G., Pollard, D.D., Nielsen, S., 2009. Static stress drop associated with brittle slip events on exhumed faults. *J. Geophys. Res.* 114, B02402, doi:10.1029/2008JB005879.

Han, R., Hirose, T., Shimamoto, T., 2010. Strong velocity weakening and powder lubrication of simulated carbonate faults at seismic slip rates. *J. Geophys. Res.* 115, B03412, doi:10.1029/2008JB006136.

Hanks, T.C., 1982. Fmax. *Bull. Seism. Soc. Am.* 72, 1867-1879.

Hanks, T.C., 1977. Earthquake stress drops, ambient tectonic stresses and stresses that drive plate motions. *Pure. Appl. Geophys.* 1, 15, 441-458.

Hansen, A., Schmittbuhl, J., Batrouni, G., 2001. Distinguishing fractional and white noise in one and two dimensions. *Phys. Rev. E*, 062102-1.

Hansen, A., Schmittbuhl, J., Batrouni, G., Oliveira, F.A., 2000. Normal stress distribution of rough surfaces in contact. *Geophys. Res. Lett.* 27, 3639–3643.

Harrington, R.M., Brodsky, E.E., 2011. Energy and Rupture Dynamics are different for earthquake on mature vs. immature faults. *J. Geophys. Res.* submitted.

Hernandez, B., Cotton, F., Campillo, M., 1999. contribution of radar interferometry to a two step inversion of the kinematic process : variability of the rupture front velocity during the 1992 landers earthquake. *J. Geophys. Res.*, 104:14925–14945.

Herrero, A., Bernard, P., 1994. A kinematic self-similar rupture process for earthquakes. *Bull. Seismol. Soc. Am.*, 84(4), 1216–1288.

Hirata, T., 1989. Fractal Dimension of Fault Systems in Japan: Fractal Structure in Rock Fracture Geometry at Various Scales. *Pure Appl. Geophys.* 131, 157–170.

Hirth, J.P., Rice, J.R., 1980. On the Thermodynamics of Adsorption at Interfaces as it Influences Decohesion. *Metallurgical Transactions*, 11A, pp. 1501-1511.

Hok, S. (2008), Vers l'arrêt spontané de la rupture en dynamique de la source : non-élasticité du milieu et loi de friction hétérogène. Ph. D. Thesis, Univ. Joseph Fourier, Grenoble.

Horowitz, F.G., Ruina, A., 1989. Slip patterns in a spatially homogeneous fault model. *J. Geophys. Res.* 94(B8), doi:10.1029/JB094iB08p10279

Hough, S.E., Ben-Zion, Y., Leary, P., 1994. Fault-zone Waves Observed at the Southern Joshua Tree Earthquake Rupture Zone. *Bull. Seismol. Soc. Am.*, 84, 761-767.

Hubert-Ferrari, A., Armijo, R., King, G., Meyer, B., and Barka, K., 2002, Morphology, displacement, and slip rates along the North Anatolian Fault, Turkey. *J. Geophys. Res.* 107(B10), 2235, doi:10.1029/2001JB000393.

Ide, S., Beroza, G.C., 2001. Does apparent stress vary with earthquake size? *Geophys. Res. Lett.* 28, 3349-3352.

Ide, S., Beroza, G.C., Prejean, S.G., Ellsworth, W.L., 2003. Apparent break in earthquake scaling due to path and site effects on deep borehole recordings. *J. Geophys. Res.* 108, doi:10.1029/2001JB001617.

Imanishi, K., Ellsworth, W.L., 2006. Source scaling relationships of microearthquakes at Parkfield, CA, determined using the SAFOD pilot hole seismic array, in Eathquakes: Radiated Energy and the Physics of Faulting, edited by Abercrombie, R. E., McGarr, A., Kanamori, H., Di Toro, G., *Geophysical Monograph Series*. 81-90, AGU.

Johnson, A. M., Fletcher, R.C., 1994. Folding of Viscous Layers: Mechanical Analysis and Interpretation of Structures in Deformed Rock, Columbia University Press.

Kamb, B., 1970. Sliding motion of glaciers: theory and observation. *Reviews of Geophysics*, 8(4):673-728.

Kanamori, H., Anderson, D.L., 1975. Theoretical basis of some empirical relations in seismology. *Bull. Seism. Soc. Am.* 65, 1073-1095.

Kanamori, H., Mori, J., Heaton, T.H., 1990. The 3 December 1988, Pasadena Earthquake (ML = 4.9) recorded with the very broadband system in Pasadena. *Bull. Seism. Soc. Am.* 80, 483-487.

Kanamori, H., Mori, J., Hauksson, E., Heaton, T.H., Hutton, L.K., Jones, L.M., 1993. Determination of earthquake energy release and ML using TERRAscope. *Bull. Seism. Soc. Am.* 2, 330-346.

Kanamori, H., 1994. Mechanics of earthquakes. *Annu. Rev. Earth Planet. Sci.* 22, 207-237, doi:10.1146/annurev.ea.22.050194.001231.

Kanamori, H., Heaton, T.H., 2000. Microscopic and macroscopic physics of earthquakes, in GeoComplexity and the Physics of Earthquakes, J. Rundle, D. Turcotte, and W. Klein (Editors), *American Geophysical Monograph* 120, 147-183.

Kanamori, H., Brodsky, E.E., 2004. The physics of earthquakes, *Reports On Progress In Physics.* 67, 1429-1496.

Kanamori, H., Rivera, L., 2006. Energy partitioning during an earthquake, in Earthquakes: Radiated Energy and the Physics of Faulting, *Geophysical Monograph Series* 170.

Klinger, Y., Xu, X.W., Tapponnier, P., Van der Woerd, J., Lasserre, C., King, G., 2005. High-resolution satellite imagery mapping of the surface rupture and slip distribution of the Mw 7.8, 14 November 2001 Kokoxili Earthquake, Kunlun Fault, northern Tibet, China. *Bull. Seismol. Soc. Am.*, 95(5), 1970-1987, doi:10.1785/0120040233.

Klinger, Y., Michel, R., King, G.C.P., 2006. Evidence for an earthquake barrier model from Mw similar to 7.8 Kokoxili (Tibet) earthquake slip-distribution. *Earth Planet. Sci. Lett.*, 242(3-4), 354–364, doi:10.1016/j.epsl.2005.12.003.

Klinger, Y., 2010. Relation between continental strike-slip earthquake segmentation and thickness of the crust. *J. Geophys. Res.* 115, B07306, doi:10.1029/2009JB006550.

Knuepfer, P.L., 1989. Implications of the characteristics of end-points of historical surface fault ruptures for the nature of fault segmentation, U.S. Geol. Surv. Proc. of Workshop XLV: Fault Segmentation and Controls of Rupture Initiation and Termination. OFR89-315, 193–228.

Kondo, H., Awata, Y., Emre, Ö., Doğan, A., Özalp, S., Tokay, F., Yıldırım, C., Yoshioka, T., Okumura, K., 2005. Slip distribution, fault geometry, and fault segmentation of the 1944 Bolu-Gerede earthquake rupture, North Anatolian Fault, Turkey. *Bull. Seismol. Soc. Am.*, 95, 1234-1249, doi:10.1785/0120040194.

Kondo, H., Özaksoy, V., Yıldırım, C., 2010. Slip history of the 1944 Bolu-Gerede earthquake rupture along the North Anatolian fault system: Implications for recurrence behavior of multisegment earthquakes. *J. Geophys. Res.* 115, B04316, doi:10.1029/2009JB006413.

Kurushin, R.A., Bayasgalan, A., Ölziybat, M., Enhtuvshin, B., Molnar, P., Bayarsayhan, C., Hudnut, K., Jian, L., 1997. The surface rupture of the 1957 Gobi-Altay, Mongolia, Earthquake. *Spec. Pap. Geol. Soc. Am.*, 320, 142 p.

Kuwahara, Y., Ito, H., 2000. Deep Structure of the Nojima Fault byTrapped Wave Analysis, USGS, Open-file Report 00–129, 283–289.

Lachenbruch, A.H., 1980. Frictional heating, fluid pressure, and the resistance to fault motion. *J. Geophys. Res.* 85, 6097–6112.

Lavallée, D., Archuleta, R.J., 2005. Coupling of the random properties of the source and the ground motion for the 1999 Chi Chi earthquake. *Geophys. Res. Lett.*, 32.

Lay, T., H., Kanamori, H., Ruff, L., 1982. The asperity model and the nature of large subduction zone earthquakes. Earthquake Prediction Research, 1, p. 3–71.

Leary, P., Li, Y.G., AKI, K., 1987. Observations and Modeling of Fault Zone Fracture Anisotropy, I, P, SV, SH Travel Times. *Geophys. J. R. Astron. Soc.* 91, 461–484.

Lee, J.J., Bruhn, R.L., 1996. Structural anisotropy of normal fault surfaces. *J. Struct. Geol.* 18, 1043-1059.

Li, Y.G., Leary, P., Aki, K., Malin, P., 1990. Seismic Trapped Modes in the Oroville and San Andreas Fault Zones. *Science* 249, 763-766.

Libicki, E., Ben-Zion, Y., 2005. Stochastic Branching Models of Fault Surfaces and Estimated Fractal Dimensions. *Pure and Appl. Geophys.* 162, 1077-1111, doi: 10.1007/s00024-004-2662-7.

Lindanger, R, Øygaren, M., Gabrielsen, R.H., Mjelde,R., Randen,T., Tjøstheim, B.A., 2004. Analogue (plaster) modelling and synthetic seismic representation of hangingwall fault blocks above of rampflat ramp faults. First Break 22, 22-30.

Lindanger, M., Gabrielsen, R.H., Braathen, A., 2007. Analysis of rock lenses in extensional faults. *Norwegian Journal of Geology*, 87, 361-372.

Madariaga, R., 1979. On the relation between seismic moment and stress drop in the presence of stress and strength heterogeneity. *J. Geophys. Res.* 84, 2243-2250.

Maerten, L., Willemse, E.J.M., Pollard, D.D., Rawnsley, K., 1999. Slip distributions on intersecting normal faults. *J. Struct. Geol.* 21, 259-271.

Mai, P.M., Beroza, G.C., 2002. A spatial random field model to characterize complexity in earthquake slip. *J. Geophys. Res.* 107, doi:10.1029/2001JB000588.

Main, I.G., 2000. A damage mechanics model for power law creep and earthquake aftershock and foreshock sequences. *Geophys. J. Int.* 142, 151-161.

Mandelbrot, B.B., 1983. The Fractal Geometry of Nature, 468 pp., Freeman, New York.

Mandelbrot, B.B., 1985. Self-affine fractals and fractal dimension. *Phys. Scripta.* 32, 257-260.

Mandelbrot, B.B., 1986. Fractals in Physics. Elsevier, Amsterdam.

Manighetti, I., Campillo, M., Bouley, S., Cotton, F., 2007. Earthquake scaling, fault segmentation, and structural maturity. *Earth Planet. Sci. Lett.*, 253(3-4), 429-438, doi:10.1016/j.epsl.2006.11.004.

Marone, C., 1998. Laboratory-derived friction laws and their application to seismic faulting. *Annu. Rev. Earth Planet. Sci.*, 26, 643–696.

Marrett, R., Allmendinger, R.W., 1992. Amount of extension on "small" faults: An example from the Viking graben. *Geology*, 20, 47-50.

Marsan, D., 2006. Can coseismic stress variability suppress seismicity shadows? Insights from a rate-and-state friction model. *J. Geophys. Res.* 111, B06305, doi:10.1029/2005JB004060.

Mauduit, T., Dauteuil, O., 1996. Small-scale models of oceanic transform zones. *J. Geophys. Res.* 98, 12251-12265.

Mayeda, K., Malagnini, L., Walter, W.R., 2003. A new spectral ratio method using narrow band coda envelopes: Evidence for non-self-similarity in the Hector Mine sequence. *Geophys. Res. Lett.* 34, L11303, doi:10.1029/2007GL030041.

McGarr, A., 1999. On relating apparent stress to the stress causing earthquake fault slip. *J. Geophys. Res.* 104, 3003–3011.

McGarr, A., Fletcher, J.B., 2003. Maximum slip in earthquake fault zones, apparent stress, and stick-slip friction. *Bull. Seismol. Soc. Am.* 93, 2355–2362.

Meakin, P., 1998. Fractals: Scaling and Growth far From Equilibrium. Cambridge Univ. Press, New York.

Méheust, Y., 2002. Ecoulements dans les fractures ouvertes. Ph. D. Thesis, Univ. Paris VI and Ecole Normale Superieure, Paris.

Mitchell, T.M., Faulkner, D.R., 2009. The nature and origin of off-fault damage surrounding strike-slip fault zones with a wide range of displacements: A field study from the Atacama fault system, northern Chile. *J. Struct. Geol.* 31, 802-816.

Munguia, L., Brune, J.N., 1984. High stress drop events in the Victoria, Baja California earthquake swarm of 1978. *Geophys. J. R. Astron. Soc.* 76,725–752.

Nadeau, R.M., Johnson, L.R., 1998. Seismological studies at Parkfield VI: moment release rates and estimates of source parameters for small repeatinge arthquakes. *Bull. Seism. Soc. Am.* 88, 790-814.

Nishigami, K., Ando, M., Tadokoro, K., 2001. Seismic Observations in the DPRI 1800m Borehole Drilled into the Nojima Fault Zone, Southwest Japan, Island Arc, 10, 288-295.

Ohnaka, M., Shen, L., 1999. Scaling of the shear rupture process from nucleation to dynamic propagation : Implications of geometry irregularity of the rupturing surfaces. *J. Geophys. Res.*, 104(B1), 817-844.

Okaya, D.A., Thompson, G.A., 1985. Geometry of Cenozoic extensional faulting: Dixie Valley, Nevada. *Tectonics*, 4, 107-125.

Okubo, P.G., Aki, K., 1987. Fractal Geometry in the San Andreas Fault System. *J. Geophys. Res.* 92, 345-355.

Oldroyd, J.G., 1950. On the formulation of rheological equations of state. Proceedings of the Royal Society of London Series A - Mathematical and Physical Sciences, 200, 523-541.

Olson, J., 1993. Joint pattern development: effect of subcritical crack growth and mechanical crack interaction. *J. Geophys. Res.* 101, 20195-20209.

Olson, J., Pollard, D.D., 1989. Inferring paleostresses from natural fracture patterns: a new method. *Geology* 17, 345-348.

Otsuki, K., Dilov, T., 2005. Evolution of hierarchical self-similar geometry of experimental fault zones: Implications for seismic nucleation and earthquake size. *J. Geophys. Res.* 110, B03303, doi:10.1029/2004JB003359.

Palumbo, L., Benedetti, L., Bourles, D., Cinque, A., Finkel, R., 2004. Slip history of the Magnola fault (Apennines, Central Italy) from 36Cl surface exposure dating: Evidence for strong earthquakes over the Holocene. *Earth Planet. Sci. Lett.* 225, 163–176.

Parsons, T., 2008. Persistent earthquake clusters and gaps from slip on irregular faults. *Nature Geoscience*, 1, 59-63, doi:10.1038/ngeo.2007.36.

Perfettini, H., Schmittbuhl, J., Vilotte, J., 2001. Slip Correlations on a Creeping Fault. *Geophys. Res. Lett.* 28(10), 2133-2136.

Peyrat, S., Olsen, K.B., Madariaga, R., 2004. Which Dynamic Rupture Parameters Can Be Estimated from Strong Ground Motion and Geodetic Data? *Pure and Appl. Geophys.* 161, p. 2155–2169, doi: 10.1007/s00024-004-2555-9.

Poliakov, A.N., Dmowska, R., Rice, J.R., 2002. Dynamic shear rupture interactions with fault bends and off-axis secondary faulting. *J. Geophys. Res.* 107(B11), 2295, doi:10.1029/2001JB000572.

Pollard, D.D., Segall, P., Delaney, P.T., 1982. Formation and interpretation of dilatant echelon cracks. Geol. Soc. Am. Bull. 93, 1291.

Pollard, D.D., Aydin, A., 1984. Propagation and Linkage of Oceanic Ridge Segments. *J. Geophys. Res.* 89, 10017.

Power, W.L., Tullis, T.E., Brown, S.R., Boitnott, G.N., Scholz, C.H., 1987. Roughness of natural fault surfaces. *Geophys. Res. Lett.* 14, 29-32.

Power, W.L., Tullis, T.E., Weeks, J.D., 1988. Roughness and wear during brittle faulting, *J. Geophys. Res.* 93, 15268-15278.

Power,W. L., Tullis, T.E., 1989. The relationship between slickenside surfaces in fine-grained quartz and the seismic cycle. *J. Struct. Geol.*, 11, 879-893.

Power, W.L., Tullis, T.E., 1991. Euclidean and fractal models for the description of rock surface roughness. *J. Geophys. Res.* 96, 415-424, doi:10.1029/90JB02107.

Power, W.L., Tullis, T.E., 1992. The contact between opposing fault surfaces at Dixie Valley, Nevada, and implications for fault mechanics. *J. Geophys. Res.* 97, 15425-15435, doi:10.1029/92JB01059.

Power, W.L., Durham, W.B., 1997. Topography of natural and artificial fractures in granitic rocks: Implications for studies of rock friction and fluid migration. *Int. J. Rock Mech. Min. Sci.* 34, 979-989.

Prejean, S.G., Ellsworth, W.L., 2001. Observations of earthquake source parameters and attenuation at 2 km depth in the Long Valley caldera, eastern California, *Bull. Seism. Soc. Am.* 91, 165-177.

Press, W.H., Teukolsky, S.A., Vetterling, W.T., Flannery, B.P., 2007. Numerical Recipes, 3rd ed., Cambridge Univ. Press: Cambridge, UK.

Prieto, G.A., Shearer, P.M., Vernon, F.L., Kilb, D., 2004. Earthquake source scaling and self-similarity estimation from stacking P and S spectra. *J. Geophys. Res.* 109, B08310, doi:10.1029/2004JB003084.

Prieto, G.A., Thomson, D.J., Vernon, F.L., Shearer, P.M., Parker, R.L., 2007. Confidence intervals for earthquake source parameters. *Geophys. J. Int.* 168, 1227-1234.

Pritchard, M.E., Simons., M., 2006. An aseismic slip pulse in northern chile and along-strike variations in seismogenic behavior. *J. Geophys. Res.* 111:B08405, doi:10.1029/2006JB004258.

Rabinowicz, E., 1951. The nature of the static and kinetic coefficients of friction. *J. Appl. Phys.* 22, 1373-1379.

Railsback, L.B., Andrews, L.M., 1995. Tectonic stylolites in the undeformed Cumberland Plateau of southern Tennessee. *J. Struct. Geol*. 17, 911-915.

Ramanathan, S., Fisher, D., 1997. Dynamics and Instabilities of Planar Tensile Cracks in Heterogeneous Media. *Phys. Rev. Lett.* 79, 877–880.

Renard, F., Voisin, C., Marsan, D., Schmittbuhl, J., 2006. High resolution 3D laser scanner measurements of a strike-slip fault quantify its morphological anisotropy at all scales. *Geophys. Res. Lett.*, 33, L04305.

Renard, F., Gratier, J.-P., Jamtveit, B., 2000. Kinetics of crack-sealing, intergranular pressure solution, and compaction around active faults. *Journal of Structural Geology*, 22:1395-1407.

Resor, P. G., Meer, V. E., 2009, Slip heterogeneity on a corrugated fault. *Earth Planet. Sci. Lett.* doi:10.1016/j.epsl.2009.10.010.

Ripperger, J., Ampuero, J.-P., Mai, P.M., Giardini, D., 2007. Earthquake source characteristics from dynamic rupture with constrained stochastic fault stress. J. Geophys. Res. 112:B04311. Doi :10.1029/2006JB004515.

Rubin, A.M., Gillard, D., Got, J.-L., 1999. Streaks of microearthquakes along creeping faults. *Nature,* 400, 635–641.

Rutter, E.H., 1976. The kinetics of rock deformation by pressure solution. Philosophical Transactions of the Royal Society of London, 283:203-219.

Sagy A., Brodsky, E.E., Axen, G.J., 2007. Evolution of fault-surface roughness with slip. *Geology*, 35, 283-286.

Sagy, A., and Brodsky, E. E., 2009. Geometric and Rheological Asperities in an Exposed Fault Zone. *J. Geophys. Res.* 114(B02301), doi:10.1029/2008JB005701.

Sammis, C.G., Nadeau, R.M., Johnson, L.R., 1999. How strong is an asperity? *J. Geophys. Res.* 104, pp. 10609-10619, doi:10.1029/1999JB900006.

Sammis, C.G., AN, L., Ershaghi, I., 1992. Determining the 3-D Fracture Structure of the Geysers Geothermal Reservoir, Proc. 17th Workshop on Geothermal Reservoir Engineering, Stanford University, Stanford, CA, Jan. 29–31.

Sammis, C.G., Rice, J.R., 2001. Repeating earthquakes as low-stress-drop events at a border between locked and creeping fault patches. *Bull. Seism. Soc. Am.* 91, 532– 537.

Saucier, F., Humphreys, E., Weldon R., II, 1992. Stress near geometrically complex strike-slip faults: application to the San Andreas Fault at Cajon Pass, southern California. *J. Geophys. Res.* 97(B4):5081-5094.

Savage, H.M., Brodsky, E.E., 2011. Collateral Damage: Capturing Fault Strand Formation in Fracture Profiles. *J. Geophys. Res.* in press.

Schaff, D.P., Bokelmann, G.H.R., Beroza, G.C., Waldhauser, F., Ellsworth, W.L., 2002. High-resolution image of Calaveras fault seismicity. *J. Geophys. Res.* 107, doi:10.1029/2001JB000633.

Schlische, R.W., Young, S.S., Ackermann, R.V., Gupta, A., 1996. Geometry and scaling relations of a population of very small rift related normal faults. *Geology*, 24, 683–686.

Schmittbuhl, J., Gentier, S., Roux, R., 1993. Field measurements of the roughness of fault surfaces. *Geophys. Res. Lett.* 20, 639-641.

Schmittbuhl, J., Vilotte, J., Roux, S., 1995a. Reliability of self-affine measurements. *Phys. Rev. E.* 51, 131-147.

Schmittbuhl, J., Schmitt, F., Scholz, C.H., 1995b. Scaling invariance of crack surfaces. *J. Geophys. Res.* 100, 5953-5973.

Schmittbuhl, J., Vilotte, J., 1999. Interfacial Crack Front Wandering: Influence of Correlated Quenched Noise. *Physica A* 270, 42-56.

Schmittbuhl, J., Delaplace, A., Maloy, K., Perfettini, H., Vilotte, J., 2003. Slow Crack Propagation and Slip Correlations. *Pure. Appl. Geophy*. 160, 961-976, doi:10.1007/PL00012575.

Schmittbuhl, J., Hansen, A., Batrouni, G.G., 2003. Roughness of Interfacial Crack Fronts: Stress Weighted Percolation in the Damage Zone. Phys. Rev. Lett., DOI: 10.1103/PhysRevLett.90.045505.

Schmittbuhl, J., Chambon, G., Hansen, A., Bouchon, M., 2006. Are stress distributions along faults the signature of asperity squeeze? *Geophys. Res. Lett.* 33, doi:10.1029/2006GL025952.

Schmittbuhl, J, Steyer, A., Jouniaux, L., Toussaint, R., 2008. Fracture morphology and viscous transport. *Int. J. Rock. Mech. Min. Sci.*, 45, 422-430.

Scholz, C.H., Aviles, C.A., 1986. The fractal geometry of faults and faulting, in 5th Ewing Symposium, Earthquake Source Mechanisms, *Geophys. Monogr. Ser.*, 37, edited by Das, S., Boatwright, J., Scholz, C. H. pp. 147-156, AGU, Washington D. C.

Scholz, C.H., Dawers, N.H., Yu, J.-Z., Anders, M.H., Cowie, P.A., 1993. Fault Growth and Fault Scaling Laws: Preliminary Results. *J. Geophys. Res.* 98, 21951-21961.

Scholz, C.H., 2002. The mechanics of earthquakes and faulting, 2nd edition, Cambridge Univ. Press, New York.

Scholz, C.H., 2007. In:Watts, A.B. (Ed.), Fault Mechanics. Treatise on Geophysics, vol. 6. Elsevier, pp. 441e483.

Scholz, C.H., 2010. A note on the scaling relations for opening mode fractures in rock. *J. Struct. Geol.* doi:10.1016/j.jsg.2010.09.007.

Schulz, R.A., 1988. Stress intensity factors for curved cracks obtained with the displacement discontinuity method. *Int. J. Fracture*, 37, 31-34.

Schultz, R.A., Okubo, C.H., Wilkins, S.J., 2006. Displacement–length scaling relations for faults on the terrestrial planets. *J. Struct. Geol.* 28, 2182–2193.

Schultz, R.A., Soliva, R., Fossen, H., Okubo, C.H., Reeves, D.M., 2008. Dependence of displacement-length scaling relations for fractures and deformation bands on the volumetric changes across them. *J. Struct. Geol.* 30, 1405-1411.

Segall, P., Pollard, D.D., 1980. Mechanics of discontinuous faults. *J. geophys. Res.* 85, 4337-4350.

Shankar, V., Kumar, S., 2004. Instability of viscoelastic plane couette flow past a deformable wall. *Journal of Non-Newtonian fluid mechanics*, 116, 371-393.

Shearer, P.M., Prieto, G.A., Hauksson, E., 2006. Comprehensive analysis of earthquake source spectra in southern California. *J. Geophys. Res.* 111, doi:10.1029/2005JB003979.

Shipton, Z., Soden, A.M., Kirkpatrick, J.D., 2006. Earthquakes: Radiated energy and the physics of faulting, chapter How thick is a fault? Fault displacement-thickness scaling revisited, page 193. American Geophysical Union.

Sibson, R.H., 1973. Interactions between temperature and fluid during earthquake faulting: a mechanism for partial or total stress relief. *Nature*, 243, 66–68.

Sibson, R.H., 1977. Fault rocks and fault mechanisms. *J. Geol. Soc.*, 133, 191– 213, doi:10.1144/gsjgs.133.3.0191.

Sibson, R.H., 1985. Stopping of earthquake ruptures at dilational fault jogs. *Nature*, 316, 248-25.

Simonsen, I., Hansen, A., Nes, O.M., 1998. Using wavelet transforms for Hurst exponent determination. *Phys. Rev. E.* 58, 2779-2787.

Simonsen, I., Vandembroucq, D., Roux, S., 2000. Wave scattering from self-affine surfaces. *Phys. Rev. E.* 61, 5914-7.

Singh, S., Suárez, G., 1988. Regional variation in the number of aftershocks ($m_b \geq 5$) of large, subduction-zone earthquakes ($M_w \geq 7.0$). *Bull. Seism. Soc. Am.* 78(1), 230-242.

Skjetne, E., Hansen, A., Gudmundsson, J.S., 1999. High-velocity flow in a rough fracture. *Journal of Fluid Mechanics*, 383:1-28.

Smith, R.B., 1977. Formation of folds, boudinage, and mullions in non-Newtonian materials. *Geol. Soc. Amer. Bull.* 88, 312-320.

Stein, M.L., 2002. Fast and exact simulation of fractional Brownian sufaces. *J. Comput. Graph. Statist.* 11, 587-599.

Tchalenko, J.S., Berberian, M., 1975. Dasht-e Bayaz fault, Iran: earthquake and earlier Related structures in bed rock. *Bull. Geol. Soc. Am.* 86, 703-709.

Tchalenko, J.S., 1970. Similarities between Shear Zones of Different Magnitudes. *Bull. Geol. Soc. Am.* 81, 1625-1640.

Tchalenko, J.S., Ambraseys, N.N., 1970. Structural analysis of the Dasht-e Bayaz (Iran) earthquake fractures. *Bull. Geol. Soc. Am.* 81, 41–60.

Thomas, A.L., Pollard, D.D., 1993. The geometry of echelon fractures in rock: implications from laboratory and numerical experiments. *J. Struct. Geol.* 15, 323-334.

Thouvenot, F., 1998. The ML 5.3 Epagny (French Alps) earthquake of 1996 July 15: A long-awaited event on the Vuache Fault. *Geophys. J. Int.* 135, 876-892.

Tinti, E., Spudich, P., Cocco, M., 2005. Earthquake fracture energy inferred from kinematic rupture models on extended faults. *J. Geophys. Res.* 110, doi:10.1029/2005JB003644.

Twiss, R. J., Moores, E.M., 1992. Structural Geology, W. H. Freeman, New York.

Vallée, M., Landès, M., Shapiro, N. M., Klinger, Y., 2008, The 14 November 2001 Kokoxili (Tibet) earthquake: High-frequency seismic radiation originating from the transition between sub-Rayleigh and supershear rupture velocity regimes. *J. Geophys. Res.* 113, B07305, doi:10.1029/2007JB005520.

Voss, R.F., 1985. Scaling Phenomena in Disorder Systems, Plenum, New York.

Wallace, R.E., Whitney R.A., 1984. Late Quaternary history of the Stillwater Seismic Gap, Nevada. *Bull. Seismol. Soc. Am.* 74, 301-314.

Wallace, E.W., Morris, H.T., 1986. Characteristic of faults and shear zones in deep mines. *Pure Appl. Geophys.*, 124, 107-125.

Wechsler, N., Ben-Zion, Y., Christofferson, S., 2010. Evolving Geometrical Heterogeneities of Fault Trace Data. *Geophys. J. Int.* in press.

Venkataramn, A., Kanamori, H., 2004. Observational constraints on the fracture energy of subduction zone earthquake. *J. Geophys. Res.* 109, doi:10.1029/2003JB002549.

Voisin, C., Campillo, M., Ionescu, I., Hassani, R., Nguyen, Q.-L., 2002a. Process and signature of initiation on a finite fault system: a spectral approach. *Geophys. J. Int.* 148, 120-131.

Voisin, C., Ionescu, I., Campillo, M., 2002b. Crack growth resistance and dynamic rupture arrest under slip dependent friction. *Physics of the Earth and Planetary Interiors*, 131, 279-294.

Voss, R.F., 1985. Scaling Phenomena in Disorder Systems, Plenum, New York.

Wald, D.J., Heaton, T., 1994. Spatial and temporal distribution of slip for the 1992 Landers, California, earthquake. *Bull. Seism. Soc. Am.* 84, 668-691.

Walsh, J.J., Watterson, J., 1988. Analysis of the relationship between Displacements and dimensions of faults. *J. Struct. Geol.* 10(3), 239-247.

Watterson. J., 1986. Fault dimensions, displacements and growth. *Pure Appl. Geophys.* 124, 365-373.

Wesnousky, S.G., 1988. Seismological and structural evolution of strike-slip faults. *Nature*, 335(22), 340-343, doi:10.1038/335340a0.

Wesnousky, S., 2006. Predicting the endpoints of earthquake ruptures. *Nature*, 444(7117), 358-360, doi:10.1038/nature05275.

Wesnousky, S., 2008. Displacement and Geometrical Characteristics of Earthquake Surface Ruptures: Issues and Implications for Seismic-Hazard Analysis and the Process of Earthquake Rupture. *Bull. Seismol. Soc. Am.*, 98, 1609-1632.

Willemse, E.J.M., Pollard, D.D., Aydin, A., 1996. Three-dimensional analyses of slip distributions on normal fault arrays with consequences for fault scaling. *J. Struct. Geol.* 18, 295-309.

Woodcock, N.H., Schubert, C., 1994. Continental strike-slip tectonics. In Hancock, P. L. (eds.): Continental Deformation, Pergamon Press, 251-263.

Woodcock, N.H., Mort, K., 2008. Classification of fault breccias and related fault rocks. *Geol. Mag.* 145, 435-440.

Zhanyu, W., Honglin, H., Feng, S., Xiang, G., Changpeng, X., 2010. Topographic characteristics of rupture surface associated with the Wenchuan earthquake of Mw7.9, in May 12, 2008. *Bull. Seismol. Soc. Am.*, in press.

Zöller, G., Holschneider, M., Ben-Zion, Y., 2005. The role of heterogeneities as a tuning parameter of earthquake dynamics. *Pure Appl. Geophys.* 162, 1027-1049. doi :10.1007/s00024-004-2660-9.